ASPECTS OF MOLTEN FLUORIDES AS HEAT TRANSFER AGENTS FOR POWER GENERATION

PROEFSCHRIFT

TER VERKRIJGING VAN DE GRAAD VAN DOCTOR IN DE TECHNISCHE WETENSCHAPPEN AAN DE TECHNISCHE HOGESCHOOL DELFT, OP GEZAG VAN DE RECTOR MAGNIFICUS PROF. DR. IR. F.J. KIEVITS VOOR EEN COMMISSIE AANGEWEZEN DOOR HET COLLEGE VAN DEKANEN, TE VERDEDIGEN OP WOENSDAG 14 FEBRUARI 1979 DES MIDDAGS OM 13.30 UUR

DOOR

BAUKE VRIESEMA

werktuigkundig ingenieur

geboren te Uithoorn

Dit proefschrift is goedgekeurd door de promotor
PROF. IR. D. G. H. LATZKO

	page
TABLE OF CONTENTS	0.5
LIST OF SYMBOLS	0.10
ABSTRACT	0.13
1. INTRODUCTION	1.1
2. FLOW MEASUREMENTS	2.1
2.1. Introduction	2.1
2.2. Venturi flow meter	2.2
2.2.1. Special features	2.2
2.2.2. Description of equipment	2.3
2.2.2.1. The venturi	2.3
2.2.2.2. The control system	2.3
2.2.2.3. Safety	2.4
2.2.2.4. Instrumentation	2.5
2.2.3. Accuracy	2.5
2.3. Thermal flow measurement	2.6
2.3.1. Introductory remarks	2.6
2.3.2. Description of the method	2.6
2.3.3. Description of the equipment	2.8
2.3.3.1. Probe	2.8
2.3.3.2. Electronic output adjustment	2.8
2.3.4. Accuracy	2.9
2.4. Transit time measurement	2.11
2.4.1. Introductory remarks	2.11
2.4.2. Description of the method	2.12
2.4.3. Description of equipment	2.14
2.4.4. Accuracy	2.16
2.5. Test program for flow measurements	2.18
2.6. Experimental results	2.19
2.7. Conclusions	2.19
3. TURBULENT HEAT AND MOMENTUM TRANSFER	3.1
3.1 Introduction	3.1
3.2. Heat transfer	3.1
3.2.1. Introductory remarks	3.1
3.2.2. Description of the test module	3.1
3.2.3. Description of the loop	3.2
3.2.4. Outline of the method	3.2
3.2.5. Instrumentation	3.2
3.2.6. Data reduction and processing	3.3
3.2.7. Calibration	3.4
3.2.8. Accuracy	3.5
3.2.9. Test program	3.8

page

3.2.10. Experimental results 3.8
3.2.11. Discussion of results 3.8

3.3. Momentum transfer 3.9

3.3.1. Introductory remarks 3.9
3.3.2. Description of the method 3.9
3.3.3. Description of equipment 3.10

3.3.3.1. Test tube 3.10
3.3.3.2. Differential pressure measurement 3.10

3.3.4. Test program 3.11
3.3.5. Experimental results 3.11
3.3.6. Accuracy 3.11
3.3.7. Discussion of results 3.11

4. BAYONET TUBE STEAM GENERATOR 4.1

4.1. Introduction 4.1

4.1.1. General back-ground 4.1
4.1.2. The bayonet tube steam generator 4.2

4.1.2.1. Design characteristics 4.2
4.1.2.2. Potential interest 4.4

4.1.3. Aims and scope of the present investigations 4.4

4.1.3.1. Steady state behaviour 4.5
4.1.3.2. Dynamic behaviour 4.6

4.1.3.2.1. Large transients 4.6
4.1.3.2.2. Stability 4.6

4.2. Basis for analysis 4.7

4.2.1. General assumptions 4.7
4.2.2. Balance equations 4.8

4.2.2.1. Single-phase flow 4.9
4.2.2.2. Two-phase flow 4.9

4.2.2.2.1. Thermal equilibrium 4.9
4.2.2.2.2. Thermal non-equilibrium 4.10

4.2.2.3. Energy balance of the wall 4.11

4.2.3. Empirical relations 4.12

4.2.3.1. Transition criteria 4.12

4.2.3.1.1. Preheat-subcooled 4.12
4.2.3.1.2. Subcooled-saturation boiling 4.12
4.2.3.1.3. Saturation boiling-mist flow 4.12
4.2.3.1.4. Mist flow-superheat 4.13

4.2.3.2. Heat transfer correlations 4.13
4.2.3.3. Frictional pressure drop correlations 4.14
4.2.3.4. Slip correlations 4.15
4.2.3.5. Heat distribution parameter 4.16

4.3. Test facility 4.16

4.3.1. Test module 4.16

page

4.3.1.1. Heating fluid 4.16
4.3.1.2. Flow pattern 4.16
4.3.1.3. Process conditions 4.17
4.3.1.4. Dimensions 4.17

4.3.2. Water/steam loop 4.17

4.3.2.1. General 4.17
4.3.2.2. Feedwater supply system 4.18
4.3.2.3. Heat sink 4.18

4.3.3. Instrumentation and control 4.18

4.3.3.1. Loop instrumentation and control 4.18
4.3.3.2. Test instrumentation 4.19

4.3.3.2.1. Instrumentation for steady state and transient experiments 4.19
4.3.3.2.2. Instrumentation for the stability experiments 4.20
4.3.3.2.3. Calibration 4.20

4.3.4. Operational procedures 4.21

4.4. Steady state 4.22

4.4.1. Analysis 4.22

4.4.1.1. Additional assumptions 4.22
4.4.1.2. Modified equations 4.23
4.4.1.3. Solutional procedure 4.24

4.4.2. Experiments 4.24

4.4.2.1. Data acquisition 4.24
4.4.2.2. Test program 4.27
4.4.2.3. Experimental results 4.28

4.4.3. Evaluation of results 4.28

4.5. Transients 4.28

4.5.1. Introduction 4.28
4.5.2. Analysis 4.29

4.5.2.1. Modified equations 4.29
4.5.2.2. Solution in Eulerian co-ordinates (DYBRU) 4.30
4.5.2.3. Solution in Lagrangian co-ordinates (DSTS) 4.31

4.5.3. Critique of the methods employed 4.33
4.5.4. Experiments 4.34

4.5.4.1. Data acquisition 4.34
4.5.4.2. Test program 4.36
4.5.4.3. Experimental results 4.36

4.5.5. Evaluation of results 4.37

4.5.5.1. Introductory remarks 4.37
4.5.5.2. Comparison of DYBRU with an experiment 4.37
4.5.5.3. Comparison of DSTS with an experiment 4.37

4.6. Stability 4.37

4.6.1. Analysis 4.37

page

4.6.1.1. Introductory remarks 4.37
4.6.1.2. Identification of characteristic sections 4.42

4.6.1.2.1. Linearized analysis of the total system 4.42
4.6.1.2.2. Linearized description of subsystems 4.43
4.6.1.2.3. Stability criteria 4.45

4.6.1.3. Analysis in the time domain 4.49

4.6.1.3.1. Introductory remarks 4.49
4.6.1.3.2. Additional assumptions 4.49
4.6.1.3.3. Modified equations 4.50
4.6.1.3.4. Solutional procedure 4.50

4.6.1.4. Analysis in the frequency domain 4.52

4.6.1.4.1. Extensions in the model 4.52
4.6.1.4.2. Modified equations 4.57
4.6.1.4.3. Solutional procedure 4.58
4.6.1.4.4. Program structure 4.61

4.6.2. Stability experiments 4.63

4.6.2.1. Introductory remarks 4.63
4.6.2.2. Experimental procedure and data acquisition 4.64
4.6.2.3. Test program 4.65

4.6.3. Evaluation of analytical and experimental results 4.65

4.6.3.1. Introductory remarks 4.65
4.6.3.2. Preliminary program verification in the frequency domain 4.65

4.6.3.2.1. Eigenvalue analysis 4.65
4.6.3.2.2. Frequency analysis 4.65

4.6.3.3. 1 MW_{th} steam generator experiments 4.66

4.6.3.3.1. Outline of experiments 4.66
4.6.3.3.2. Eigenvalue analysis 4.66
4.6.3.3.3. Frequency analysis 4.66

4.6.3.4. SWISH experiments 4.67

4.6.3.4.1. Outline of experiments 4.67
4.6.3.4.2. Frequency analysis 4.67

4.6.3.5. Bayonet tube experiments 4.67

4.6.3.5.1. Time domain analysis 4.67
4.6.3.5.2. Frequency domain analysis 4.68
4.6.3.5.3. Additional remarks 4.68

5. CONCLUSIONS AND RECOMMENDATIONS 5.1

ACKNOWLEDGEMENTS 6.1

REFERENCES 7.1

SAMENVATTING 8.1

		page
APPENDIX 2A	Thermal conductivity of FLiNaK	2A.1
APPENDIX 3A	Error analysis of the friction pressure drop measurement	3A.1
APPENDIX 4A	Energy balances for the subcooled region	4A.1
APPENDIX 4B	An adapted version of the Bankoff-Jones slip correlation	4B.1
APPENDIX 4C	The derivative of the specific mass of two-phase mixtureswith respect to the mixture enthalpy	4C.1
APPENDIX 4E	Derivation of the equations describing the total system	4E.1
APPENDIX 4F	Explanation for the existence of predominant modes ofparallel channel instability	4F.1
APPENDIX 4G	Zero's of $H_{p\phi}$ and $\|M\|_{res}$	4G.1
APPENDIX 4H	Details of discretization, linearization and substitution steps in the solutional procedure	4H.1
APPENDIX 4J	Example of an application of the SLINQ program for substitution of linear equations	4J.1
APPENDIX 4K	Power method and vector deflation as applied for determining eigenvalues in the CURSSE program	4K.1
REFERENCES PERTAINING TO APPENDICES		9.1

LIST OF SYMBOLS

A	= area	m^2
C	= coefficient	-
c	= specific heat	J/kg ^0C
D	= diameter	m
E	= mathematical expectation	-
f	= friction factor	-
g	= gravity constant	m/s^2
G	= mass flux	kg/m^2s
h	= enthalpy	J/kg
H	= transfer function	-
Im	= imaginary part	-
K	= total conductivity	J/m^2 ^0C
	= heat distribution factor	-
l,L	= length	m
M	= mass	kg
Nu	$= \frac{\alpha D}{\lambda}$ = Nusselt number	-
O	= perimeter	m
p	= pressure	N/m^2
P	= power	J/s
Pr	= Prandtl number	-
q	= heat flux	J/m^2s
Q	= heat flow	J/s
r	= radius	m
R	= covariance function	-
Re	= Reynolds number	-
	= Real part	-
s	= Laplace operator	-
	= slip factor	-
S	= spectral density function	-
t	= time	s
u	= internal energy	J/kg
v	= velocity	m/s
w	= width	m
x	= steam quality	-
z	= axial co-ordinate	-
Z	= impedance	-

GREEK SYMBOLS

α	= heat transfer coefficient	$J/m^2\ ^0C$
	= void fraction	-
δ	= small variation	-
	= small distance	m
ε	= error	-
	= angle with upward vertical	rad
ζ	= pressure loss coefficient	-
η	= dynamic viscosity	Ns/m^2
θ,ϑ	= temperature	^0C
λ	= thermal conductivity	$J/m\ ^0C$
	= real part of eigenvalue	-
ρ	= specific mass	kg/m^3
τ	= delay time	s
	= wall shear stress	N/m^2
$\emptyset$	= mass flow rate	kg/s
	= heat flow rate	J/s
ω	= angular velocity	rad/s
	= imaginary part of eigenvalue	-

SUBSCRIBTS

b	= bulk
c	= correction
	= cross-sectional
cr	= critical
d	= delay
Do	= dry-out
E	= Eulerian
EV	= evaporator channel
f	= finish
fl	= film
fr	= friction
FL	= FLiNaK channel
g	= gas
h	= heated
inc	= inconel
H	= header
	= hydraulic
l	= liquid
	= lower

lg = evaporating
= latent

L = Lagrangian

m = mass
= measured

p = pressure
= primary (salt) channel

r = released

res = resulting

s = start
= steam
= secondary (water/steam) channel

sat = saturated

t = transferred

tf = two-phase

tot = total

u = upper

v = volume

ve = venturi

w = wall

MISCELLANEOUS

- = average value,
= mixture property

^ = maximum value

ABSTRACT

The present thesis consists of two distinct parts. The first of these deals with the potential application of a molten salt mixture as heat transfer agent at temperatures well beyond 500 ^{0}C. The need for such applications, which exclude more usual low pressure fluids, may arise from new chemical processes. The fluid in question, the ternary eutectic of the fluorides of lithium, sodium and potassium known as FLiNaK, is highly corrosive.
Chapter 2 evaluates three different methods for measuring mass flow rates of such a corrosive liquid at elevated temperatures, based on venturi, "hot finger" and transit time techniques, respectively. The evaluation was performed on pilot plant scale in a molten salt loop.
The same loop was then used to establish empirical correlations for heat transfer and frictional pressure drop. These experiments, using a salt-to-air heat exchanger and a calibrated tube respectively, are reported in Chapter 3 together with the resulting correlations.
The second part of the thesis deals with the thermo-hydraulic performance of bayonet tube steam generators. The relation with the first part is given by the fact that this design offers the only possibility for subcritical steam raising plant heated by FLiNaK or other fluoride mixtures because of the high melting points of these fluids. The need for such steam raising plant may result from continued development of molten salt thermal breeder reactors. For each of the three aspects of thermo-hydraulic design covered in Chapter 4, viz.:

- steady state behaviour (full and part load)
- transient behaviour
- hydro-dynamic stability,

one or more computer programs were developed and subsequently verified by comparison with experimental results obtained on a single tube test module with rated steam conditions of 18 MPa/540 ^{0}C.
In the course of developments in the latter area it became clear that a continuing need existed for a simulation program capable of predicting operating limits imposed by either parallel channel or loop instability for once-through steam generators of various geometries. To that end a modular user-oriented program (CURSSE) was developed in the frequency domain and verified by comparison with experimental results obtained both on the above bayonet tube test module and on two different steam generators tested elsewhere.
The conclusions for both parts of the thesis as presented in Chapter 5 may be summarized as follows:

- FLiNaK appears well suited as heat transfer agent in the 500 - 700 ^{0}C temperature range
- bayonet tube design present a technically promising, though perhaps economically questionable, alternative for raising steam in molten salt breeder reactor systems
- the CURSSE program was proven a flexible and reliable tool for predicting the stability limits of once-through steam generators of various geometries.

1. INTRODUCTION

The research project underlying the present thesis originated in 1963 as a joint undertaking between Euratom Joint Research Center (Petten Establishment) and Delft University of Technology, Laboratory for Thermal Power Engineering. The project's aim was to generate knowledge in the field of heat transfer by molten fluorides, notably regarding:

- heat transfer and heat transport capability, with special reference to a ternary eutectic mixture of NaF, LiF and KF further to be referred to as FLiNaK
- the technology of a heat transfer system operating in the 500 - 700 ^{0}C temperature range at an semi-industrial (= pilot plant) scale
- special instrumentation capable of reliable service for prolonged periods in heat transfer systems such as described in the preceding paragraph.

The Euratom interest in the development of molten salt technology stemmed from their potential of these fluids as fuel carrier in fluid fuel nuclear reactors, as demonstrated by the operation of the 10 MWth Molten Salt Reactor Experiment (MSRE) at Oak Ridge National Laboratory from 1966 to 1970.
The University's interest was mainly focussed on the second objective mentioned above, bearing in mind that molten salts constitute one of the two groups of heat transfer agents capable of operation in the 500 - 700 ^{0}C temperature range at near atmospheric pressures without chemical stability problems. The fact that the other group, viz. liquid metals, were already under extensive study both worldwide and in the Netherlands in connection with the development of fast breeder reactor cooling systems and the fire hazard associated with their use suggested the study of molten salts as potential heat transfer agents in high temperature process plant as a worthwhile object for a technologically oriented university laboratory.
Continuing development work on the molten salt reactor concept at Oak Ridge made it increasingly apparent that its eventual transition into the electric power generating stage would require the solution of a number of difficult problems in connection with the design of a molten salt heated steam generator.
These problems are mainly due to the high melting point of the heating salt, combined with the thermal stress problems inherent to high temperature liquid systems. With the solution of these problems at Oak Ridge National Laboratory being delayed by budgetary restrictions the laboratory for Thermal Power Engineering was presented with an opportunity for active participation in this area by investigating the so-called bayonet tube design as a possible solution.
The availability of the FLiNaK primary loop made it possible to construct a salt-heated steam generator test facility with relatively little effort.
Feasibility of the bayonet tube steam generator was investigated with respect to three aspects of the thermo-hydraulic design:

- steady state behaviour at various loads
- transient behaviour
- hydrodynamic stability.

The last two aspects appeared of particular interest because of the extensive work on steam generator dynamics under way for other projects in the same laboratory.
The present author's association with the above project further to be referred to as the Delft Molten Salt Project (DMSP), lasted from August 1969 until its termination in April 1978. Accordingly the work described in

this thesis covers both phases of the project. Investigations concerning the thermo-hydraulic behaviour of FLiNaK and the associated special measuring techniques form the subjects of Chapter 2 and 3. Analytical and experimental investigations of the bayonet tube steam generator thermo-hydraulics are dealt with in Chapter 4.
Any research report covering a period of over 8 years is liable to contain parts which are either obsolete by the time of publication and/or make the author realise in hindsight that a different approach or some supplementary effort might have yielded better results. The latter is particularly true in the area of steam generator transient analysis, where the impending termination of the project foreclosed both additional experiments and further elaboration of simulation codes. It is the author's hope that the work reported in this area and some of the analytical work on steam generator stability may prove of sufficiently general interest for others to extend and improve upon it.
These aspects which have been studied both analytically by computer simulations and experimentally in the specially designed single tube test facility are discussed in Chapter 4.

2. FLOW MEASUREMENTS

2.1. Introduction.

The availability of a suitable flow measuring device is essential for the application of any fluid as an industrial heat transfer agent. For most fluids differential pressure type flow meters (e.g. using a venturi-type restriction) are entirely adequate; with this type of device a vast amount of industrial experience has been accumulated over many years.
However, in the case of molten fluorides and similar high melting salts the very high temperature level (500 - 700 ^{0}C) and the corrosivity of the fluid exclude the application of such standard flow meters.
Fluids posing similar problems are:

- toxic fluids
- corrosive liquids (acids)
- liquid metals (e.g. sodium)

Especially in the latter case the problems are very similar to those for molten salts, and considerable efforts have been made for their solution within the framework of LMFBR development activities.
However, unfortunately for the project under discussion, by far the largest and most successful part of these efforts has gone into the development of electromagnetic devices. In these devices a magnetic field is induced in the flowing liquid at right angles to the magnetic field and to the velocity.
To pick up this e.m.f. two electrodes are provided in the wall of the tube. Unless the resistivity of the fluid approximates that of the pipe wall material, as is the case for liquid metals, the electrodes have to be electrically insulated from the pipe wall. Up till now no insulated electrodes are available that are leaktight at the molten salt operating temperature level, thereby excluding application of this method in molten salt systems.
Of the other flow measuring systems considered by the author the following two seemed most promising for this latter application:

- transit time flow meter
- thermal flow meter

Their advantages and disadvantages are discussed in detail in TURNER [2.1-1]. In the following only their potential for molten salt flow measurement will be taken into consideration.
On the other hand it was evident that of the two parts making up a differential flow meter, viz.

- the restriction causing the pressure differential
- the differential pressure measurement

only the latter gives rise to serious problems for the application envisaged here.
Thus two alternative and complementary roads towards a practical and reliable flow measuring device seemed open to the author:

- development of a diffential pressure transmitter suitable for molten salts; in practice this meant transforming the pressure of the salt into that of an other fluid of easier handling characteristics
- investigation of the other measuring principles mentioned above.

The former approach, in addition to adhering to normal industrial practice, has the major advantage of offering the possibility for reliable analytical determination of its characteristics, so that calibration of the flow meter

is unnecessary unless a very high accuracy is needed (better than 2%, which is the maximum accuracy that can be obtained for a venturi, manufactured in accordance with the V.D.I. DURCHFLUSZMESZREGELN [2.2-2]).
Where calibration is required, the results obtained in a water system can be converted for application in any fluid, including molten salts.
On the other hand, transit time flow meters offer the potential of high long term reliability through a minimum of equipment in the molten salt environment, while the thermal flow meter, in addition to being also a relatively simple device, would capatalize on the heat transfer measurement techniques extensively investigated in the remainder of the project.
Hence both roads were pursued; the results are described in the next sections.

2.2. Venturi flow meter.

2.2.1. Special features.

The principle of measuring flows through pressure differences across orifices such as venturi tubes has been successfully applied in industrial practice for many years. The discussion in the present thesis will therefore be restricted to the special features resulting from its application to molten fluorides at up to 700 ^{0}C.
The high temperature and the corrosivity of the salt make it impossible to fill the piping to the differential pressure transmitter and the transmitter itself with the fluid to be measured, as is customary in venturi liquid flow measurements.
This problem can be solved by the application of an intermediate system filled with a different fluid of easier handling characteristics between the venturi and the differential pressure meter.
One possibility is the use of a liquid, separated from the salt by a membrane. This fluid has to be proof against the operating temperature and should preferably be in the liquid state at room temperature.
This approach, shown in figure 2.2-1, has been tested in the Oak Ridge National Laboratory using NaK as intermediate fluid (cf. BRIGGS [2.2.1]).
There are, however, a number of disadvantages to this all-welded design:

- while the dP-meter can be of standard design, it has to be specially fabricated and filled with NaK
- calibration after installation is not possible
- the instrument proved rather sensitive to temperature changes in the system
- in case of breakdown replacement of the dP-meter is difficult.

The major advantage of the all-welded design is its complete leaktightness.
An other possibility is the use of a gas as intermediate fluid. This system was tested in our laboratory. To transform salt pressure into gas pressure use is made of two small vessels between the venturi and the differential pressure transmitter, each connected to one of the pressure taps of the venturi. In these vessels the FLiNaK level is kept at a constant height by adjusting the cover gas (argon) supply to - or release from - the gas-filled space (cf. figure 2.2-2).

The resulting cover gas pressure difference between the two vessels is the same as the pressure difference across the two venturi taps.
This transforms the problem of measuring the molten salt pressure differential into the much simpler one of measuring a differential gas pressure.

2.2.2. Description of equipment.

2.2.2.1. The venturi.

The venturi itself was designed and machined according to the V.D.I. DURCHFLUSZMESZREGELN [2.2-2] (cf. figure 2.2-3).
Normally such a venturi does not require calibration. In this case, however, the dimensions were somewhat below the normal DIN range and a calibration was therefore considered necessary.
This calibration, performed by the staff of the "Waterloopkundig Laboratorium Delft" (VERBEEK [2.2-3]) using water as the working fluid, resulted in the following characteristic formula:

$$\phi_m = 1.15 \times 10^{-3} \sqrt{\Delta p \, \rho} \pm 1.2\% \text{ kg/s} \qquad (2.2\text{-}1)$$

(Δp in N/m^2, ρ in kg/m^3)

The accuracy stated above resulted from the calibration and is valid for Re-numbers over 1.4×10^4.

The Re-number for FLiNaK in this venturi in the range of interest is given in figure 2.2-4 as a function of mass flow and temperature.

2.2.2.2. The control system.

As stated in subsection 2.2-1 the method requires equalization of the salt levels in the two expansion vessels by adjusting the cover gas pressures where required.
While it would be sufficient to maintain both levels at the same (varying) height, this is more difficult to achieve in practice than to keep them both constant.
Because of the problems encountered in designing a level gauge capable of continuous level measurement, the idea of applying a continuous control system was abandoned in favour of a simple on-off control system.
Two alternative control systems based on the above method of level detection were successively tested.
The second and final system will be described first. In this system (cf. schematic diagram figure 2.2-5) the level is detected by three electrodes making or breaking contact with the fluid in the expansion vessels. These electrodes are mounted in the upper part of the expansion vessels by means of a gastight ceramic insulation (figure 2.2-6).
By measuring the electric resistance between the electrode and the vessel it is possible to detect whether the salt level is above or below the tip of the electrode.
If the level rises and passes the tip, contact is made and the electrical resistance drops to a very low value. However, if the level falls and passes the tip of the electrode contact is maintained until the liquid column developing under the electrode as a result of capillary forces (figure 2.2-7) collapses. The maximum height of this FLiNaK column was found to be about 2.5 mm for an electrode with a flat tip, decreasing as the tip of the electrode is sharpened. This phenomenon introduces a sort of dead band in the action of the electrode.
The shortest electrode forms no part of the control, but is part of the safety system, to be discussed in the next section.
The other two electrodes define a discrete interval in height within which the level is maintened by the control system. If the level rises above the tip of the shorter electrode gas is supplied to the gas-filled space in the

expansion vessel, thus driving the level down again until contact is broken. On the other hand, if the level falls below the tip of the longer electrode, gas is released from the vessel to allow the level to rise again until contact is re-established.
Under steady state conditions the level remains in the interval between the ends of the electrodes without any action of the control system; fluctuations within this interval are discernible as ripples in the output signal of the flowmeter, as e.g. in figure 2.2-8, showing a change in flow from one steady state value to another and the reactions of the control system.
The control system described above was developed from an earlier version, originally thought to be simpler amd more accurate. In that system each vessel contained only one control electrode (schematic diagram figure 2.2-9). During operation gas was released from the vessels at a constant rate. If the salt level rose so high that contact was made with the electrode, gas was supplied at a rate exceeding the release rate, thus driving down the level. As in the previous system the salt column under the electrode introduced a dead band in the system's reaction.
This seemingly simpler system was found to possess a number of disadvantages:

- although for steady state conditions the maximum deviation of the level equals the maximum height of the salt column, much greater deviations could occur under dynamic conditions without being recognized as excessive by the control system.
- the salt level is never at rest. There is always salt flowing from the venturi to the vessel or vice versa, causing a frictional pressure drop across the connecting tube even under steady state conditions. This pressure drop causes an additional error in the differential pressure measurement, which in our experiments proved to be greater than the level deviations proper, as could be deduced from the response of the control system. This results in a greater total inaccuracy compared to the system described first.
- an additional inconvenience is the oscillatory behaviour of the system under steady state conditions as illustrated in figure 2.2-10 which shows a recording of the output signal.
- the "breathing" of the system causes a constant consumption of cover gas.

In view of these disadvantages the first system is considered preferable.

2.2.2.3. Safety.

The third or "alarm" electrode is added for safety. If for any reason an insufficient amount of gas is supplied to the vessel by the control system after the fluid has contacted the shortest control electrode, the level keeps rising and flooding of both expansion vessel and differential pressure transmitter might result.
To avoid this accident a large flow of cover gas at full pressure (6 bar) is admitted to the vessel as soon as the rising fluid contacts the alarm electrode. This ensures that the level is maintained in the vessel, unless a very large leakage occurs.
A further protective measure in the control systems is made necessary by mechanical vibrations in the loop, which induce waves on the salt surfaces in the expansion vessels. These waves can make and break the contact with the electrode very rapidly, causing rattling of the magnetic valves in the control system. This rattling - a very ominous sound for the operator - may result in excessive wear, decreasing the life time of the valves.

To avoid this effect a time delay was included in the electronic circuitry for each electrode in the manner shown diagrammatically in figure 2.2-11. This device slows down the reaction of the electrode. Contact must be closed for over 1 sec. before the magnetic valve reacts.

2.2.2.4. Instrumentation.

In addition to the equipment described above the instrumentation specific for the venturi flow measurements consists of:

- a differential pressure transmitter
- a voltmeter

The differential pressure transmitter used in our experiments is a 613 DM Foxboro d/p transmitter.

The voltmeter is part of the Hewlett & Packard 2012 D data acquisition system used for the data handling of all our experiments.
A schematic diagram of this part of the instrumentation is given in figure 2.2-12.

2.2.3. Accuracy.

In a venturi flow measurement there are two error sources:

- the equipment
- the density of the fluid

The equipment consists of four elements:

- the venturi
  The accuracy of the venturi used in our system is 1.2%, as explained in subsection 2.2.2.1.
- the differential pressure transformer, described in subsection 2.2.2.2.
  The simplicity of this system has to be paid for by a less accurate control action under dynamic conditions: during periods of gas supply or release (indicated by a signal from the control system) following flow transients the measurement is unreliable.
  Under steady state conditions, however, the additional error caused by the transformation from differential liquid pressure to differential gas pressure is very small. In the tested system the difference in lenght between the two control electrodes which equals the maximum difference in salt head is 10 mm. The pressure difference across the venturi taps at maximum flow (10 kg/s) and 650 ^{0}C is 0.037 MN/m^{2}, equivalent to 1830 mm of salt column.
  Thus the accuracy of the pressure transformation at maximum flow is $\approx$ 0.5%. As the absolute error is approximately constant, this inaccuracy is proportional with the reciproce of the flow.
- the differential pressure transmitter
  The accuracy of the Foxboro d/p cell transmitter type G13 DM is 1% of the span (5000 mm Wc).
- the voltmeter
  The Hewlett Packard data logger type 2012 D, used to measure the output voltage of the d/p cell, has an overall accuracy of 0.015% for the range used (0 - 100 mV).

The fluid density as given in the table shown in figure 2.2-13 for FLiNaK, is known within 5%. According to the Gaussian error law (cf. BEVINGTON [2.2-4]) the above inaccuracies yield a total inaccuracy of:

$$\varepsilon = \sqrt{(1.2^2 + 0.5\ (1^2 + 0.5^2 + 0.015^2) + 0.5*5^2)} = 4\%$$

of the maximum flow (10 kg/s).
This result may seem rather poor, but it should be noted that this is mainly due to the inaccuracy of the specific density. Without this factor the inaccuracy would be less than 1.5%.

2.3. Thermal flow measurement.

2.3.1. Introductory remarks.

Another type of flow measurement potentially suitable for highly corrosive fluids at high temperatures that has been tested is the so called thermal flow meter. There are two groups of thermal flow meters, each based on a different principle (cf. BENSON [2.3-1]). The first group measures the flow by adding heat to it. The resulting temperature rise is measured and related to the flow rate (cf. figure 2.3-1). The amount of heat that has to be transferred to the flow limits the application of this principle to small flow rates.
The second group, an example of which is discussed here, is based on the effect of the flow velocity on the temperature of a heated body inserted in the fluid. A well-known example of this group is the hot wire anemometer. The instrument described here was selected for its expected suitability for plant measurements under severe conditions, where ruggedness and reliability take precedence over high accuracy.

2.3.2. Description of the method.

When a heated probe is inserted in a fluid flow (cf. figure 2.3-2), it will rise in temperature until a state of equilibrium is reached between the heat transferred from the probe to the fluid and the heat generated in the probe.
Assume the total heat release rate to be ϕ_{w_r}. The heat transfer rate is:

$$\phi_{w_t} = \alpha\ A_h\ \Delta\theta \qquad (2.3\text{-}1)$$

Setting both heat rates equal yields the relation for the equilibrium temperature difference:

$$\Delta\theta = \frac{\phi_{w_r}}{A_h\ \alpha} \qquad (2.3\text{-}2)$$

The heat transfer coefficient of the fluid depends on the velocity and hence on the flow rate of the fluid. At a higher flow rate the heat transfer coefficient increases and if the heat release rate is kept constant, the temperature difference across the boundary layer decreases. This relationship between flow rate and temperature difference forms the basis of the method descibed. The nature of this relationship depends on the heat transfer correlation valid for the conditions in the flow meter. As established in subsection 3.2, a corrected version of the Dittus-Boelter correlation is valid for FLiNaK. Extending this correlation by a correction factor for annular flow derived in subsection 2.3.4 one obtains:

$$Nu = 0.020\ Re_b^{0.8}\ Pr_b^{0.4}\ \{\ 0.87\ (\frac{Di}{Do})^{-n}\ \} \qquad (2.3\text{-}3)$$

The exponent n in the correction for annular flow depends on the diameter ratio. A survey of the literature in this field (cf. subsection 2.3.4) yielded $n = 0.23 \pm 0.05$ as the most likely value for the diameter ratio of the thermal flow meter ($Di/Do = 0.51$).
Combination of equation (2.3-3) with the continuity equation:

$$\phi_m = \rho\ v\ A_c \qquad (2.3\text{-}4)$$

and with equation (2.3-2) yields the following relationship between mass flow rate and temperature difference across the boundary layer:

$$\phi_m = A_c\ (\frac{\phi_{w_r}}{A_h})^{1.25}\ (0.020)^{-1.25}\ \lambda_b^{-0.75}\ (\frac{\nu_b\ \rho_b}{c_p})^{0.5}\ D^{0.25}$$

$$\{0.87\ (\frac{Di}{Do})^{-n}\}^{-1.25}\ (\Delta\theta_m - \frac{\phi_{w_r}}{A_h}\ C_\theta)^{-1.25} \qquad (2.3\text{-}5)$$

In this relationship $\Delta\theta$ has been replaced by $(\Delta\theta_m - \frac{\phi_{w_r}}{A_h}\ C_\theta)^{-1.25}$,

where $\Delta\theta_m$ is the temperature difference actually measured by the equipment described in the next section, which will also contain the explanation for the correction factor C_θ.

This equation shows that the mass flow rate depends not only on the temperature difference, but also on a number of physical properties of the fluid and hence on its temperature. The table shown in figure 2.2-13 gives the relationships between these properties and temperature. While the density ρ and the kinematic viscosity ν are seen to vary significantly with temperature, the table indicates that λ and c may be considered independent of temperature for practical purposes.
Figure 2.3-3 compares thermal flow meter readings obtained from equation (2.3-5) using the data of table 2.2-13 at various temperatures to the venturi outputs. The temperature dependence evident in the former was found from a least squares analysis to be adequately described by:

$$f(\theta) = 5.15 - 0.0107\ \theta + 0.63\ 10^{-5}\ \theta^2 \pm 1.5\% \qquad (2.3\text{-}6)$$

where θ is the FLiNaK temperature (^0C).
It follows that the mass flow is defined by:

$$\phi_m = C_g\ f(\theta)\{\ \frac{\phi_{w_r}}{\Delta\theta_m - \frac{\phi_{w_r}}{A_h}\ C_\theta}\ \}^{1.25} \qquad (2.3\text{-}5A)$$

2.3.3. Description of the equipment.

2.3.3.1. Probe.

Figure 2.3-4 shows the first prototype of the thermal flow meter. For design reasons the probe was inserted in a bend of the primary loop in counterflow direction.
To avoid vibration and to ensure a fixed concentric position, the probe was provided with three radial fins at the tip.
An electrical resistance element was inserted in the hollow core for heating the probe. Four thermocouple pairs (1 mm Ø sheathed type) were installed for measuring the temperature difference over the boundary layer, each pair consisting of one thermocouple for measuring the bulk temperature of the fluid and another for measuring the wall temperature.
All thermocouples were fixed in grooves in the probe wall, leading from the measuring point to the passage through the outer tube wall.
This was done by metal spraying the probe until the grooves were completely filled, followed by milling to obtain a smooth surface.
The wall thermocouples were imbedded in the wall of the probe to ensure good contact between the couple and the surrounding metal.
In order to avoid distortion of the cilindrical shape of the probe, with its possible consequences on local heat transfer coefficients and thus on the temperature differences, the thermocouples had to be located below the surface of the probe. (cf. figure 2.3-5). This results in larger temperature differences being measured, due to the additional temperature drop across the metal layer between the thermocouple and the probe wall surface.
A number of investigators (e.g. MOELLER [2.3-2]) have studied this problem. They concluded that if the brazing material used to fasten the thermocouple in the wall has about the same thermal conductivity as the probe material, the temperature actually measured by the thermocouple is that which would occur in the probe at the same location (centerline of the thermocouple) if no couple were present. Figure 2.3-6 illustrates this conclusion.
In our case we have thermocouples sheated in Inconel-600 and brazed into the Inconel-600 probe with micro-braze of about the same chemical composition as Inconel-600, thus satisfying the above condition.
For obtaining the actual temperature difference across the boundary layer it therefore suffices to decrease the measured temperature difference by a correction:

$$\Delta\theta_c = \frac{\phi_w \, \delta}{A_h \, \lambda_{inc}} \qquad (2.3\text{-}7)$$

where, $\lambda_{inc.}$ is the thermal conductivity of the probe material and δ is the distance between thermocouple centerline and probe surface (cf. figure 2.3-5).
At maximum flow $\Delta\theta_c$ is about 50% of the total temperature difference measured.

2.3.3.2. Electronic output adjustment.

It is evident from equation 2.3-5 that the output from this type of flow meter, viz. the temperature difference, is not proportional to the measured flow. On the contrary, the measured temperature difference decreases with increasing flow.
For practical applications in power and process plant flow measurement a linear scale was considered essential, resulting in the need for electronic

output adjustment.
Figure 2.3-7 shows the design of an electronic correction device for linearization.
Another undesirable effect in the output of this flow meter requiring correction is its temperature dependence, as defined above by equation (2.3-6). An electronic correction device could also have been applied for this purpose. Prior to its implementation, however, the development of this type of flow meter was terminated. A computational correction according to equation (2.3-6) was applied to the flow meter output instead.

2.3.4. Accuracy.

The repeatability of the thermal flow measurement depends both on the magnitude of the variations in heat release rate and on the repeatability of the temperature difference measurement.
The heat release rate is proportional to $\frac{V^2}{R}$ where V is the supply voltage and R is the electrical resistance of the element.
Fluctuations of 10% (200 - 240 Volt) which can appear in the supply voltage V would cause errors of over 20% in the generated heat.
There are two different types of solution for this problem. Solutions of the first type control the heat release rate, either by means of an AC voltage stabilizer or by controlling the electrical power direcly by means of a thyristor power control system. However, for the power rating of the thermal flow meter - about 2 kW - both these solutions are rather expensive. The second possibility is to allow the heat release rate to vary, but to correct the reading of the measurement electronically for these variations. For this latter method only low current electronics are needed which are less expensive than the high current electronics applied in the two former solutions. Besides, an electronic correction device is needed anyhow, for the reasons stated in subsection 2.3.3.2, hence a power correction unit could easily be incorporated.
Utilizing standard electronic components such a system, had it been installed, which was not the case because deficiencies described hereafter led us to abandon the entire concept, might haved reduced the error caused by supply voltage fluctuations to less than 1%.

The repeatability of the temperature difference measurement can be divided into two parts:

- that of the thermocouple pair
- that of the amplifier and voltage measurement.

For both parts the two aspects "zero" and "gain" have to be considered. "Gain" is defined for the thermocouples as the ratio between an increase in temperature difference and the resulting rise in e.m.f. from the thermocouples. "Zero" is the e.m.f. measured at the couple pair if both thermocouples are at the same temperature. The change in gain is typically within 1% for the thermocouple used. The zero e.m.f., however, can be substantial in temperature difference measurements at high temperature levels.
The repeatability of the electronics (amplifier and electronic voltmeter depends on the quality of the instruments: for the kind of equipment used here the gain is typically constant within 0.1%. Possible changes in "zero" of both thermocouples and electronics can be corrected by a simple online calibration procedure. If the power supply to the electrical element is cut off, the temperature differences across the thermocouple pairs become zero. By correcting the level of the

amplifier both its own "zero" deviation and that of the thermocouple pair can be compensated. This brings the total repeatability of the thermal flow meter within the range of 2%. (two paired couples).
The accuracy of the flow meter can be established in two ways:

- by calibration
- by computation

In the first case the established accuracy equals the repeatability of the thermal flow meter, increased according to [2.2-4] with the accuracy of the standard flow meter used for calibration.

For a full-size flow meter (e.g. tube diameter 500 mm Ø) where calibration will be out of the question in most cases, the accuracy will have to be predicted by computation from the individual variables constituting the right-hand side of equation (2.3-5).

This relationship, derived in subsection 2.3.2, contains three sources of inaccuracy:

a) the correlation used for the heat transfer coefficient
b) the material proporties appearing in this correlation
c) the thermocouple measurements

ad a.:

The correlation applied is an adapted version of the well known Dittus-Boelter correlation, corrected for annular flow. Validation of this ccorrelation for molten salt heat transfer formed a separate aim of this project, discussed in section 3.2.
The coefficient 0.020 valid for flow in circular tubes is accurate within 3%.
However, the accuracy of the correction for annular flow of the usual form:

$$C\left(\frac{Di}{Do}\right)^{-n} \qquad (2.3\text{-}8)$$

requires some discussion.
The literature on this subject yields a great number of different values for both constant C - representing the ratio of the heat transfer coefficient for flow between two parallel plates and in a circular tube - and exponent n (cf. [2.3-3] through [2.3-9]). The value of 0.87 for the constant C is a theoretical prediction (cf. KAYS [2.3-9]) backed by experimental evidence; this value is considered accurate within 5%. The value of 0.23 chosen for n is the mean of a cluster of values given by a number of investigators for heat transfer in an annulus with a diameter ratio of about 0.5 (cf. figure 2.3-8).
The annulus correction given above is valid for an exactly concentric position of the heating element. This however, is very difficult to achieve. Therefore the effect of small eccentricities must be considered in the error analysis. As mentioned in subsection 2.3.3 the temperature difference in equation (2.3-5) is obtained by averaging the readings of the couple pairs positioned along the circumference of the heating element.
Thus only the effect of eccentricities on the mean temperature difference and therefore on the mean heat transfer coefficients has to be considered. Figure 2.3-9 shows results of an investigation by LEE [2.3-8] giving the effect of eccentricity on the mean heat

transfer coefficient for two different diameter ratios. The maximum eccentricity of the element is estimated al less than 0.5 mm or 5% when expressed relative to the gap width. Figure 2.3-9 shows that for a diameter ratio $\frac{Di}{Do} = 0.5$ a relative eccentricity of 0.05 causes a decrease in average heat transfer coefficient by about 2%.

ad b.:

The table given in figure 2.3-10 lists values for the various properties appearing in equation (2.3-5) and their inaccuracies. Amongst these, the FLiNaK thermal conductivity requires some comment. As discussed in Appendix 2A the accuracy of this physical property is insufficiently known. Lacking this information, a maximum error of 10% was assumed to yield a realistic overall accuracy.

ad c.:

The temperature differences are measured directly by connecting both thermocouples so that the resulting e.m.f. is the difference of the e.m.f.'s of the two separate couples. An accuracy of 1% can be obtained in this way after correction for zero reading errors caused by slight differences between individual thermocouples. To avoid effects of drift and of thermo-cycling on the thermocouples each series of measurements starting at a new temperature level was preceded by a zero reading calibration.

An error analysis, taking into account the above three sources of inaccuracy and the inaccuracies mentioned in connection with the repeatability, yields an overall inaccuracy of the mass flow of 15% at the maximum flow of 10 kg/s.
While this would at first sight seem a rather poor showing, one should keep in mind that this type of flow measurement has the unusual property of increasing accuracy with decreasing mass flow, whereas in general the accuracy of a measurement decreases with the measured value. As discussed before, this phenomenon is due to the opposite behaviour of the mass flow rate and the temperature difference related to it.
In conclusion it may be stated that the above error analysis has revealed two major disadvantages of this method, viz. the great number of physical properties occurring in equation (2.3-5) and the dependence on the accuracy of a heat transfer correlation. In combination these disadvantages tend to result in an unsatisfactory overall accuracy. Hence development of this type of flow meter was discontinued.

2.4. Transit time measurement.

2.4.1. Introductory remarks.

This method was included in the DMSP test program for two purposes:

- to provide a method entirely independent of physical properties of the fluid as a reference for the other measurements
- to verify the possibility for using simple temperature sensors in lieu of more elaborate and hence failure-prone devices for flow measurements in hostile environments.

2.4.2. Description of the method.

The principle of applying correlation techniques to instrument output signals for the purpose of measuring transit times and hence velocities is well-known and has been extensively described elsewhere (e.g. ALBERS [2.4-1], BENTLEY [2.4-2] and RANDALL [2.4-3]). We shall therefore restrict ourselves to a brief introductory outline.
As applied in our case the transit time measurement refers to thermal disturbances in the fluid traveling through a certain part of the DMSP loop (cf. figure 2.4-1). Two temperature sensors are installed a well-defined distance apart and the signals of both sensors are recorded. If no distortion of the temperature profile were to occur in the fluid the signal recorded from the downstream sensor would be identical to the signal of the upstream sensor, except for a delay time: the transport time from upstream to downstream sensor.
However, distortion of signals does occur in practice due to the following effects:

- flow disturbance
- electrical noise

which exclude determination of the transport times by visual inspection of the two recorded signals.
Flow disturbances affect the signal in two different ways, a predictable and a random one.
The predictable effect of such flow disturbances as turbulence and radial velocity gradients is to smooth the temperature profile present in the fluid. Several investigators, e.g. TAYLOR [2.4-7, 2.4-8] and SCHMIDTL [2.4-4], have shown that the result of these effects on the distribution of the mean cross-sectional temperature of turbulent flow in tubes can be described by the diffusion equation:

$$\frac{\partial \bar{u}}{\partial t} = k \frac{\partial^2 \bar{u}}{\partial x^2} \qquad (2.4\text{-}1)$$

Where k is the so-called Taylor diffusivity, a pseudo-diffusion coefficient, comparable with the thermal diffusivity $a = \frac{\lambda}{\rho c}$ in conduction heat transfer
The value of k can be approximated by:

$$k = 10.1\ R \sqrt{\frac{\tau_o}{\rho}} \qquad (2.4\text{-}2)$$

(cf. [2.4-8]).
x is a coordinate in a system moving in the direction of the tube axis with the average fluid velocity. This pseudo diffusivity is predictable and is part of the process in the tube between the two sensors. Its effect on the established delay times will be discussed later.
The second effect of the flow disturbances is the occurrence of a temperature noise superposed on the average temperature in a cross-section. The presence of these random disturbances requires the application of statistical techniques. Consider the block diagram of a time delay. The input signal is a random one, the output signal is the delayed input signal. The cross-covariance function of these two signals, defined as:

$$f(\tau) = E\{\delta v_1(t,\zeta) \cdot \delta v_2(t + \tau,\zeta)\} \qquad (2.4\text{-}3)$$

has the general shape of curve a in figure 2.4-2.

The covariance function $f(\tau)$ is maximum for $\tau = \tau_d$, i.e. the delay time.
If the output signal is influenced by some disturbance uncorrelated to the input signal the statistical technique applied reduces the effect of this noise. The cross-covariance function maintains its general shape and in particular the location of the top remains the same. However, if the correlated components in the signals are so weak that they are drowned in the thermal and electrical noise (insufficient signal/noise ratio) this method will also fail.
The cross-covariance function itself cannot be determined, but it can be estimated by a time integration:

$$\hat{f}(\tau) = \frac{1}{t_f - t_s} \int_{t_s}^{t_f} \delta v_1(t) \cdot \delta v_2(t + \tau) dt$$

where t_s and t_f define a time interval.
In the remainder of this section the term covariance function will be used both for this function proper and for the estimator $\hat{f}(\tau)$.
Figure 2.4-3 shows a typical cross-covariance function of our test signals. The top of this function is curved. The "radius" of this curvature depends on the highest frequency present in the signals. The higher the frequency the steeper the top, which increases the measuring accuracy of the transport time. A number of investigators (BENTLEY [2.4-2], RANDALL [2.4-3, 2.4-4], MUREY [2.4-5]) have tested this method of flow measurement for various fluids (air, water, sodium) and for particulate suspensions.
These tests can be divided into two categories:

1. measurement of the local velocity, e.g. for turbulence studies:
   the distance between the two sensors is in the order of the channel diameter.
2. measurement of the mean velocity:
   the distance between the two sensors is in the order of ten to one hundred channel diameters.

A condition for practical applications of the first category is the availability of fast sensors such as hot wire anemometers with a time constant small compared to the transport time. The use of normal thermocouples as sensors is limited to the second category because of their relatively large time constant. Even in this case - the one of interest for the present thesis - there are upper limits to the time constants which must be observed in order to obtain the desired accuracy.
Excessive time constants would filter the higher frequencies and thus cause an unfavourable ratio of transport time to width of the top of the cross correlation function.
The 1 mm thickness of the Inconel-sheathed thermocouples selected for the present measurements was considered a practical minimum for obtaining an adequate life time in the highly corrosive molten salts. A typical time constant of this type of thermocouples is 0.3 sec. (cf. GORDOV [2.4-6]). This is sufficiently low to obtain a satisfactory accuracy (cf. subsection 2.4.4.) for the application discussed here.
Furthermore, differences between the response characteristics of the two sensors must be avoided, as they might introduce a pseudo-delay decreasing the accuracy of the measurement.
In all the references relevant to measurements of the mean velocity ([2.4.2.], [2.4.3.], [2.4.4.], [2.4.5.]) the introduction of

artificial temperature disturbances has been found necessary for accurate measurement, because in practical cases the signal due to natural noise in the mean temperature is so weak that the correlated signals are drowned in the noise of the instruments used, in particular where high current devices for heating are present in the immediate surroundings.

2.4.3. Description of the equipment.

In our case a straight part of the primary loop was selected for the correlation flow measurement (cf. figure 2.4-5). The shape of the cross-covariance function is strongly dependent on sensor distance, as borne out by a comparison between figures 2.4-3 and 2.4-4, showing this function for our test signals as obtained with sensor spacings of 3200 and 200 mm, respectively. To determine the optimum distance between the sensing thermo-couples a series of 7 sensors with increasing spacing was applied (cf. figure 2.4-6). Each sensor consisted of four 1 mm. thermo-couples connected as a thermopile (cf. figure 2.4-7) in order to increase the signal of the sensor and thereby to obtain a higher signal-to-noise ratio. To obtain a high amplification without overloading the amplifier it is necessary to remove the dc component from the signal. To suppress the dc component in the signal the sensor was compensated by a series of four thermo-couples attached to the wall of the tube. These "slow" couples only follow the mean temperature of the salt. Thus the differences between the sensor and these compensating couples represented the fluctuations of the FLiNaK temperature. A diagram of the electronic equipment is given in figure 2.4-8. After the first amplifier the signal is filtered by means of a low pass filter (cut-off frequency 10 c/s) to remove high frequency noise which might overload the subsequent equipment. A high pass filter (cut-off frequency 0.7 c/s) is provided to suppress long-term drift which could shift the signals beyond the useful dynamic range of the amplifier. After the second amplifier the signal is either recorded on tape or on a line recorder, or directly connected to the correlator. The correlator used is a so called polarity coincidence correlator. Rather than computing the correlation function proper given in equation (2.4.1) this equipment only determines whether the signals have the same polarity or not. Mathematically this is given by:

$$\hat{p}(\tau) = \frac{1}{t_f - t_s} \int_{t_s}^{t_f} \text{sign}\,(v_2(t)) \cdot \text{sign}\,(v_1(t-\tau))\,dt \qquad (2.4\text{-}4)$$

VELTMAN [2.4-11] shows in detail that determination of the delay time from the pcc-correlation function yields the same result as from the correlation function proper, provided the frequency distribution function fulfills certain conditions. The accuracy of the correlation function thus obtained is somewhat lower, as the standard deviation of the pcc covariance function is a factor $\sqrt{\pi}$ greater than that of the covariance function proper. This is further discussed in subsection 2.4.4. The pcc-correlator is obviously much simpler and less expensive than a real correlator, which is an advantage for practical application of this method.
Figures 2.4-3, 2.4-4 and 2.4-9 show examples of pcc-correlation functions as recorded on an x-y recorder. The delay time is directly measured from this diagram.

Signals:

Tests have been carried out with three different types of signals:

- natural temperature noise
- artificial random signals
- thermal shocks

As mentioned above the tests with natural temperature noise failed as expected. Correlation could only be found over short distances and even for that case the response of the thermo-couples proved too slow for sufficient accuracy (cf. figure 2.4-9).
The introduction of artificial noise by diverting a small part of the flow through an air-cooled bypass somewhat sharpened the top of the correlation function, but did not lead to a significant improvement. The thermal shock type of signal was realized by stepwise increase of the heat supplied to the system in the main heater. This caused a temperature profile along the loop as shown in figure 2.4-10. It will be clear that with this single disturbance of the temperature the correlation technique could not be applied and the transit time had to be computed from the delay in response and the known distance between the sensors. An example of the line recordings of the two sensor signals is given in figure 2.4-11. While this method proved successful, it was recognized that the need for a sizeable stepwise power change severely limits its practical applicability. Moreover the averaging effect of the correlation technique is lacking in this case. Therefore a different way of introducing artificial noise was subsequently tested. A square wave generator was connected to the controller of the main heater and adjusted to generate fluctuations with an amplitude of 20% of full power. The frequency of the wave was varied at random, resulting in random fluctuations of the mean temperature of $\approx 0.1\ ^{0}C$ in a cross section. Correlation of these signals proved to be successful. The results will be discussed in section 2.6.

Note: The results of the measurements utilizing temperature fluctuations induced by thermal shocks show systematic deviations from the results obtained from the measurements utilizing artificial random temperature variations, the values obtained by the first method being consistently higher than those obtained by the second method.
These deviations can be explained by considering the mechanism of the turbulent mixing process present in the flow. This mixing does not affect the delay time obtained from the correlation of the two signals, corresponding to the mean velocity of the fluid in the cross-section. In the case of the thermal shock method, however, the velocity is derived from the delay of the first effect of a disturbance.
As there are always fluid particles, however few, which remain in the area of maximum velocity, especially in turbulent flow with its flat velocity profile, the first effect of a temperature disturbance is transported with a velocity very near the maximum velocity in the cross section. The mass flow rate derived from this delay time must therefore be corrected for this effect.
The correction factor, i.e. the mean velocity/maximum velocity ratio is given by HINZE [2.4-10] as:

$$\bar{v}/\hat{v} = \frac{2}{(n+1)(n+2)} \qquad (2.4\text{-}5)$$

where n is a function of Re.

In the range of measurements Re varies from $\approx 10^4 - 10^5$.
The corresponding range for n is from $\frac{1}{6.5}$ to $\frac{1}{7}$, yielding a correction of .805 - .817. The effect of this correction will be discussed in section 2.6.

2.4.4. Accuracy.

The possible sources of error in the correlation flow measurement can best be traced by following the path of the signal:

a. the first source of inaccuracy could lie in the process itself. If next to the delay time other mechanisms (e.g. turbulent mixing, wall effects) were to play a significant role, the top of the correlation function would shift away from $\tau = \tau_d$.

b. a second source of inaccuracy lies in the equipment for signal pick-up and processing. The theory deals with the signal as present in the fluid. In fact, however, the correlated signals have been influenced by the sensor and the subsequent filtering and amplification.

c. a third source of inaccuracy lies in the application of the correlation technique itself (finite observation time) and more in particular in the application of the polarity coincidence correlation technique (pcc).
In the following each of these sources of error will be discussed in some detail.

ad a.:

The presence of other mechanisms than the delay time proper would follow from the shape of the cross covariance function, viz. any process shifting the top away from $\tau = \tau_d$ causes an asymmetric shape of the cross covariance function.
This can be understood by assuming an arbitrary transfer function, solely characterized by the fact that the cross covariance function $R_{xy}(\tau)$ of the input signal x and the output signal y is symmetrical with respect to $\tau = \tau_d$. Assume a random input signal with arbitrary spectral density $S_{xx}(\nu)$. Random signal theory shows that for this signal the covariance function R_{xy} can be computed from:

$$R_{xy}(\tau) = \int_{-\infty}^{+\infty} S_{xy}(\nu)\, e^{j2\pi\nu\tau}\, d\nu \qquad (2.4\text{-}6)$$

where the cross spectral density is:

$$S_{xy}(\nu) = H(\nu)\, S_{xx}(\nu) \qquad (2.4\text{-}7)$$

Introduction of a new independent variable $\tau^{\star} = \tau - \tau_m$ and rearrangement of this equation yields:

$$R_{xy} = \int_{-\infty}^{+\infty} S_{xx}\{Re(H(\nu)).\ \cos(2\pi\nu\tau_m) + Im(H(\nu)).\ \sin(2\pi\nu\tau_m)\} * $$

$$* \cos(2\pi\nu\tau^{\star})d\nu$$

$$- \int_{-\infty}^{+\infty} S_{xx}\{Im(H(\nu))\cos(2\pi\nu\tau_m) + Re(H(\nu))\sin(2\pi\nu\tau_m)\} *$$

$$* \sin(2\pi\nu\tau^{\star})d\nu \qquad (2.4\text{-}8)$$

The first integral in the right hand side of this equation is symmetrical with respect to $\tau^{\star} = 0$ and therefore with respect to $\tau = \tau_m$. The second integral, however, is not.
To fulfill the assumed condition of symmetry it is therefore necessary that the second integral vanishes for any value of $\tau^{\star}$.
This means:

$$\{Im(H(\nu)\cos(2\pi\nu\tau_m) + Re(H(\nu))\sin(2\pi\nu\tau_m)\} = 0$$

which shows that the initial assumption of a symmetric cross-covariance function can only be valid if the transfer function satisfies the condition:

$$H(\nu) = A(\nu)\ e^{-j2\pi\nu\tau_m}$$

where $A(\nu)$ is a real function. In words: the transfer function must consists of a combination of a frequency dependent attenuation (or amplification) and a delay time of $\tau_d = \tau_m$.
As the cross-correlation functions of the measured signals have only a very slight asymmetry (cf. subsection 2.6) the delay times found are considered infinitely accurate as far as this aspect is concerned.

ad b.:

Although the dynamic behaviour of a thermocouple is more complicated Than that of a simple first order system, the time constant - defined as the time needed for a 63% response to an imposed temperature step - is a good measure for the rise time of the sensor in this application. For the 1 mm sheathed thermocouples utilized here the aforementioned time constant is 0.3 second ± 10% for a temperature step caused by dipping the couple in water.Although the non-linearity of the sensors does distort the signals, it does not affect the resulting delay time if the sensors are identical. Differences between the two sensors, however, cause an error in the delay time measured. As a first approximation this error can be defined by an additional positive or negative delay between the two sensors, equal to the difference in time constant of the two sensors.
The maximum error of 0.03 second in the sensor time constant causes a maximum additional delay time of 0.04 second (Gaussian error law). The maximum relative error occurs at the maximum velocity of approximately 5 m/s.
The maximum distance between two sensors in our experiments is 3.20 m corresponding to a delay time of 0.64 seconds at the maximum velocity.

Hence the maximum error due to differences between the two sensors will be 4%.

The subsequent electronic equipment does not cause additional delays; the absence of additional delays has been checked by interchanging the equipment used for the processing of both signals.
As the pcc-correlation only detects the polarity of the signals the accuracy of the amplification is of no account.

ad c.:

For a signal with e.g. a Gaussian distribution function it can be proven that the position of the top of the curve and thereby the established delay time is the same for the two types of functions VELTMAN [2.4-11]. It is very difficult, however, to derive the relationship between the correlation function proper and the polarity coincidence correlation function (pcc) for a signal with an arbitrary distribution function.
There is, however, a way around this problem. If each of the signals of the sensors is mixed with an artificial signal having a uniform distribution function, the resulting pcc function is an attenuated copy of the cross-covariance function of the two original signals, independent of the distribution function of these signals [2.4-11].
This technique was applied to some of the measurements in order to check the validity of the method applied.

As no difference in delay time could be detected between the signals processed with and without extra signals, it was concluded that the nature of signals proper obviated the need for these extra signals.
The effect of finite observation time is again difficult to evaluate theoretically. Therefore a number of measurements were processed for ten times the standard observation time (160 seconds). As this did not result in a noticeable shift of the derived delay time the standard observation time was considered adequate. The delay time is derived from the pcc-curve as shown in figure 2.4-3.
The error caused by the inaccuracy of this method of determination is estimated at 5%.
Combined with the error found under b) this yields a total error of 7% for the present case.

2.5. Test program for flow measurements.

The purpose of the test program was to gain practical experience with the different methods proposed and to verify the predicted accuracies. In the abcense of a reference the latter aim could only be fulfilled in a relative way by mutual comparison of the results of the different measurements.
Two series of measurements were performed:

series A: comparing the results of the venturi measurement to those of the thermal flow meter
series B: comparing the results of the venturi measurement to those of the transit time measurements.

The venturi used during these tests was of the compact type utilizing the two-electrode dP-converter (the final design with three electrodes in the dP-converter did not become available until much later).
During each test the flow was varied from ~ 2 to 9 kg/s (the maximum range that could be obtained with the FliNaK pump because of its limited controllability) at three temperature levels to detect possible temperature

effects.
Each test of series A was repeated after an interval of one week to check the occurrence of time dependent drift in the thermocouples.

2.6. Experimental results.

Figure 2.6.1 presents the results of the series A measurements. The result of the second part of this series (675, 625, 575 ^{0}C) showed less scatter than the results of the first three runs. This may well be due to the experience obtained in performing these experiments and operating the loop in general. All thermal flow measurements are within a band of 0 - 20% above the corresponding venturi measurements. This deviation is larger than the 15% predicted in section 2.3.4. In the author's opinion this should be ascribed to the fact that the annular correction of the heat transfer correlation is still somewhat optimistic. This latter problem grows worse for smaller diameter ratio's, such as would occur for practical applications of this type of flow meter (tube diameters up to 500 mm).
The results of the series B measurements are presented in figures 2.6-2 through 2.6-5.
The first four of these figures show the results of the "thermal shock" measurements.
For each measurement two values are plotted: the mass flow computed directly from the delay time found, and a value corrected for the mean velocity/max. velocity ratio (cf. subsection 2.4.3).
The latter are in better agreement with the venturi measurements, supporting the validity of the assumption that the temperature disturbances were transported more or less at the maximum velocity.
These corrected values lie within 10% of the venturi measurements.
The agreement is even better for the correlation flow measurements applying artificial random signals, vix. within 5% of the venturi results.
Figure 2.6-6 shows the results of this type of measurements performed at two different temperature levels (625 ^{0}C and 675 ^{0}C).
All results confirm that both types of transit time flow measurement are independent of the fluid temperature and thus of the physical properties of the fluid.

2.7. Conclusions.

All three methods for flow measurement discussed above have their advantages and disadvantages.
The venturi was found to be the most practical instrument for measuring stationary flows. It was also the one with the highest accuracy, although the value of 4% seems rather disappointing by normal industrial standards. This, however, is mainly due to the limited accuracy (5%) of the FLiNaK density value rather than to inaccuracies inherent to the method. Furthermore it is the method easiest to adapt for larger diameters.
Its main disadvantage is its slow response to transients.

The thermal flow meter has proven a reliable instrument but its characteristics have to be determined by calibration due to uncertainties in the applied heat transfer correlation and the physical properties of the fluid for its evaluation.
This calibration presents a difficult problem for large diameters and mass flows.

The correlation flow measuring technique looks promising for application in molten fluorides except for its 7% margin of inaccuracy. This inaccuracy is mainly caused by the "blunt" top of the cross correlation function. This top might be "sharpened" absolutely by applying faster temperature sensors or relatively by increasing the distance between the sensors.
However, even granting such improved accuracy, the method may prove difficult to develop for every day use, as up till now it requires application of artificial temperature fluctuations.
In the author's opinion it is most suited, because of the simplicity and small dimensions of the sensors, for special applications under circumstances preventing or rendering difficult the installation of other types of flow meter.

3. TURBULENT HEAT AND MOMENTUM TRANSFER

3.1. Introduction.

The availability of accurate heat transfer and pressure drop correlations is an essential prerequisite for the adequate design of heat exchanging equipment. Acquisition of this information for FLiNaK formed the main objective of the original Delft Molten Salt Project experimental program formulated in 1965 (cf. LATZKO [3.1-1]).

3.2. Heat transfer.

3.2.1. Introductory remarks.

Upon completion of a series of preliminary tests in simplified molten salt loops a special salt-to-salt heat exchanger was designed and built during 1968 and 1969. Due to its complex geometry (cf. figure 3.2-2) and the severe operating conditions combining elevated temperatures and a highly corrosive medium, instrumentation of this test module with thermocouples unfortunately proved to be beyond our technological capability at that stage. To a large extent this was due to the decision to determine the heat flux by measuring the temperature drop across the channel wall. In order to obtain a temperature drop of sufficient magnitude for accurate results, the heat resistence of the metal tube wall had to be significantly augmented. The only practical solution for this problem seemed the application of a double metal wall separated by a stagnant liquid, as the difference in thermal expansion practically excluded the application of a solid insulating layer. The temperature drop across the liquid layer - in this case a molten salt - was measured by means of thermocouples embedded in the two metal walls.

Unfortunately these measurements failed for two reasons:

- failure of the major part of the thermocouples during the first day of operation, due to an inadequate technique for fabricating thermocouple penetrations
- from the evaluation of the experimental data obtained with the remaining thermocouples it became clear that the shape of the salt-filled gap was not only not exactly annular, but also changed unpredictably with time due to thermal expansion and relaxation of post-weld residual stresses in the material.

As immediate replacement of the heat exchanger was impossible the experimental program proceeded with frictional pressure drop measurements and flow meter tests, later followed by extensive tests of the steam generator discussed in Chapter 4. In the course of all these experiments enough experience had been gained to start in 1976 the design of a second heat exchanger for the heat transfer measurements discussed in the remainder of this section.

3.2.2. Description of the test module.

A simple salt-to-air heat exchanger was chosen as test module for the second series of heat transfer experiments to simplify instrumentation as much as possible. Figure 3.2-3 shows its basic geometry. The heat exchanger consists of two concentric tubes. The inner tube forms the salt channel, while the air flows upward through the annular gap between the two tubes in counterflow with the molten salt.

3.2.3. Description of the loop.

The test module was built into the same molten salt loop as used for the flow meter experiments.
The air inlet was situated at the bottom of the heat exchanger, while the hot air was blown off to atmosphere at the top (cf. figure 3.2-4). To obtain a sufficiently high heat transfer coefficient between wall and air, the air pressure in the heat exchanger was raised by throttling the air outlet by means of a manually controlled valve. The process conditions are listed in the table shown in figure 3.2-5.

3.2.4. Outline of the method.

The heat transfer coefficient α is defined as:

$$\alpha = \frac{q}{(\vartheta_b - \vartheta_w)} \qquad (3.2\text{-}1)$$

Contrary to the temperatures appearing in this equation, the heat flux q cannot be measured directly and has to be derived either from the temperature drop across the channel wall or from the heat balance of one or both of the media. In view of the experience from the earlier experiments the former method was rejected in favour of the second one. Experience with the preceding steam generator experiments had taught us that determination of the transferred heat from the small ($< 5\ ^0C$) temperature drop of the salt would not yield a satisfactory degree of accuracy.
Therefore a series of thermocouples were provided in the air gap to measure the rise in air temperature ($> 400\ ^0C$).

3.2.5. Instrumentation.

Three pairs of salt and wall thermocouples were placed equidistantly along the circumference of the inner tube at five different levels, as shown in figure 3.2-6. In addition, three thermocouples equidistantly spaced along the circumference were provided in the air gap at 10 levels. The wall penetrations for the thermocouples measuring the bulk temperature of the salt (cf. figure 3.2-7) were brazed under vacuum using a nickel-braze similar in composition to that of INCONEL-600, to provide the required corrosion resistance. To minimize the number of penetrations, the couples for measuring the wall temperatures were placed in grooves machined into the outside of the tube wall. These slots were closed by brazed-in wedges of INCONEL-600 (figure 3.2-8). For this purpose a normal type of silver-braze could be used as there was no contact with the salt.
In addition to the aforementioned local temperatures the following variables were measured (cf. figure 3.2-4):

salt inlet temperature	(Pt resistance thermometer)
salt outlet temperature	(Pt resistance thermometer)
salt mass flow	(venturi flow meter)
air inlet temperature	(Pt resistance thermometer)
air outlet temperature	(Pt resistance thermometer)
air inlet pressure	(Bourdon pressure transmitter)
air outlet pressure	(Bourdon pressure transmitter)
air mass flow	(floating body flow meter = rota meter)

Wall temperature correction.

Measurement of the true surface temperature is impossible due to the finite dimensions of the measuring element. The temperatures measured by the thermocouples, - embedded in the wall - therefore have to be corrected for the resulting finite temperature differences between wall and thermocouple tip. Additional uncertainties are introduced by imperfections of the thermocouples (eccentricity of the hot junction (cf. figure 3.2-9) and of the brazing (cf. figure 3.2-10).
To reduce these uncertainties the special calibrating equipment shown in figure 3.2-11 was built and operated. The central part of this equipment was formed by a heat exchanger into which the different instrumented sections of FLiNaK tube were fitted in turn after completion of the measurements (cf. figure 3.2-12).
The inside of the tube was heated by steam at atmospheric pressure, while at the outside the wall was cooled by water boiling under reduced pressure. In view of the very high heat transfer coefficients associated with both condensation and boiling, the inner and outer wall surfaces were assumed to be at the saturation temperatures corresponding to the respective local pressures.
Under the assumption of a linear temperature gradient through the wall, the location of the embedded thermocouples could be determined from the readings of the three thermocouples, as shown in figure 3.2-13. The temperature differences between tube wall and salt thermocouples, obtained during the actual heat transfer tests, could then be corrected by subtracting the temperature drop between tube wall surface and equivalent thermocouple location, expressed as:

$$\Delta\vartheta_{true} = \Delta\vartheta_{meas} - q\,\frac{\delta}{\lambda}_{inc} \qquad (3.2\text{-}2)$$

3.2.6. Data reduction and processing.

Data reduction.

For each measurement including the calibration runs all signals were scanned ten times to reduce the influence of random errors. These values were recorded on paper tape for further processing on an IBM 370/158 computer.
Data reduction was performed by a special program, MEANTAB, available from the laboratory program library. This program averages the values obtained from a number of scans and checks for excessive deviations. The computed average signals are tabulated with their standard deviations and transferred to disk.

Data processing.

The data set thus obtained was processed by a special purpose program consisting of three consecutive stages:

a. determination of the calibration constants for the various thermocouples (cf. also subsection 3.2.7).
b. determination of the heat transfer coefficient α from the data by a procedure called FLILU.
c. fitting of all measured α-values by a standard correlation in procedure APPROX.

ad.b.:

A part of the second stage requiring some elaboration is the increased accuracy obtained for the heat flux q by means of a least squares curve fitting technique applied to the air temperature measurements.

For this curve the approximation $\vartheta_{air} = e^{p(z)}$ was chosen, where p(z) is a polynomial in z, i.e. the axial coordinate of the heat exchanger.
The local heat flux is determined from the steady state energy balance for the air:

$$\pi D_i q = \phi_m c_p \frac{\partial \vartheta_{air}}{\partial z} \qquad (3.2\text{-}3)$$

by substituting the z-derivative of the obtained approximation of the air temperature distribution. A correction of less than one percent is applied to q to take into account expansion work in the air due to the small axial pressure drop.

ad.c.:

The experimental data is approximated by a correlation of the general form:

$$Nu = C\ Re_b^m\ Pr_b^n \qquad (3.2\text{-}4)$$

The coefficient C and the exponents m and n have to be determined so as to fit the experimental results as closely as possible.
To make this problem amenable to linear regression analysis the natural logarithm of equation (3.2-4) was taken, yielding:

$$\ln Nu = C^{\star} + m \ln Re_b + n \ln Pr_b \qquad (3.2\text{-}5)$$

$$(C^{\star} = \ln C)$$

It should be noted that this approach minimizes the sum of the squares of the *relative* errors instead of that of the *absolute* errors.

3.2.7. Calibration.

- platinum resistance thermometers

  The platinum resistance thermometers were calibrated by the manufacturer to a guaranteed accuracy within 0.25 ^{0}C.

- local thermocouples

  - temperature differences
    As in the thermal flow meter (cf. subsection 2.3) the temperature differences were measured directly by connecting the wall and bulk thermocouple in such a way that the resulting e.m.f. is the difference between the two separate e.m.f's.
    As explained in subsection 2.3.4 this connection results in an accuracy of 1%; obtained by calibration during isothermal operation.

- absolute air temperatures
  These thermocouples are calibrated against the FLiNaK Pt-resistance thermometers during isothermal operation of the loop (no air flow). In this way an accuracy of better than 1 ^{0}C is obtained.
- FLiNaK venturi flow meter
  For the calibration of the venturi flow meter the reader is referred to subsection 2.2.3, where an accuracy of 4% is mentioned for this instrument.
- pressure transducers
  The pressure transducers are calibrated against a special high accuracy manometer to an overall accuracy of 2%.
- air flow meter
  The air flow meter of the float-type was calibrated by the manufacturer to a guaranteed accuracy within 2%.

3.2.8. Accuracy.

a. of the computed heat transfer coefficient.

The heat transfer coefficient α is computed from:

$$\alpha = q/ (\Delta\vartheta_{meas} - q\delta/\lambda_{inc}) \qquad (3.2\text{-}6)$$

where $q = \phi_{m_{air}} \cdot c_{p_{air}} \cdot \frac{\partial\vartheta_{air}}{\partial z} /(\pi D_i)$ + correction for expansion work (< 1%) (3.2-7)

The accuracy of the different variables will now be discussed in the order of their appearance in equations (3.2-7) and (3.2-6) respectively:

- $\phi_{m_{air}}$ = accurate to within 2%

- $c_{p_{air}}$

  the specific heat of the air depends on temperature and pressure and thus on the measured values of these two variables:

  the limits of inaccuracy of the absolute air temperature and the air pressure have been established in the previous section at 1 ^{0}C and 2% respectively. Using the temperature dependence of $c_{p_{air}}$ tabulated in [3.2-3], this amounts to a relative error in $c_{p_{air}}$ of < 0.5%

- $\frac{\partial\vartheta_{air}}{\partial z}$

  The accuracy of the axial derivative of the air temperature is the most difficult to establish due to the complex method applied for its determination.
  An upper bound can be estimated by assuming $\frac{\partial\vartheta}{\partial z}$ to be simply determined from two adjacent air gap thermocouples as:

$$\frac{\partial \vartheta}{\partial z} = \frac{\vartheta_l - \vartheta_u}{\Delta z_{lu}} \qquad (3.2\text{-}8)$$

The average temperature difference $(\vartheta_l - \vartheta_u)$ amounts to some 50 ^{0}C, while the maximum absolute error in this difference is $\sqrt{2}$ times the absolute error in the separate temperatures, i.e. $\sqrt{2} \times 1 = 1.4$ ^{0}C. For a maximum relative error in Δz of 0.5% the total relative error in $\frac{\partial \vartheta}{\partial z}$ is less than 3%. ★)

- D_i

Measurement of the inner diameter D_i of the test module is accurate within 0.25%. ★)
The relative inaccuracy of q resulting from these inaccuracies is:

$$\varepsilon_q = \sqrt{2^2 + 0.5^2 + 3^2 + 0.25^2} = 4\%$$

- $\Delta\vartheta$

The actual measured temperature difference between bulk and wall thermocouples is accurate within 1% (cf. subsection 2.3.4).

- λ_{inc}

The thermal conductivity is accurate within 5% (cf. [3.2-1]).

- δ

The equivalent embedding depth is determined from the temperatures measured in the special calibration heat exchanger shown in figure 3.2-13, as:

$$\delta = \frac{\vartheta_i - \vartheta_m}{\vartheta_i \quad \vartheta_o} s$$

Typical values for ϑ_i, ϑ_m and ϑ_o are 40 ^{0}C, 75 ^{0}C and 100 ^{0}C respectively. The accuracy of the thermocouple measurements in this range was 1 ^{0}C. Evaluation of the inaccuracy of δ yields:

$$\varepsilon_\delta = \sqrt{\frac{1^2 + 1^2}{60^2} + \frac{1^2 + 1^2}{25^2}} = 6\%$$

Noting from equation 3.2-6 that for the maximum FLiNaK flow, the wall correction term $q\,\delta/\lambda_{inc}$ is about 40% of the measured temperature difference $\Delta\theta$, the maximum total relative error in the locally

★) *including thermal expansion effects.*

measured heat transfer coefficient amounts to:

$$\varepsilon_\alpha = \sqrt{(\frac{10}{6}\ .1)^2 + (\frac{4}{6}\ .4)^2 + (\frac{4}{6}\ .6)^2 + (\frac{4}{6}\ .5)^2 + 4^2} = 9\%$$

The final value for the heat transfer coefficient is determined as an average of 9 measured values - the top and lowest of the five different measuring levels having been omitted because of reduced thermocouple quality - thus reducing the error to:

$$\varepsilon_\alpha = \sqrt{\frac{1}{9}\ .\ 9\%} = 3\%$$

b. accuracy of Reynolds numbers.

The Reynolds number is given by:

$$Re_{fl} = \frac{v\ D_i}{\nu} = \frac{\phi_{m_{fl}}\ D_i}{\pi/4\ D_i^2 \rho\nu} = \frac{4\ \phi_{m_{fl}}}{\pi\ D_i \rho\nu} \qquad (3.2\text{-}9)$$

The FLiNaK mass flow is measured by means of the venturi flow meter discussed in section 2.2 with an accuracy of 4%.
As stated at the end of subsection 2.2.3 the main cause of this inaccuracy is the inaccuracy of the density value of FLiNaK. For this purpose the mass flow meter can be represented by:

$$\phi_{m_{fl}} = c_{ve}\ (\Delta p\ \rho)^{0.5} \qquad (3.2\text{-}10)$$

where c_{ve} is accurate within 1.2% (cf. subsection 2.2.3).
Substitution of this relation into equation (3.2-9) yields:

$$Re_{fl} = \frac{4}{\pi}\ \frac{c_{ve}\ \Delta p^{0.5}}{D_i \rho^{0.5} \nu} \qquad (3.2\text{-}11)$$

This representation shows that the direct influence of the density on the accuracy of the Reynolds number and that via the FLiNaK mass flow measurement cancel out to some extent. The margin of uncertainty for Re_{fl} resulting from the combined inaccuracies of c_{ve}, D - cf. above - ρ and ν amount to 6% (cf. figure 2.2-13).

c. accuracy of Prandtl numbers.

$$Pr = \frac{\nu}{a} = \frac{\rho c \nu}{\lambda}$$

the maximum relative error in Pr based on the inaccuracies of the physical constant as given in the table shown in figure 2.2-13 amounts to:

$$Pr = \sqrt{(5^2 + 5^2 + 2^2 + 10^2)} = 13\%$$

d. accuracy of the computed heat transfer coefficients.

It would appear from the above that the accuracy of α-values computed from the proposed Dittus-Boelter type correlation, i.e. based on the computed Reynolds and Prandtl values, will be poor. However, a closer look at the Dittus-Boelter type correlation indicates that errors in the Reynolds and Prandtl numbers caused by the same inaccurate physical properties tend to cancel out:

$$\alpha = \frac{\lambda}{D_H} Re^{0.8} Pr^{0.4} = \frac{\lambda}{D} \left(\frac{\phi_m D}{\rho \pi/4 D^2 \nu}\right)^{0.8} \left(\rho \frac{\nu c}{\lambda}\right)^{0.4}$$

$$= \frac{4}{\pi} \frac{\lambda}{D} \frac{c_{ve}^{0.8}}{D^{0.8} \nu^{0.8} \rho^{0.4}} \times \frac{\rho^{0.4} \nu^{0.4} c^{0.4}}{\lambda^{0.4}}$$

$$= \frac{4}{\pi} c_{ve}^{0.8} \lambda^{0.6} \nu^{-0.4} c^{0.4} D^{-0.8} \qquad (3.2\text{-}12)$$

The total relative error thus amounts to:

$$\sqrt{(0.8\text{x}1.2)^2 + (0.6\text{x}10)^2 + (0.4\text{x}2)^2 + (0.4\text{x}5)^2 + (1.8\text{x}0.25)^2} = 6\%$$

and is dominated by the error margin of the FLiNaK thermal conductivity.

3.2.9. Test program.

Four series of heat transfer measurements were carried out with consecutively increasing air mass flow. The increase in secondary mass flow resulted in augmented heat transfer rates and consequently in an improved overall accuracy. The test conditions of the last and most accurate series are shown in figure 3.2-14 giving the Reynolds and Prandtl numbers for FLiNaK of each measurement based on the properties given in figure 2.2-13. The Reynolds number ranged from 1.3×10^4 to 9.3×10^4, while the Prandtl number was varied from 4.0 to 6.8 corresponding to a temperature range of 575 - 675 ^{0}C.

3.2.10. Experimental results.

The table given in figure 3.2-15 shows the results of the measurements performed at maximum air mass flow.
The same table shows the results of the correlating procedure described in subsection 3.2.6. The resulting correlation:

$$Nu = 0.0137 \; Re^{0.83} \; Pr^{0.41} \qquad (3.2\text{-}13)$$

fits 90% of the measurements to within 2.5%.
The table given in figure 3.2-16 shows a comparison of the measurements with values computed according to a corrected version of the Dittus-Boelter correlation:

$$Nu = 0.020 \; Re^{0.8} \; Pr^{0.4} \qquad (3.2\text{-}14)$$

3.2.11. Discussion of results.

Of the three differences between the correlation given in equation (3.2-13) and the Dittus-Boelter correlation:

$$Nu = 0.023 \; Re^{0.8} \; Pr^{0.4} \qquad (3.2\text{-}15)$$

- which is seen to overestimate the actual heat transfer coefficient by approaximately 17% - the slight difference in exponent of the Prandtl number is of little consequence, as the corresponding change in value of the coefficient amounts to 3% only. The increased value of the exponent of the Re-number, however, has a significant effect on the value of coefficient C (25%), partly explaining the lower value of the coefficient appearing in equation (3.2-13). Higher values than 0.8 for the exponent of the Re-number occur in several other heat transfer correlations (cf. e.g. BISHOP (equation 4.2-21) and GROENEVELD [3.2-2] mentioning exponents of 0.886 and 0.853.
However, even retaining coefficients of 0.8 and 0.4 (cf. equation (3.2-14) the best fit of the experimental data requires a decreased coefficient: C = 0.20 instead of 0.23.
The overestimation of the heat transfer coefficient by the original Dittus-Boelter correlation may well be due to inaccuracy of the FLiNaK thermal conductivity (cf. APPENDIX 2A) - as compared to λ = 1.3 W/m ^{0}C used here -. A value of λ = 1.03 W/(m ^{0}C) would yield a very close fit of the measured heat transfer data by the Dittus-Boelter correlation.
In view of the wish to conform as much as possible to the Dittus-Boelter correlation and the very limited loss of accuracy, equation (3.2-14) was preferred over equation (3.2-13) for the computations for the thermal flow meter discussed in section 2.3.

3.3. Momentum transfer.

3.3.1. Introductory remarks.

As stated in section 1 the heat transport capability, defined as the ratio of thermal power removed to pumping power required, determines to a large extent the effectiveness of a fluid as a heat transfer agent.
As the heat transport capability is directly proportional to the friction factor f of the fluid determination of this factor for FLiNaK was included in the aims of the original DMSP program.

3.3.2. Description of the method.

The friction losses in a straight tube are usually obtained from the formula:

$$\Delta p_f = f \frac{L}{D} \tfrac{1}{2} \rho v^2 \qquad (3.3\text{-}1)$$

where f is the so-called friction factor, solely depending on the Re-number and the roughness of the tube wall.
The purpose of this study was to determine the friction factor f as a function of Re in the turbulent flow regime and to verify whether this relationship may be represented by one of the usual formulae or graphs, such as the Blasius formula [3.3-1]:

$$f = 0.3164 \; Re^{-.25} \qquad (3.3\text{-}2)$$

or the Moody chart (cf. figure 3.4-1).
The friction factor was obtained from pressure drop measurements across a calibrated straight tube in the DMSP primary loop.
The fluid velocity has not been measured directly but was calculated from the venturi mass flow measurements described in section 2.2 by evaluating:

$$v = \frac{\phi_m}{\rho\ \pi/4\ D^2} = \frac{c_{ve}\sqrt{\Delta p_{ve}\ \rho}}{\rho\ \pi/4\ D^2} = \frac{c_{ve}}{\pi/4\ D^2}\sqrt{\frac{\Delta p_{ve}}{\rho}} \qquad (3.3\text{-}3)$$

where Δp_{ve} stands for the pressure drop measured across the venturi.

To validitate the above formula the loop was operated isothermally during these measurements, viz. with a uniform density. Combining equations (3.3-1) and (3.3-3) yields:

$$f = \frac{2\ (\pi/4)^2\ D}{L\ c_{ve}^2}\ \frac{\Delta p_f}{\Delta p_{ve}} \qquad (3.3\text{-}4)$$

where the specific mass ρ of the fluid has been eliminated.
The Re-number is obtained from equation (3.2-11).

3.3.3. Description of equipment.

3.3.3.1. Test tube.

The test tube consists of a length of tube mounted in the DMSP loop between the main heater and the heat exchanger, at a downward angle of 6^0 with the horizontal in the flow direction for drainability (cf. figure 3.3-2). The dimensions of the test tube are shown in figure 3.3-3. In accordance with [3.3.2] straight sections of 30 D upstream and 10 D downstream were provided to ensure the necessary undisturbed fully developed flow. The pressures were measured through single bore pressure taps, flush at the inside tube wall. For this type of taps it is essential:

- that they are at a right angle with the centerline of the tube
- that the tube has a perfectly cylindrical shape in the vicinity of the holes.

To fulfill these requirements two solid studs were welded into the tube at the specified locations and subsequently drilled at right angles with the center line, so as to avoid errors caused by post-welding distortion. The main tube was then internally ground over the full upstream and downstream lenghts to obtain a perfectly cylindrical bore. Subsequent to this machining the tube bore was measured at a number of cross sections. The results of these measurements are given in figure 3.3-4. Another important property of the test tube bore is its surface roughness. The mean height δ of the roughness was 15 ru, corresponding to a relative roughness of $\delta/D = 1.10^{-5}$.
According to [3.3-1] a tube with this relative roughness may be considered completely smooth.

3.3.2.2. Differential pressure measurement.

The differential pressure measurement device used for the friction pressure drop measurements is essentially the same as that of the earlier version of the venturi (two-electrode type) described in subsection 2.2.2.2 and shown in figure 3.3-5. To reduce the error caused by friction losses the connecting tubes (cf. subsection 2.2.3) the control gas release rate was further reduced to about 2 cc/min. The gas pressure difference was transformed into an electrical signal by a combination of a differential pressure cell and an amplifier. This signal was recorded on a line recorder.

3.3.4. Test program.

As the tube may be considered completely smooth the only remaining quantity influencing the friction factor is the Reynolds number. For the given diameter Re could only be changed by varying the mass flow and the FLiNaK temperature. Tests were performed at three temperature levels; approximately 575 C, 625 C and 675 C. At each temperature level the mass flow was varied over the range 2 - 9 kg/s (cf. figure 3.3-6).

3.3.5. Experimental results.

The table in figure 3.3-7 gives the results of the various measurements. In addition to the two differential pressures and the temperature of the FLiNaK measured during each experiment this table compares the measured friction factor to the one computed from the Blasius formula by listing both their absolute and relative difference.
By applying the least squares procedure APPROX a best fit of the measured friction factors is obtained, reading:

$$f = 0.265 \times Re^{-0.2058} \qquad (3.3\text{-}5)$$

(cf. figure 3.3-8).
Figure 3.3-9 shows a graphical comparison between the test results (drawn line) and the Blasius formula (dotted line).

3.3.6. Accuracy.

The friction factor f is calculated from equation (3.3.4):

$$f = \frac{2(\pi/4)^2 D^5}{L c_{ve}^2} \frac{\Delta p_f}{\Delta p_{ve}} \qquad (3.3\text{-}6)$$

The values and the maximum errors of the various quantities appearing in this formula are given in the table in figure 3.3-10.
These inaccuracies amount to a total of 3% of the maximum value $f_{max} = 0.03$ (cf. Appendix 3A).
The accuracy of the Reynolds number is better than 7% (cf. subsection 3.2.8).

3.3.7. Discussion of results.

As evident from figure 3.3-10 the shape of the experimental curve closely resembles that of the Blasius correlation, but the absolute values of the fraction factor show a consistent "overshoot" of approx. 20%.
No scientifically convincing explanation could be found for this phenomenon. The author is inclined to attribute at least a significant part of the discrepancy to the fact evidenced in figure 3.3-4, viz. that, despite the accurate machining, small diameter variations with a relatively large wave length are present along the tube length. Although these variations cannot be considered as roughness proper the experimental results indicate that they may have induced an additional pressure drop.
For reasons of expediency repetition of the experiments with a different tube bore proved impossible.

4. BAYONET TUBE STEAM GENERATOR

4.1. Introduction.

4.1.1. General background.

All concepts for molten salt breeder reactor power plants published so far incorporate an intermediate coolant for heat transport from the intensely radioactive circulating fuel primary circuit to the steam cycle. Compatibility and high temperature stability requirements limit the choice of this secondary coolant to fluoride salt mixtures, thereby entailing some specific design problems for the steam generator.
These problems result from two properties of the salt mixture (cf. figure 2.2-13). The first of these concerns the high heat capacity, causing a small temperature drop of the heating fluid and hence a very large difference between the salt outlet and feedwater inlet temperatures and correspondingly large thermal stresses in the tube wall separating the two fluids.
For those familar with the design of other high temperature steam generators such as those heated by sodium, this problem by itself will hardly appear specific to the use of molten fluorides.
It must be borne in mind, however, that in addition to the aforementioned much smaller temperature drop of the hot fluid, its inlet temperature will be some 100 ^{0}C higher in the case of the salt, increasing the steady state temperature difference at the cold end of the steam generator by a factor of about 3 as compared to sodium heating (for the same feedwater inlet temperature).
The second property of the salt causing problems is the high melting point, because it raises the danger of salt freezing on the outer tube walls in the economiser section.
As briefly mentioned in the introduction to this thesis, the presence of the DMSP molten fluoride system in the author's laboratory offered an attractive possibility for contributing to the solution of these problems because of the availability of:

- the molten salt loop described earlier, containing a 250 kW electrical heater
- the necessary special instruments

Apart from these, there was the knowledge and experience in designing and operating a molten salt system.
Prior to the definition of an experimental program, a choice had to be made between the two basic alternatives for avoiding the aforementioned problems, viz. raising the feedwater inlet conditions to some 350 ^{0}C through the adoption of supercritical operating conditions or interposing an additional thermal barrier between the primary and secondary fluids.
The former alternative, selected in the MSBR design reported by ROSENTHAL [4.1-1] was rejected for the present study on the following grounds:

- in Europe there is considerably less experience with supercritical steam plants than in the U.S.A.
- at the time of taking the decision no such plant was operating in the Netherlands at all ★)
- it was deemed desirable to make the present tests as relevant as possible for the (subcritical) sodium-heated steam generator development being carried out in the Netherlands.

★) *at the time of completion of this thesis two 600 MW$_e$ units had started operating at supercritical steam conditions in the Netherlands.*

A number of possible design solutions for the subcritical alternative chosen here were evaluated by FRAAS [4.1-2], viz.:

- double walls, separated by a heat barrier
- re-entry or bayonet tube boiler

On a number of grounds not reproduced here for brevity's sake he arrived at the conclusion, shared by the present author, that the bayonet tube boiler is the most promising design for overcoming the aforementioned problems.

4.1.2. The bayonet tube steam generator.

4.1.2.1. Design characteristics.

The bayonet concept schematically shown in figure 4.1-1 combines the evaporator and the superheater in one system. The tube bundle with the molten salt flowing around it consists of a great number of so-called bayonet tube sets, each made up of two concentric tubes (cf. figure 4.1-2). The outer tube, closed at the top, is the pressure tube which separates the salt and water regions, while the inner tube contains the economiser and evaporator sections.
Feedwater enters this inner tube at the bottom, is preheated, evaporated and slightly superheated before it reaches the top. There the steam flow is reversed and the steam is superheated while flowing downward through the annular gap to the steam outlet at the bottom of the steam generator.
The steam layer in the superheater gap acts as an effective thermal barrier between salt and water. In order to prevent excessive heat loss from the superheated steam to the incoming feedwater the lower part of the evaporator tube is covered by an insulating layer of sprayed-on Z_rO_2.
As to the thermal stresses, both the evaporator tube and the pressure tube can expand freely without causing stresses, while the thermal stresses resulting from the radial temperature gradient across the tube walls are limited due to the insulating steam layer.
Another advantage of this concept lies in the fact that the cyclic thermal stresses resulting from the fluctuating dry-out location occur in the evaporator tube which has no load-bearing function, rather than in the mechanically highly loaded pressure tube.
The single tube steam generator model forming the test module for the investigations to be described in this chapter was designed according to the principle just explained.
The feedwater and steam conditions were chosen in accordance with modern subcritical power plant practice, viz.:

steam pressure	= 18 MN/m^2
feedwater temperature	= 280 ^0C
steam temperature	= 540 ^0C

The primary inlet temperature was fixed at 625 ^0C to ensure a reasonable margin with respect to the primary circuit operating limit, while at the same time maintaining similarity with MSBR design studies (cf. [4.1-1]).
The one remaining process variable, the primary mass flow rate, should be optimized to yield the highest value for $k.\Delta\theta_{LMTD}$ still giving an acceptable primary pressure drop.
A preliminary optimization (IPENBURG [4.1-3]) indicated mass flow ratios of about 9 for subcritical steam cycles, resulting in a primary temperature drop of the order of 125 ^0C. For given process conditions the design of any steam generator should be optimized for minimum capital costs. To do so would however require intimate knowledge of not only material and semi-finished products prices for all the constituent parts, but also of the

unit costs and standard times of all the manufacturing steps concerned. Such a task was considered beyond the scope of the present thesis. Therefore optimization was limited in the sense of: minimum heating surface. The three principal dimensions to be determined are: diameter of the evaporator tube, width of the superheater gap, and length of the bayonet tube. Simple considerations of enthalpy rise and estimated heat transfer coefficients indicate that the length of the evaporator tube, needed for preheating and complete evaporation of the feedwater, far exceeds the length of the steam gap required for superheating.
Hence the length of the bayonet is determined by the length of the evaporator.
The average heat transfer coefficient in the steam generator can be increased by raising the feedwater mass flow rate. However, as most of the local heat transfer coefficients are proportional to the mass flow rate to the power 0.8, while nucleate boiling heat transfer and heat conduction through the wall are even flow independent, the increase will be less than proportional. As on the other hand the required heat is proportional to the flow rate, this means that a longer evaporator tube is required for obtaining the same outlet conditions at the top of the evaporator.
The length of the evaporator wil be limited by building height requirements. Once this limit is reached further increase in flow rate is still possible by reducing the inner diameter of the evaporator tube and thus improving the ratio of heated perimeter and cross-sectional area. Although there is a small decrease of the heat transfer coefficient associated with a reduction of the diameter the net effect of mass flow rate increase and diameter reduction on the average heat transfer coefficient remains possitive. Once the economical and/or technical limit for reduction of the evaporator tube diameter is reached the last possibility to increase the overall heat transfer coefficient lies in reduction of the superheater gap width.
The effect of this reduction on the heat transfer coefficient to the two adjacent walls can be derived from the relevant superheated steam heat transfer correlation. In our case the correlation of BISHOP [4.1-4]:

$$Nu = 0.0073\ Re^{0.886}\ Pr^{0.6}\ (1 + 2.76\ \frac{D_H}{L}) \qquad (4.1\text{-}1)$$

has been applied for reasons discussed in subsection 4.2.3.
Transformation of this correlation shows the total effect of the gap width w on the heat transfer coefficient:

$$\alpha = 0.0073\ \frac{\lambda}{2w}\ (\frac{2\ \bar{\phi}_v}{\pi D})^{0.886}\ Pr^{0.6}\ (1 + 2.76\ .\ \frac{2w}{L}) \qquad (4.1\text{-}2)$$

i.e. one of approximately inverse proportionality (for constant mean gap diameter D).
In summary an optimum design is obtained by combining the following measures:

- maximum bayonet tube length
- minimum evaporator tube diameter
- minimum superheater gap width
- maximum flow rate (under the condition that evaporation is completed in the central tube)

The following practical limits to these measures were observed in the optimization:

- 15 m for the evaporator tube length, corresponding to a total length of 20 m for the entire steam generator. This total length of 20 m is about equal to that of the contemporary straight tube sodium heated steam generators
- 3/8" (17.2 mm O.D.) for the evaporator tube because of the steeply increasing cost per unit of heat transfer surface below this diameter and structural requirements concerning the slenderness of the bayonet tube
- 2 mm for the minimum gap width compatible with spacing and assembly requirements.

  N.B. Superheater pressure drop restrictions may increase this minimum even further.

4.1.2.2. Potential interest.

While the above characteristics explain the potential interest of the bayonet tube design for MSBR steam generators, it should be noted that a similar design has also been proposed for application in LMFBR's.
To the author's knowledge KINYON [4.1-5] was the first to do so. His proposal has been followed by several other authors: BARRATT [4.1-6], PETREK [4.1-7], HUNSBEDT [4.1-8], of which Hunsbedt reported actual performance tests on a seven tube experimental steam generator. These designs, however, although featuring a bayonet tube, differ essentially from the design proposed by Fraas and discussed here in that they do not combine the superheater and the evaporator in the same bayonet tube. They are provided with a separate superheater, sometimes contained in a separate pressure vessel. The bayonet tube serving as evaporator only is reversed in position (closed end down with the feedwater flowing downward through the inner tube and evaporation taking place during upward flow in the annulus). While this type of evaporator does not solve the aforementioned special problems posed by the high melting point and high average operating temperature of the heating salt, its application to LMFBR's holds two important advantages:

- problems caused by different thermal dilatation of tube bundle and shell are avoided, thus eliminating the need for differential expansion devices such as bellows
- the tube-to-tubesheet connections are not in touch with the sodium, which decreases corrosion and thermal stress problems.

Application of the Fraas type bayonet tube steam generator to the LMFBR would add the advantage of reducing the sodium-water reaction through decreased mass flow into the surrounding sodium because of the substitution of superheated steam for two-phase mixture or even water. It would, however, require a substantial raise of the primary temperatures.

4.1.3. Aims and scope of the present investigations.

The general aim of the present investigations is a first assessment of the suitability of the once-through bayonet tube concept for high pressure steam generation. To the author's knowledge this is the first use of a bayonet tube steam generator operating in the once-through mode with steam conditions representative for modern power station practice.
The present study is restricted to the thermal-hydraulic performance of such a steam generator.

The thermo-hydraulic design of a steam generator has to cover three aspects:

- steady-state behaviour
- dynamic behaviour under large transients
- flow stability

4.1.3.1. Steady state behaviour.

An essential prerequisite for the design of a steam generator is the availability of information needed for a realistic assessment of the necessary heat transfer area, preferably in the form of a computer code. The second step in steady state performance analysis is the prediction of fluid outlet conditions, internal temperature distribution and total pressure drop at partial loads.
In the case of the present investigation this information was also required as input for the dynamic stability simulation program discussed in section 4.6.
The accuracy of the above thermo-hydraulic performance predictions is directly dependent upon the accuracy of the heat transfer and pressure drop correlations applied.
An extensive survey and evaluation of the available information was presented by TEN WOLDE [4.1-9] in 1972. The additional information published since (e.g. by CAMPOLUNGHI [4.1-10]) does not in the author's opinion warrant modifications in the set of correlations recommended by Ten Wolde (cf. subsection 4.2.3.2).

Recognizing that the best available correlations were only of limited accuracy, two courses of action were open at the initiation of this project:

- experimental investigations of heat transfer and pressure drop correlations under conditions valid for the bayonet tube steam generator, followed by computer simulation of the steady state performance using these experimentally determined correlations
- development of a computer code utilizing the available correlations, and subsequent verification of the results of this code in an experimental bayonet tube steam generator so as to define the causes of, and qualitatively explain, possible discrepancies.

The former course would be more appropriate for a laboratory specializing in heat transfer than for one mainly aiming at equipment development. It would also be beyond or at best in the margin of the present scope of investigations. It was therefore decided to follow the second course.

The question may arise whether both types of investigation could not have been combined in one experimental program. The present author's answer to this question is an emphatic no. The complex geometry of the experimental bayonet tube steam generator permitted only a very limited amount of internal instrumentation. Any attempt to instrument the test module to the extent required for establishing or verifying individual heat transfer correlations would have invited the kind of problems typical for multi-purpose applications of highly complex test equipment, as exemplified by the salt-to-salt heat exchanger experience discussed in subsection 3.2.1. This experience convinced the author that such experimental apparatus should serve one single purpose only, so as to permit the simplest and most reliable design possible.

To check the overall performance and to locate and qualitatively explain possible discrepancies between experiment and simulation a limited amount

of instrumentation was sufficient.
The selection of this instrumentation is discussed in subsection 4.3.3.2.

4.1.3.2. Dynamic behaviour.

4.1.3.2.1. Large transients.

A thorough knowledge of the dynamic behaviour of steam generators under large transients is essential for the safety assessment of any nuclear plant. It is also highly desirable for the design of control systems for new or extrapolated steam supply systems if one is to avoid surprises at the commissioning stage. Such knowledge should preferably be at the designer's disposal in the form of a computer code, suitable for accurate simulation of the highly non-linear processes in the steam generator.
A further aim of the DMSP-program concerned development of such a program for the complex geometry of a once-through bayonet tube steam generator and subsequent verification of the results of this program by comparison with experimental data obtained in the test facility mentioned above (cf. section 4.5).

4.1.3.2.2. Stability.

Secondary side flow instabilities in steam generators are well known as a cause for tube failures: by thermal fatigue through oscillations in the location of the dry-out point; by mechanical fatigue through sustained forced vibrations; by local overheating due to temporary flow starvation or by combination of the aforementioned effects.
The absence of such instabilities within the normal range of operating conditions (including start up and shut down) is therefore essential for sound steam generator design.
A number of different types of oscillatory flow have been identified in the literature. The following summary classification follows the excellent review by BOURE [4.1-11].
The first distinction to be made is between static and dynamic instability. The static or Ledinegg instability, characterized by incidental random oscillations between metastable steady state conditions, occurs if the slope of the channel pressure drop-versus-flow rate curve is algebraically smaller than the slope of that curve for the remainder of the loop (cf. figure 4.1-3). This may result in severe flow excursions, as in this case a change in flow is reinforced rather than opposed by the resulting change in pressure drop. This mechanism, though aperiodic by nature, may under certain conditions cause an apparent oscillation (cf. STENNING [4.1-12], but this notwithstanding it is essentially the steady state that is unstable.
The so-called dynamic instabilities can be divided into two classes.
The first class is characterized by the propagation of pressure waves through the steam generator, while the second class is characterized by the occurrence of density waves. These two types can easily be distinguished by their frequencies. In the case of the density wave oscillations these are related to the fluid velocity, while the frequency of the pressure wave oscillations depends on the velocity of sound in the fluid, resulting in much higher values (e.g. 10 versus 0.1 - 1.0 c/s). This study is restricted to the former type of oscillation as being the more potentially damaging one to steam generators, because the temperature variations of much higher frequency caused by pressure wave oscillations are of smaller amplitude and effectively damped by the heat capacity of the wall.

The original aim of developing a computer code suitable for the assessment of the stability of once-through bayonet tube steam generators, followed by experimental verification, was extended as the project progressed.
From a literature survey (discussed in detail in subsection 4.6.1.1) it became clear that even for simpler geometries the accuracy of predictions leaves much to be desired. To a large extent this appears to be due to the absence of sufficiently accurate empirical relations, in particular for subcooled boiling and two-phase frictional pressure drop.
During the development of a special purpose program, restricted to stability simulations for once-through bayonet tube steam generators (cf. subsection 4.6.1.2) it became more and more apparent that a need existed for a very flexible program, suitable for different geometries and process conditions, while facilitating eventual replacement of all empirical relations by newer, more accurate ones.
The last period of the project was devoted to the development of such a program, viz. the CURSSE program discussed in subsection 4.6.1.4.

4.2. Basis for analysis.

4.2.1. General assumptions.

The thermo-hydraulic processes in a steam generator consisting of a great number of parallel tubes between a common inlet header and a common outlet header are very complex. It is impossible to simulate these processes in all detail. The commonly accepted procedure is to select a subsection of the steam generator whose behaviour under load is considered characteristic for the entire component. The usual choice for this characteristic section is one single, so-called "characteristic", tube representing the average behaviour of all tubes in the steam generator. This approach is obvious for the stationary and transient simulations. It is also customary for the simulation of hydro-dynamic stability. This application will be discussed in detail in subsection 4.6.1.2.
While limitation of the simulation to a single tube represents a considerable simplification, the momentum and heat transfer processes occurring in a single tube are still highly complex.
A brief introductory and qualitative description of these processes therefore appears in order with special reference to the bayonet tube design discussed in the preceding section.
Subcooled water entering the evaporator at the bottom is heated by single-phase forced convection until the temperature of the tube wall inner surface exceeds the saturation temperature by a sufficient margin to allow bubble formation (subcooled boiling).
In this transition region a significant and sharp increase of the effective heat transfer coefficient to the water occurs due to bubble detachment and transport and the resulting partial destruction of the laminar boundary layer. This augmented heat transfer is maintained as the water reaches saturation temperature and the bubbles leaving the tube wall no longer condense, but become dispersed in the water. As vapour generation continues and the void fraction increases, the flow pattern changes from bubble - via slug - to annular flow, where the vapour forms the continuous phase in the core of the tube, with the liquid either flowing in the form of an annulus along the tube wall or dispersed as droplets.
Continuing evaporation reduces the thickness of the liquid film until the void fraction reaches the critical value, where the annular ring of liquid disappears resulting in a dry tube wall and a sharply decreased heat transfer coefficient: dry-out.

The remainder of the water is evaporated in the mist flow region where the flow consists of steam with entrained droplets and thermal non-equilibrium - i.e. vapour superheating at qualities $x < 1$ - may exist. Finally, at $x = 1$ the true superheat region is entered, where all the heat supplied is used to superheat the steam.
The processes described above, governed by the well-known conservation laws for mass, momentum and energy, are essentially two-dimensional. Velocity, temperature and pressure variations are present in two different directions and on two different scales: local variations over the cross section, i.e. in the radial direction, and the axial distribution of the mean values along the length of the channel. The cross-sectional variations, determining the local heat transfer and the friction pressure drop, are of too complex a nature to be analysed in detail. To avoid these problems it has become common engineering practice to assume uniform distributions based on the mean values and to define the heat and momentum exchange between the fluid and its boundary by heat transfer and pressure drop correlations defined with respect to these values.
This one-dimensional approach, elaborated in a number of textbooks (e.g. WALLIS [4.2-1]), essentially consists of the replacement of the mean value of a product by the product of the mean values of its constituent factors. Although this is known to cause only marginal errors in single phase turbulent flow, it may cause significant errors in two-phase flow, notably in studies concerning momentum transfer. This fact is mainly due to the non-uniform radial void distribution.
Two possible solutions have been proposed for this problem. In the first, adopted by HANCOX and NICOLL [4.2-2], the product of mean values is multiplied by a correction factor based on assumed radial distribution functions of the properties concerned.
The value of this factor will of course tend towards unity as the system pressure increases towards the critical pressure. Values based on experimental data for steam/water flow at pressures up to 11 MN/m^2 are presented in [4.2-2].
In the second method a separate mean velocity is introduced for each of the two phases. The ratio of the average gas and liquid velocities is called slip. This latter approach, underlying i.a. the well known slip correlation proposed by BANKOFF [4.2-3], was adopted for the two-phase flow region in the present thesis because of easier application.
Having thus eliminated the radial dimension, one is left with the one-dimensional problem of determining the distribution of the average values along the length of the channel by solving the system of one-dimensional mass, momentum and energy balance equations completed with the empirical heat transfer and pressure drop correlations.

4.2.2. Balance equations.

In addition to the energy balance for the tube wall, balance equations for the fluid are required for the following regimes:

- single-phase flow (pre- and superheating)
- two-phase flow
  - thermal equilibrium (saturated boiling and post-dryout mist flow)
  - thermal non-equilibrium (subcooled boiling)

In adopting the above subdivision no account is taken of non-equilibrium effects in the post-dryout mist flow region. For a justification of this approach at the pressure level of interest for this thesis ($\geqslant 17$ MN/m^2) the reader is referred to GROENEVELD [4.2-4]. An extensive review of the

pertinent balance equations with their derivations was given by TEN WOLDE [4.1-9].
The remainder of the present section is therefore limited to a listing of these equations with additional comments for the case of thermal non-equilibrium.

4.2.2.1. Single phase flow.

The mass balance equation reads:

$$\frac{\partial \rho}{\partial t} + \frac{\partial G}{\partial z} = 0 \qquad (4.2\text{-}1)$$

The momentum balance reads:

$$\rho \left\{ \frac{\partial v}{\partial t} + v\frac{\partial v}{\partial z} \right\} = - \frac{\partial p}{\partial z} - \frac{\tau O}{A} + \rho g \sin \varepsilon \qquad (4.2\text{-}2)$$

while the energy balance equation reads:

$$\rho \left\{ \frac{\partial h}{\partial t} + v\frac{\partial h}{\partial z} \right\} = \frac{\partial p}{\partial t} + v\frac{\partial p}{\partial z} + \frac{qO}{A} \qquad (4.2\text{-}3)$$

For the three applications given in sections 4.4 through 4.6 additional assumptions have been made which will be discussed in the pertinent sections.

4.2.2.2. Two-phase flow.

An exact description of two-phase flow would require the explicit inclusion of the equations for the two separate components in the simulation, resulting in twice the number of basic equations as for single-phase flow. In addition the boundary conditions are more complex, involving interaction forces and heat transfer between the two-phases.
However, knowledge of these interaction processes is still too limited for practical application of such a detailed mathematical description. Hence the usual engineering approach of applying mixture balances has been chosen for this study.

4.2.2.2.1. Thermal equilibrium.

This refers to the saturated boiling regime and the post-dryout mist flow region.

mass balance:

$$\frac{\partial \bar{\rho}}{\partial t} + \frac{\partial G}{\partial z} = 0 \qquad (4.2\text{-}4)$$

where mixture density $\bar{\rho} = (1 - \alpha)\, \rho_l + \alpha \rho_g$ (4.2-5)

and mass velocity $G = (1 - \alpha)\, \rho_l v_l + \alpha \rho_g v_g$ (4.2-6)

momentum balance:

$$\frac{\partial G}{\partial t} + \frac{\partial}{\partial z}\{ (1 - \alpha)\ \rho_l v_l^2 + \alpha \rho_g v_g^2 \} =$$
$$= - \frac{\partial p}{\partial z} - \frac{\tau O}{A} + \bar{\rho} g \sin \varepsilon \qquad (4.2\text{-}7)$$

The above momentum balance equation of the mixture is obtained by addition of the two balance equations for the separate phases, thus eliminating the interaction forces between the two phases. Consequently their effect, viz. the slip, has to be accounted for by an empirical correlation of the general form:

$$\frac{v_g}{v_l} = s = f_s\ (p, \bar{h}, G)$$

For further discussion of the slip correlation actually applied the reader is referred to subsection 4.2.3.4.

energy balance:

This balance will be written in the internal energy u in accordance with TEN WOLDE [4.1-9]:

$$\frac{\partial}{\partial t}(\rho_g\ u_g\ \alpha) + \frac{\partial}{\partial z}(\rho_g\ u_g\ \alpha\ v_g)$$
$$+ \frac{\partial}{\partial t}(\rho_l\ u_l\ (1 - \alpha) + \frac{\partial}{\partial z}(\rho_l\ u_l\ (1 - \alpha)\ v_l)$$
$$= - p \frac{\partial}{\partial z}(\alpha\ v_g + (1 - \alpha)\ v_l) + \frac{O}{A} q \qquad (4.2\text{-}8)$$

where $u = h - \frac{p}{\rho}$.

4.2.2.2.2. Thermal non-equilibrium.

The principal consequences of the absence of thermal equilibrium for the balance equations are threefold:

- the thermo-hydraulic state of the mixture is no longer uniquely determined by three variables (e.g. p, h, G for fully developed boiling) but requires a fourth variable (e.g. x)
- the ratio of the amounts of heat transferred to each of the two phases depends on the rate of heat transfer between the two phases
- the physical properties of the subcooled liquid are a function of both pressure and temperature of the bulk.

While the mass and momentum balances for subcooled boiling are identical to those for fully developed, i.e. saturated boiling - be it that the physical properties depend on bulk pressure and temperature - the above mentioned consequences of thermal non-equilibrium indicate the need for two separate energy balances and thereby raise the problem of quantifying energy transfer between the phases, i.e. the very problem avoided so far by the use of mixture balances.

BOWRING [4.2-5] formulated these two separate energy balances by dividing the total heat supplied into the parts kq used for evaporation and (1-k)q serving to heat the remaining water. The two energy equations are derived in Appendix 4A.
The constant k is determined from a semi-empirical relation of general appearance:

$$k = f\,(h,\ P,\ G,\ x,\ \theta_w) \tag{4.2-9}$$

The exact relation applied in this study will be discussed in subsection 4.2.3.5.

For a channel of constant cross-sectional area - postulated throughout this section - the two energy equations read:

- for evaporation:

$$\alpha\,\rho_g\,\frac{\partial u_g}{\partial t} + \alpha\,\rho_g\,v_g\,\frac{\partial u_g}{\partial z} +$$

$$+\ \{\ p\ (\frac{1}{\rho_g} - \frac{1}{\rho_l}) + (u_g - u_l)\ \}\ \phi_{lg}$$

$$-\ \frac{p}{\rho_g}\ (\alpha\,\frac{\partial \rho_g}{\partial t} + \alpha\,v_g\,\frac{\partial \rho_g}{\partial z}) = kq\,\frac{O}{A} \tag{4.2-10}$$

where ϕ_{lg} = the amount of evaporated water per unit of volume and time:

$$\phi_{lg} = \frac{\partial \rho_g \alpha}{\partial t} + \frac{\partial}{\partial z}\,(v_g \rho_g \alpha) \tag{4.2-11}$$

- for preheating of the water:

$$(1 - \alpha)\,\rho_l\,\frac{\partial u_l}{\partial t} + (1 - \alpha)\,\rho_l\,v_l\,\frac{\partial u_l}{\partial z}$$

$$-\ \frac{p}{\rho_l}\ ((1 - \alpha)\,\frac{\partial \rho_l}{\partial t} + (1 - \alpha)\,v_l\,\frac{\partial \rho_l}{\partial z}) = (1 - k)\,q\,\frac{O}{A} \tag{4.2-12}$$

4.2.2.3. Energy balance of the wall.

From an extensive study of the subject TEN WOLDE [4.1-9] concluded that a "zero layer" aproximation is sufficiently accurate for simulating steam generator transient dynamics.
This model only considers the heat resistance of the tube wall, as defined by the equation:

$$q = \lambda\,\frac{\vartheta_o - \vartheta_i}{r_o\ \ln \frac{r_o}{r_i}}\quad (\text{q referring to the outer surface}) \tag{4.2-13}$$

and hence neglects storage effects.

This model has been applied in the transient analysis. In the stability simulation program, however, a "multi layer" model has been implemented for reasons discussed in subsection 4.6.1.4.1.

4.2.3. Empirical relations.

Following the flow path of the fluid the subdivision of the steam generating process described in subsection 4.2.1. results in the following five consecutive regions: (cf. figure 4.2-1)

1. preheat region
2. subcooled region
3. saturated boiling ★) region
4. mist flow region
5. superheat region

The empirical relations required for a mathematical model of the steam generator can be divided into the following categories:

- transition criteria defining the boundaries between the above regions
- heat transfer correlations
- pressure drop correlations
- slip correlations
- inter-phase exchange correlations

4.2.3.1. Transition criteria.

4.2.3.1.1. Preheat - subcooled.

Bubble growth starts, where the wall temperature slightly exceeds saturation temperature. For high pressure systems this wall superheat amounts to only a few degrees (cf. JENS and LOTTES [4.2-6]) and has therefore been neglected in this study: i.a.v. transition from the preheat to the subcooled region is considered to occur where the wall reaches saturation temperature.

4.2.3.1.2. Subcooled - saturated boiling.

This transition occurs where the bulk of the fluid reaches saturation temperature and the mixture resumes a state of thermo-dynamic equilibrium. The transition equation reads:

$$\bar{h} = h_{l_{sat}} \qquad (4.2\text{-}14)$$

4.2.3.1.3. Saturated boiling - mist flow.

This transition, defined as "dry-out" in subsection 4.2.1, has been the subject of extensive studies. Numerous dry-out correlations can be found in literature, each with its own ranges of validity with respect to pressure, heat flux, mass flux, channel diameter, etc.
The dry-out correlation selected after TEN WOLDE [4.1-9] was first proposed by LEE [4.2-7]:

$$x_{DO} = \frac{778}{h_s - h_w} \left(0.5 - \frac{0.201}{G^{0.575}} q\right) \qquad (4.2\text{-}15)$$

(h in kJ/kg ^{0}C and q in kJ/m^{2}s).

★) *Sometimes called nucleate boiling.*

This correlation is valid for:

$$\begin{array}{lcll} 13.8 & < P < & 18.5 & MN/m^2 \\ 2000 & < G < & 4400 & kg/m^2 \\ 0.009 & < D < & 0.020 & m \\ 0.2 & < x_{DO} < & 0.4 & \end{array}$$

4.2.3.1.4. Mist flow - superheat.

The transition from mist flow to superheating occurs theoretically where the steam quality reaches unity (x = 1.0). In reality however this transition is less abrupt, the steam being already superheated before the last droplets have been evaporated. For high pressures, however, the theoretical schematization can be adopted without loss of accuracy (cf. GROENEVELD [4.2-4]).
Hence the transition equation reads:

$$\bar{h} = h_{g_{sat}} \qquad (4.2\text{-}16)$$

4.2.3.2. Heat transfer correlations.

The heat transfer correlations as selected by TEN WOLDE [4.1-9] for the various regions defined above are given here without further comments.

1. (convective preheat region)

Dittus-Boelter

$$Nu = 0.023\ Re_f^{0.8}\ Pr_f^{0.4} \qquad (4.2\text{-}17)$$

limits of application:

$10^4 < Re < 6.10^5$
$0.6 < Pr < 120$

2 and 3. (subcooled and saturated boiling)

Rohsenow

$$q = C_1\ C_2\ (\vartheta_w - \vartheta_{sat})^3 \qquad [\,kJ/m^2s\,] \qquad (4.2\text{-}18)$$

where:

$$C_1 = C_{pl}^3\ \eta_l\ (\rho_l - \rho_g)^{0.5}\ g^{0.5}\ Pr^{-5.1}\ /\ (h_{lg}^2\ \sigma^{0.5})$$

$$C_2 = 1.4\ 10^3 \text{ for water/steel} \qquad (4.2\text{-}19)$$

The correlation given above applies to clean surfaces. Although fouling affects its accuracy, such deviations are of little importance for the bayonet tube case, where the overall heat resistance across the evaporator tube wall is dominated by the superheated steam film coefficient.
Therefore no special attention has been paid to this aspect.

4. (mist flow region)

Bishop - Sandberg - Tong

$$Nu_f = 0.0193\ Re_f^{0.8}\ Pr_f^{1.23}\ (\rho_g/\bar{\rho})^{0.68}\ (\rho_g/\rho_l)^{0.068} \qquad (4.2\text{-}20)$$

limits for application

$$10.0 < P < 20.0 \quad MN/m^2$$
$$1100 < G < 5000 \quad kg/(m^2s)$$
$$0.0 < x_{DO} < 0.4$$

5. (superheat region)

Bishop - Krambeck - Sandberg

$$Nu_f = 0.0073\ Re_f^{0.886}\ Pr_f^{0.61} \qquad (4.2\text{-}21)$$

limits for application

$$16.5 < P < 21.5 \quad MN/m^2$$
$$0.236\ 10^6 < q < 2.5\ 10^6 \quad J/(m^2s)$$
$$660 < G < 3280 \quad kg/(m^2s)$$
$$0.0025 < D < 0.005$$
$$1.1\ 10^5 < Re_b < 6\ 10^5$$
$$0.93 < Pr_b < 610$$

4.2.3.3. Frictional pressure drop correlation.

1. Single phase flow.

In the single phase flow regions the well known Blasius correlation for the friction factor f is applied:

$$\frac{\partial p}{\partial z}_{fr} = \frac{0.316}{Re^{0.25}}\ \frac{1}{D_H} \cdot \frac{1}{2}\ \rho\ v^2 \qquad (4.2\text{-}22)$$

2. Two-phase flow.

In contrast with single phase flow no simple and accurate correlations are available for the determination of two-phase frictional pressure drop due to the complexity of the physical processes involved. A large number of semi-empirical correlations has been proposed in literature, but all show considerable deviations in comparison with experimental data. WISMAN e.g. [4.2-8] compared the well known correlation of MARTINELLI - NELSON [4.2-9] and a correlation proposed by DUKLER [4.2-10] with one of himself. The latter correlation proved to be by far the most accurate of the three, yet shows a mean deviation of 28% in comparison with experimental data. In the simulations to be discussed later a further development of the original Wisman correlation has been used, thought to be more accurate at that time.

The correlation reads:

$$\left(\frac{\partial p}{\partial z}\right)_{fr} = \frac{1}{2}\frac{\lambda}{D_H}\left((1-\alpha)\ \rho_l\ v_l^2 + \alpha\ \rho_g\ v_g^2 \right) \qquad (4.2\text{-}23)$$

where:

$$\lambda = \frac{0.316}{Re_{tf}^{0.25}} \qquad (4.2\text{-}24)$$

$$Re_{tf} = \left((1-\alpha)\ \rho_l\ v_l + \alpha\ \rho_g\ v_g \right) / \left((1-\alpha)\ \eta_l + \alpha\ \eta_g \right) \qquad (4.2\text{-}25)$$

However, subsequent comparison with the experimental data used in [4.2-8] yielded a mean deviation of 40%. Hence the original correlation of Wisman is recommended as the most accurate two-phase flow friction correlation available as yet. It will be clear, however, that for accurate simulations, especially those concerned with hydrodynamic stability, improved accuracy in predicting two-phase frictional pressure drop is required.

4.2.3.4. Slip correlation.

As discussed above a slip correlation is required not only to account for the actual difference in gas and liquid velocities but also to correct for non-uniform distributions of the separate phases. The derivation of the well-known Bankoff slip correlation was even solely based on the latter effect as the local gas and liquid velocities were assumed to be equal. The numerical value of the Bankoff constant K_B, however, was obtained by fitting actual slip data, thus incorporating physical slip as well (cf. BANKOFF [4.2-3]).

Formulation of a universal physically well-founded slip correlation being hampered by the complexity of the physical processes involved, a great number of semi-empirical relationships have been proposed in literature, each with its own ranges of validity.

A very widely applied correlation is the so called Bankoff - Jones slip correlation (cf. JONES [4.2-11]). In our case a slightly adapted vension of this correlation is proposed. The reasons for this adaptation are discussed in detail in Appendix 4B.

The adapted version reads:

$$s = \frac{(1+\delta - \alpha)}{(K_B+\delta) + (1-K_B)\ \alpha^r - \alpha} \qquad (4.2\text{-}26)$$

where:

$$K_B = 0.71 + 0.29\ \frac{p}{p_{cr}} \qquad (4.2\text{-}27)$$

$$r = 3.33 + 0.577\ \frac{p}{p_{cr}} + 4.74\ \left(\frac{p}{p_{cr}}\right)^2 \qquad (4.2\text{-}28)$$

$$\delta = 0.04 \qquad (4.2\text{-}29)$$

4.2.3.5. Heat distribution paramater.

For reasons explained in the foregoing the only coefficient needed in this category is the k factor suggested by Bowring (cf. subsection 4.2.2.2.2.1). After comparing a number of different correlations with the experimental evidence available for this constant VAN VONDEREN [4.2-12] recommended the following correlation:

$$k = \left(\frac{\vartheta_b - \vartheta_r}{\vartheta_{sat} - \vartheta_r} \right)^2 \qquad (4.2\text{-}30)$$

where ϑ_b is the local bulk temperature and ϑ_r is the bulk temperature at the initial point of net vapour generation.

4.3. Test facility.

4.3.1. Test module.

While this unit was meant to resemble as closely as possible one module of a possible future full-size steam generator, this tendency was limited by several constraints imposed by practical considerations. The acceptance of such constraints and of the resulting non-optimized thermo-hydraulic design of the test module appeared justified in view of the explorative nature of the study.
In order to put the resulting compromise into proper perspective, these constraints will be discussed under the following headings:

- heating fluid
- flow pattern
- process conditions
- dimensions

4.3.1.1. Heating fluid.

Contrary to later MSBR design studies (cf. ROSENTHAL [4.1-1]) proposing a mixture of sodium fluoride and sodium fluoroborate for intermediate heat carrier, mainly because of its lower melting point (385 ^{0}C), FLiNaK was retained because of its availability in our laboratory from the earlier experiments and because of the experience accumulated with this salt mixture.

4.3.1.2. Flow pattern.

In any large size steam generator the shell-side salt flow would be baffled for effective heat transfer, resulting in partial crossflow.
In our test module the shell consists of a third concentric tube of slightly larger diameter than the pressure tube, forming an annular space through which the salt flows downward in pure parallel flow.
While it is obvious that the resulting straight counterflow will not be representative of the complex shell-side flow in a baffled exchanger, this was considered to be of minor importance in view of the aims of the present investigation.

4.3.1.3. Process conditions.

The conditions given in section 4.1 were slightly modified for the experimental single tube steam generator. While the water/steam side temperatures and the salt inlet temperature proposed for the full size steam generator could be maintained, the salt outlet temperature had to be raised significantly above the value of 460 ^{0}C proposed in [4.1-1] in order to avoid salt flow rates too small for the operating range of the pump (3-10 kg/s for the primary circuit under consideration).
An additional reason for raising the salt outlet temperature was given by the melting point of the salt. For the proposed MSBR coolant the margin between its melting point of 385 ^{0}C and the proposed outlet temperature of 460 ^{0}C would be quite adequate; however, for FLiNaK with its melting point at 453 ^{0}C this margin is far too small.
As a result of these considerations the primary temperature drop during the experiments ranged from 0 - 12 ^{0}C, the latter value corresponding to a rated mass flow rate of 6.8 kg/s. As the main aim of the experiments was to verify the performance predictions obtained from analysis this deviation from the proposed condition was not considered of vital importance.

For fixed in- and outlet conditions the secondary mass flow would normally be determined by the primary heat source, i.e. the 250 kW electrical heater. However, for reasons resulting from the design and therefore to be discussed in a subsequent section, the maximum amount of heat to be transferred in the steam generator is limited to about 130 kW, corresponding to a secondary mass flow rate of 0.065 kg/s.
The nominal process conditions discussed above are summarized in the table given in figure 4.3-1 and indicate that - for the reasons mentioned above - the optimal primary secondary mass flow ratio of 9 proposed in 4.1.1 had to be raised to about 105.

4.3.1.4. Dimensions.

The dimensions of the test module are listed in the table given in figure 4.3-2. These dimensions correspond to the results of the optimization discussed in subsection 4.1.2.1 with the exception of the evaporator length and hence the dimensions of the ceramic insulation layer.
As the design of the test module was completed before the optimization, the importance of the evaporator length was not yet fully appreciated at that time. The length was restricted to 9.1 m in view of the maximum building height in our laboratory.
Again considering the aim of these investigations this is not considered of vital importance.

4.3.2. Water/steam loop.

4.3.2.1. General.

Figure 4.3-3 gives a flowsheet of the DMSP bayonet tube steam generator test facility. The left part of the figure shows the molten salt loop. This loop is identical to the loop used for the FLiNaK heat transfer measurements described in section 3.2. The right part of the flowsheet shows the water/steam loop comprising the feedwater supply system and the heat sink. Both loops are thermally connected by the test module, i.e. the single-tube experimental steam generator.

4.3.2.2. Feedwater supply system.

At rated conditions feedwater should enter the steam generator at a temperature of 280 ^{0}C and a pressure sufficient to provide for a steam exit pressure of 18 MN/m^{2}.
Demineralized and deaerated water is obtained from a central make-up tank serving several test facilities in the laboratory. The water stored in this tank is kept at a pH close to 7 and a conductivity below 20 µS.
The feedwater is pressurized by a duplex piston pump of variable capacity and subsequently preheated in a counterflow oil-heated preheater. The heated oil is obtained from a separate oil-fired heater. The heating oil temperature can be adjusted to provide the kind of variation of feedwater temperature with secondary mass flow typical for a steam turbine plant.
A small pressurizer filled with nitrogen is provided to damp the fluctuations due to the piston pump.
During pre-operational testing of the facility the steam generator showed a certain tendency to develop flow oscillations at start-up. Therefore an adjustable restriction in the form of a pneumatically adjustable valve was provided downstream of the pressurizer. The pressure ahead of this control valve was maintened at a constant value of some 1.5 MN/m^{2} above system pressure so as to provide an additional stabilizing single phase pressure drop in the system.

4.3.2.3. Heat sink.

The superheated steam leaving the steam generator at about 18 MN/m^{2} and 540 ^{0}C is first throttled to atmospheric pressure by a pneumatic control valve and subsequently cooled by a desuperheating spray obtained from the same make-up tank to approximately 150 ^{0}C. This low pressure, low temperature steam is led into a condenser, whence the condensate is returned to the make-up tank, thus closing the water/steam loop.

4.3.3. Instrumentation and control.

Distinction can be made between loop operational instrumentation with control panel display and experimental instrumentation pertaining to the experiments proper and connected to a data acquisition system with punched tape output. A number of instruments, such as those for flowrate, pressure, and some of the temperatures are used for both purposes.

4.3.3.1. Loop instrumentation and control.

Figure 4.3-4 shows an operational instrumentation diagram. The controlled variables of the system are:

- salt inlet temperature
- feedwater flow
- feedwater inlet temperature
- feedwater (pressurizer) pressure
- outlet steam pressure
- waste steam temperature after pressure reduction

The salt inlet temperature is controlled as described in subsection 3.2.2, i.e. by adjusting the electrical power supplied to the main heater to the amount of heat transferred in the steam generator (load following).

The feedwater flow is measured by an orifice with integrated pneumatic differential pressure transmitter. The signal of this transmitter is converted to an electrical input signal for an electronic PI controller with manual setpoint adjustment.

The controller output signal is reconverted into a pneumatic signal actuating a control valve in the bypass across the feedwater pump ★). The feedwater inlet temperature is controlled indirectly in order to avoid stability problems resulting from the large distance (some 60 m) between the oil heater and the preheater.
The fact that the preheater proved to be of ample capacity, resulting in a very small temperature difference between the oil inlet and feedwater outlet temperatures, offered the possibility to avoid this problem by remote manual adjustment of the oil heater control setpoint. In this simple way a nearly constant feedwater temperature could be obtained, as only small adjustments of the oil heater control setpoint were required to restore the feedwater temperature to its original value even for large changes in power.
The feedwater (pressurizer) pressure was controlled by a pneumatic PI controller positioning the inlet throttle valve so as to adapt the amount of throttling to the load.
For controlling the outlet steam pressure a pressure signal is picked up at the outlet of the steam generator and transmitted to a pneumatic PI controller governing the throttling valve downstream of the steam generator.
For controlling the waste steam temperature a temperature signal is picked up downstream of the spray cooler and transmitted to a pneumatic PI controller governing the spray water supply valve.

4.3.3.2. Test instrumentation.

4.3.3.2.1. Instrumentation for steady state and transient experiments.

As mentioned before the aim of these experiments is to provide information on the temperature distribution in the steam generator for comparison with the results of the computer programs discussed in sections 4.4, 4.5 and 4.6.
This means that local pressures and temperatures should be determined in addition to the overall conditions of the steam generator.
The overall conditions measured and the instruments used for this purpose are:

at the primary side of the steam generator:

- FLiNaK mass flow (venturi flow meter: cf. section 2.2)
- FLiNaK inlet and outlet temperatures (Pt-thermometers)

at the secondary side:

- feedwater mass flow (integrated-orifice flowmeter)
- feedwater temperature (Pt-thermometer)
- feedwater pressure } (Bourdon pressure transmitters)
- outlet steam pressure }
- pressure drop across the steam generator (diaphragm pressure-differential transmitter)
- outlet steam temperature (Pt-thermometer)

Unfortunately only a limited amount of internal instrumentation for local measurements was possible due to the following reasons:

- extreme conditions: a highly corrosive salt at a temperature of about 625 ^{0}C

★) *This double conversion was imposed by the availability of equipment in the author's laboratory.*

- complex geometry of the bayonet tube
- the necessity to avoid disturbances in the evaporator flow that could prematurely start and thus unduly affect the boiling process.

The geometry of the bayonet made it impossible to tap secondary pressures at more points than at the in- and outlet of the water/steam channel, as the salt channel completely surrounds the bayonet.
As regards the temperature distributions, thermocouples were installed at eighteen levels in the outer (salt) gap for measuring the primary temperature profile. The necessity to avoid flow disturbances in the evaporator tube prohibited the installation of thermocouples in the central tube. Therefore the only temperature profile to be measured at the secondary side was the temperature distribution in the superheater gap, where a total of 25 thermocouples was installed. The location of the various thermocouples in the steam generator is shown in figure 4.3-5.
While this may seem rather poor, a method will be discussed in subsection 4.4.3.2 by which the enthalpy profile in the evaporator can be estimated fairly accurately from the measured salt and steam temperatures, permitting a detailed comparison of experimental results and computer simulations.

4.3.3.2.2. Instrumentation for the stability experiments.

As will be discussed in subsection 4.5.1 verification of the analytical simulations of the bayonet tube hydro-dynamic stability behaviour required measurements of the response of the total secondary side pressure drop to harmonic perturbations in the feedwater mass flow rate.
The only instrumentation needed for these measurements proper consisted of a fast flow meter for the secondary inlet mass flow rate and a differential pressure meter for measuring the secondary side pressure drop variations. The latter instrument was the same as used in the other experiments, described in subsection 4.3.3.2.1.
The fast flow meter, installed in order to avoid uncertainties due to dynamic effects in orifice-type mass flow measurement, was a turbine flow meter with excellent dynamic properties (time constant τ = 0.05 s).

4.3.3.2.3. Calibration.

The calibration of the different instruments will be discussed in the order of their appearance in subsection 4.3.3.2.1.
According to the analysis of section 2.2 the accuracy of the venturi flow meter amounts to 4% of full scale. The only part of the venturi prone to drift, viz. the differential pressure meter, was repeatedly calibrated against a dead weight tester (a special instrument for calibration of pressure transmitters). This instrument was applied for the calibration of all pressure meters in the system.
The platinum resistance thermometers had been calibrated by the manufacturer and calibration sheets were included in the delivery. To avoid sealing problems these thermometers were inserted in the loop in thermowells welded in the wall of the tubing. The additional heat resistance between the thermometer and the thermowell is taken into account by adding 0.15 ^{0}C to the measured values after applying the inaccuracy correction of 0.1 ^{0}C given by the manufacturer for the thermometers proper. A check after the measurements showed no noticeable drift from the data given in the calibration sheets.
The flowmeters for the feedwater mass flow rate were calibrated by the "bucket and weight" method (the time for a certain amount of water, determined by weighing, to flow into a vessel is measured). In this way the total chain of instruments between flow and reading of the electrical

instrument is calibrated at once, thus avoiding accumulation of errors, possible if all links are calibrated separately.
The thermocouples for local temperature measurement were calibrated against the pt-resistance thermometers in the salt channel during isothermal operation of the loop, as discussed in section 3.2.

4.3.4. Operational procedures.

It seems useful to mention some operating experiences gained during the experiments on this special type of steam generator.
In the first place the start-up is completely different from the customary procedure. In normal steam generators the procedure starts with the circulation of the feedwater at a low pressure. Then ignition of the burner follows and generation of steam commences (in sodium heated steam generators the temperature of the primary fluid is raised). The desired conditions are reached by simultaneous raising of the outlet steam temperature and the pressure.
For the salt-heated bayonet tube this scheme fails because of the high melting point of the salt. It is not possible to start the heat transfer gradually as the system must be filled at a temperature a sufficiently far above the melting point. Failure to observe this margin would not only give rise to the danger of plugging the channels by frozen salt, but also cause intolerable thermal stresses.
Therefore the primary fluid must be in circulation before water enters the steam generator. Now the stress problem is reversed, as it is equally disastrous to inject feedwater into the steam generator that has attained a uniform temperature of about 600 ^{0}C. To solve these problems a start-up boiler was applied, capable of delivering a small mass flow (10% of the maximum capacity) of steam at a lower pressure (7 MN/m^{2}). This steam, superheated to 280 ^{0}C, was fed into the steam generator to cool down the central tube. The much smaller heat transfer coefficient of steam compared to feedwater ensured a slow and smooth cooling of the interior of the bayonet. When the temperatures were stabilized to some degree, the pressure of the steam was gradually raised, causing first saturated and then increasingly wet steam to enter the steam generator, until at last zero quality (water) was obtained at the entrance. Careful execution of this procedure ensured a trouble free start-up.
During the first steam generator tests it became clear that an additional restriction in the feedwater line would be required to avoid the occurence of spontaneous oscillations. After installation of this restriction stable operation of the steam generator proved possible over the entire range of interesting conditions.
The cause and significance of this so-called loop-instability will be discussed in subsection 4.6.2.2.
Shutdown proved a more delicate operation than start-up. The procedure followed was the reverse of the start-up procedure. Nevertheless sometimes oscillations occurred, during which the top temperature (exit of the central tube) fluctuated severely, in some cases over 100 ^{0}C (cf. figure 4.3-6), indicating that saturated water reached the thermocouples located at the exit of the evaporator tube.
This example of loop instability (cf. figure 4.6.2.2) was probably triggered off by flow-pattern transitions in the two-phase region (cf. BOURE [4.1-11]).

4.4. Steady state.

4.4.1. Analysis.

4.4.1.1. Additional assumptions.

The balance equations in subsection 4.2.2. contain a minimum of simplifying assumptions. However not all the simulations reported here require these complete equations. Furthermore the development of the different simulation programs took place over a period of several years, in the course of which increased insight and experience in simulation techniques sometimes led to a different approach.
The following additional assumptions were made for the steady state analysis:

a) equal mean velocities of gas and liquid i.e. homogeneous flow (s = 1)

b) neglection of the pressure terms in the energy equation

c) a value of k = 0 for the Bowring constant, i.e. no net vapour production in the subcooled boiling region.

ad.a) Experimental evidence shows that the slip s decreases rapidly with increasing pressure. This effect is often explained by the decrease in buoyancy of the bubbles, due to the decreasing difference in density between the liquid and the gas phase. This explanation, however, appears incomplete for the following reasons: the buoyancy is proportional to the difference in density between liquid and gas. This difference decreases far less rapidly with pressure than the slip values given by JONES [4.2-12] (the former by a factor of 0.75, the latter by a factor of 0.25 between 8 and 18 MN/m^2). To the author's opinion part of the rapid decrease in slip, is due to the rapid decrease in surface tension with increasing pressure.
It is this surface tension which mainly determines the bubble size (cf. WISMAN [4.4-1]). The resulting much smaller bubbles at higher pressures have a greater specific flow resistance, i.e. do not rise as fast as larger bubbles, and are more uniformly distributed by the turbulence in the fluid, thereby decreasing the effects of non-uniform radial void distribution. These two effects might offer a more complete explanation for the lower slip values observed at higher pressures.

ad.b) TEN WOLDE [4.1-9] shows that in high pressure steam generators the pressure terms in the energy balance amount to only 0.1% of the total and may therefore safely be neglected.

ad.c) The assumption made in subsection 4.2.3.2 that the Rohsenow heat transfer correlation, developed for saturated boiling, will also be valid for the subcooled region implies that taking $k_{Bowring} = 0$ for the entire subcooled region will only have a limited local effect. The fact that the void fraction and the velocities thus obtained for this region differ from the true values will not affect the amount of heat transferred to the mixture, nor the enthalpy distribution.
Consequently the conditions in the downstream regions will be predicted correctly.

4.4.1.2. Modified equations.

With these additional assumptions the two-phase balance equations for steady state simplify to (cf. TEN WOLDE [4.1-9]):

- mass balance:

$$G = \text{constant} \tag{4.4-1}$$

- momentum balance:

The pressure distribution was considered of little interest because of its negligible effect on mass flow rate in a once-through steam generator. Therefore the momentum balance is omitted from the steady state analysis.

- energy balance:

$$G \frac{\partial \bar{h}}{\partial z} = q \frac{O}{A} \tag{4.4-2}$$

For the primary fluid, where the specific heat is taken constant, the enthalpy can be written as:

$$h = c\, \vartheta \tag{4.4-3}$$

Substitution of this equation yields:

$$G\, c \frac{\partial \vartheta}{\partial z} = q \frac{O}{A} \tag{4.4-4}$$

Set of equations.

The total set of equations to be solved in the steady state is formed by the energy balances for the three different channels (cf. figure 4.1-1):

- primary channel:

$$G_p\, c_p \frac{\partial \vartheta_p}{\partial z_p} = - q_{p \to SH} \frac{O_p}{A_p} \tag{4.4-5}$$

- superheater gap:

$$G_S \frac{\partial h_{SH}}{\partial z_{SH}} = q_{p \to SH} \cdot \frac{O_p}{A_{SH}} - q_{SH \to EV} \cdot \frac{O_{SH}}{A_{SH}} \tag{4.4-6}$$

- evaporator channel:

$$G_S \frac{\partial h_{EV}}{\partial z_{EV}} = q_{SH \to EV} \frac{O_{SH}}{A_{EV}} \tag{4.4-7}$$

note: all axial coordinates are positive in the respective flow direction.

The heat fluxes are given by:

$$q_{p\rightarrow SH} = k_{p\rightarrow SH} \, (\vartheta_p - \vartheta_{SH}) \qquad (4.4\text{-}8)$$

and:

$$q_{SH\rightarrow EV} = k_{SH\rightarrow EV} \, (\vartheta_{SH} - \vartheta_{EV}) \qquad (4.4\text{-}9)$$

In keeping with common engineering practice the overall heat transfer coefficients refer to the outer tube surfaces.

4.4.1.3. Solutional procedure.

This set of first order differential equations is solved by direct integration. More or less for historical reasons the author has selected this procedure despite its infrequent use in heat exchanger analysis, caused by its inherent numerical stability problems in pure counterflow applications. Stability analysis of the present case, however, proved that, provided the following condition:

$$\frac{k_{p\text{-}SH} \, O_p}{A_p \, G_p \, c_p} + \frac{k_{SH\text{-}EV} \, O_{SH}}{A_{EV} \, G_{EV} \, c_{EV}} + \frac{k_{p\text{-}SH} \, O_p + k_{SH\text{-}EV} \, O_{SH}}{A_{SH} \, G_{SH} \, c_{SH}} > 0$$

is fulfilled, only a very weakly instable component, not posing problems, remains in the solution. For integration from top to bottom (cf. figure 4.1-1, G_p and G_{EV} negative, G_{SH} positive) the stability criterion mentioned above will always be fulfilled, due to the weak thermal flux of the superheater steam. Against this advantage of direct integration stands the disadvantage that the boundary conditions for both primary and secondary sides are prescribed at the bottom of the steam generator. This necessitates an iterative procedure following an initial guess of the conditions at the top of the steam generator. In spite of this iterative approach downward integration has proved to be an efficient method, requiring only five iteration steps to converge as compared to ten iterations for the CSDT method applied by TEN WOLDE [4.1-9] for a pure counterflow once-through steam generator.
The integration algorithm actually applied is the HEUN predictor corrector method (cf. e.g. LEE [4.4-2]). This algorithm reduces the accumulation of rounding-off errors while allowing application of relatively large integration steps. Figure 4.4-2 shows a simplified flow sheet of the program. For a detailed description the reader is referred to IPENBURG [4.4-3]. Figures 4.4-3 and 4.4-4 show typical results of the program: a print-out and a plot respectively. In view of the direction of integration the origin of the axial coordinate has been located at the top of the steam generator. For reasons of consistency this choice, though somewhat illogical from the point of view of geometry, has been maintained throughout this thesis.

4.4.2. Experiments.

4.4.2.1. Data acquisition.

To reduce the effect of random errors all measuring points were scanned ten times for each steady state measurement by means of a H.P. data logger and the output was transferred to punched tape. These tapes were read into the computer (IBM 370/158) off line and processed by means of a special data reduction program (MEANTAB), yielding the average millivolt value for each

measuring point.
Excessive deviations (> 1.5 σ) were automatically deleted and signaled in the output.
The obtained average values for all measuring points were transferred to a special purpose data processing program (SMEBT) for:

- transformation of millivolt values into the associated physical values
- deriving evaporator data from the salt and superheated steam measurements
- tabulation and plotting of data as shown in figures 4.4-4 and 4.4-5 respectively.

The second point requires some elaboration.
The original idea was to obtain evaporator temperatures or qualities from energy balances for small sections of the steam generator. Assuming perfect insulation such a balance states that the heat transferred to the evaporator equals the heat removed from the salt decreased by the heat retained in the steam:

$$Q_{EV} = Q_p - Q_{SH} \tag{4.4-10}$$

The two right hand side terms were to be determined from the measured temperature distribution in the primary and superheater channels by applying steady state energy balances to small sections of the steam generator. The amounts of heat released by the salt and retained by the steam in an element of length $\Delta\ell$ (cf. figure 4.4-6) are given by:

$$Q_p = G_p A_p c_p (\vartheta_{p_{out}} - \vartheta_{p_{in}}) \tag{4.4-11}$$

$$Q_{SH} = G_s A_{SH} (h_{SH_{out}} - h_{SH_{in}}) \tag{4.4-12}$$

respectively.
The amount of heat absorbed in the evaporator is given by:

$$Q_{EV} = G_s A_{EV} (h_{EV_{out}} - h_{EV_{in}}) \tag{4.4-13}$$

As motivated in subsection 4.4.1.1 expansion work has been neglected.
The boundaries of the sections have been chosen at the locations of the thermocouples (0.5 m apart) with the exeption of the lowest section that has its lower boundary at the resistance thermometer in the feedwater inlet (cf. figure 4.3-5).
Combination of equations (4.4-10), (4.4-11), (4.4-12) and (4.4-13) yields the final expression for the evaporator enthalpy at the top of a section:

$$h_{EV_{out}} = h_{EV_{in}} + \frac{G_p A_p c_p (\vartheta_{p_{out}} - \vartheta_{p_{in}}) - G_s A_{SH} (h_{SH_{out}} - h_{SH_{in}})}{G_s A_{EV}} \tag{4.4-14}$$

Starting at the feedwater inlet repeated application of this formula to the successive sections should have yielded the complete enthalpy distribution in the evaporator and hence - in combination with the local pressure - the temperature or quality distribution in this channel.

Unfortunately this scheme failed due to insufficient accuracy of the FLiNaK temperature measurements. Application of equation (4.4-11) yielded errors in Q_p of up to 50%. Therefore the alternative described below had to be applied.
The total amount of heat transferred from the salt to the water/steam side could be determined very accurately from:

$$P_{tot} = \phi_{ms} \left(h_{s_{out}} - h_{w_{in}}\right) \tag{4.4-15}$$

thanks to the large difference in enthalpy and the accuracy of the Pt thermometers located at the feedwater inlet and steam outlet.
The problem was to determine the distribution of this heat along the length of the steam generator. The overall heat transfer coefficient from salt channel to superheater gap could be assumed fairly constant along the length of the steam generator, its only significant varying component being the film coefficient in the superheater gap. This film coefficient varied with steam temperature and mass flow. Thus the overall heat transfer coefficient may be written as:

$$k_{p \to SH} = \frac{1}{a + b\, f(\phi_m)\, g(\vartheta)} \tag{4.4-16}$$

The functions f and g were determined from the heat transfer correlation of BISHOP (cf.subsection 4.2.3.2):

$$\alpha = \frac{\lambda}{D}\, 0.0073\, Re^{0.886}\, Pr^{0.6} \left(1 + 2.76 \frac{D_H}{L}\right) \tag{4.4-17}$$

From this equation it follows that:

$$f(\phi_m) = (\phi_m)^{-0.886} \tag{4.4-18}$$

while $g(\vartheta)$ turns out to be proportional to:

$$\frac{\lambda\, Pr^{0.6}}{\nu^{0.886}} \tag{4.4-19}$$

For steam of 18 MN/m^2 this term can be approximated to within 1% by a polynomial:

$$g(\vartheta) = P_0 + P_1\, \vartheta + P_2\, \vartheta^2 + P_3\, \vartheta^3 \qquad (\vartheta \text{ in } {}^0C) \tag{4.4-20}$$

where $P_0 = 12.44$

$P_1 = -6.47\ 10^{-2}$

$P_2 = 1.17\ 10^{-4}$

$P_3 = -0.07\ 10^{-6}$

for a temperature range from 350 ^0C to 700 ^0C. The total amount of heat transferred from the salt to the water/steam side can now be found by integrating:

$$P_{tot} = \phi_{ms} (h_{s_{out}} - h_{w_{in}}) = \int_0^L k_{p\to SH} \pi D_o (\vartheta_F - \vartheta_S) \, d\ell$$

$$= \pi D_o \int_0^L \frac{(\vartheta_F - \vartheta_S)}{a + b \; f(\phi_m) \; g(\vartheta)} \, d\ell \qquad (4.4\text{-}21)$$

The only unknowns in this equation are a and b. These two unknowns were determined from a number of steady state measurements by minimizing:

$$\sum_{i=1}^{n} \varepsilon^2 = \sum_{i=1}^{n} (P_{meas_i} - P_{calc_i})^2 \qquad (4.4\text{-}22)$$

As this is a non-linear regression problem a special optimization routine had to be applied. This optimization yielded the following values:

$$a = 3.42$$

$$b = 0.308$$

As apparent from the table in figure 4.4-7 substitution of these values into equation (4.4-21) yields very accurate results for most of the measurements. Introducing a correction factor f_c for each measurement to adapt the total power determined from the latter equation to the power actually transferred according to equation (4.4-15), the local heat flux between salt and superheater channel may be determined from:

$$q_{p\to SH} = f_c \, k_{p\to SH} \, (\vartheta_F - \vartheta_{SH}) \qquad (4.4\text{-}23)$$

Substitution of this heat flux and of equations (4.4-12) and (4.4-13) into equation (4.4-14) yields:

$$h_{EV_{\ell+\Delta\ell}} = h_{EV_\ell} + \frac{\pi D_o \, f_c \, k_{p\to SH} \, (\vartheta_p - \vartheta_{SH}) \, \Delta\ell - G_s \, A_s (h_{SH_{out}} - h_{SH_{in}})}{G_s \, A_{EV}} \qquad (4.4\text{-}24)$$

Application of this equation for the successive sections starting at the feedwater inlet yields the enthalpy distribution in the evaporator. The temperature or quality distribution can be derived from this distribution provided the pressure distribution is also known. As in the present case only the pressure at the feedwater inlet and steam outlet could actually be measured, an approximate pressure distribution had to be derived. A rough analysis showed that 80% of the pressure drop was concentrated in the superheater gap due to the high velocities occurring there. The remaining part was assumed to be uniformly distributed along the length of the evaporator.
In view of the small total pressure drop values (< 3 bar at the maximum secondary flow rate) the effect of this approximation was very small.

4.4.2.2. Test program.

The conditions for the reported experiments are summarized in figure 4.4-8.

4.4.2.3. Experimental results.

The results of these experiments are given in subsection 4.4.3, where they are compared with computed temperature and quality distributions (cf. figures 4.4-9a through 4.4-9k).

4.4.3. Evaluation of results.

Comparison of the analytical and experimental results for higher feedwater flow rates (ϕ_m > 0.035 kg/s ≈ 50% load) shows excellent agreement. For lower feedwater mass flow rates analysis and experiment tend to differ. Examination of figures 4.4-9k and 4.4-9j indicates that these differences are the result of underestimation of the heat transfer coefficient in the superheater gap. The values of the local mass fluxes occurring under those conditions (G < 325 kg/m^{2}s vs G = 605 kg/m^{2}s at full load) are well below the range of validity of the heat transfer correlation applied (equation (4.2-21); range: 660 < G < 3280 kg/m^{2}s).
Extrapolation below G = 325 kg/m^{2}s is clearly not justified and hence more accurate predictions would require new heat transfer correlations valid for this lower range of mass fluxes. The preliminary optimization discussed in IPENBURG [4.1-3], however, yields a mass flux in the superheater gap of 1019 kg/m^{2}s at full load and correspondingly higher values at part load, thus obviating the need for new correlations except for very low loads (< 25%).
For loads ranging from 25% to full load the applied set of correlations is found to be adequate and thus the BASTA program proves a suitable tool for optimization purposes and part load prediction.

A remarkable property of the bayonet tube concept is evidenced by the figures of the various part loads: the steam outlet temperature is almost completely independent of load. This is easily understood, by visualizing this temperature as result of "equilibrium" between the salt and feedwater inlet temperatures. This property is completely at variance with the operating characteristics of other steam generator designs, where the steam outlet temperature normally exhibits a strong inverse relation with load. In the present case the steam temperature will follow the salt inlet temperature, a dependence that could well be used for controlling the steam outlet temperature, thus obviating or reducing desuperheating usually applied for this purpose.

4.5. Transients.

4.5.1. Introduction.

A significant number of mathematical models for simulation of the transient behaviour of once-through steam generators had been published in the open literature prior to the steam generator test program described in the present thesis. Some of these were (multiple) lumped models, e.g. SANATHANAN [4.5-1], others distributed parameter models, e.g. TEN WOLDE [4.1-9].
It appears worth while here to point out that the difference between these two groups is gradual rather than one of principle, as the inevitable discretization of the partial differential equations occurring in the solution procedure of the distributed parameter models results in finite difference equations that are in fact overall balances for lumps the size of which is determined by the spacing. Except for some earlier models, e.g. HÖLD [4.5-2], all models found in literature solve the original, non-linear equations, linearization being inadequate for predicting large

transients. For a review of the various approaches, with particular emphasis on distributed parameter models, the reader is referred to BRUENS [4.5-3].
None of the models available in literature was found readily adaptable to the complex geometry of the bayonet tube steam generator and a new model had to be developed for this purpose. Previous steam generator transient simulations at the author's laboratory had all been performed on hybrid computers. At that time, however, the rapid development of digital computing hardware heralded a shift from hybrid to purely digital simulation and it was therefore decided to follow the latter route. However, in order to take full advantage of the experience gained in hybrid modeling it was decided to adopt basically the same solutional technique by applying a special language: Continuous System Modeling Program (CSMP), developed for using the analog approach on a purely digital computer (cf. [4.5-3]). Due to causes discussed later this CSMP program, called DYBRU, yielded an undesirably high ratio of computing to process time. In an attempt to improve this ratio a new transient model was developed from a program originally generated for simulating the bayonet tube steam generator's hydro-dynamic stability behaviour in the time domain (cf. subsection 4.6.2.3). This model utilizes the Lagrangian description of fluid dynamics, i.e. it describes the behaviour of fluid particle travelling from inlet to outlet. In this respect it differs from the models mentioned earlier in this introduction which are based on the Eulerian description, where the conservation equations are formulated for a stationary control volume (lump or grid step).
In the remainder of this section both approaches will be described and their results compared to measurements. In order to explain the limited effort spent on the development, verification and improvement of these models their limitation to the bayonet tube geometry should be emphasized and contrasted with the aim of general applicability for part of the work on stability reported in subsection 4.6.3.

4.5.2. Analysis.

4.5.2.1. Modified equations.

For the transient models the same simplifying assumptions have been made as for the steady state model (listed in subsection 4.4.1.1). The basic conservation equations given in subsection 4.2.2 hence simplify to (cf. TEN WOLDE [4.1-9]:

mass balance:

$$\frac{\partial \bar{\rho}}{\partial t} + \frac{\partial \bar{\rho} v}{\partial z} \text{ ★)} = 0 \qquad (4.5\text{-}1)$$

momentum balance:

$$\bar{\rho} \left\{ \frac{\partial v}{\partial t} + v \frac{\partial v}{\partial z} \right\} = - \frac{\partial p}{\partial z} - \frac{\tau O}{A} \pm \bar{\rho} g \qquad (4.5\text{-}2)$$

(- for upward flow, + for downward flow)

★) *In case op two-phase flow the upper bar denotes mixture values as defined in subsection 4.2.2.2.1.*

energy balance:

$$\bar{\rho} \left\{ \frac{\partial \bar{h}}{\partial t} + v \frac{\partial \bar{h}}{\partial z} \right\} = \frac{q_O}{A} \qquad (4.5\text{-}3)$$

4.5.2.2. Solution in Eulerian coördinates (DYBRU).

The equations underlying this approach differ from the set of equations given in the previous subsection because of an additional assumption: the mass storage effect is neglected for both single and two-phase flow, reducing the mass balance (4.5-1) to:

$$G = G(t) \qquad (4.5\text{-}4)$$

where:

$$G = \bar{\rho}\, v$$

This assumption, implying that not only $\frac{\partial \rho}{\partial t}$ but also $\frac{\partial \alpha}{\partial t}$ is zero, introduced as part of the overall effort to reduce computing times but evidently unrealistic for the two-phase mixtures under consideration, was dropped from subsequent dynamic models for the secondary flow.
The basic solution technique applied here is identical to the one applied by TEN WOLDE [4.1-9] on a hybrid computer, viz. CSDT (Continuous Space Discrete Time).
The set of partial differential equations in z and t is transformed into a set of ordinary differential equations in z by replacing the differentials $\frac{\partial}{\partial t}$ by finite differences. The analog part of a hybrid computer is perfectly suited for integrating these ordinary differential equations along the length of the steam generator. The problem of avoiding numerically unstable integration is solved by consistently integrating the channels in the direction of flow, while assuming the conditions in adjacent counterflow channels to remain constant (cf. figure 4.5-1). Iteration starts by assuming arbitrary conditions in the superheater gap and integrating the evaporator and salt channel from inlet to top. Then the process is reversed, with the superheater being integrated in the flow direction starting from the top, while conditions in the evaporator and salt channels are assumed constant. This process is repeated until the temperature at the top remains constant within a certain limit.
This approach was implemented in CSMP (Continuous System Modeling Program). CSMP was developed by IBM to provide a sophisticated digital method for simulating analog systems with the objective to combine the advantages of both methods.
To make its application as simple as that of an analog computer a significant number of actions are performed automatically by the system, e.g.:

- integrating step size is selected dynamically so as to obtain the specified accuracy
- in a system with a number of integrators, an iterative module is assembled automatically. This module is repeatedly executed for each time step so as to approximate simultaneous integration as closely as possible, be it at the expense of an increased number of operations.

For our application, these automatic system actions proved disadvantageous; though simplifying operation, they give the system a certain degree of rigidity hampering adjustment to special requirements.
For example in the CSDT method, where integration is performed with respect to the axial coördinate instead of time, free selection of integration step size is not possible as the boundaries of the different flow regions have to coincide with the end of a step. Special measures required to prevent free selection of step size in the neighbourhood of region boundaries, not only increased computing time but also severely complicated programming.
Hence the expected advantages of easy and clear programming proved to a large degree absent, whereas the drawback of increased computing time proved much worse than anticipated (computing time = 100 à 120 times real time), leading to the abandonment of this approach. For further details the reader is referred to BRUENS [4.5-4].

4.5.2.3. Solution in Lagrangian coördinates (DSTS).

For a solution in Lagrangian coördinates the equations (4.5-1) through (4.5-3) have to be transformed to take account of the fact that in a Lagrangian description a moving coördinate system is assigned to each fluid particle, with the origin located in its center.
The following relationship holds between a time derivative in the Lagrangian and one in the Eulerian system:

$$\left(\frac{\partial \rho}{\partial t}\right)_L = \left(\frac{\partial \rho}{\partial t}\right)_E + \left(\frac{\partial \rho}{\partial z}\right)_E \frac{\partial z}{\partial t} = \left(\frac{\partial \rho}{\partial t}\right)_E + v\left(\frac{\partial \rho}{\partial z}\right)_E \qquad (4.5\text{-}5)$$

where v is the velocity of the particle under consideration.
Combination of this expression with the mass balance of equation (4.5-1) yields:

$$\left(\frac{\partial \rho}{\partial t}\right)_L = - \rho \left(\frac{\partial v}{\partial z}\right)_E \qquad (4.5\text{-}6)$$

Applying a similar process to the energy balance of equation (4.5-3) yields:

$$\rho \left(\frac{\partial h}{\partial t}\right)_L = \frac{q\ O}{A} \qquad (4.5\text{-}7)$$

If pressure effects on the density are neglected as assumed, the following relationship holds between variations of ρ and h:

$$\delta \rho = \frac{d\rho}{dp} \delta p \qquad (4.5\text{-}8)$$

Combination of equations (4.5-6), (4.5-8) and (4.5-7) yields:

$$\left(\frac{\partial \rho}{\partial t}\right)_L = \frac{\partial \rho}{\partial h} \left(\frac{\partial h}{\partial t}\right)_L = \frac{\partial \rho}{\partial h} \frac{q\ O}{\rho\ A} = - \rho \frac{\partial v}{\partial z} \qquad (4.5\text{-}9)$$

or after rearranging:

$$\frac{\partial v}{\partial z} = - \frac{1}{\rho^2} \frac{\partial \rho}{\partial h} \frac{q\ O}{A} \qquad (4.5\text{-}10)$$

For two-phase flow, where as derived in Appendix 4C:

$$\frac{\partial \rho}{\partial h} = \frac{\rho_g - \rho_l}{\rho_g \rho_l} \quad \bar{\rho}^2 \frac{1}{r} \tag{4.5-11}$$

equation (4.5-10) yields:

$$\frac{\partial v}{\partial z} = \frac{\rho_g - \rho_l}{\rho_g \rho_l} \frac{q_o}{r A} \tag{4.5-12}$$

An interesting aspect of equations (4.5-10) and (4.5-12) is that, though valid under dynamic conditions, they do not contain time derivatives.

The dynamic behaviour of the bayonet tube steam generator is determined by observing the behaviour of a number of particles distributed along the length of the channels on their way from inlet to outlet.
By integrating equation (4.5-12) along the length of the channels, starting with the prescribed velocity at the inlet, the velocity distribution in the steam generator can be determined. Then the velocity of all observed particles is known. It is now assumed that during a small time step these velocities remain constant, thus enabling determination of the approximate location of the particles at the end of the time step. During this time step heat has been transferred to these particles. The increase in enthalpy of each particle is determined by application of equation (4.5-7), where q is the average heat flux along the distance a particular particle has travelled during the time step. The location and enthalpy of each particle is registered in a special table. The heat flux distributions along the length of the channels based on these new conditions are derived and the process can be restarted for the next time step. At each time step a new particle is assumed to enter at the inlet of a channel to replace particles leaving the channel at the end. Figure 4.5-2 shows the displacement of particles during a time step.
The initial steady state conditions may be derived by application of approximately the same algorithm, as can be understood by keeping in mind that a steady state may be considered the response to a zero disturbance. As the conditions at the inlet are known it is possible to derive enthalpy and location at the end of a time step of the particle just entering the channel at the start of that time step (cf. figure 4.5-3). Now the conditions of a particle somewhat downstream of the inlet are known and based on these conditions its displacement and enthalpy rise during the next time step can be derived. At the start of this time step a new particle enters the channel and, due to the steady state conditions, copies the behaviour of his predecessor. This process is repeated until the first particle leaves the evaporator. Now the conditions are known for a complete set of particles and the simulation of dynamics as described above may start. The problem of interaction between the channels, ignored so far is solved in the same way as discussed in subsection 4.5.2.3, i.e. by iteration.
During the first iteration the heat fluxes are based on assumed temperature distributions which are improved during further iterations in the fashion shown in figure 4.5-1.
For engineers the method of following particles holds the attraction of transparency. However, some inherent problems were encountered in the implementation of this method:

- an inherently uneven distribution of particles along the length of the secondary channel, due to the change in fluid velocity caused by evaporation and thermal expansion. This effect, already a disadvantage at the high pressure of interest here, (for p = 18 MW/m^2 there is a ratio of approx. 6 between particle distances at inlet and outlet of the secondary channel) would cause a prohibitive rise in computing time with decreasing pressure. This rise results from the enormous number of particles required in the preheat and early two-phase region for obtaining an adequate particle distance in the superheat region
- the addition of special routines to the program to account for particles crossing boundaries of flow or heat transfer regions during the time step.

For further information the reader is referred to PRINS [4.5-5].
In view of the above mentioned problems this approach was found less favourable than originally expected and hence was also abandoned.

4.5.3. Critique of the methods employed.

In retrospect the approach of developing special purpose programs for describing bayonet tube steam generator dynamics was far from optimal. Apart from the high computing times characterizing the final versions of both programs the essential objection seen by the author is the unfavourable ratio between the numbers of test runs and production runs. This unfavourable ratio is likely to be inherent to a research laboratory studying one-of-a kind objects, but was aggravated in our case by the complex formulation of the governing equations and the interconnection between their formulation and solution.
Rather than following such an ad-hoc approach one should, from the very beginning of an investigation such as the present one, look for a uniform mathematical description applicable to a wide variety of dynamical problems. In the author's opinion such a description is presented by the state-space approach, e.g. discussed by ZADEH [4.5-6]. In this approach any dynamic problem is transformed to a set of first order ordinary differential equations:

$$\frac{d\underline{x}}{dt} = \underline{f}\ (\underline{x}) + \underline{g}\ (\underline{u}) \qquad (4.5\text{-}13)$$

where $\underline{x}$ is the so-called state vector and $\underline{u}$ the vector of boundary conditions.
A linearized version of this equation reads:

$$\frac{d\underline{x}}{dt} = |A|\ \underline{x} + |B|\ \underline{u} \qquad (4.5\text{-}14)$$

In recent years subroutines have been and are being developed for the solution of such sets of equations (cf. e.g. HOFER [4.5-7]).

The general applicability of these subroutines justified a considerable effort for their development by teams containing skilled mathematicians, thus yielding high quality and reliability.
In summary it is the author's present opinion that dynamic problems - such as that of the bayonet tube steam generator - should be described in state variables, yielding a set of first order ordinary differential equations in

time. The resulting simulation programs should contain separate modules for the ad-hoc formulation of these equations and for their solution, the latter consisting of standard routines.
In this way the investigator, rather than devoting a significant effort to the design and testing of computer programs, may concentrate on his specific analytical and experimental problems.

4.5.4. Experiments.

4.5.4.1. Data acquisition.

During the transients all (32) measuring points were continuously scanned in succession (0.45 chan/s). To obtain a number of profiles (all values at specific intervals in time) these data had to be processed by a special computer program (MASCARA) developed in the course of an earlier project (cf. GOEMANS [4.5-8]). The transformation of these data to physical values was performed in roughly the same way as for the steady state experiments. Determination of the temperature and quality distributions in the evaporator from these data, however, posed additional problems connected to storage effects in the evaporator. Due to the varying void fraction and the resulting variation in specific mass of the mixture, the two-phase region has a certain mass storage capacity ★).
Following a drop in inlet mass flow rate it will take some time to displace the excess mass present in the evaporator tube and consequently to reduce the outlet mass flow rate to the reduced inlet mass flow rate. This dynamic behaviour complicates the formulation equivalent to equation 4.4-24 for the evaporator.
The heat released from the salt was determined in the same way as for the steady state experiments from equation 4.4-23, be it that the value of the correction factor f_c was determined in a different way to be discussed later. To determine the amount of heat accumulated in the steam ★★), equation 4.4-12 had to be extended with a dynamic term to:

$$Q_{SH} = G_s A_{SH} (h_{SH_{out}} - h_{SH_{in}}) + \Delta\ell A_{SH} \bar{\rho} \frac{\partial \bar{h}}{\partial t} \qquad (4.5\text{-}15)$$

or, in terms of figure 4.5-4:

$$Q_{SH} = A_{SH} \frac{1}{4} \{\rho_{t-1,\ell-1} + \rho_{t-1,\ell} + \rho_{t,\ell-1} + \rho_{t,\ell}\}$$

$$\frac{1}{2} \{(h_{SH_{t,\ell}} + h_{SH_{t,\ell-1}}) - (h_{SH_{t-1,\ell}} + h_{SH_{t-1,\ell-1}})\} /dt$$

$$+ \frac{1}{4} A_{SH} (G_{SH_{t-1}} + G_{SH_t}) \{(h_{SH_{t,\ell}} + h_{SH_{t-1,\ell}})$$

$$- (h_{SH_{t-1,\ell-1}} + h_{SH_{t-1,\ell-1}})\}/d\ell \qquad (4.5\text{-}16)$$

★) *Mass storage effects due to compressibility of water and steam have been neglected as justified by TEN WOLDE [4.1-9].*

★★) *Heat storage effects due to the heat capacity of the wall have been neglected as justified by TEN WOLDE [4.1-9].*

Under the assumption - justified in section 4.2.4.1.1 - that slip in the two-phase region may be neglected the local energy balances for the evaporator are similar to equation (4.5-16):

$$Q_{EV} = A_{EV} \frac{1}{4} \{\rho_{t-1,\ell-1} + \rho_{t-1,\ell} + \rho_{t,\ell-1} + \rho_{t,\ell}\} +$$

$$\frac{1}{2} \{(h_{t,\ell} + h_{t,\ell-1}) - (h_{t-1,\ell-1} + h_{t-1,\ell})\}/\Delta t$$

$$+ \frac{1}{8} A_{EV} (G_{t-1,\ell-1} + G_{t-1,\ell} + G_{t,\ell-1} + G_{t,\ell})$$

$$\{(h_{t-1,\ell-1} + h_{t-1,\ell}) - (h_{t,\ell-1} + h_{t,\ell})\}/\Delta \ell$$

(4.5-17)

The dynamic mass flux G(z) appearing in both equations (4.5-16) and (4.5-17) could not be measured and therefore had to be derived from the available data.
The decision to omit a steam outlet mass flow meter, made in view of the well-known problems of accurately measuring steam flows at high pressures and temperatures, was much regretted in later stages of the experimental program. The experiences gathered during both transient and stability experiments have convinced the present author that such a measurement would have been very valuable for verifying the steam generator dynamic simulations. Therefore such a device should be incorporated in any steam generator test rig.
Assuming no slip, equation (4.5-12) may be used to determine the dynamic axial velocity distribution by simple integration with respect to z.
An expression for heat flux q is obtained by combination of equations (4.4-10), (4.5-16) and (4.4-23).
The latter equation, though derived for steady state conditions, is considered to retain its validity for the dynamic case because of the nearly constant value of $k_{p \to SH}$. The second equation contains the superheater mass flux $G_{SH} = \rho_{SH} v_{SH}$ which is the result of the integration of equation 4.5-12. This mutual dependence requires solution by an interative scheme. In this scheme it is first assumed that the mass flux distribution at time t was identical to the known distribution at time t-Δt. Based on this assumption the heat flux distribution and - by application of equation (4.5-7) - the enthalpy and thus the specific volume distribution at time t are computed. Integration of the spatial derivative of the velocity v combined with the local specific density yields a first approximation of the mass flux distribution at time t. This procedure is repeated until it converges and the final distribution is obtained, after which the next step can be started.
As equation 4.4-21 is not valid during a transient and consequently can not be used to determine the heat flux correction factor f_c appearing in equation 4.4-23, this correction factor was varied until the process outlined above would yield a steam temperature at the top of the evaporator channel matching the measured value.
Figure 4.5-5 shows a typical result.

The values of the correction factor f_c for the various time steps, also given in this figure, show that the heat flux has to be adapted less than 10%. It may therefore be concluded that the axial distribution in the evaporator thus obtained will be fairly accurate.

4.5.4.2. Test program.

Two different types of transient were investigated in the experiments, viz. positive and negative stepwise variations of:

- feedwater mass flow (steam outlet pressure constant) ★)
- steam outlet pressure (feedwater flow constant)

Limitations in the test equipment precluded fast variations in inlet temperature and primary mass flow rate.
The table shown in figure 4.5-6 lists the conditions of the experiments reported in detail by VAN LEEUWEN [4.5-9].
The first 10 experiments are stepwise feedwater mass flow variations, the remaining 8 are stepwise variations in steam outlet pressure.

4.5.4.3. Experimental results.

Figures 4.5-7b through 4.5-7g (exp. no. 10 of figure 4.5-6) show the effects of an (approximately) stepwise negative variation in feedwater mass flow shown in figure 4.5-7a.
Figure 4.5-7b shows the resulting steam outlet temperature during this transient. It confirms the remarkable flow independence of the steam outlet temperature observed earlier for different steady state loads.
Within the steam generator itself, however, temperatures do vary, as witnessed by figures 4.5-7c and d showing the variations in temperature at various locations within the steam generator gap. The temperatures are numbered 01 through 18. The table figure 4.5-8 relates these numbers to the corresponding thermocouple numbers given in figure 4.3-5. It is clear from these figures that superheater temperature variations increase with distance from the steam outlet.
The behaviour of secondary inlet and outlet pressures shown in figure 4.5-7e clearly demonstrates the inadequate steam outlet pressure control action mentioned above. Finally FLiNaK temperatures at four locations are shown for the sake of completeness in figure 4.5-7f. Thermal inertia in the primary system's heat supply, not designed to cope with such steep transients, caused the FLiNaK temperatures to increase for a considerable time after the stepwise feedwater flow increase, explaining the continuing increase of superheater temperatures.
The responses given so far are the results of direct measurements. The responses of evaporator conditions, derived in the way discussed in subsection 4.5.3.1, are given in figure 4.5-7g.
Similar results of a "stepwise" increase in steam outlet pressure from 16.2 to 18.3 MN/m^2, shown in figures 4.5-7h through 4.5-7m, indicate the

★) *Control of the steam outlet pressure proved very difficult due to the large pressure drop - down to atmospheric - across the control valve (cf. figure 4.3-3).*
In the author's opinion a high pressure condenser of ample capacity, mounted directly behind the steam generator outlet and connected to it through a large duct, would have been required for adequately maintaining a constant outlet pressure. The absence of this equipment was due to financial reasons.

weak effects of such pressure variations. The increase in saturation temperature propagates into the superheat region of the evaporator tube and slowly decreases in the superheater gap. At the steam outlet hardly any effect is noticed. For similar results of the other experiments reference is made to VAN LEEUWEN [4.5-9].

4.5.5. Evaluation of results.

4.5.5.1. Introductory remarks.

Due to the problems discussed in subsection 4.5.2.4, encountered in simulating the bayonet tube's transient behaviour, only a limited effort has been made to simulate the experiments.

4.5.5.2. Comparison of DYBRU with an experiment.

To assess the accuracy of DYBRU e.g. experiment nr. 10 of figure nr 4.5-6 has been simulated. Figure 4.5-9 shows the result of this simulation. Inspection of this figure yields two differences between the responses of the top temperatures in experiment and simulation, viz.:

- in the simulation the reaction is faster
- in the simulation the final increase in top temperature is smaller

The faster reaction of the simulated top temperature can be explained by the fact that the storage capacity of the two-phase region has been neglected in the simulation. As a result of this assumption the transit time through the evaporator changes abruptly following the change in feedwater flow, whereas in reality the original velocities are maintained for some time as a result of the storage capacity, causing a delayed increase in enthalpy and thus in temperature.
The difference in final top temperature is caused by the limited validity of the applied empirical relations, pointed out earlier in subsection 4.4.3 on partial load simulation.

4.5.5.3. Comparison of DSTS with an experiment.

In addition to the simulation of a stepwise change by DYBRU figure 4.5-9 also shows a similar result obtained by DSTS (Lagrangian approach). The hysteresis immediately following the steps is simulated better by this program, because of the fully implemented mass balance. The total response however is much too fast compared to the experimental results. The development of this program was discontinued for reasons explained above before the cause of this deviation could be established.

4.6. Stability.

4.6.1. Analysis.

4.6.1.1. Introductory remarks.

As already stated in subsection 4.1.3.3 this study is restricted to the so-called density wave or void flow instability ★) of evaporators. The physical cause of this type of instability is illustrated in figure 4.6-1

★) *In our case a system is considered stable if it is asymptotically stable which means that following some small disturbance, the system returns to its original steady state conditions.*

showing the effect of a stepwise increase in the feedwater mass flow rate for a heated evaporator tube with uniform and constant heat supply. An increase in feedwater mass flow rate leads to an opposite variation in mixture density: the same amount of steam (constant heat supply) is, as it were, mixed with a larger amount of water. This density variation propagates through the evaporator at approximately the speed of the mixture. The dynamic storage of water, caused by the decrease in average void fraction, delays the response of the velocities and hence of the pressure drops further down-stream in the evaporator. As the frictional pressure drop is concentrated near the end of the evaporator tube ★) where velocities are highest, the pressure drop response of the entire tube will be delayed. Under unfavourable conditions this time delay between disturbance (feedwater flow variation) and reaction (opposing pressure drop variation) may result in a positive feedback causing a diverging oscillation. As the propagation velocity of the density waves approximates that of the mixture the frequency of this type of oscillation is strongly dependent on the residence time of the water in the evaporator. From the above it will be clear that density wave oscillations are more likely to occur as the pressure drop is more markedly concentrated near the end of the steam generator, i.e. at high exit qualities and/or lower system pressures.
The purpose op the present chapter, namely to predict the onset of void-flow stability for steam generators, may be achieved by either one of two distinct approaches:

a application of an empirical relation obtained by curve-fitting of a great number of experimental data

b simulation of the steam generator's dynamic behaviour by applying a mathematical model

Both approaches have their advantages and disadvantages.

ad.a) The main advantage of this approach, taken e.g. by SHOTKIN [4.6-1] and UNAL [4.6-2], lies in the potentially high accuracy.
Unal has developed a relation correlating the outlet quality of the steam generator at the stability limit with: the system pressure, the L/d ratio of the heated channel part and the amount of subcooling Δh. This empirical correlation predicts the stability limits within 6% for 95% out of some hundred experimental data obtained on single tube once-through steam generator models. The approach however also has some significant disadvantages:

- it requires experimental evidence obtained on actual steam generators or large scale models under operating conditions (mass flow rate, pressure, temperature, etc.) matching those of the steam generator design under investigation.
- due to their empirical origin - curve-fitting techniques applied to experimental data - the correlations hardly contribute to the physical understanding of the void-flow mechanism.
- it follows from the above that the availability of experimental data is doubtful. Any general relation defining the limits of density wave instability would have to include all dimensionless numbers that can

★) *Frictional pressure drop will increase with mass flow ϕ_m because of its proportionality with $\frac{\phi_{m^2}}{\rho}$ and will predominate over the concurrent increase in hydrostatic head.*

be constructed from the geometrical- and process constants governing the phenomenon in question.
For identifying the effects of changes in the various dimensionless numbers (and possibly concluding that some of them may be neglected) the experimental data should consist of separate sets, for each of which only one particular dimensionless number varies over a sufficiently wide range. This implies so large a volume of experimental data as to be almost prohibitive in engineering practice. A further complication is that some effects, notably those due to spatial distribution like that of the heat flux variation along the length of the channel, can hardly be accounted for in the correlation. Different correlations for different types of heating may prove to be required. A case in point is the aforementioned empirical stability limit derived by Unal. His set of experimental data in UNAL [4.6-2] contained one group of experiments on a tube with uniform electrical heating and extreme L/d ratio ($\cong$ 9000), whereas the remainder concerned channels of lower L/d ratio ($<$ 4000) heated non-uniformly by sodium. Unal fitted these experiments solely by adjusting the L/d ratio dependence of his correlation, though it is quite probable that the difference in heat transfer distribution also has a significant effect on the stability limits. This assumption is corroborated by the experimental results of DIJKMAN [4.6-3], who found that the change from a uniform heat flux to a sine-shaped heat flux significantly improved the stability of his evaporator. It is the present author's opinion that, unless additional data is provided to make up for this deficiency in experimental basis, the accuracy of extrapolations to sodium heated steam generators with high L/d ratio's ($>$ 6000) may well be less than the 6% stated in UNAL [4.6-3].

ad.b) The mathematical modeling underlying this approach is based on physical insight in the mechanism combined with empirical knowledge of (single- and two-phase) pressure drop, heat transfer and void fraction vs quality relations. Although largely analytical in nature this method is inevitably based on a number of these empirical relations of limited accuracy.
Simulations reported in literature suggest that these inaccuracies and those caused by deficiencies in the mathematical model tend to accumulate. Hence an accuracy of 10%, obtained in some cases, is already considered an excellent result, which compares unfavourably with the abovementioned value of 6%. Though significant improvement of this accuracy may prove difficult, it is the author's opinion that it is possible to at least maintain it over wide ranges of conditions and geometries by applying a sufficiently flexible computer program. Furthermore this approach will extend the understanding of the physical process, e.g. by allowing a designer to study the sensitivity of his design to variations in the various geometrical and process constants. The need for experimental evidence, if existing at all to support new designs, is thus greatly reduced through the reduction in the number of variables to be studied. Thus applied, simulation can in combina-tion with the former method improve the accuracy and reliability of stability threshold predictions.

Two different classes of simulation models can be distinguished:

b 1 time domain models
b 2 frequency domain models

ad.b1) Here the dynamic response of an evaporator tube to a given perturtubation is computed as a function of time for the boundary conditions relevant to parallel channel instability, i.e. constant inlet and outlet pressure and constant inlet enthalpy (cf. section 4.6.1.2.3).
Stability behaviour is derived from the inlet mass flow response. In a stable system this mass flow will return to its original value following perturbations. In unstable systems the inlet mass flow will start to oscillate either with a limited or with a diverging amplitude. Models operating in the time domain may or may not be linearized, depending upon the desired accuracy for simulating the steam generator's actual physical behaviour. Non-linearized models reproduce - within the accuracy of the model - the exact response of the real system. Examples of this approach are given by SPIGT [4.6-4], DIJKMAN [4.6-3] and VAN VONDEREN [4.6-5]. The application of their programs is limited to the case of prescribed heat flux, viz. electrically heated tubes, as opposed to the case of a prescribed primary mass flow and inlet temperature typical for actual steam generators. Even for this simplified case the increase in accuracy has to be bought by considerable increases in computing time over that needed for linearized models. By contrast the accuracy of the latter group of models is limited.
In stability studies this loss in accuracy of the physical modeling due to linearization is most evident with respect to limit cycle behaviour. This behaviour is characterized by constant amplitude oscillations, occurring under unstable conditions when stabilizing and unstabilizing forces balance as a result of a difference in amplitude dependence between driving forces and damping forces due to the strong non-linearity of the latter (cf. figure 4.6-2). The amplitude of a limit-cycle depends on how far operating conditions are pushed beyond the stability limit, as illustrated e.g. by figure 4.6-3 taken from VAN VONDEREN [4.6-5]. This figure confirms the author's own experience that a relatively small excess of the stability limits causes large flow excursions. Where non-linearity is the cause of limit cycle behaviour it will not be predicted by linear models. This inability is sometimes singled out as an argument against the use of linearized models by those who consider the prediction of limit cycles to be important for the purpose of assessing structural damage incurred during temporary flow oscillations e.g. during startup or shutdown. With reference to this argument it is the author's opinion that as a result of unpredictable deviations from prescribed operating conditions, combined with the observed strong dependence of oscillation amplitudes on variations in operating conditions, such predictions of structural damage will fail to yield sufficiently accurate results to be of any practical value. Thus linearized models, predicting solely the stability limit, should suffice for engineering purposes.

ad.b2) Frequency domain models consider the evaporator as a feedback system, the loop gain of which is investigated. As transformation from time domain to frequency domain is only possible for linearized systems, this class of models is incapable of simulating limit cycles. An advantage of models in this class is the insight in the physical mechanism to be gained from amplitude and phase relations between the various process conditions in the steam generator. Furthermore this information allows of a detailed experimental verification by frequency analysis of the systems (cf. POTTER [4.6-6]).

Over the years a great number of these models have been built. One of the first, mainly intended for demonstrating the void-flow mechanism very clearly, was given by DAVIES [4.6-7]. As for clarity's sake the solutional procedure was largely analytical, the results were not very accurate. A more accurate description is applied in the program of JONES [4.6-8]. In an evaluation of several models NEAL [4.6-9] reports that this model predicts stability limits within 20% for 70% of the experimental data available. The STABLE program of [4.6-8] contains no provisions for DNB and mist flow simulations, hence its use is restricted to steam generators with low outlet quality. EFFERDING [4.6-10] extended the Jones program to once-through steam generator simulation by including these provisions. Other examples of this approach are given by HALOZAN [4.6-11] and SHITTKE [4.6-12]. The accuracy of their models is hard to judge as comparisons with experiments are omitted in their reports. The same applies to two Japanese models by TAKAHASHI [4.6-13] and SUZUOKI [4.6-14]. The former has made some restricting assumptions such as: no wall dynamics, void fraction linearly dependent on the space coördinate throughout the entire two-phase region and no slip between the two phases. Suzuoki also assumes homogeneous flow. The nature of additional assumptions is very difficult to derive from his report. As regards experimental verification, Suzuoki reports comparison of the computed and measured frequencies only, which agree very well. Neither reports on comparisons of stability limits. Both Japanese models differ in solutional procedure from the models mentioned earlier by computing the eigenvalues of the oscillations rather than a transfer function of the system. This approach will be elaborated in subsection 4.6.1.3 in connection with the CURSSE program which also has this option.
A program, remarkably free of limiting assumptions is reported by DEAM [4.6-15]. In this respect his basic equations are equivalent to the set given in subsection 4.2.2. Although the dynamic variation of the location of transitions is omitted in the model the comparisons given in the report indicate a high degree of accuracy. A comparison with other models in this respect is difficult as he computes the inlet throttling required to obtain stable operation, whereas the others compare computed and measured maximum power transferred. This program, which is not available, appears to share with, all the others a lack of the geometrical flexibility required to simulate a bayonet tube steam generator.

In conclusion it may therefore be stated that, of the models reviewed so far, those in the time domain were found inadequate for actual steam generators due to the imposed boundary condition, viz. heat flux rather than primary mass flow, whereas none of the various models in the frequency domain was suited to the particular geometry of the bayonet tube steam generator. For these reasons it was decided to develop new models suitable for the bayonet tube configuration and to do so both in the time and frequency domains.
As work progressed it became gradually more evident that a time domain model of sufficient accuracy for the bayonet tube would have an unacceptably low process time/simulating time ratio. Hence most of the effort was shifted towards the frequency domain model, the more so as it was found that this approach could more easily be extended to cover a broad range of geometries and conditions.

4.6.1.2. Identification of characteristic sections.

4.6.1.2.1. Linearized analysis of the total system.

The task of avoiding void flow instabilities by proper design is complicated by the fact that actual steam generators consist of a large number of parallel tubes, connected at the bottom and the top by feedwater and steam headers, respectively.
While these tubes are generally geometrically identical, their thermal loadings may differ according to their location in the total bundle, thus causing non-uniform behaviour. Further complexity is introduced by possible effects of feedwater and steam line characteristics (cf. figure 4.6-4) on hydrodynamic stability of the entire system.
Any stability analysis aimed at verifying that a given steam generator design will behave in a stable manner for all operating conditions foreseen (including start-up and shut-down periods) will have to take into account the aforementioned complexities. It does not, however, seem practicable to simulate the behaviour of the entire system because - apart from the high computing costs - it would require a larger computer than presently available.
The approach generally adopted in simulations is to limit the extent of the study by identifying a characteristic section whose behaviour will be identical to that of the entire steam generator if subjected to the same conditions.
Most investigators choose a single tube as characteristic section of the steam generator. The resulting problem of defining the boundary conditions, i.e. the pressure at the inlet and outlet of the single tube, is usually solved by keeping these pressures constant.
This choice of boundary conditions is based on the somewhat vague reasoning that in an evaporator consisting of a large number of parallel tubes the various tubes will oscillate with random mutual phase shifts, thus leaving the total mass flow and consequently the in- and outlet pressures unaffected.
This assumption was experimentally verified for two and three parallel tubes by CROWLEY [4.6-16], D'ARCY [4.6-17] and VAN VONDEREN [4.6-5].
In a number of these experiments the latter has however observed yet another mode of instability, where the total mass flows and consequently the in- and outlet pressures did vary. While no further discussion of this mode is included in [4.6-5], its very occurrence contradicts the general validity of the afore mentioned assumption. Hence, in the following a mathematical description is presented of the entire system, i.e. the steam generator proper - consisting of headers, interconnected by parallel channels - as well as the associated feedwater supply and steam utilization subsystems.
In this way the various possible modes of oscillation and their associated characteristic sections and boundary conditions are derived from the set of governing equations and thus given a mathematical basis.
This analysis is performed in the frequency domain for convenience and to obtain results that can be directly compared with the results of the stability experiments on the DSMP-bayonet tube to be discussed in subsection 4.6.2.
The stability criteria for the various modes are expressed in the transfer functions of the different subsystems. As these transfer functions can be measured in a single tube test facility this approach, in addition to avoiding the limitations discussed above, offers the advantage of requiring only one type of experiment, i.e. frequency response analysis,

for both control studies and stability analysis.
As the title of this subsection indicates, all mathematical descriptions in this analysis are linearized.
The state space description given in section 4.5:

$$\frac{d}{dt}\underline{x} = A\,\underline{x} + B\,\underline{u} \qquad (4.6\text{-}1)$$

$$\underline{y} = C\,\underline{x} + D\,\underline{u}$$

is less suitable for the present purpose, hence it will be transformed into a description in the frequency domain.
Replacing the time derivative by the Laplace operator s and rearranging results in:

$$\underline{y} = \{C.\,[\,s.E - A\,]^{-1}.\,B + D\,\}\,\underline{u} = H(s).\,\underline{u} \qquad (4.6\text{-}2)$$

giving the direct relation between input vector $\underline{u}$ and output vector $\underline{y}$ through transfer function matrix H(s). Each element of this matrix is the transfer function between one input and one output variable and is a function of the complex Laplace operator $s = \lambda + i\,\omega$.

Note: Positive, zero, or negative values of λ indicate that the amplitudes of the signals in the system diverge, remain constant or damp out respectively:

$$\underline{x} = \hat{\underline{x}}\, e^{\lambda t} \sin \omega t \qquad (4.6\text{-}3)$$

4.6.1.2.2. Linearized description of subsystems.

Single evaporator channel.

In the case of a single evaporator channel two input and two output signals may be distinguished: variations in inlet mass flow and outlet pressure are considered to be inlet signals whereas variations in outlet mass flow and inlet pressure are seen as outlet signals (cf. figure 4.6-5).
Equation (4.6-2) reads for this case:

$$\begin{vmatrix} \delta p_{in} \\ \delta \phi_{out} \end{vmatrix} = \begin{vmatrix} H_{pp}(s) & H_{p\phi}(s) \\ H_{\phi p}(s) & H_{\phi\phi}(s) \end{vmatrix} \cdot \begin{vmatrix} \delta p_{out} \\ \delta \phi_{in} \end{vmatrix} \qquad (4.6\text{-}4)$$

This equation shows that the evaporator's behaviour is fully described by four transfer functions:

$$H_{pp}(s),\quad H_{p\phi}(s),\quad H_{\phi p}(s),\quad H_{\phi\phi}(s)$$

The second of these transfer functions, $H_{p\phi}$, which plays a central part in this analysis, is usually referred to as the input impedance.
Figure 4.6-6 shows an idealized shape of the inlet impedance curve of an evaporator, measured by applying test signals of constant amplitude. The shape of this curve can be understood by recollecting the physical mechanism. The increase in phase shift with rising frequency between pressure drop and inlet flow oscillation is caused by the time delay present in the system as explained in subsection 4.6.1.1.

Feedwater system.

The feedwater supply system consists of the pump, the main feedwater line and the inlet header. Velocities and hence pressure differences in the header are so small that uniform pressure can be assumed throughout the entire header.
For constant pump speed the pressure at the inlet header is solely dependent on the total mass flow into the evaporator. Therefore a system with one inlet and one outlet suffices:

$$\delta\, p_{in} = -Z_{in}(s).\ \delta\, \phi_{in_{tot}} \qquad (4.6\text{-}5)$$

where transfer function Z_{in} is called the impedance of the feedwater system.

Outlet system.

A similar description holds for the outlet system, consisting of outlet header, main steam line, turbine and condenser.
Excluding external disturbances the pressure at the outlet of the tubes is given by:

$$\delta\, p_{out} = Z_{out}(s).\ \delta\, \phi_{out_{tot}} \qquad (4.6\text{-}6)$$

Total system.

The foregoing component descriptions shall now be combined to form one mathematical description of the entire system (cf. figure 4.6-7).
To define the governing equations of the system the mass balances of the headers are first derived.

Feedwater header:
$$\delta\, \phi_{in_{tot}} = \sum_{i=1}^{n} \delta\, \phi_{in_i} \qquad (4.6\text{-}7)$$

Steam header:
$$\sum_{i=1}^{n} \delta\, \phi_{out_i} = \delta\, \phi_{out_{tot}} \qquad (4.6\text{-}8)$$

where n is the number of tubes in the bundle.

Suitable transformations, given in detail in APPENDIX 4E, yield a number of n linear equations with the n different inlet mass flows $\delta\, \phi_{in_i}$ for the separate steam generating channels as unknowns.
The general form of these equations is:

$$H_{p\phi_i}\, \delta\, \phi_{in_i} + \sum_{j=1}^{n} \left\{ \left(Z_{in} + H_{pp_i} \frac{Z_{out}\, H_{\phi\phi_j}}{\left(1 + Z_{out} \sum_{k=1}^{n} H_{\phi p_k}\right)} \right) \delta\, \phi_{in_j} \right\} = 0 \qquad (4.6\text{-}9)$$

By introducing two new functions defined as:

$$A_i(s) = H_{p\phi_i}(s) \qquad \text{and} \qquad (4.6\text{-}10)$$

$$B_{ij}(s) = Z_{in} + H_{pp_i} \frac{Z_{out}\, H_{\phi\phi_j}}{(1 + Z_{out} \sum_{k=1}^{n} H_{\phi p_k})} \qquad (4.6\text{-}11)$$

equation (4.6-9) can be simplified to:

$$A_i\, \delta\, \phi_{in_i} + \sum_{j=1}^{n} B_{ij}\, \delta\, \phi_{in_j} = 0 \qquad (4.6\text{-}12)$$

In matrix notation equation 4.6-12 reads:

$$\begin{vmatrix} A_1 + B_{1,1} & B_{1,2} & B_{1,3} & B_{1,n-1} & B_{1,n} \\ B_{2,1} & A_2 + B_{2,2} & B_{2,3} & B_{2,n-1} & B_{2,n} \\ & & & & \\ B_{n-1,1} & B_{n-1,2} & B_{n-1,3} & A_{n-1}+B_{n-1,n-1} & B_{n-1,n} \\ B_{n,1} & B_{n,2} & B_{n,3} & B_{n,n-1} & A_n + B_{n,n} \end{vmatrix} \times \begin{vmatrix} \phi_{in_j} \\ \phi_{in_2} \\ \\ \phi_{in_{n-1}} \\ \phi_{in_{n-2}} \end{vmatrix} = \begin{vmatrix} 0 \\ 0 \\ \\ 0 \\ 0 \end{vmatrix}$$

(4.6-13)

4.6.1.2.3. Stability criteria.

After a disturbance the total system described in the previous subsection will start to oscillate.
This oscillation, that may be damped, have a constant amplitude or diverge, is described by the solution of the system of homogeneous linear equations (4.6-12).
The complex frequency $s = \lambda + i\omega$ characterizing the oscillation is the root of the equation $D = 0$ where D is the determinant of the coefficient matrix of equations (4.6-13), as a non-zero solution can only exist if this determinant vanishes (cf. e.g. PIPES [4.6-18].
The real part of this root determines whether the oscillation diverges and thus whether the system is stable ($\lambda < 0$). marginally stable ($\lambda = 0$) or unstable ($\lambda > 0$).
Hence our stability criterion reads:
a system is stable if the real parts of all s_i are $\leqslant 0$, where s_i represents the roots of equation $D(s) = 0$.
Expansion of this determinant for a general case yields a very complex condition.
However, if the tube bank can be subdivided into sets of identical channels we can factorize the determinant. This may be illustrated for the simple case of a tube bank consisting of three tubes, of which tubes 1 and 2 are identical.

In this case matrix (4.6-13) reads:

$$D(s) = \begin{vmatrix} A_1 + B_{11} & B_{11} & B_{13} \\ B_{11} & A_1 + B_{11} & B_{13} \\ B_{31} & B_{31} & A_3 + B_{33} \end{vmatrix} \qquad (4.6\text{-}14)$$

The determinant can be rearranged by subtracting the second row from the first and separating the common factor A_1:

$$D(s) = A_1(s) \cdot \begin{vmatrix} A_1 + B_{11} & B_{11} & B_{13} \\ -1 & +1 & 0 \\ B_{31} & B_{31} & A_3 + B_{33} \end{vmatrix} \qquad (4.6\text{-}15)$$

In the general case this process can be applied to each set of identical tubes present in the bundle in succession, yielding:

$$D = A_1^{n_1-1} \cdot A_2^{n_2-1} \ldots\ldots\ldots\ldots |M_{res}| \qquad (4.6\text{-}16)$$

consisting of a product of the powers of the coefficient A_i, representative for each set of identical channels, and a residue of the original matrix. The exponents are the numbers of identical channels in each particular set minus one.
The above shows that there are two different types of factors in the expansion of D.

1. $A_i(s) = 0$ (4.6-17)

2. $|M_{res}(s)| = 0$ (4.6-18)

each yielding a different stability criterion.

ad.1) If the real part of a root of equation:

$$A_i(s) = H_{p\phi}(s) = 0 \qquad (4.6\text{-}19)$$

is positive or zero, the system is unstable.
The mode of oscillation connected with this instability can be found by substituting $A_i = 0$ into the set of equations (4.6-13).
After this substitution the columns with identical coefficients can be added. Thus a new set of equations is formed with a smaller number of unknowns.
For equations (4.6-14) this process yields:

$$\begin{vmatrix} B_{11}(\phi_1 + \phi_2) + B_{13} \\ B_{11}(\phi_1 + \phi_2) + B_{13} \\ B_{31}(\phi_1 + \phi_2) + A_3 + B_{33} \end{vmatrix} \times \begin{vmatrix} \phi_3 \\ \phi_3 \\ \phi_3 \end{vmatrix} = \begin{vmatrix} 0 \\ 0 \\ 0 \end{vmatrix} \qquad (4.6\text{-}20)$$

The two unknowns in this set of equations are $\Phi = \phi_1 + \phi_2$ and ϕ_3.

As the upper two equations are identical one of them can be omitted, yielding a set of two homogeneous equations with two unknowns. As it is very unlikely that the determinant of the coefficient matrix of this set of equations vanishes for the value of s_i for which $H_{p\phi_i} = A_i = 0$, only the zero solution holds.

For the above case this means that $\phi_1 + \phi_2 = 0$ and $\phi_3 = 0$, i.e. the total mass flow through the set of two identical tubes is constant (the mass flows through the individual tubes may oscillate in counterphase), whereas the mass flow through the third tube is also constant.
As in this case the oscillation is restricted to a number of parallel itubes, DAVIES [4.6-7] called this type of instability: parallel channel instability.

Generalization of this result for a steam generator consisting of a number of sets of two or more identical channels and possibly a number of channels different of all others, yields that each set of identical channels may be unstable. The stability of a particular set can be checked by determining the real parts of the roots of equation $A_i = H_{p\phi_i} = 0$, where A_i is representative for the channels of this set.
A positive real part indicates unstability. The total mass flow through each unstable set of identical channels will be constant. As the mass flow through each tube not forming part of such a set is also constant, it follows that the total mass flow through the steam generator is constant too, and hence so are inlet and outlet pressures.
The results agree with the experimental data gained to date. For example VAN VONDEREN [4.6-5] observed the following three different modes of instability in his experimental evaporator, consisting of one set of three identical parallel channels (cf. figure 4.6-8):

1. all three tubes oscillating with the same amplitude, each with a phase shift of 120^0 with respect to the others
2. two tubes oscillating in phase and with the same amplitude, with the third one oscillating in counterphase at twice this amplitude
3. one tube remaining stable while the other two oscillated with the same amplitude but in counterphase.

All three modes agree with the above mentioned condition. The first mode was the most common one; if the system started to oscillate in one of the other modes it always changed to the first mode after some time. A possible explanation for this phenomenon is given in APPENDIX 4F.
For very unstable conditions VAN VONDEREN [4.6-5] observed yet another mode of instability, mixed with one of the modes mentioned above, viz. oscillation of the total mass flow at a frequency slightly below the frequency of the other mode. To explain this type of instability we shall need the second criterion.

ad.2) A second type of instability occurs if the root of equation (4.6-18):

$$\left|\left| M_{res}(s) \right|\right| = 0 \qquad (4.6\text{-}21)$$

has a positive or zero real part ($\lambda \geqslant 0$).
Expansion of this determinant again yields a very complex stability criterion.
The mode of oscillation associated with this criterion involves all channels as well as the inlet and outlet systems.
DAVIES [4.6-7] called this type of instability loop instability.
Combination of equations (4.6-18) and (4.6-15) yields the following set of equations for the system represented by equation (4.6-14):

$$\begin{vmatrix} A_1 + B_{11} & B_{11} & B_{13} \\ -1 & 1 & 0 \\ B_{31} & B_{32} & A_3 + B_{33} \end{vmatrix} \times \begin{vmatrix} \phi_1 \\ \phi_2 \\ \phi_3 \end{vmatrix} = \begin{vmatrix} 0 \\ 0 \\ 0 \end{vmatrix} \qquad (4.6\text{-}22)$$

From the second row it follows that $\phi_1 = \phi_2$: the mass flows through identical tubes are the same. It will be clear that this result holds analogously for the general case: each set of n identical channels behaves as a single one of n-fold capacity. In an analysis they can be replaced by such a channel, thus reducing the size of the problem.

The results of the above analysis may be summarized as follows:

steam generators consisting of parallel steam raising channels, with their associated feedwater supply and steam discharge systems, may exhibit two different types of void flow instability:

1. parallel channel instability
2. loop instability

ad 1. parallel channel instability should better be called identical parallel channel instability as it can only occur in a group of identical parallel channels within a steam generator bundle. During parallel channel instability the total mass flow through this group of channels and consequently the pressures at the in- and outlets remain constant.
To determine the stability of the design of a steam generator at certain operating conditions all sets of identical parallel channels have to be examined to find the one that is most susceptible to parallel channel instability.

The stability behaviour of a set of identical parallel channels is the same as that of a single tube provided that the inlet and outlet pressures of that tube are kept constant. These are the characteristic section and boundary conditions normally chosen in stability analyses.

ad 2. During loop instability all tubes within a set of identical tubes behave in an identical manner and may therefore be assumed to be replaced by a single tube of n-fold capacity where n is the number of tubes present in the set. Thus a steam generator consisting of a large number of tubes that can be divided into a small number of sets of identical channels may, as far as loop instability is concerned, be replaced by a limited number of larger tubes with the same total capacity.

The question whether the limits for parallel channel instability are reached before those for loop instability has no general answer.

A case where loop instability occurs before parallel channel instability can be found in KAKAC [4.6-19]. In experiments on four parellel tubes the density wave oscillations in all four tubes are in phase for all observed cases of instability.
The criteria developed for parallel channel and loop instability may be applied in analyses in the form given above. They can however be transformed so as to become applicable both for analytical and for experimental determination of stability limits. In APPENDIX 4G a relation is derived between the criteria and the behaviour of transfer functions for signals of constant amplitude. These transfer functions can be obtained either by simulation or by experiments.
As regards parallel channel instability the derivation of APPENDIX 4G shows that the number of roots of the inlet impedance $H_{p\phi}(s)$ with positive real parts equals the net number of clockwise encirclements of the origin by the complete inlet impedance curve (anti-clockwise encirclements are counted negative). If the contour does not encircle the origin the system is stable. Although in principle the impedance curve has to be determined for all frequencies from zero to infinity, in practical measurements it often becomes apparent from the results that above a certain frequency no further encirclements will occur. The range of frequencies measured can be restricted accordingly.

In the case of loop instability a similar relationship holds (cf. APPENDIX 4G).

4.6.1.3. Analysis in the time domain.

4.6.1.3.1. Introductory remarks.

Figure 4.6-9 schematically compares the principles of the two methods for stability analysis in the time domain to be discussed. Whereas for the second method it suffices to determine the pressure drop response for a prescribed inlet mass flow variation, the first method additionally requires a feedback loop to fulfill the prescribed boundary condition of constant inlet and outlet pressures.
In the following subsections the digital simulation program and its two underlying methods will be discussed. The two alternative applications of this program formed our first attempts to predict the hydro-dynamic stability of the bayonet tube steam generator. They contain simplifying assumptions subsequently omitted from the frequency domain program. Furthermore no attempt was made to extend their applicability to other geometries. Hence they are less accurate and less complete than the frequency domain program to be discussed in subsection 4.6.1.4.

4.6.1.3.2. Additional assumptions.

- subcooled boiling is treated in much the same way as in the steady state, model BASTA, viz. by taking into account the resulting increase in heat flux, but assuming no vapour generation before the average enthalpy h reaches the saturation value h_ℓ
- as the present model was developed exclusively for the bayonet tube steam generator and hence for a system pressure of approximately 18 MN/m^2, homogeneous flow (s = 1) was assumed in view of the slip data presented in APPENDIX 4B.
- in view of the very small relative pressure variations, occurring during onset of instability, the physical properties were assumed independent of pressure

- as this model constituted our first attempt to simulate bayonet tube stability behaviour, it was further simplified by taking the inter-channel heat fluxes constant in time.
  For the primary channel this assumption results in a constant temperature distribution, eliminating it from further consideration.
- even for constant heat fluxes, the temperature in the superheater gap would vary due to the varying mass flow rate. However, measurements during the stability experiments discussed in subsection 4.6.2 showed that only in a minor part (near the top) these variations were significant. Hence it was assumed as a first approximation that the temperature in the superheater also remains constant.

4.6.1.3.3. Modified equations.

The assumption of homogeneous flow (s = 1) greatly simplifies the two-phase balance equations presented in subsection 4.2.2.2.1.
These equations reduce to those given earlier by equations (4.5.1), (4.5.2) and (4.5.3).
The equations actually applied in this model are obtained by combining these basic equations. Combination of the mass and energy balance equations yields:

$$\frac{\partial v}{\partial z} = \frac{(1 - \frac{\rho_g}{\rho_\ell})}{\rho_g (h_g - h_\ell)} = \frac{qO}{A} \qquad (4.6\text{-}26)$$

An interesting feature of this equations is the absence of dynamic terms. Combining this equation and the mass balance for steam yields:

$$\frac{\partial \alpha}{\partial z} = \frac{1}{v} \{ \frac{qO}{A} \frac{1}{\rho_g (h_g - h_\ell)} (1-\alpha(1 - \frac{\rho_g}{p_\ell})) - \frac{\partial \alpha}{\partial t} \} \qquad (4.6\text{-}27)$$

4.6.1.3.4. Solutional procedure.

The constant input values of the heat fluxes are obtained from the steady state program BASTA (cf. section 4.4).
The assumption of constant heat fluxes implies thermal decoupling of the channels, permitting each channel to be treated separately.
The assumption of pressure independent physical constants decouples the momentum balance equation from the mass and energy balances. As a result it is possible to start by solving the combination of mass and energy balance and subsequently to compute the total pressure drop.

Evaporator channel.

In this program three different regions are distinguished in the central tube; viz.:

- preheat region (up to $h = h_\ell$)
- two-phase flow region ($h_\ell < h < h_g$)
- superheat region ($h > h_\ell$)

Preheat region.

For determination of the preheat length the same Lagrangian description was adopted as used in the DSTB transient simulation program discussed in subsection 4.5.2.3. In fact, as the earlest version of this stability simulation program was developed before this transient program it was our first application of this approach. For details reference is therefore made to the aforementioned subsection.

Two-phase region.

As shown in equation (4.6-26), the spatial derivative of velocity v depends solely on the prescribed heat flux q, hence the velocity distribution can be obtained by direct integration starting from the end of the preheat length. Subsequently the void fraction distribution is derived by integrating equation (4.6-27). For this purpose the latter equation is transformed by substituting:

$$\frac{\partial}{\partial t} = \frac{\alpha_t - \alpha_{t-\Delta t}}{\Delta t} \qquad (4.6\text{-}28)$$

which yields an ordinary differential equation:

$$\frac{\partial \alpha_t}{\partial z} = \frac{1}{v_t}\left[\frac{qO}{A\rho_g (h_g - h_\ell)} \left\{ 1 - \alpha \left(1 - \frac{\rho_g}{\rho_\ell}\right) \right\} - \frac{\alpha_t - \alpha_{t-\Delta t}}{\Delta t} \right] \qquad (4.6\text{-}29)$$

The suffixes t and t-Δt denote the current and previous time levels, respectively. Integration is continued until void fraction α becomes unity, indicating that the end of the two-phase region is reached.

Superheat region.

In the superheat region of the central tube the temperature is assumed constant in time and equal to the steady state values obtained by BASTA.

Superheater channel.

Assuming a constant temperature distribution and thus neglecting the effect of varying density on pressure drop, the superheater gap may be replaced by a single restriction at the outlet of the evaporator tube.

Total pressure drop.

Having determined the enthalpy (void fraction) distribution throughout the evaporator the total pressure drop acorss the secondary channel can be computed by direct integration of the momentum balance equation (4.6-23). The frictional pressure loss is accounted for by substitution of the relevant frictional pressure drop correlation from the set given in subsection 4.2.3.3.
Repeated application of the above procedure for subsequent time steps yields the total pressure drop response $p_{in}(t) - p_{out}(t)$ to a variation of the inlet velocity $v_o(t)$.

Method 2.

By application of the above procedure for a harmonic variation of the mass flow rate the harmonic response of the total pressure drop is computed. From these input and output signals, computed for a range of frequencies, the inlet impedance curve may be constructed and hence by application of the criterion given in subsection 4.6.2 the stability behaviour of the bayonet tube derived.
Figure 4.6-10 shows a typical result for the bayonet steam generator.

Method 1.

In this method the boundary conditions of constant inlet and outlet pressures are prescibed.
For application of this method determination of the pressure drop response following an initial perturbation, as discussed above, must be extended with an iterative procedure. This iteration starts by assuming a small increase of the feedwater inlet velocity and computing the resultant variation of the inlet pressure for a constant outlet pressure. If this variation is negative the next step of the iteration is started with a further increased feedwater velocity and vice versa. The iteration procedure is continued until the inlet pressure remains constant. Then the program progresses with the next time step, etc. In this way the response of the system following an initial disturbance is computed.
Under unstable conditions the system will start a diverging oscillation, whereas under stable condition the initial disturbance will damp out.
Figures 4.6-11 through 4.6-15 show plots of the results of this method applied to a uniformly heated tube for increasing degrees of inlet throttling. The stabilizing effect of throttling is clear from these figures (c5 is the inlet gag pressure loss coefficient).

4.6.1.4. Analysis in the frequency domain.

4.6.1.4.1. Extensions in the model.

As mentioned in subsection 4.1.3.2.2 a new frequency domain program was developed aiming at highest flexibility and general applicability. The acronym CURSSE for: Computer program for UniveRsal Simulation of Stability Experiments-proved a very appropriate name in view of the programming and testing efforts involved.
One way to provide the required geometrical flexibility mentioned in the introductory remarks of subsection 4.6.1.1 would have been the incorporation in the program of a number of standard geometries. This system was rejected as not sufficiently flexible in favour of a "building block" approach defining the geometry by three basic parts:

- channels
- headers (and connecting nozzles)
- heat exchanging walls

By application of these "building blocks" it is possible to construct a great number of different geometries. It is for example possible to include feedwater and steam systems for simulating loop instability or to study the behaviour of a number of non-identical parallel tubes.

channels:

a channel is characterized by the vertical location of its inlet and outlet header and its length. For an inclined channel (e.g. a helically coiled tube) this length exceeds the difference in height between the two headers

headers:

a header is characterized by the location and number of its channel connections and its volume.

If present, flow restrictions are assumed to be located in the nozzles connecting the system with the surroundings and the in- and/or outlets of the individual channels.
Separate modeling of the headers yields a set of equations additional to the equations given in subsections 4.2.2 and 4.2.3.
Figure 4.6-16 shows the general form of a header consisting of a vessel provided with inlet and outlet nozzles. These may be either proper nozzles or channel out- or inlets respectively.
Before deriving the conservation equations for such a header a number of simplifying assumptions should be made:

- the pressure is uniform throughout the entire header vessel. The pressure drops are supposed to be concentrated in the nozzles (this assumption appears justified by the low velocities in the header vessel).
- perfect mixing takes place, i.e. all outlet conditions immediately ahead of the outlet restrictions are identical to the bulk conditions in the header.
- the pressure drop across a nozzle restriction can be described by the general equation:

$$\Delta p = c \cdot \frac{1}{2} \frac{G^2}{\bar{\rho}} \tag{4.6-30}$$

for both single and two-phase flow, if the specific mass $\bar{\rho}$ for the latter case is defined by:

$$\bar{\rho} = \rho_\ell \, (1 - \alpha) + \rho_g \, \alpha$$

The validity of equation (4.6-30) for single phase flow is generally accepted. The application of this equation to two phase flow is supported by experimental results published by TREMBLAY [4.6-22].
With these assumptions the conservation equations for a header can be formulated as follows:

- mass:

$$\sum_{j=1}^{n} A_{in_j} \, G_{in_j} - \sum_{j=1}^{m} A_{out_j} \, G_{out_j} = V_H \, \frac{\partial \bar{\rho}}{\partial t} \tag{4.6-31}$$

- momentum:

the following momentum balance can be formulated for each inlet nozzle:

$$p_{in_i} - p_H = \frac{c_i}{2} \frac{G^2_{in_i}}{\bar{\rho}_{in_i}} \tag{4.6-32}$$

where C_i represents the loss coefficient for inlet nozzle nr. i and p_H is the uniform pressure inside the header.
The corresponding equation for an outlet nozzle reads:

$$p_H - p_{out_i} = \frac{C_i}{2} \frac{G^2_{out_i}}{\rho_{out_i}} \tag{4.6-33}$$

- energy:

this equation reads:

$$\sum_{j=1}^{n} A_{in_j} G_{in_j} h_{in_j} - \sum_{j=1}^{m} A_{out_j} G_{out_j} h_{out_j} = \frac{\partial (M_H u_H)}{\partial t} \tag{4.6-34}$$

Expansion of the right hand side yields:

$$\frac{\partial}{\partial t} (M_H u_H) = M_H \frac{\partial u_H}{\partial t} + u_H \frac{\partial M_H}{\partial t} \tag{4.6-35}$$

Substitution of:

$$u_H = h_H - \frac{p}{\rho} \tag{4.6-36}$$

and of equation (4.6-35) into equation (4.6-34) yields for the energy balance of the header:

$$\sum_{j=1}^{n} A_{in_j} G_{in_j} h_{in_j} - \sum_{j=1}^{m} A_{out_j} G_{out_j} h_{out_j} =$$

$$V_H \rho_H \frac{\partial h_H}{\partial t} + V_H h_H \frac{\partial \rho_H}{\partial t} - V_H \frac{\partial p_H}{\partial t} \tag{4.6-37}$$

As the throttling process in the nozzle restrictions leaves the enthalpy constant the energy balances of the nozzles yields:

$$h_{out_i} = h_H \tag{4.6-38}$$

for outlet nozzle nr. i

The above extensive description of the header behaviour may appear overdone for most headers occurring in practice.
Unfortunately the possible simplifications differ from case to case, requiring a number of simplified models for the different types of headers (compare e.g. a main steam header to the top of the bayonet tube connecting the evaporator and superheater parts).
Therefore the analysis of the header behaviour given above was considered the best approach to retain the desired universality.

heat exchanging walls:

a heat exchanging wall, always in the shape of a tube, separates two channels in the structure.
As the CURSSE program was meant to serve as a reference program, it was deemed desirable to implement a two capacity wall-model instead of the zero-capacity model discussed in subsection 4.2.2.4, in order to verify the general validity of the conclusion by TEN WOLDE [4.1-9] that the latter model is sufficiently accurate for simulating steam generator dynamics. Originally the wall model given by DE GREEF [4.6-23] was implemented in the CURSSE program. In this model the total capacity of the wall is divided amongst two capacities located at the inner and outer surfaces of the wall, respectively. During test runs it became clear that this model has distinct disadvantages. If the boundary layer heat resistance $1/\alpha$ is very low, as is the case with boiling heat transfer, the heat capacity is more or less "short circuited" to the adjacent medium. Changes in bulk temperature result in very high heat fluxes between medium and capacity. It will be clear that this is at variance with the actual behaviour of the wall. To remedy this deficiency the locations of the capacities were changed to those shown in figure 4.6-17, i.e. some distance below the surface of the tube wall. In our model the two capacities are arbitrarily located at such radii r_1 and r_2, that the corresponding circles divide the cross-sectional area of the tube wall into: one quarter outside r_1, one half between r_1 and r_2 and the remaining quarter inside r_2. Optimization of the values for r_1 and r_2 should improve the accuracy of this mathematical model.
In this way there always remains a heat resistance between the bulk of the medium and the adjacent capacity, even if the boundary layer resistance tends to vanish. The energy balance equation for the outer capacity (per unit tube length) reads:

$$\frac{1}{2}\pi\,(r_o^{\,2} - r_i^{\,2})\,\rho c\,\frac{d\vartheta_1}{dt} = \frac{(\vartheta_b - \vartheta_1)}{R_o} + \frac{(\vartheta_2 - \vartheta_1)}{R_m} \qquad (4.6\text{-}39)$$

The heat resistance R_o between the bulk of the outer medium and the outer capacity, located at r_1 is composed of the boundary layer resistance and the tube wall located between r_o and r_1:

$$R_o = \frac{1}{2\,\pi\,r_o\,\alpha_o} + \frac{\ln\frac{r_o}{r_s}}{2\,\pi\,\lambda} \qquad (4.6\text{-}40)$$

The resistance between the two capacities is:

$$R_m = \frac{\ln\frac{r_1}{r_2}}{2\,\pi\,\lambda} \qquad (4.6\text{-}41)$$

The equation for the inner capacity is analogous.
In connection with the structure of the program the temperatures ϑ_1 and ϑ_2 were expressed in the basic variables ϑ_o and ϑ_i and the bulk temperature as:

$$\vartheta_1 = \vartheta_o + \frac{r_o \alpha_o \ln \frac{r_o}{r_i}}{\lambda} (\vartheta_o - \vartheta_b)$$

$$\vartheta_2 = \vartheta_i + \frac{r_i \alpha_i \ln \frac{r_o}{r_i}}{\lambda} (\vartheta_o - \vartheta_{b_o}) \qquad (4.6\text{-}42)$$

Figure 4.6-18 shows the aforementioned schematization for the bayonet tube applying the building blocks discussed above.

A second set of additional equations stems from the transitions in the evaporating process as mentioned in subsection 4.2.1.
Such a transition occurs where the local values of the basic variables (p, h, G, (x), θ_w) fulfill the transition equation given in subsection 4.2.3.1. In general:

$$f\ (h_z,\ G_z,\ p_z,\ (x_z),\ \theta_z) = 0 \qquad (4.6\text{-}43)$$

During oscillations in the inlet mass flow rate the location of these transitions will oscillate as well. In a time-domain program this does not pose a problem, as the locations of the transitions can be recalculated for each time step. In a frequency domain program such as the CURSSE program, however, this is not possible. The method by which this problem has been solved requires introduction of a number of additional equations. To illustrate the problem let us consider the dynamic behaviour of basic variable v. Figure 4.6-19 shows a possible behaviour of v as a function of the spatial coordinate z in two adjacent elements. The boundary between the two elements has been chosen to coïncide with the steady state location of the transition. At the location of the transition the gradient of the v-function shows a discontinuity. Under dynamic conditions (e.g. increased mass flow rate, heat supply, etc.) the transition will shift from its steady state position, to for example the one indicated by the dotted line in figure 4.6-19. The region of the pre-transition processes is extended, that of the post-transition processes is reduced.
However, in a frequency domain model those regions remain constant due to the fixed location of the transitions.
As only one set of correlations can be applied in a single element this results in a distribution in the downstream element according to the straight line F-H, rather than to the discontinuity in gradient as E-K-H. The requirement of continuity would result in the faulty distribution along G-E-I. This problem can be solved by introducing a double value for v at the boundary coïnciding with the steady state transitions: v_F and v_E. The discontinuity $\Delta v = v_F - v_E$ can be derived from the up- and downstream conditions and the transition shift δz, as follows:

$$v_F - v_E = \delta z \left(\frac{v_E - v_G}{\Delta z_U} - \frac{v_H - v_F}{\Delta z_D}\right) \qquad (4.6\text{-}44)$$

Replacing the dynamic value of v by the sum of its steady state value and a variation such as e.g.:

$$v_G = v_A + \delta v_A \tag{4.6-45}$$

yields, after neglecting second order terms:

$$\delta v_F - \delta v_E = \delta z \left(\frac{v_B - v_A}{\Delta z_U} - \frac{v_C - v_B}{\Delta z_D}\right) = \delta z \left(tg\alpha_U - tg\alpha_L\right) \tag{4.6-46}$$

Thus the discontinuity in an arbitrary basic variable is expressed in its steady state distribution and the value of the dynamic shift δz. The latter is determined from the transition equation mentioned above (cf. equation (4.6-43)). The local values of the basic variables appearing in this equation can be expressed in the steady state values of these variables at the boundaries of the upstream element and their variations as exemplified by the following equation (cf. figure 4.6-20):

$$v_z = v_B + \delta v_E + tg\alpha_L \, \delta z \tag{4.6-47}$$

Substitution of similar equations for all appearing basic variables in equation (4.6-43) yields a relation between the variations of the upstream variables δv_E and the transition shift δz:

$$g(\delta v_E, \delta z) = 0 \tag{4.6-48}$$

from which the shift can be determined. This equation is combined with equations (4.6-46), each providing an additional relation for the corresponding additionally introduced double value of the variations at the transition, to form the so-called coupling equations.

4.6.1.4.2. Modified equations.

The basic set of equations, given in subsections 4.2.2 and 4.2.3, extended with the additional equations consists of:

- partial differential equations in z and t
- ordinary differential equations in t
- algebraic equations.

The set is modified in two steps:

1. the solutional procedure starts with the spatial discretization of the partial differential equations. For this purpose the steam generator is axially subdivided into elements. Replacement of the spatial derivatives by finite differences results in a set consisting of ordinary differential equations and algebraic equations. Figure (4.6-21) shows the location of the basic model variables for a channel and a wall element. A channel element requires nodal variables at the upper and lower boundaries because of the appearance of spatial derivatives in the pertinent conservation equations, whereas the definition of nodal temperatures solely at the center of the element suffices for a wall element.

2. the next step is linearization of the equations. All equations are expanded in Taylor series and truncated after the first order terms, thus neglecting second and higher order effects:

$$\delta f(x, y, z, \ldots) = \frac{\partial f}{\partial x}_o \delta x + \frac{\partial f}{\partial y}_o \delta y + \frac{\partial f}{\partial z}_o \delta z + \ldots . \qquad (4.6\text{-}49)$$

After discretization and linearization around the steady state conditions the set consists of:

- linear ordinary differential equations in t
- linear algebraic equations.

4.6.1.4.3. Solutional procedure.

The bulk of the variables contained in these equations can be eliminated by substituting all algebraic equations into the differential equations, retaining only the following variables:

- for the channels: h, G, p
- for the walls: ϑ_i and ϑ_o
- for the headers (and nozzles): h_H, p_H (h_N, p_N, G_N)

These are called basic variables.
Discretization, linearization and substitution yield a set of equations expressed in variations of the basic variables and their time derivatives:

$$|A|\ \underline{v} + |B|\ \frac{\partial \underline{v}}{\partial t} = \underline{R}(t) \qquad (4.6\text{-}50)$$

where $\underline{R}(t)$ represents the forcing functions at the boundaries. APPENDIX 4H illustrates these processes by application to the single phase mass balance equation.
Though elimination of the dependent variables by combination of the linearized equations is relatively simple in certain cases such as the example shown in APPENDIX 4H, it proved very complex, time-consuming and error-prone in cases such as the two-phase balance equations, involving up to 88 equations.
Therefore a special purpose program SLINQ, written in PL1, was developed for the automatic substitution of linear equations. APPENDIX 4J shows an example of application of this program. A special and in our view indispensable feature of SLINQ is the incorporation of a check that is completely independent of the substitution process. All independent variables and constants are given arbitrary values. Evaluation of both the original set of equations and the result of the substitution process yields two numerical values. Comparison of these two values yields a reliable check on the correct performance of the substitution. During application of SLINQ this check has proven very valuable for detection of input errors.

There are two ways in which this set of equations (4.6-50) may be utilized for stability studies, each corresponding to a different formulation of the boundary conditions.

These are:

a. the actual boundary conditions for parallel channel instability: i.e. constant inlet and outlet pressures. Thus the r.h.s. of the equations ($\underline{R}(t)$) becomes zero.

Laplace transformation of equation (4.6-50) transforms the problem into a generalized eigenvalue problem:

$$|A|\ \underline{v} + s\ |B|\ \underline{v} = 0 \qquad (4.6\text{-}51)$$

This is the straightforward approach to stability analysis.

As derived is subsection 4.6.1.2 parallel channel instability may also be determined from the shape of the transfer function $H_{p\phi}$, leading to:

b. frequency response analysis by sinusoidal variation of the inlet pressure, i.e. retaining the $\underline{R}(t)$ term at the r.h.s. of the equations. This indirect approach obviates the need for constant inlet pressure.

For reasons described in subsection 4.6.2 the experimental facilities did not permit to maintain a constant inlet pressure, imposing the use of approach b for a proper comparison of analysis and experiments. However, in view of the aim of general applicability set for the CURSSE program, both approaches are retained as options in this program and will hence be described in some detail.

ad.a. The A and B matrices of the generalized eigenvalue problem, defined by equation (4.6-51), are non-symmetric. In this case two different classes of eigenvalues and associated eigenvectors are possible.

- real eigenvalues $s = \lambda$ combined with real eigenvectors $\underline{V}$.
  They describe non-oscillatory transients of the steam generator from one state to an other:

$$\underline{v} = a\ \underline{V}\ e^{\lambda\ t} \qquad (4.6\text{-}52)$$

- conjugated pairs of complex eigenvalues $s = \lambda \pm i\ \omega$ and associated eigenvectors $\underline{V}$ and $\underline{\bar{V}}$, representing damped or diverging oscillatory behaviour of the system:

$$\underline{v} = a\ \underline{V}\ e^{\lambda\ t}\ \sin(\omega\ t) \qquad (4.6\text{-}53)$$

  Inspection of equations (4.6-52 and 4.6-53) shows that the system is stable if all λ values are less than zero.

  The size of the matrices can become considerable for the steam generator problem under consideration due to the large number of small elements required for obtaining sufficient accuracy. (up to 500 x 500).
  The resulting problem of core memory storage capacity was overcome by concentrating the non-zero elements of the relatively sparse matrices in a narrow band ★) around the principal diagonal and only storing the elements of the band.

★) *possible because the conservation equations for a particular element involve only the variables defined at the boundaries of that element.*

This, however, imposed the choice of the so-called power-method for solving the eigenvalue problem, as a literature survey by PAULUSMA [4.6-24] showed that only this method permitted full use of the band structure storage mode.

The power method outlined in APPENDIX 4K is an iterative procedure requiring the repeated solution of a set of linear equations with varying right hand side vectors, but unchanged coefficient matrix and yielding the largest absolute eigenvalue of the system and its associated eigenvector (cf. WILKINSON [4.6-25]). Two methods exist to extend its use for the determination of additional eigenvalues, viz. matrix deflation and vector deflation.
The former could not be applied in our case as it destroys the band structure of the original matrices. The second method, i.e. vector deflation, is based on careful selection of the "arbitrary" starting vector of the power method. Both power method and vector deflation, described in detail by WILKINSON [4.6-25], had to be adapted in our case in order to be applicable to the generalized eigenvalue problem. For these adaptations the reader is referred to APPENDIX 4K, except for the following point. As explained in said Appendix application of the power method to our generalized eigenvalue yields the smallest instead of the largest absolute eigenvalue. This suits our aims perfectly as our interest is focussed on the fundamental oscillation and possibly a few of the higher harmonics, due to the fact that higher order harmonics are more stable than lower order ones.

ad.b. The frequency response analysis, as described e.g. in OLDENBURGER [4.6-26], is initiated by imposing a harmonic perturbation on one of the boundary variables of the system. For this situation the vector $\underline{R}(t)$ changes into:

$$\underline{R}(t) = \underline{R} \sin (\omega t) \tag{4.6-54}$$

where $\underline{R}$ is a vector of zero elements except in the case of the perturbed boundary variable and ω represents the angular velocity of the perturbation. Combination of equations (4.6-51) and (4.6-54) yields:

$$A\,\underline{v} + B\,\frac{\partial \underline{v}}{\partial t} = \underline{R} \sin (\omega t) \tag{4.6-55}$$

A solution of this set of equations is obtained by substituting the trial solution:

$$\underline{v} = \underline{a} \sin \omega t + \underline{b} \cos \omega t$$

into the set of equations (4.6-55).
This substitution, followed by some rearrangements, yields a system of linear equations:

$$\begin{vmatrix} |A| & -\omega\,|B| \\ \omega\,|B| & |A| \end{vmatrix} \begin{vmatrix} \underline{a} \\ \underline{b} \end{vmatrix} = \begin{vmatrix} \underline{R} \\ \underline{o} \end{vmatrix} \tag{4.6-56}$$

By solving this set of equations for perturbed inlet mass flow and constant inlet enthalpy and outlet pressure, one point of the transfer function $H_{p\phi}$ is determined.

Repeated application of this process for a range of frequencies yields the complete curve of this transfer function. By applying the criterion derived in APPENDIX 4G the stability of the steam generator under consideration can be determined from the shape of this curve.

4.6.1.4.4. Program structure.

Around the time of initiation (≅ 1975) a vast amount of publications - cf. r.g. SPAAS [4.6-37], BRUKX [4.6-28], STEVENS [4.6-29] and [4.6-30] - appeared on improved programming techniques, aiming at more transparent programs. The latter quality in particular appears of overriding importance in actual use.

In our view a clear distinction should be made between two essentially different parts of the simulation program: the analytical part consisting of the conservation equations for mass, momentum and energy and the empirical or semi-empirical correlations for friction, heat transfer and slip.

The analytical part may be considered the framework of the program; hence subsequent changes would involve adjustments throughout the entire program and should therefore be avoided. For this reason as much detail as practically possible was incorporated in this part of the program right from the start. In view of the excellent results on stability analysis reported by VAN VONDEREN [4.6-5] his formulation of the balance equations for the channels, followed essentially in subsection 4.2.2, was considered to embody sufficient detail to be used as a starting point. As regards the second, (semi-)empirical part, the pursuit of maximum accuracy implies the use of empirical relations with limited ranges of validity. In view of the considerable number of well-documented correlations available to date and the continuing addition of new and possibly more accurate ones the goal of general applicability of the program required easy exchange of these correlations. This led to their incorporation as separate subroutines, in accordance with the modular approach. A further requirement for flexibility concerns the data transfer between the various subroutines. In order to avoid compatibility problems in case of replacement of a correlation the data transferred has to be general and complete. In view of the above the values of all basic variables were transferred in all cases involving empirical relations. The structure of the CURSSE-program, based on these principles, in shown in the hierarchy table given in figure 4.6-22. This table shows the highly modular structure of the program (106 subroutines). The following five basic sections can be distinguished, each controlled by the main program and calling a number of lower level subroutines:

1. INPUT

   purpose:
   - input and preliminary processing of all data (including steady state conditions)

2. SYSEQ

   purpose:
   - determination of all coefficients of the total set of linear equations

3. PRELUD

purpose:
- composition of the band structured coefficient matrices

4. EIGVEC

purpose:
- determination of a prescribed number of eigenvalues and associated eigenvectors

5. TRANSF

purpose:
- determination of the solution vectors of the frequency analysis problem (cf. equation (4.6-5) for a prescribed number of different frequencies.

ad 1)

In addition to the actual input of data the INPUT routine takes care of the generation of keys, identifying each of the "nodal points" in the system.
This identification system is needed to facilitate future operations, e.g. computation of the coefficients of the equations.
Each key is an eight digit number (2 digits for each item) consisting of (cf. figure 4.6-23):

- the type number of the part
(channel, wall, header, nozzle: primary or secondary)
- the serial number of that particular part (e.g. 2nd wall)
- the level number. The total geometry is divided into sections by a number of levels indicating the presence of either a header or a transition in one of the channels
- the element number. Between each two consecutive levels the geometry is divided into as many elements as required to obtain the desired accuracy.

As in a keyed system the sequence of operations on the various elements of the system can be based on logic rather than on the particular geometry of the case at hand, such a description of the topology has proven a powerful aid for obtaining programming flexibility and yields a transparency otherwise impossible to achieve.

ad 2)

In the SYSEQ part of the program the coefficients of all equations of the total system are determined and stored as two rows of numbers (A and B matrices). Simultaneously their location in the matrices is recorded by storing their row and column numbers.
In this way the amount of storage required in this stage is reduced to only those elements of the matrix that contain actual coefficients.

ad 3)

The first action performed in PRELUD is generation of the band matrices proper. This action has to await the determination of the location of the last coefficients in SYSEQ, prior to which determination of the actual band width is impossible. Where determination of

eigenvalues is required PRELUD subsequently performs scaling of the matrices and L U decomposition. The purpose of the scaling operations is to improve the numerical conditioning of the system of equations. By means of iterative multiplication of rows and columns by scaling factors it is tried to keep the largest absolute values of the elements in each row and column within a specified range.

ad 4)

EIGVEC is explained in some detail in Appendix 4K and in OP DEN BROUW [4.6-31].

ad 5)

The algorithm of TRANSF is explained above in subsection 4.6.1.4.3, whereas programming aspects of this subroutine are discussed in [4.6-31].

The results of the program are given both as tables (cf. figure 4.6-24) and in graphical form (cf. figure 4.6-25).
In the latter both the amplitudes and the phase shifts of the various basic variables are displayed, but in addition a sort of three-dimensional plot is given to illustrate the total effect. Figure 4.6-25 shows p, H and G in the evaporating channel of the DMSP-bayonet tube test module during a frequency response test.

4.6.2. Stability experiments.

4.6.2.1. Introductory remarks.

Over the last two decades a considerable number of publications have dealt with experimental investigations of hydro-dynamic instability in particular density wave oscillations in parallel evaporator channels. The bulk of these experiments are based on the following approach. Evaporator tubes - either single or in sets of up to four identical or non-identical parallel tubes - are operated over a wide range of process conditions, under the boundary conditions of constant in- and outlet pressure.
In practice these boundary conditions are fulfilled by keeping both the outlet pressure and the pressure drop across the test section constant. For the outlet pressure this is achieved either by a downstream control valve or by installing a high-pressure condenser immediately downstream of the test section. The latter method, though more complicated, appears preferable, as has been discussed in subsection 4.4.3.
Maintaining a constant pressure drop across a single tube is achieved by installing a non-heated bypass of sufficiently large capacity. As shown in subsection 4.6.1.2 this condition is automatically fulfilled in the case of a number of identical parallel tubes.
The stability boundaries are determined by changing the steady state conditions until spontaneous oscillations occur. This "proof of the pudding" method is very direct, reliable and accurate, provided the boundary conditions are satisfied with sufficient accuracy. However, this method contributes but little to the understanding of the physical phenomena involved. Moreover the results of experiments with non-identical parallel channels are only valid for that particular tube arrangement and its inlet and outlet systems and hence yield no information for the design of other tube banks, as has been shown in subsection 4.6.1.2.3.

By contrast, application of the frequency response analysis widely used in control studies, holds the following advantages over the purely empirical approach mentioned above:

- by not implying the assumption of constant in- and outlet pressures it avoids the need for a bypass in the test rig and makes the experimental results more directly applicable to actual steam generators
- through its systematic determination of the transfer functions between the different evaporator process variables it provides an insight into the physical phenomena and allows detailed comparisons between experimental evidence and analytical predictions.

However, the method has so far found only limited application in the determination of hydrodynamic stability limits.
To the author's knowledge the only publications on its use for this purpose are those of GOODYKOONTZ [4.6-32], STEVENS [4.6-33], KREJSA [4.6-34] and DORSCH [4.6-35], who studied boiler-feed system coupled instability in a mono-tube boiler. They did not, however, consider either the effects of parallel tubes or those of an outlet system.
Frequency response measurements were also performed by SPIGT [4.6-4] and DIJKMAN [4.6-3] in a steam generator consisting of three parallel tubes and by PAUL and RIEDLE [4.6-36] on a single tube evaporator using FREON-11 as evaporating fluid. None of these authors did however utilize the experimentally obtained transfer functions for the purpose of deriving stability limits.

4.6.2.2. Experimental procedure and data acquisition.

Limitations of our experimental facility, concerning secondary mass flow and heat generating capacity, excluded the application of a large bypass and of parallel tubes. Hence it was decided to apply frequency response analysis for the investigation of the stability behaviour of the bayonet tube steam generator in the way suggested in subsection 4.6.1.2.3, i.e. by measuring the inlet-impedance of a single tube.

Bij superimposing a signal to that from the controller to the control valve (cf. figure 4.3.4) a variation of the feedwater mass flow rate was obtained. During the stability experiments both this mass flow variation and the resulting variation of the total pressure drop across the test tube were recorded. The outlet pressure was kept (more or less) constant by means of the steam pressure control valve also shown in figure 4.3-4. Correlation of the two recorded signals yields the amplification and phase shift of the inlet impedance $H_{p\phi}$ as a function of frequency.
In our experiments two different types of signal have been applied:

- binary noise
- harmonic oscillation

As a binary noise signal contains a range of frequencies, application of this type of signal has the advantage that all information needed for a complete Bode diagram can be obtained in a single test. Figure 4.6-26 shows a typical result of this approach obtained by processing the recorded signals on a PDP-8 digital computer.
As it proved difficult to maintain the steady state conditions over the long recording periods required for obtaining the desired accuracy over the frequency range of interest (0.01 - 0.6 c/s), this method was rejected in favour of harmonic analysis. Moreover the latter method facilitated the investigation of amplitude dependency of the results, required for the

assessment of non-linear effects. In this method a single harmonic oscillation is super-imposed on the feedwater mass flow to the test section. From a simultaneous recording of both this flow rate and the variation of the total pressure drop on a multi-line recorder the amplification and phase-shift of the inlet impedance can be derived for the particular frequency of the test signal. Figure 4.6-27 shows a typical example of such a recording. Repeated performance of this test for a number of different frequencies yields the information required for constructing a complete Bode diagram. Although less sophisticated than the binary noise approach this method proved sufficiently accurate and very reliable. Figure 4.6-28 shows a typical Bode diagram of the DMSP bayonet tube obtained by this type of impedance measurement.

4.6.2.3. Test program.

Stability tests on the DMSP bayonet tube test module were performed at two FLiNaK inlet temperatures, two steam outlet pressures, three feedwater inlet temperatures and three feedwater mass flow rates.
The combinations of these variables which were actually tested are listed in figure 4.6-29.

4.6.3. Evaluation of analytical and experimental results.

4.6.3.1. Introductory remarks.

In contrast to the other simulation programs under discussion, which were specially developed for the bayonet tube steam generator geometry, the much wider applicability of the CURSSE-program made it desirable to extend the verification of this latter program to other geometries. For this purpose CURSSE simulations of experiments performed elsewhere on two sodium heated steam generator geometries, straight tube and helically coiled tube respectively, will also be discussed below.

4.6.3.2. Preliminary program verification in the frequency domain.

Prior to the development of the universal CURSSE program the solutional methods underlying it and described in subsection 4.6.2.4 were tested by applying them to a simplified problem, viz. a single uniformly electrically heated evaporator tube fed by saturated water and producing steam of 95% quality at a pressure of 18.0 MN/m^2.
Further particulars are given in figure 4.6-30.

4.6.3.2.1. Eigenvalue analysis.

Eigenvalue analysis by application of the power method vector deflation yielded the values given in figure 4.6-31.
These values were found to be in exact agreement with those obtained applying the so-called QR-method (cf. WILKINSON [4.6-25]), whose applicability is restricted to relatively small problems.

4.6.3.2.2. Frequency analysis.

Determination of the inlet impedance for this simple case yields the curve shown in figure 4.6-32.
The point designated by A represents the frequency corresponding to that of the first eigenvalue of figure 4.6-31.

4.6.3.3. 1 MW_{th} steam generator experiments.

4.6.3.3.1. Outline of experiments.

Experiments reported by SANO [4.6-37] have been performed on a 1 MW_{th} sodium heated test module consisting of two parallel helically coiled evaporator channels (cf. figure 4.6-33). Heat was transferred in counterflow from the downward flowing sodium to the upward flowing water/steam mixture.
Four experiments reported in [4.6-37] were simulated using CURSSE. The required input data concerning steady state conditions were derived from computer output kindly made available by the experimenter.
The four experiments may be characterized as follows:

M1	full load	R = 9.5	stable
M2	part load 62%	R = 11	stable
M3	part load 62%	R = 12	unstable
M4	part load 62%	R = 13	unstable

where R is the sodium/water mass flow ratio.
During the experiments steam outlet pressure was kept constant at approximately 14.5 MN/m^2.

4.6.3.3.2. Eigenvalue analysis.

Contrary to our expectation that only a very limited number of real eigenvalues would have low absolute values, a considerable number of such eigenvalues were found in this case (cf. figure 4.6-34).
As will be clear from APPENDIX 4K the power method will fail under such conditions as the vector deflation method is restricted to a limited number of eigenvalues.
Due to this unforseen complication the eigenvalue option failed in the present case. This failure indicates the need for a different method for determinating eigenvalues. Time did not, however, permit the implementation and verification of such an alternative method.

4.6.3.3.3. Frequency analysis.

Applying the frequency analysis option of the CURSSE-program the inlet impedance curves for the four experiments mentioned in subsection 4.6.3.3.1 have been determined.
These curves are shown in figures 4.6-35a through 4.6-35d.
The full load case (experiment 1) is evidently stable. The curves for the remaining three experiments enclose the origin and thus should be unstable. Comparison with the above table shows these findings to agree with the experiments, except for experiment nr. 2. Examination of the impedance curve (figure 4.6-35b) shows, however, that the curve passes just to the left of the origin, whereas passage to the right would have implied an anti-clockwise encirclement and hence stability.
As a general point of interest it should be noted that comparatively small differences resulting from changes in R *for a given load* are reflected in the CURSSE results for experiments M2 through M4, whereas such effects are completely neglected in some of the other approaches published (cf. UNAL [4.6-2]).

4.6.3.4. SWISH experiments

4.6.3.4.1. Outline of experiments.

These experiments were performed by TNO in their sodium heated steam generator test facility operated at Apeldoorn, Holland. In this single tube test facility (cf. figure 4.6-36) the pressure drop is maintained constant by applying a non-heated by-pass.
The conditions of the five straight tube experiments simulated are summarized below.

	G kg/m^2 s	p MN/m^2	P kW	$T_{ond.}$ ^0C	x_{uit}	results of exp.	results of anal.
M1	1500	14.41	183.78	31.0	0.43	stable	unstable
M2	1393	11.91	180.48	64.5	0.50	unstable	unstable
M3	1391	11.97	180.15	64.9	0.50	unstable	unstable
M4	1797	12.05	196.69	63.5	0.38	stable	stable
M5	1324	12.04	175.91	65.6	0.52	unstable	unstable

4.6.3.4.2. Frequency analysis.

The computed inlet impedance curves for these experiments are shown in figures 4.6-37a through 4.6-37e.
Except for the first one the simulations agree with the experiments. During the experiments it was found that very small variations in conditions could change the system from stable into highly unstable. This probably explains the faulty prediction for experiment nr. 1 found by JANSSEN [4.6-38] to be closest to the stability boundary.
For further details on these tests and verifications the reader is referred to JANSSEN [4.6-38].

4.6.3.5. Bayonet tube experiments.

4.6.3.5.1. Time domain analysis.

Figures 4.6-38a through 4.6-38f show the results of inlet impedance measurements on the bayonet tube test module for two different loads (30% and 60% load) and of time domain simulations as discussed in subsection 4.6.1.3; simulation by the time domain program of the 90% load experiment proved impossible, due to certain restrictions in the mathematical description.
The results are presented also in the form of Bode-diagrams, showing separate amplification and phase shift responses, as this form of presentation was selected earlier for the results of the experiments. These figures show, that although phase shifts are approximated fairly accurate amplification is strongly underestimated. This must probably be attributed to progressive disintegration of the zirconia thermal

insulation layer discussed in subsection 4.1.2 ★).
This effect was revealed during steam generator disassembly following termination of the experiments.
While this progressive failure had no noticable effect on the overall thermal behaviour, the resulting obstruction in the superheater gap caused a slowly progressing but ultimately substantial increase in total pressure drop. Though pressure drop recordings over the entire test period indicate that cracking of the insulation was a slowly increasing process, the destabilizing effect of this downstream restriction must have made itself felt fairly early in the series of experiments. It explains in all probability why the system, after showing stable behaviour during the first start-up without any restriction in the feedwater flow,to our surprise subsequently required the installation of a feedwater throttling valve (cf. subsection 4.3.3.1) as a prerequisite to stable operation.
Due to the unknown history of the cracking process, comparison of the inlet impedance amplification obtained by experiment and simulation becomes doubtful. By contrast the phase shifts are hardly affected by this increase in down stream pressure drop and hence detailed comparison remains possible for that part of the results (figures 4.6-38b and 4.6-38c).

4.6.3.5.2. Frequency domain analysis.

In addition to the experimental results figures 4.6-38a through 4.6-38i also show the results of the CURSSE simulations. Frequency domain simulation of the 90% load case proved possible due to the increased flexibility of CURSSE.

4.6.3.5.3. Additional remarks.

Although the phase shifts computed by CURSSE approximate the experimental results somewhat closer than those computed by the time domain program both types of simulations yield to a large degree identical results. With increasing frequency the phase shifts obtained by simulation follow the experimental results rather closely up to a point where a sudden jump to higher phase shifts for the former occurs while the experimentally obtained phase shifts vary more gradually. As the frequencies increase further the three lines tend to coïncide again.
The sudden jump in the simulated curves is better understood if the results are shown in a polar plot. The simulated curves pass much closer to the origin than the experimental one, which explains the jump (cf. figure 4.6-38c).
The discrepancies may be caused by imperfections in either the models or the experiments. First considering the mathematical models, it is remarkable that the two different models developed independently, yield approximately the same results. In the authors opinion this eliminates the possibility of programming errors in the simulation programs.

★) *This failure of the insulation layer in the DMSP test module should not be considered proof of that spraying of ZO_2 is not a viable solution for the present application.*
A layer sprayed on a smooth tube was tested for 300 hours in 400 ^0C steam, with cooldown to ambient temperature and subsequent rapid reheating occuring every 30 hours and found to remain intact without a trace of cracking. It seems likely that the failure in the test module was due to severe weakening of the layer by the presence of thermo-couple wires embedded in the tube wall.

TECHNISCHE HOGESCHOOL DELFT
Bibliotheek
Postbus 98, 2600 MG Delft Nederland

Tel. 015-78 5679
Telexnr. 38070
IFLA-telecode

J. H. den Boon
Vlamingstr. 59
Delft

Onze ref.:
Uw ref. : 1152 1601
1152 2038

Delft, 6-3-80
Doelenstraat 101

mag.contr.
aanw./afw.

HERINNERING

Betr. Molten Fluorides

Boeknr. Vriesema

Wij verzoeken u het hierboven vermelde werk waarvan de uitleentermijn is verstreken, binnen 2 dagen te retourneren.

De uitleentermijn kan niet meer verlengd worden.

Indien u aan dit verzoek niet voldoet, zijn wij genoodzaakt u een rekening te presenteren voor de vervangingswaarde van het werk. Tevens zullen wij u administratie- en verwervingskosten in rekening moeten brengen.

afd. Uitlening

Verzoeke bij beantwoording onze referentie aan te halen

As regards the experimental conditions, it is assumed in the simulations that the outlet pressure is kept constant. As mentioned in subsection 4.5.4 this proved impossible in the test facility. On the contrary, substantial steam outlet pressure variations up to 0.7 MN/m^2 occurred during the frequency response tests. These pressure drop variations could not be simulated. It is probably this effect which causes the differences between experimentally and analytically obtained phase shifts.

5. CONCLUSIONS AND RECOMMENDATIONS

The first objective of this study, viz. assessment of the potential of FLiNaK as a high temperature heat transfer agent, has led to the following conclusions:

- *regarding equipment performance:* prolonged trouble-free operation is attainable with equipment made of INCONEL-600 provided the (TIG) welding is performed by qualified welders and 100% X-rayed
- *regarding heat and momentum transfer:* the validity of the correlations in general use for single-phase turbulent heat and momentum transfer of fluids with Prandtl numbers not too far different from unity was unequivocally confirmed
- *redarding flow measurements:* the venturi type flow meter was the only one yielding adequate accuracy and releability under prolonged operation.

The second objective of this study, viz. assessment of the beyonet tube design for molten salt heated steam generators, has led to a positive overall conclusion regarding its expected *performance*. A notable operating advantage is the almost uniform steam outlet temperature obtained over a wide range of loads (from 100 down to about 30% of rated power).
Although some preliminary design work on large (about 625 MWth) bajonet tube units was undertaken within the DMSP framework KNAAP [5-1] and VAN DER KROCHT [5-2] the results were not reported in this thesis because they were neither followed by an in depth evaluation comparing this design to the single tube super-critical alternative proposed by ROSENTHAL [5-3] nor by a serious search for design improvements.
If further development of this design were to be considered for either salt- or sodium-heated applications the following points would require additional study:

- long term integrety of the evaporator tube's thermal insulation layer
- amount of inlet throttling required for hydro-dynamic stability of the optimized geometry with its much higher superheater pressure drops
- means for preventing reducing instability during shutdown.

The following conclusions appear in order concerning the third objective of the study, viz. computer modeling of steam generator thermo-hydraulics:

- the steady state program BASTA has proven to be an adequate tool for the design of bayonet tube steam generators
- no satisfactory solution was found for the computer time consuming problem of non-linear transient analysis.
  Both the reasons for these negative findings and suggestions for improvement are given in subsection 4.5.3.
- the CURSSE program was found to be a very flexible and universally applicable tool for establishing the stability limits of geometrically complex steam generators. The very complete form of the basic balance equations incorporated in CURSSE enables the user to perform detailed sensitivety analyses. The simple way in which improved empirical relations can be implemented forms an additional advantage.
- use of the eigenvalue option incorporated in CURSSE did not produce an adequate number of eigenvalues. Improvement would require replacing the power method by a different solution scheme

- use of the frequency analysis option in combination with properly defined stability criteria resulted in generally correct predictions for the "parallel channel" stability behaviour of three different steam generator designs
- the same approach opens the possibility for predicting the "loop" stability behaviour of complex systems consisting of non-identical parallel tubes or tube banks
- further application of CURSSE preferably for the stability analysis of operating multi-tube steam generators appears desirable.

ACKNOWLEDGEMENTS

The work reported in this thesis was performed in the Laboratory for Thermal Power Engineering of the Delft University of Technology and stretches over a good number of years.
It would be impossible to name everyone who has contributes to it, some however have to be mentioned.
The author feels indebted to Neratoom B.V. and TNO which contributed to the systems design and programming of the CURSSE program, and to the Oak Ridge National Laboratory for providing equipment as well as know-how on molten salt technology.
Though the author gratefully acknowledges the contributions of all the staff of the Laboratory, special thanks are due to Messrs Hoppesteyn, Maissan and Vincenten who in addition to all their valuable work in designing and building the loops, under difficult circumstances cleared away the mess caused by a mayor salt spill, which resulted from leak in the loop.
Thanks also go to the students, who in the course of their graduate studies actively participated in the investigations.
The author whishes to thank Mr Op de Brouw, whose contributions gave a professional touch to teh CURSSE program and to Mr Middelkoop who supervised the design erection and testing of the loops.
Messrs Wessling and Brouwer and Mrs Van Kampen translated the authors hieroglyphs into drawings, graphs and carefully typewritten pages respectively.
Last but not least the author thanks his wife and children for enduring his ugly moods during the last period of this work.

REFERENCES CHAPTER 2

2.1.1. TURNER, G.E.
Liquid metal flow measurement: state-of-the-art study.
LMEC - Memo 68-9, June (1968).

2.2.1. BRIGGS, R.B.
Molten salt reactor program: semi annual progress report for period ending August 31, 1965.
ORNL - 3872 (1965).

2.2.2. V.D.I. Durchfluszmeszregeln.
DIN-1952, Nov. (1948).

2.2.3. VERBEEK, P.R.H.
IJking verturi tuiten (in Dutch).
Report Waterloopkundig laboratorium Delft, March (1973).

2.2.4. BEVINGTON, P.R.
Data reduction and error analysis for the physical sciences.
Mc.Graw-Hill (1968).

2.2.5. COHEN, S.I.
A physical property summary for ANP Fluoride mixtures.
ORNK-2150, Oak Ridge National Laboratory (1956).

2.2.6. OYE, H.A.
University of Trondheim, Instutt for uorganisk kjemi.
Private Communication (1977).

2.3.1. BENSON, J.M.
Survey of thermal devices for measuring flow.
Symposium on flow, Pittsburg, Pa. May 10 - 14 (1971).

2.3.2. MOELLER, R und TSCHOEKE, H.
Theoretische Untersuchungen zur Wandtemperaturmessung an simulierten Brennstäben für thermodynamische Experimente in Natrium.
KFK 1555, Apr. (1972).

2.3.3. LEUNG, E.Y.
Heat transfer in concentric and eccentric annuli with constant and variable heat flux.
AHT-4, Stanford University (1962).

2.3.4. CROOKSTON, R.B.
Turbulent heat transfer in annuli.
Int. J. of Mass and Heat Transfer, Vol. 11, pp. 415-426 (1968).

2.3.5. JUDD, R.L. and WADE, J.T.
Forced convection heat transfer in eccentric annular passages.
Stanford University Press, pp. 272-288 (1963).

2.3.6. PRESSER, K.H.
Wärmeübergang und Druckverlust an innenbeheizten Ringspalten bei Hochdruck-Gaskühlung.
Chemie-Ing. Tech. no. 38, pp. 180-181 (1966).

2.3.7. QUARMBY, A.
Some measurements of turbulent heat transfer in the thermal entrance region of concentric annuli.
Int. J. of Heat and Mass Transfer, Vol. 10, pp. 267-276 (1967).

2.3.8. LEE, Y and BARROW, H.
Turbulent flow and heat transfer in concentric and eccentric annuli.
I. Mech. E. Convention, Cambridge (1964).

2.3.9. Kays, W.M. and LEUNG, E.Y.
Heat transfer in annular passages. Hydro-dynamically developed flow with arbitrarily prescribed heat flux.

2.4.1. ALBERS, H.J.
Correlatie-snelheidsmetingen aan een hoge druk stoomketel (in Dutch).
A-6. Lab. Meet- en Regeltechniek University of Technology, Delft (Neth.) (1964).

2.4.2. BENTLEY, P.G.
Fluid flow measurements by transit time analysis of temperature fluctuations.
Trans. of the Soc. of Instrument Technology, Sept. (1966).

2.4.3. RANDALL, R.L.
Transit time flow meter employing Noise Analysis Techniques
Part 1. Water loop tests.
AI-AEC-12802, March (1969).

2.4.4. RANDALL, R.L.
Transit time flow measurement employing Noise Analysis Techniques.
Part 2. 2" sodium loop tests.
AI-AEC-12941 (1971).

2.4.5. MURI, R.J. de
Transit time flow meter: six-inch-diameter water and sodium testing summary.
LMEC-72-4, Aug. (1972).

2.4.6. GORDOV, A.N.
An experimental investigation of the inertia of micro-thermocouples.
High Temperature Vol. 3, (1965) pp. 268-273.

2.4.7. TAYLOR, C.
The dispersion of matter in turbulent flow through a pipe.
Proc. Roy. Soc. A-223 (1954).

2.4.8. TAYLOR, C.
Diffusion by continuous movements.
Proc. London Math. Soc. (2), (1922).

2.4.9. SCHMIDTL, H.
Die Dynamik der axialen Wärmeübertragung bei turbulenter Rohrströmung.
Int. J. of Heat and Mass Transfer, Vol. 16, pp. 12-13 (1973).

2.4.10. HINZE, J.O.
Turbulence.
McGraw-Hill (1975).

2.4.11. VELTMAN, B.P.Th und KWAKERNAAK, H.
Theorie und Technik derPilaritätskorrelation für dynamische Analyse niederfrequenter Signale und Systeme.
Regelungstechnik, Vol. 9 (1961), pp. 357-364.

REFERENCES CHAPTER 3

3.1-1 LATZKO, D.G.H.
Delft Molten Salt Project: Design Summary Report.
DMSP-G-8, Laboratory for Thermal Power Engineering.
Delft University of Technology, aug. (1966).

3.2-1 Engineering properties of INCONEL alloy 600.
Technical bulletin T-7, Huntington.
Alloy products Division.

3.2-2 GROENEVELD, D.C.
Post-dryout heat transfer: physical mechanisms and a survey of prediction methods.
Nuclear Engineering and Design, Vol. 32 (1975), pp. 283-294.

3.2-3 BAEHR, H.D.
Gleichungen und Tafeln der Thermodynamische Funktionen von Luft und einem Model-Verbrennungs Gas zur Berechnung von Gasturbinen Prozessen.
Fortschritt Berichte Reihe 6, nr. 13, V.D.I. Verlag Düsseldorf.

3.3-1 V.D.I.-Wärme-atlas, Berechnungsblätter für den Wärmeübergang.
V.D.I.-Verlag, Düsseldorf (1963).

3.3-2 V.D.I., Durchfluszmeszregeln.
DIN-1952, nov. (1948).

REFERENCES CHAPTER 4

4.1-1. ROSENTHAL, M.W.
The developemnt status of molton salt breeder reactors.
ORNL-4812, Oak Ridge National Laboratory, Aug (1972).

4.1-2. FRAAS, A.P.
A new approach to the design of steam generators for molton salt reactor power plants.
ORNL-TM-2953, Oak Ridge National Laboratory, June (1971)

4.1-3. IPENBURG, P.
Optimalisatie bajonetpijp stoomgenerator.
KR-434, Laboratory for thermal power engineering,
Delft University of Technology, Dec. (1975).

4.1-4. BISHOP, A.A., KRAMBECK, F.J.K. and SANDBERG, R.O.
Forced convection heat transfer to superheated steam at high pressure and high Prandtl numbers.
ASME, 65-WA/MT (1965).

4.1-5. KINYON, B.W., ROMANOS, N.D. and RITLEDGE, G.A.
Steam generator utilizing steam boundary to transfer heat from sodium to evaporating water.
ASME 69-WA/NE-20, Nov. (1969).

4.1-6. BARRATT, R.
Selection of the steam generator for the proposed 350-MW(e) demonstration plant.
ASME 71-NE-5, March (1971).

4.1-7. PETREK, J.P.
Bayonet sodium-in-tube steam generator.
ASME 73-Pwr-13 (1973).

4.1-8. HUNSBEDT, A.
Thermal-hydraulic performance of a 2 MWt sodium-heated, forced recirculation steam generator model.

4.1-9. TEN WOLDE, D.G.
Transient behaviour of nuclear steam generators.
Thesis, Delft University of Technology, Apr. (1972).

4.1-10. CAMPOLUNGHI, F., CUMO, M., FERRARI, G., LEO, R. and VACARRO, G.
An experimental study on heat transfer in long, sub-critical once-through steam generator.
Proc. of International Meeting on Reactor Heat Transfer, Karksruhe, Oct. 9-11 (1973).

4.1-11. BOURE, J.A., BERGLES, A.E. and TONG, L.S.
Review of two-phase flow instability.
ASME 71-HT-42 (1971).

4.1-12. STENNING, A.H., VEZIROGLU, T.N. and CALLAHAN, G.M.
Pressure drop oscillations in forced convection flow with boiling.
Proc. of symposium on two-phase flow dynamics, Eindhoven, The Netherlands, Sept. 4-9 (1967).

4.2-1. WALLIS, G.B.
One-dimensional two-phase flow.
McGraw-Hill, Inc., New York (1961).

4.2-2. HANCOX, W.T. and NICOLL, W.B.
A general technique for the prediction of void distributions in non-steady two-phase forced convection.
J. of Heat Mass Transfer, Vol. 14 (1971), pp. 1377-1394.

4.2-3. BANKOFF, S.G.
A variable density single-fluid model for two-phase flow with particular reference to steam-water flow.
J. of Heat Transfer, ASME, Series C, Vol. 82 (1960).

4.2-4. GROENEVELD, D.C. and DELORME, G.G.J.
Prediction of thermal non-equilibrium in the post-dryout regime.
Nuclear Engineering and Design, Vol. 36 (1976), pp. 17-26.

4.2-5. BOWRING, R.W.
Physical model, based on bubble detachment, and calculation of steam-voidage in the subcooled region of a heated channel.
OECD Halden Reactor Project, HPR 10 (1962).

4.2-6. JENS, W.M. and LOTTES, P.A.
Analysis of heat transfer, burn-out, pressure drop and density data for high pressure water.
ANL-4627 (1951).

4.2-7. LEE, D.H.
Studies of heat transfer and pressure drop relevant to subcritical once-through evaporators.
IAEA-SM-130/56 (1970).

4.2-8. WISMAN, R.
Analytical pressure drop correlation of addiabatic vertical two-phase flow.
Applied Scientific Research, Vol. 30, March (1975), pp. 367-380.

4.2-9. MARTINELLI, R.C. and NELSON, D.B.
Prediction of pressure drop during forced-circulation boiling of water.
Transactions of ASME, Aug. (1948).

4.2-10. DUKLER, A.E., WICKS, M. and CLEVELAND, R.G.
A comparison of existing correlations for pressure loss and holdup, an approach through similarity analysis.
A.I.Ch.E. Journal, Vol. 10 (1964).

4.2-11. JONES, A.B.
Hydrodynamic stability of a boiling channel.
KAPL-2170 (1961).

4.2-12. VAN VONDEREN, A.C.M.
On the hydrodynamic behaviour of parallel boiling water channels.
Thesis, Laboratory for Heat Transfer and Reactor Engineering, Eindhoven University of Technology, March (1971).

4.4-1. WISMAN, R.
Fundamental investigations on interaction forces in bubble swarms and its application to the design of centrifugal separators.
Thesis, Delft University of Technology, to be published shortly.

4.4-2. LEE, J.A.N.
Numerical analysis for computers.
Reinhold, New York (1966).

4.4-3. IPENBURG, P.
Stationaire stoomgenerator proeven DMSP. (in dutch)
KR-418, Delft University of Technology, Laboratory for Power Engineering Nov. (1975).

4.5-1. SANATHANAN, C.K.
Dynamic modeling of a large once-through steam generator.
Nuclear Engineering and Design, Vol. 23 (1972), pp. 321-330.

4.5-2. HÖld, A.
Linear analytical one-dimensional model describing the frequency response behaviour of shell-and-tube type counterflow heat exchangers with respect to primary and secondary inlet temperature and mass flow perturbations.
Nuclear Engineering and Design, Vol. 26 (1974), pp. 231-241.

4.5-3. BRUENS, N.W.S.
Modeling of nuclear steam generators.
Proc. of the Second Power Plant Dynamics, Control and Testing. Symposium, Tennessee, Sept. 3-5 (1975).

4.5-4. BRUENS, N.W.S.
Digitaal computerprogramma voor de simulatie van het dynamische gedrag van de DMSP-bajonetpijp stoomgenerator.
KR-357, Delft University of Technology, Laboratory for Power Engineering, Aug. (1973).

4.5-5. PRINS, R.T.G.
DSTB, digitaal computerprogramma voor de simulatie van het dynamisch gedrag van de DMSP-bajonetpijp stoomgenerator, met een N.L.-model.
EV-1014, Laboratory for Thermal Power Engineering, Delft University of Technology, The Netherlands, June (1978).

4.5-6. ZADEH, L.A. and DESOUR, C.A.
Linear system theory.
McGraw-Hill Book Company, New York.

4.5-7. HOFER, E.
A partially implicit method for large stiff systems of ode's with only few equations introducing small time-constants.
Siam J. Numer. Anal., Vol. 13, no. 5, Oct. (1976).

4.5-8. GOEMANS, T., VAN MAREN, D. and TEN WOLDE, D.G.
MASCARA: a multi-variable data-prosessing code for quasi- and non-stationary measurements.
Delft University of Technology,
Dept. of Mechanical Engineering, WTHD-18, Feb. (1970).

4.5-9. LEEUWEN, H.N.
Metingen van het dynamisch gedrag van de DMSP-bajonetpijp stoomgenerator.
KR-419, Delft University of Technology,
Laboratory for Power Engineering, Aug. (1975).

4.6-1. SHOTKIN, L.M.
Stability considerations in two-phase flow.
Nuclear Science and Engineering, Vol. 28 (1967), pp. 317-324.

4.6-2. ÜNAL, H.C. and VAN GASSELT, M.L.G.
Dynamic instabilities in tubes of a large capacity, straight-tube, once-through sodium heated steam generator.
Int. J. Heat Mass Transfer, Vol. 20 (1977), pp. 1389-1399, and private communications.

4.6-3. DIJKMAN, F.J.M.
Some hydro-dynamic aspects of a boiling channel.
Thesis, University of Technology, Eindhoven, The Netherlands (1969).

4.6-4. SPIGT, C.L.
On the hydraulic characteristics of a boiling water channel with natural circulation.
Thesis, University of Technology, Eindhoven, The Netherlands (1966).

4.6-5. VAN VONDEREN, A.C.M.
On the behaviour of parallel boiling water channels.
Thesis, University of Technology, Eindhoven, The Netherlands (1971).

4.6-6. POTTER, R.
A review of two-phase flow instability aspects of boiler dynamics.
Proc. of Symposium on Power Plant Dynamics, Control and Testing, Knoxville, Tennessee, Oct. 8-10 (1973).

4.6-7. DAVIES, A.L. and POTTER, R.
Hydraulic stability: an analysis of the causes of unstable flow in parallel channels.
Proc. of Symposium on two-phase flow dynamics, Eindhoven, The Netherlands, Sept. 4-9 (1967).

4.6-8. JONES, A.B.
Hydro-dynamic stability of a boiling channel.
KAPL-3070, Aug. (1964).

4.6-9. NEAL, L.G. and ZIVI, S.M.
Hydro-dynamic stability of natural circulation boiling systems.
A comparative study of analytical models and experimental data.
TWR-Systems, STL 372-14 (1), (1965).

4.6-10. EFFERDING, L.E.
DYNAM: A digital computer program for study of the dynamic stability of once-through boiling flow with steam superheat.
GAMD-8656 (1958).

4.6-11. HALOZAN, H.
Statische und dynamische Instabilität der Zweiphasenströmung. (german)
Thesis, Technological University of Graz, Mai (1973).

4.6-12. SHITTKE, H.J.
Berücksichtigung von Druck und Zweiphasen-Impulsaustausch bei der Dynamik eines konvectiv beheizten Zwangdurchlaufdampferzeugers.
Zwischenbericht nr. 5.
Institut für Verfahrenstechnik und Dampfkesselwesen, Dec. (1975).

4.6-13. TAKAHASHI, R. and FUTAMI, T.
Theoretical study of flow instability of a sodium heated steam generator.
Nuclear Engineering and Design, Vol. 41 (1977), pp. 103-204.

4.6-14. SUZUOKI, A. and YAMAKAWA, M.
Studies of thermal-hydrodynamic flow instability.
Bulletin of the JSME, Vol. 19, No. 132, June (1976), pp. 619-626.

4.6-15. DEAM, R. and MURRAY, J.
The prediction of dynamic stability limits in once-through boilers using DYMEL.
Paper: European Two-Phase Flow Group Meeting, Erlangen, May (1976).

4.6-16. CROWLEY, J.D., DEANE, C. and GOUSE, S.W.
Two-phase flow oscillations in vertical, parallel, heated channels.
Proc. of Symposium on two-phase flow dynamics,
Eindhoven, The Netherlands, Sept. 4-9 (1967).

4.6-17. D'ARCY, D.F.
An experimental investigation of boiling channel flow instability.
Proc. of Symposium on two-phase flow dynamics,
Eindhoven, The Netherlands, Sept. 4-9 (1967).

4.6-18. PIPES, A.L.
Matrix methods for Engineering.
Prentice-Hall (1963).

4.6-19. KAKAC, S., VEZIROGLU, T.N., LEE, S.S. and OZBOYA, N.
Transient boiling flow instability in a multi-channel upflow system.
Wärme und Stoffübertragung, Vol. 10 (1977), pp. 175-188.

4.6-20. JANSEN, J.B.
Simulatie hydro-dynamische stabiliteitsgedrag van de DMSP-bajonetpijp stoomgenerator in het tijdsdomein. (in dutch).
EV-1035, Delft University of Technology,
Laboratory for Power Engineering, Jan. (1978).

4.6-21. BLOEM, J.R.
Digitale simulatie in het tijdsdomein der hydro-dynamische instabiliteit in de DMSP-bajonetpijp stoomgenerator. (in dutch).
KR-421, Delft University of Technology,
Laboratory for Power Engineering, Aug. (1975).

4.6-22. TREMBLAY, P.E.
Thermo-hydrodynamic instabilities in a boiling channel in parallel with a finite by-pass.
Thesis, University of Toronto, Oct. (1972).

4.6-23. DE GREEF, J.F.
Cylindrical thermal equations for the analog computer.
Annales de l"Association Internationale pour le Calcul Analogique, Vol. 9, Oct. (1967), pp. 195-197.

4.6-24. PAULUSMA, J.C.P.
Een methode voor het oplossen van een gegeneraliseerd eigenwaarden probleem met niet-symmetrische bandmatrices van grote orde t.b.v. een stabiliteits rekenprogramma voor stoomgeneratoren.
EV-1041, Laboratory for Thermal Power Engineering,
Delft University of Technology, June (1976).

4.6-25. WILKINSON, J.H.
The algebraic eigenvalue problem.
Academic Press, New York (1966).

4.6-26. OLDENBURG, R. (editor)
Frequency response.
McMillan, New York (1956).

4.6-27. SPAAS, H.A.C.M.
Some contributions to the structural design and analysis of pressure vessel and piping components.
Thesis, Delft University of Technology, March (1977).

4.6-28. BRUKX, J.F.L.M. and BUIS, J.P.
Hybrid simulation of LMFBR heat transfer system dynamics.
AICA Symposium on Hybrid computation in dynamic systems design, Rome, Nov. 11-14 (1974).

4.6-29. STEVENS, W.P., MYERS, G.J. and CONSTANTINE, L.L.
Structured design.
I.B.M. Systems Journal, Vol. 13 (1974), pp. 115-118.

4.6-30. HIPO - A design aid and documentation technique.
IBM, publ. no. GC20-1851-1.

4.6-31. OP DEN BROUW, H.
Programmers Manual to CURSSE.
Delft University of Technology, EV-1066.
Laboratory for Power Engineering, June (1978).

4.6-32. GOODYKOONTZ, J.H.
Frequency response of forced-flow single-tube boiler with inserts.
NASA TN D-4189, Oct. (1967).

4.6-33. STEVENS, G.H.
Frequency response of a forced-flow single-tube boiler with inserts and exit restriction.
NASA TN D-5023, Feb. (1969).

4.6-34. KREJSA, E.A.
Frequency response of a forced-flow single-tube boiler.
NASA TN D-4039, June (1967).

4.6-35. DORSCH, R.G.
Frequency response of a forced-flow single-tube boiler.
Proc. of Symposium on two-phase flow dynamics,
Eindhoven, The Netherlands, Sept. 4-9 (1967).

4.6-36. PAUL, F.W. and RIEDLE, K.J.
Experimental frequency response characteristics for diabatic two-phase flow in a vertical mono tube vapor generator.
Journal of Heat Transfer, Vol. 96, Nov. (1974), pp. 504-510.

4.6-37. SANO, A.
1 MW_t steam generator operating experience.

ASME, 73-HT-53 (1973).

4.6-38. JANSSEN, J.B.
Simulatie hydrodynamisch stabiliteitsgedrag van diverse stoomgeneratorgeometrieën m.b.v. het CURSSE-programma. (in Dutch).
EV-1049 Delft University of Technology.
Laboratory for Power Engineering, March (1978).

REFERENCES CHAPTER 5

5.1. KNAAP, M.H.
Enige constructive aspecten van doorpomp-bajonetpijpen in een door gesmolten zouten verhitte 680 MW_{th} stoomgenerator.
KR-248 Laboratory for thermal power engineering,
Delft University of Technology, Apr. (1970).

5.2. VAN DER KROCHT, C.A.J.
Keramische isolatie van een deel van de verdamperpijp en afstoppen van beschadigde pijpen van een door gesmolten zouten verhitte 680 MW_{th} stoomgenerator met doorpomp-bajonetpijpen. (in dutch)
KR-254, Laboratory for thermal power engineering,
Delft University of Technology, June (1970).

5.3. ROSENTHAL, M.W.
The development status of molten salt reactor power plants.
ORNL-TM-2953, Oak Ridge National Laboratory, June (1971).

SAMENVATTING

Dit proefschrift bestaat uit twee delen.
In het eerste deel worden de mogelijkheden besproken, die een mengsel van gesmolten zouten biedt voor toepassing als warmteoverdrachts medium bij temperaturen boven 500 ^{0}C.

De behoefte aan een dergelijke warmtedrager kan ontstaan uit nieuwe chemische processen, waarvoor meer gebruikelijke lage druk warmteoverdrachts media niet toepasbaar zijn. Het hier besproken zoutmengsel - het ternaire entecticum van natrium-, kalium- en lithium fluoride bekend onder de naam FLiNaK - is zeer korrosief.
In hoofdstuk 2 wordt de bruikbaarheid van drie verschillende methoden voor het meten van de massastroom van een dergelijke korrosieve vloeistof bij hoge temperatuur, respektievelijk gebaseerd op het principe van de venturi, de "hete vinger" en de meting van looptijden, besproken. De metingen werden uitgevoerd in een gesmolten zout kringloop op semi-technische schaal.
In dezelfde kringloop werden empirische warmteoverdrachts- en drukverlies korrelaties bepaald. Deze experimenten aan een zout-op-lucht warmtewisselaar en een speciaal gekalibreerd leidinggedeelte worden, tezamen met de gevonden korrelaties, besproken in hoofdstuk 3.

In het tweede deel van dit proefschrift wordt het thermo-hydraulisch gedrag van bajonetpijp stoomgeneratoren besproken. De relatie met het eerste deel bestaat hierin, dat dit ontwerp de enige mogelijkheid biedt voor opwekking van stoom bij subkritische kondities in een met FLiNaK of een ander fluoride-mengsel verhitte stoomgenerator, in verband met het hoge smeltpunt van deze vloeistoffen. De behoefte aan een dergelijke stoomgenerator ontstaat bij verdere ontwikkeling van thermische kweekreaktoren met gesmolten zouten als koelmiddel.
Voor ieder van de drie aspekten van het thermo-hydraulisch ontwerp, besproken in hoofdstuk 4, n.l.:

- stationair gedrag (vollast en deellast)
- gedrag bij grote verstoringen
- hydro-dynamische stabiliteit

zijn één of meer komputerprogramma's ontwikkeld en geverifieerd door vergelijking met resultaten van experimenten aan een éénpijps testmodel waarin stoom werd opgewekt van 18 MPa/540 ^{0}C.
Tijdens de ontwikkeling van de programmatuur voor het laatste onderdeel werd het duidelijk dat er behoefte bestond aan een simulatieprogramma waarmee de stabiliteitsgrenzen van doorpomp stoomgeneratoren van verschillende geometrieën zouden kunnen wordt bepaald, zowel voor "parallel channel" als voor "loop" instabiliteit. Voor dat doel werd een modulair opgebouwd, programma (CURSSE) ontwikkeld en geverifieerd door vergelijking met resultaten van experimenten aan de bovengenoemde éénpijps bajonetpijp stoomgenerator en twee verschillende, elders geteste stoomgeneratoren.

De konklusies voor beide delen van dit proefschrift, geformuleerd in hoofdstuk 5, kunnen als volgt worden samengevat:

- FLiNaK lijkt zeer geschikt als warmteoverdrachts medium bij temperaturen tussen de 500 en 700 ^{0}C
- het bajonetpijp ontwerp biedt een theoretisch veelbelovende, maar mogelijk ekonomisch minder aantrekkelijk alternatief voor de produktie van stoom in een met gesmolten zouten gekoeld kweekreaktor systeem
- het CURSSE programma is een flexibel en betrouwbaar hulpmiddel gebleken voor het voorspellen van de stabiliteitsgrenzen van doorpomp stoomgeneratoren van verschillende geometrieën.

APPENDIX 2A

Thermal conductivity of FLiNaK.

The values found in literature for the thermal conductivity of FLiNaK range from 0.6 - 5.4 W/(m ^{0}C).
COHEN [2A-1] reports a value of 2.6 W/(m ^{0}C).
EWING [2A-2], using a longitudinal heat flow apparatus, mentions values of:

$$\lambda = 2.40 - 5.38 \text{ W/(m } ^{0}\text{C) for 500 - 850 } ^{0}\text{C}$$

In a subsequent publication [2A-3] he concluded after reviewing his previous data that thermal radiation was the major transport mechanism relevant to the conductivity of FLiNaK:

$$\lambda = 0.6 \text{ W/(m } ^{0}\text{C) for 490 - 850 } ^{0}\text{C}$$

COOKE [2A-4] and [2A-5] in his studies with molten salts found radiation to be significant but made no measurements with FLiNaK. However, he estimates $\lambda = 1.2$ W/(m ^{0}C) for FLiNaK at the melting temperature (454 ^{0}C). His estimates show good agreement with measured values for several other salts.
A survey by DEBOIS-BLANC [2A-6] in 1973 recommends the following value attributed by him to J.P. Sanders of Oak Ridge National Laboratory:

$$\lambda = 1.3 \text{ W/(m } ^{0}\text{C)}$$

For consistency this latter value was uniformly used throughout this thesis. Except for being the most recent value its selection was rather arbitrary (Ref. [2A-6]) quotes no accuracy for this value.

APPENDIX 3A

Error analysis of the friction pressure drop measurement.

The pressure drop across the test tube is measured by means of the following chain of four instruments:

- de dP-transducer consisting of the two vessels with single electrode control systems
- the pressure difference transmitter
- the amplifier
- the recorder.

Figure 3A-1 shows a typical recording of the signal.
The wave line appearing on the recorder instead of the straight line expected, is explained by the control action of the single electrode control system (cf. subsection 2.2.2.2). The actual pressure drop is determined by smoothing the signal. The total error of the dP-transducer including the error caused by this smoothing is estimated at less than 2% of the maximum pressure drop (0.008 MN/m^2 # 400 mm salt head) measured. (The error due to the dead band of $\approx$ 2.5 mm is 0.6%. The ripple on the recording is estimated at $\approx$ 1.5%).
As the remainder of the chain consisting of dP-transducer, amplifier and recorder was calibrated in line, only the repeatability of these instruments needs to the considered for the error analysis. The repeatability of these instruments is 0.1%, 0.5% and 0.25% respectively. These inaccuracies amount to a total inaccuracy of less than 3% of the maximum value measured.

APPENDIX 4A

Energy balances for the subcooled region.

As stated in subsection 4.2.2.2.2 the engineering approach towards the complex heat transfer processes in the subcooled region is to define a fraction of the total transferred heat: k used for vapour generation. The remainder of the heat serves for heating of the subcooled bulk. The above indicates the need for two separate energy balances. To derive these balances we start with the energy balance for the mixture as given by equation (4.2-8):

$$\frac{\partial}{\partial t}(\rho_g u_g \alpha + \rho_\ell u_\ell (1-\alpha)) + \frac{\partial}{\partial z}(\rho_g u_g \alpha v_g + \rho_\ell u_\ell (1-\alpha) v_\ell)$$

$$+ p \frac{\partial}{\partial z}(\alpha v_g + (1-\alpha) v_\ell) = q \frac{O}{A} \qquad (4A\text{-}1)$$

The two terms of these equation on the first line represent storage and convective transport of internal energy of the mixture respectively whereas the first term on the second line represents the expansion work performed by the mixture.
Differentiation of the products in the first two terms of equation (4A-1) yields:

$$\alpha \rho_g \left(\frac{\partial u_g}{\partial t} + v_g \frac{\partial u_g}{\partial z}\right) + u_g \left(\frac{\partial}{\partial t}(\alpha \rho_g) + \frac{\partial}{\partial z}(\alpha \rho_g v_g)\right)$$

$$+ (1-\alpha) \rho_\ell \left(\frac{\partial u_\ell}{\partial t} + v_\ell \frac{\partial u_\ell}{\partial z}\right) + u_\ell \left(\frac{\partial}{\partial t}((1-\alpha) \rho_\ell)\right.$$

$$\left. + \frac{\partial}{\partial z}((1-\alpha) \rho_\ell v_\ell) + p \left\{ \frac{\partial}{\partial z}(\alpha v_g) + \frac{\partial}{\partial z}((1-\alpha) v_\ell) \right\} = q \frac{O}{A} \right. \qquad (4A\text{-}2)$$

The rate of evaporation per unit is derived by TEN WOLDE [4A-1] as:

$$\phi_{\ell g} = \frac{\partial}{\partial t}(\rho_g \alpha) + \frac{\partial}{\partial z}(\rho_g v_g \alpha) \qquad (4A\text{-}3)$$

or:

$$\phi_{\ell g} = - \frac{\partial}{\partial t}(\rho_\ell (1-\alpha)) - \frac{\partial}{\partial z}(\rho_\ell v_\ell (1-\alpha)) \qquad (4A\text{-}4)$$

Substitution of equation (4A-3) and (4A-4) in equation (4A-2) yields:

$$\alpha \rho_g \left(\frac{\partial u_g}{\partial t} + v_g \frac{\partial u_g}{\partial z}\right) \qquad \text{I}$$

$$+ \phi_{\ell g} (u_g - u_\ell) \qquad \text{II}$$

$$+ (1-\alpha) \rho_\ell \left(\frac{\partial u_\ell}{\partial t} + v_\ell \frac{\partial u_\ell}{\partial z}\right) \qquad \text{III}$$

$$+ p \left\{ \frac{\partial}{\partial z}(\alpha v_g) + \frac{\partial}{\partial z}((1-\alpha) v_\ell) \right\} = q \frac{O}{A} \qquad \text{IV} \qquad (4A\text{-}5)$$

The physical meaning of the first three terms of equation (4A-5) should be kept in mind, viz.:

I the increase in internal energy of the steam present in the mixture.
II the increase in internal energy of the evaporating water.
III the increase in internal energy of the remaining water.

Term IV of equation (4A-5) requires some discussion. Differentiation of the righthand terms of equation (4A-3) and (4A-4) yields:

$$\phi_{\ell g} = \alpha \frac{\partial \rho_g}{\partial t} + \alpha\, v_g \frac{\partial \rho_g}{\partial z} + \rho_g \left(\frac{\partial \alpha}{\partial t} + \frac{\partial}{\partial z}(\alpha\, v_g)\right) \qquad (4A\text{-}6)$$

$$-\phi_{\ell g} = (1-\alpha) \frac{\partial \rho_\ell}{\partial t} + (1-\alpha)\, v_\ell \frac{\partial \rho_\ell}{\partial z} + \rho_\ell \left(-\frac{\partial \alpha}{\partial t} + \frac{\partial}{\partial z}((1-\alpha)\, v_\ell)\right) \qquad (4A\text{-}7)$$

Combination of equations (4A-6) and (4A-7) with term IV of equation (4A-5) yields:

term IV =

$$p\, \phi_{\ell g} \left(\frac{1}{\rho_g} - \frac{1}{\rho_\ell}\right) \qquad \text{V}$$

$$-\frac{p}{\rho_g}\left(\alpha \frac{\partial \rho_g}{\rho t} + \alpha\, v_g \frac{\partial \rho_g}{\partial z}\right) \qquad \text{VI}$$

$$-\frac{p}{\rho_\ell}\left((1-\alpha) \frac{\partial \rho_\ell}{\partial t} + (1-\alpha)\, v_\ell \frac{\partial \rho_\ell}{\partial z}\right) \qquad \text{VII} \qquad (4A\text{-}8)$$

Thus term IV is divided into three parts with the following physical meaning:

V expansion work due to evaporating.
VI expansion work of the gas.
VII expansion of the water.

Having established the physical meaning of the various parts of mixture energy equation (4A-1) formulation of the two subcooled energy equations becomes straight forward.
The first energy equation, comprising all terms connected with the gas phase and the evaporating proper, reads:

I + II + V + VI =

$$= \alpha\, \rho_g \frac{\partial u_g}{\partial t} + \alpha\, \rho_g\, v_g \frac{\partial u_g}{\partial z} + \phi_{\ell g}\, (u_g - u_\ell) +$$

$$+ p\, \phi_{\ell g} \left(\frac{1}{\rho_g} - \frac{1}{\rho_\ell}\right) - \frac{p}{\rho_g}\left(\alpha \frac{\partial \rho_g}{\partial t} + \alpha\, v_g \frac{\partial \rho_g}{\partial z}\right) = \frac{k\, q\, O}{A} \qquad (4A\text{-}9)$$

whereas the second one, comprising the terms connected with the water phase, reads:

III + VII =

$$= (1-\alpha)\ \rho_\ell \frac{\partial u_\ell}{\partial t} + (1-\alpha)\ \rho_\ell\ v_\ell \frac{\partial u_\ell}{\partial z} -$$

$$- \frac{p}{\rho_\ell}\left((1-\alpha)\ \frac{\partial \rho_\ell}{\partial t} + (1-\alpha)\ v_\ell \frac{\partial \rho_\ell}{\partial z}\right) = (1-k)\ \frac{q\ O}{A} \qquad (4A\text{-}10)$$

APPENDIX 4B

An adapted version of the Bankoff - Jones slip correlation.

The Bankoff - Jones slip correlation was derived from the correlation originally formulated by BANKOFF [4B-1]:

$$S = \frac{1-\alpha}{K_B-\alpha} \qquad (4B\text{-}1)$$

where:

$$K_B = 0.71 + 0.29\,\frac{p}{p_{cr}} \qquad (4B\text{-}2)$$

The general shape of the s versus α curve shown in figure 4B-1 indicates that this correlation can only be valid for values smaller than the value of the constant K_B.

The need for a correlation valid over the full range of possible α values promted JONES [4B-2] to adapt the Bankoff correlation by substituting K_J for K_B in equation (4B-1):

$$S = \frac{1-\alpha}{K_J-\alpha} \qquad (4B\text{-}3)$$

where K_J reads:

$$K_J = K_B + (1-K_B)\,\alpha^r \qquad (4B\text{-}4)$$

and:

$$r = 3.33 + 0.577\,\frac{p}{p_{cr}} + 4.74\,\left(\frac{p}{p_{cr}}\right)^2 \qquad (4B\text{-}5)$$

Introduction of K_J prevents the denominator of equation (4B-2) from vanishing or becoming negative. Jones determined his $r(\alpha)$ function by fitting slip data for lower values of α ($< \approx 0.8$). Inspection of a typical Bankoff - Jones slip correlation curve (cf. figure 4B-1) shows that slip ratio s increases monotonously with α, reaching its highest value for $\alpha = 1$. This appears physically improbable as for higher α values the mixture consists of a bulk of steam containing very small droplets of water (mist flow) with a relatively high resistance against motion with respect to the surrounding steam. It hence appears probable that with increasing α values the relative velocity of the water is reduced rather than enhanced, thus decreasing the slip ratio. The Bankoff - Jones slip correlation, although succesfully avoiding numerical problems, will therefore not (nor claims to) predict accurate slip ratios for higher α values.

It follows from the above that for α values approaching unity the steam and water velocities tend to become equal. In that case the limit for the slip ratio solely depends on the cross-sectional void and velocity distributions. An upper limit for this ratio is given by the $v_{max}/\bar{v}$ ratio

(assuming all droplets to be concentrated in the region with the highest velocity). This ratio depends weakly on the Re-number but a typical value is 1.2. (cf. HINZE [4B-3]). However, it is more likely that due to turbulence effects the crosssectional void distributions will be approximately uniform, yielding a limit for s equal to unity when $\alpha \rightarrow 1$.
Seeking to correct the Bankoff - Jones correlation by a simple extension the present author investigated the following adapted version:

$$S = \frac{\delta + 1-\alpha}{\delta + K_J-\alpha} \qquad (4B-6)$$

obtained simply by adding a small quantity δ to both numerator and denominator of equation (4B-3). Figure 4B-1 shows the result of this approach: the slip ratio s increases for lower α values closely approximating the original Bankoff - Jones correlation, but decreases for higher α values until reaching unity for $\alpha = 1$. Determination of the best values for δ, chosen here rather arbitrarily as 0.04, requires fitting to reliable slip data for higher α values. It should be stressed that no physical significance is claimed for this approach.
However, in the continuing absence of accurate and physically well-based slip correlations for high α values the proposed correlation may serve as a simple formula better fitting the true relation between slip ratio and void fraction than the Bankoff - Jones correlation it is based on.

APPENDIX 4C

The derivative of the specific mass of two-phase mixtures with respect to the mixture enthalpy.

The two-phase mixture density is defined by equation (4.2-5) as:

$$\bar{\rho} = \rho_g \alpha + \rho_\ell (1-\alpha) \tag{4C-1}$$

whereas the two-phase enthalpy is defined as:

$$\bar{h} = h_g x + h_\ell (1-x) \tag{4C-2}$$

Neglecting pressure effects the derivative of $\bar{\rho}$ with respect to $\bar{h}$ can be written as:

$$\frac{d\bar{\rho}}{d\bar{h}} = \frac{d\bar{\rho}}{d\alpha} \frac{d\alpha}{dx} \frac{dx}{dh} \tag{4C-3}$$

From equations (4C-1) and (4C-2) follows respectively:

$$\frac{d\bar{\rho}}{d\alpha} = (\rho_g - \rho_\ell) \tag{4C-4}$$

and:

$$\frac{dx}{d\bar{h}} = \frac{1}{h_g - h_\ell} = \frac{1}{r} \tag{4C-5}$$

Assuming no slip (s = 1.0) the relationship between α and x is given by:

$$x = \frac{\alpha\rho_g}{(1-\alpha)\rho_\ell + \alpha\rho_g} \tag{4C-6}$$

Differentiating with respect to α yields:

$$\frac{dx}{d\alpha} = \frac{\rho_\ell \rho_g}{\bar{\rho}^2} \tag{4C-7}$$

After combination of equations (4C-4), (4C-5) and (4C-7) follows:

$$\frac{\partial\bar{\rho}}{\partial\bar{h}} = \frac{\rho_g - \rho_\ell}{\rho_g \rho_\ell} \frac{\bar{\rho}^2}{r}$$

APPENDIX 4E

Derivation of the equations describing the total system.

$$\left.\begin{aligned} \phi\, p_{in} &= H_{p\phi}(\omega)\,\delta\,\phi_{in_j} + H_{pp}(\omega)\,\delta\,p_{out} \\ \delta\,\phi_{out_i} &= H_{\phi\phi}(\omega)\,\delta\,\phi_{in_j} - H_{\phi p}(\omega)\,\delta\,p_{out} \end{aligned}\right\} \text{ for all } j \qquad (4.6\text{-}4a),\ (4.6\text{-}4b)$$

$$\delta\ _{in} = -\,Z_{in}(\omega)\,\delta\,\phi_{in_{tot}} \qquad (4.6\text{-}5)$$

$$\delta\,p_{out} = Z_{out}(\omega)\,\delta\,\phi_{out_{tot}} \qquad (4.6\text{-}6)$$

$$\delta\,\phi_{in_{tot}} = \sum_{j=1}^{n} \delta\,\phi_{in_j} \qquad (4.6\text{-}7)$$

$$\delta\,\phi_{out_{tot}} = \sum_{j=1}^{n} \delta\,\phi_{out_j} \qquad (4.6\text{-}8)$$

Combination of equations (4.6-4b), (4.6-6) and (4.6-8) yields:

$$\delta\,p_{out} = Z_{out} \sum_{j=1}^{n} (H_{\phi\phi_j}\,\delta_{in_j} + Z_{out} \sum_{j=1}^{n} (H_{\phi p}))\,\delta\,p_{out} \qquad (4E\text{-}1)$$

or after transformation:

$$\delta\,p_{out} = \sum_{j=1}^{n} \frac{H_{\phi\phi_j} \cdot Z_{out}}{(1 + Z_{out} \sum_{k=1}^{n} H_{\phi p_k})}\,\delta\,\phi_{in_j} \qquad (4E\text{-}2)$$

Substitution of equations (4E-2) and (4.6-7) in (4.6-4a) yields:

$$H_{p\phi_i}\,\delta\,\phi_{in_i} + \sum_{j=1}^{n} Z_{in}\,\delta\,\phi_{in_j} + \sum_{j=1}^{n} \frac{H_{pp_i} \cdot H_{\phi\phi_j} \cdot Z_{out}}{(1 + Z_{out} \sum_{k=1}^{n} H_{\phi p_k})}\,\delta\,\phi_{in_j} \qquad (4E\text{-}3)$$

For the sake of convenience this equation is written as:

$$A_i\,\delta\,\phi_{in_i} + \sum_{j=1}^{n} B_{ij}\,\delta\,\phi_{in_j} \qquad (4E\text{-}4)$$

where:

$$A_i = H_{p\phi_i} \qquad (4E\text{-}5)$$

and:

$$B_{ij} = Z_{in} + \frac{H_{pp_i} \cdot H_{\phi\phi_j} \cdot Z_{out}}{(1 + Z_{out} \sum_{k=1}^{n} H_{\phi p_k})} \qquad (4E\text{-}6)$$

In order to provide a better insight into the physical meaning of these equations let us divide the system into two parts: upstream and downstream of the inlet header (cf. figure 4.6-7).
A according to equation (4.6-4a) the inlet pressure of a channel is affected by the inlet mass flow and the outlet pressure. Now let us assume that the mass flow into channel j increases. This will affect the inlet pressure in two ways, viz: first directly through:

$$\delta p_{in} = H_{p\phi_j} \delta \phi_j$$

and indirectly through the outlet pressure. The latter would increase by:

$$\delta p_{out} = Z_{out} H_{\phi\phi_j} \delta \phi_j$$

if the total outlet mass flow were to increase by exactly the same amount as the mass flow through channel j . However, there is an attenuating effect. The increasing outlet pressure tends to reduce the outlet mass flow of all channels (cf. equation (4.6-4b)) and thus reduces the increase of the total outlet mass flow. This is why the outlet pressure increases only by:

$$\delta p_{out} = \frac{Z_{out} H_{\phi\phi_j} \delta \phi_j}{(1 + Z_{out} \sum_{k=1}^{n} H_{\phi p_k})}$$

The increase in outlet pressure raises the inlet pressure of an arbitrary channel i by:

$$\delta p_{in} = H_{pp_i} \frac{Z_{out} H_{\phi\phi_j}}{(1 + Z_{out} \sum_{k=1}^{n} H_{\phi p_k})} \delta \phi_j \qquad (4E\text{-}7)$$

It will be clear now that the total change in inlet pressure due to downstream effects is:

$$\delta p_{in} = H_{p\phi} \delta \phi_i + \sum_{j=1}^{n} \left(H_{pp_i} \frac{Z_{out} H_{\phi\phi_j}}{(1 + Z_{out} \sum_{k=1}^{n} H_{\phi p_k})} \delta \phi_j \right) \qquad (4E\text{-}8)$$

According to equation (4.6-5) the inlet pressure change caused by upstream effects is:

$$\delta p_{in} = \sum_{j=1}^{n} - Z_{in} \delta \phi_j \qquad (4E\text{-}9)$$

As there is only one inlet pressure the two variations given by equations (4E-8) and (4E-9) must of necessity be equal which explains equation (4E-7).

APPENDIX 4F

Explanation for the existence of predominant modes of parallel channel instability.

The linear analysis presented so far can not explain the existence of predominant modes of parallel channel oscillation as observed by VAN VONDEREN [4.6-5].
For that purpose one has to consider the effects of non-linearities.
The most notable effect of these non-linearities is the change in shape of flow oscillations with increasing amplitude.
The examinations of a line recording of a measured oscillation shown in figure (4F-1) shows that with increasing amplitude the tops become flatter whereas the bottom parts become sharper.
In addition to the original pure sine the signal now contains harmonics.
Figure (4F-2) shows a signal resulting from the addition of a sine and its second order harmonic having a third of the first order amplitude, which closely resembles the line recording. Returning to parallel channel instability we remind the reader of the main characteristic of this type of oscillation: the constant total mass flow.
In the linear analysis this condition merely yields for a set of identical channels that the sum of the oscillations in the individual channels is constant.
This condition can be met by an infinite number of combinations of sines.
However, it will be clear that the possibilities to meet this condition with oscillations as shown in figure (4F-2) are less numerous.
The variation of the second order signal of figure (4F-2) can be represented by the complex formula:

$$\delta \phi = u + cu^2 \quad \text{(u and c are complex numbers)} \qquad \text{(4F-1)}$$

The first term on the right hand side represents the basic sine whereas the second term represents the second order component.
c represents the degree of non-linearity.
Now let us consider the case of VAN VONDEREN [4.6-5] : three parallel identical channels.
The flows through these channels can according to equation (4F-2) be given by:

$$\delta \phi_1 = u_1 + c\, u_1^2$$

$$\delta \phi_2 = u_2 + c\, u_2^2 \qquad \text{(4F-2)}$$

$$\delta \phi_3 = u_3 + c\, u_3^2$$

The condition to be met for parallel channel instability is:

$$\delta \phi_1 + \delta \phi_2 + \delta \phi_3 = 0 \qquad \text{(4F-3)}$$

To chieve this all times the sum of the first order harmonics and the sum of the second order harmonics have to vanish:

$$u_1 + u_2 + u_3 = 0$$

$$c\,(u_1^2 + u_2^2 + u_3^2) = 0 \qquad \text{(4F-4)}$$

Solution of these equations yields:

$$u_2 = (-\frac{1}{2} + \frac{1}{2} i \sqrt{3})\ u_1$$
$$u_3 = (-\frac{1}{2} - \frac{1}{2} i \sqrt{3})\ u_1 \qquad (4F\text{-}5)$$

This is the predominant mode observed by VAN VONDEREN [4.6-5] : all three tubes oscillating with the same amplitude and a mutual phase shift of 120^0 (cf. figure 4F-3). This result is physically easy to understand: this mode is the only combination of "non-linear" signals satisfying the above condition, viz. that both the sum of the first order harmonics and that of the second order harmonics be zero (cf. figure 4F-4). In none of the other modes mentioned in subsection 4.6.1.2.3 the sum of the second order harmonics vanishes. It is hence to be expected that this predominant mode will generally prevail whenever the oscillation amplitude becomes large enough for the second order harmonics to assume sufficient importance.

APPENDIX 4G

Zero's of $H_{p\phi}$ and $|M_{res}|$.

The problem to be discussed in this appendix concerns the determination of the number of zero's with a positive real part of the functions $H_{p\phi}(s)$ and $M_{res}(s)$ (if any) form the polar plots obtained by frequency analysis.
In presenting the approach leading to the solution of this problem the author assumes the readers familiarity with the principles of linear system stability as described in ROUTH [4G-1], PORTER [4G-2].
Consider an arbitrary complex function F(s). For each complex value of s, this function has a value: F(s) that can be plotted in the complex plane (cf. figure 4G-1).
If s goes once clockwise around a closed contour E in the s-plane the function value describes its own contour Γ known as the map of E by F(s).
The function F(s) is assumed to have z zero's (s-values for which F(s) vanishes) and p poles (s-values for which F(s) becomes infinite) within contour E.
A theory known as "the argument principle" (cf. CHURCHILL [4.6-3]) gives a relationship between the number of zero's z, the number of poles p and the shape of the map Γ.
This theory states that map Γ encircles the origin z - p net times in clockwise direction (anti-clockwise encirclements are counted negative).

As the aim is to determine the number of zero's with a positive real part; that is: located in the right half of the complex plane the contour E has to be chosen accordingly. Such a contour enclosing the entire right half of the complex plane consists of the imaginary axis and an infinite semi-circle (cf. figure 4G-2). This curve is known as the Nyquist path.
Application of the argument principle on the map of the Nyquist path by a transfer function yields the difference between the number of zero's and the number of pole's with a positive real part of this transfer function.
As it can be shown that, neither of the two transfer functions under consideration possesses such a pole, the net number of encirclements equals the number of zero's. The existence of a pole in the right half of the complex plane for $H_{p\phi}$ would imply, that, even if the inlet mass flow and the outlet pressure were kept constant, a diverging pressure would occur at the inlet. This is physically inconsistent with the density wave mechanism as presented.

For the second criterion a similar relation exists.

The determinant $|M_{res}|$ is the sum of a number of products of A_i's and B_{ij}'s.
Therefore $|M_{res}|$ can only become infinite if one of these factors becomes infinite. That $A_i = H_{p\phi}$ does not posses a pole with a possitive real part has been shown above. That the same applies to the B_{ij}'s can be understood by examining their physical meaning (cf. APPENDIX 4E).
B_{ij} is the ratio of the variation of the inlet pressure of channel number i due to effects of a variation of the inlet mass flow in channel number j.
If B_{ij} would posses a pole with a positive real part a diverging pressure oscillation would occur at the inlet of the tubes even if the inlet mass flows of all channels, and the pressure at their outlets were kept constant.

As this is also inconsistent with the density wave mechanism, $|M_{res}(s)|$ possesses no such poles.
Consequently for both transfer functions is valid, that the net number of encirclements of the origin by the map of the Nyquist path equals the number of zero's with a positive real part. Due to the symmetry of transfer functions zero's always occur in complex adjugated pairs ($s = \lambda \pm i\omega$) constituting one mode of instability.
Now however arises the problem how to obtain the map of the Nyquist path as it can only be measured for a limited range of positive frequencies ω ($s = i\omega$) and thus for a part of the positive half of the imaginary axis. To solve this problem some additional properties of the transfer functions have to be considered. The first one, valid for all transfer functions is the symmetry with respect to ω mentioned above.

The remaining part of the Nyquist path to be mapped is formed by the infinite semi-circle enclosing the right half plane.
To derive the shape of the map of this part of the Nyquist path by each of the two transfer functions, we have to consider their limit behaviour for very high frequencies:

$H_{p\phi}$.

An harmonic variation of the inlet mass flow of an evaporator tube causes three types of pressure loss variations, viz. of the:

1. hydro-static pressure losses
2. friction pressure losses
3. acceleration pressure losses

The magnitude of the first two depends on the amplitude rather than on the frequency of the variations in the conditions within the steam generator and consequently do not increase with frequency. Acceleration forces however are proportional to the frequency for an harmonic oscillation of the inlet velocity:

$$\frac{\partial p}{\partial z} = -\rho \frac{\partial v}{\partial t} \rightarrow \frac{\partial \delta p}{\partial z} = -\rho s\, \delta v = -\rho\, i\omega\, \delta v \qquad (4G\text{-}1)$$

Due to its observed proportionality with frequency the acceleration pressure variation outgrows all other pressure losses for increasing frequency. Equation (4G-1) shows that for higher frequencies the inlet impedance tends to behave as a pure differentiator:

$$H_{p\phi} = s$$

This differentiator maps the infinite semi-circle of the Nyquist path into an identical one in the $H_{p\phi}$-plane (cf. figure 4G-3).

B_{ij} (cf. equation (4.6-11)).

At higher frequencies the damping effect of the compressibility of the steam present in the evaporator, causes $H_{\phi\phi}$ - the ratio of an outlet mass flow disturbance and its causing inlet mass flow variation - to vanish.

For the behaviour of Z_{in} - the remaining part of B_{ij} -, a similar analysis as given above for $H_{p\phi}$, yields an identical result:

$$\lim_{\omega \to \infty} Z_{in} = s$$

Inspection of $|M_{res}|$ shows that it is a sum of products of A's and B's: $A^p B^q$ where $m = p + q$ is equal for all products. m is the total number of sets of identical tubes (a tube different of all others is counted in this respect as a set of one).
As both A and B tend to s for higher frequencies, the limit of these products is:

$$\lim_{\omega \to \infty} |M_{res}| = s^m$$

Such a function maps the semi-circle into m semi-circles in the $|M_{res}|$ plane (cf. figure 4G-4 where m = 2).

APPENDIX 4H

Details of the discretization, linearization and substitution steps in the solutional procedure.

The procedure will be illustrated by applying it to the single phase mass balance:

$$\frac{\partial \rho}{\partial t} + \frac{\partial G}{\partial z} = 0$$

In the first step the spatial derivative $\frac{\partial G}{\partial z}$ is replaced by $\frac{\partial G}{\partial z} = \frac{G_2 - G_1}{\Delta z}$ (cf. figure 4.6-21) and the other properties are evaluated as the average of the two boundary values: $\rho = \frac{\rho_1 + \rho_2}{2}$, yielding:

$$\frac{1}{2}\frac{\partial \rho_1}{\partial t} + \frac{1}{2}\frac{\partial \rho_2}{\partial t} + \frac{1}{\Delta z}\delta G_2 - \frac{1}{\Delta z}\delta G_1 = 0 \qquad (4H\text{-}1)$$

The relevant algebraic equation in this case is the relation for the specific mass as a function of pressure ρ and enthalpy h:

$$\rho = \rho(p, h) \qquad (4H\text{-}2)$$

The second step is linearization. In this case the first equation is already linear. Linearization of the second one yields:

$$\delta\rho_{1,2} = \left(\frac{\partial \rho}{\partial p}\right)_{o\ 1,2} \delta p_{1,2} + \left(\frac{\partial \rho}{\partial h}\right)_{o\ 1,2} \delta h_{1,2}$$

The third step i.e. substitution yields:

$$\frac{1}{2}\left(\frac{\partial \rho}{\partial p}\right)_1 \frac{\partial}{\partial t}\delta p_1 + \frac{1}{2}\left(\frac{\partial \rho}{\partial h}\right)_1 \frac{\partial}{\partial t}\delta h_1 + \frac{1}{2}\left(\frac{\partial \rho}{\partial p}\right)_2 \frac{\partial}{\partial t}\delta p_2 + \frac{1}{2}\left(\frac{\partial \rho}{\partial h}\right)_2 \frac{\partial}{\partial t}\delta h_2 +$$

$$+ \frac{1}{\Delta z}\ G_2 - \frac{1}{\Delta z}\delta G_1 = 0$$

Thus the partial differential equation has been transformed in a linear ordinary differential equation in the basic variables. The, in this case, simple process can involve in some cases over eighty algebraic equations.

APPENDIX 4J

Example of an application of the SLINQ program for substitution of linear equations.

To derive the two-phase energy equations expressed in the basic nodal variables of a channel element $\delta h_{1,2}$, $\delta G_{1,2}$ and $\delta p_{1,2}$ (the indices 1,2 designate upper and lower boundary of the element respectively) 88 linear equations have to be combined (cf. figure 4J-1). The general coefficients given in the resulting equation represent quite complex expressions in the coefficients of the combined equations.
The purpose of a special developed computer program SLINQ is:

- to derive these expressions automatically
- to reduce computing time consumption by identifying common factors that can be evaluated before hand
- to punch these common factors and expressions as FORTRAN statements automatically, to avoid human errors during copying
- to verify by means of a separate test the correct performance of the combination process.

Figure 4J-2 shows the result of SLINQ as they are punched.
As mentioned above the substitution process is checked for correctness by evaluation of the original set of equations and the set resulting from the substitutions. For this evaluation the unknown coefficients and basic variations have been designated arbitrary values. Figure 4J-3 shows the results of the two evaluations indicating that the substitutions have been performed correctly.

APPENDIX 4K

Power method and vector deflation as applied for determining eigenvalues in the CURSSE PROGRAM.

Although described fully in WILKINSON [4K-1] the power method and vector deflation are outlined here to be able to discuss the adaptations requires for solving the generalized eigenvalue problem of equation (4.6-5).
The eigenvalue problem proper is defined by:

$$|C|\ \underline{v} = s\ \underline{v} \tag{4K-1}$$

By applying the power method, both the largest absolute eigenvalue and its associated eigenvector are determined from the vectors obtained by successive iterations.
Each subsequent iteration vector $\underline{x}_{n+1}$ is determined by a multiplication of matrix $|C|$ and its predecesser $\underline{x}_n$, starting with an arbitrary vector $\underline{\rho}$:

$$\underline{x}_1 = |C|\ \underline{\rho} \tag{4K-2}$$

$$\underline{x}_{n+1} = |C|\ \underline{x}_n \tag{4K-3}$$

The starting vector $\underline{\rho}$ may be expressed in the eigenvectors $\underline{v}_i$ of matrix $|C|$ as follows:

$$\underline{\rho} = \sum_{i=1}^{n} \alpha_i\ \underline{v}_i \tag{4K-4}$$

Combination of equations (4K-2) and (4K-4) yields:

$$\underline{x}_1 = |C|\ \underline{\rho} = |C| \sum_{i=1}^{n} \alpha_i\ \underline{v}_i$$

$$= \sum_{i=1}^{n} \alpha_i\ |C|\ \underline{v}_i = \sum_{i=1}^{n} \alpha_i\ s_i\ \underline{v}_i \tag{4K-5}$$

It will be clear that repeated multiplication by $|C|$ yields for the m^{th} iteration:

$$\underline{x}_m = \sum_{i=1}^{n} \alpha_i\ s_i^m\ \underline{v}_i \tag{4K-6}$$

Assuming s_1 to be the largest absolute eigenvalue and $\alpha_1 \neq 0$, equation (4K-6) may be written as:

$$\underline{x}_m = \alpha_1\ s_1^m\ \underline{v}_1 + \sum_{i=2}^{n} \alpha_i\ s_i^m\ \underline{v}_i$$

$$= s_1^m \{\ \alpha_1\ \underline{v}_1 + \sum_{i=2}^{n} \alpha_i\ \left(\frac{s_i}{s_1}\right)^m\ \underline{v}_i\ \} \tag{4K-7}$$

For large values of m the iteration vector $\underline{x}_m$ is seen to approximate the eigenvector $\underline{v}_1$, whereas the eigenvalue s_1 is approximated by the ratio of two successive iteration vectors:

$$\frac{\underline{x}_{m+1}}{\underline{x}_m} = s_1 \frac{1 + \sum_{i=2}^{n} \alpha_i \left(\frac{s_i}{s_1}\right)^{m+1}}{1 + \sum_{i=2}^{n} \alpha_i \left(\frac{s_i}{s_1}\right)^{m}} \cong s_1 \qquad (4K\text{-}8)$$

For the determination of additional eigenvalues vector deflation was applied. As shown above application of the power method yields the largest absolute eigenvalue s_1 provided its coefficient in the expansion of equation (4K-4) is non-zero. If however this coefficient is zero, i.e. the starting vector $\underline{\rho}$ does not possess a component in the direction of the eigenvector associated with the largest absolute eigenvalue, it will be clear that the next largest eigenvalue will be obtained provided again its coefficient in equation (4K-4) is non-zero. Hence it is possible to determine additional eigenvalues by cleaning the starting vector $\underline{\rho}$ of components associated with the previous determined eigenvalues:

$$\underline{\rho}^{\star} = \underline{\rho} - \sum_{i=1}^{j} \alpha_i \underline{v}_i \qquad (4K\text{-}9)$$

The process of removing these components from an arbitrary starting vector is called vector deflation. Determination if the α_i values is based on a property of the eigenvectors of the original eigenvalue problem, defined by equation (4K-1) and those of the so-called transposed problem:

$$|C|^T \underline{w} = s \underline{w} \qquad (4K\text{-}10)$$

Matrix $|C|$ and its transpose $|C|^T$ have the same eigenvalues s_i. Corresponding to each s_i there are eigenvectors $\underline{v}_i$ of $|C|$ and $\underline{w}_i$ of $|C|^T$ and in general these are different. However, $\underline{v}_i$ and $\underline{w}_i$ are biorthogonal, which means that, their inner product vanishes for different values of i and j:

$$\underline{w}_i^T \underline{v}_j = 0 \qquad (i \neq j) \qquad (4K\text{-}11)$$

Multiplication of the transpose of the eigenvector w_j with an arbitrary starting vector $\underline{\rho}$ yields after substitution of equation (4K-4):

$$\underline{w}_j^T \underline{\rho} = \underline{w}_j^T \sum \alpha_i \underline{v}_i = \sum_{i=1}^{n} \alpha_i \underline{w}_j \underline{v}_i \qquad (4K\text{-}12)$$

Due to the biorthogonality of $\underline{w}$ and $\underline{v}$ all elements but one vanish in the sum:

$$\underline{w}_j^T \underline{\rho} = \alpha_j \underline{w}_j \underline{v}_j \qquad (4K\text{-}13)$$

Some transformation yields:

$$\underline{\alpha}_j = \frac{\underline{w}_j \, \underline{\rho}}{\underline{w}_j \, \underline{v}_j} \qquad (4K\text{-}14)$$

After determination of all required α_j values, a cleaned starting vector can be determined as given in equation (4K-9).
The more complicated case for conjugated complex eigenvalue, discussed in detail in WILKINSON [4K-1], is based on the same principles.
The above theory on vector deflation has been resumed mainly to show that vector deflation requires determination of eigenvectors of both the original and the transposed problem.

The generalized eigenvalue problem of interest here (cf. subsection 4.6.1.3.3) and defined by:

$$|A| \, \underline{v} + s \, |B| \, \underline{v} = 0 \qquad (4K\text{-}15)$$

may be transformed to the basic form:

$$|C| \, \underline{v} = s^{\star} \, \underline{v} \qquad (4K\text{-}16)$$

by definition of two new variables:

$$|C| = |A^{-1}| \, |B| \qquad (4K\text{-}17)$$

and

$$s^{\star} = -\frac{1}{s} \qquad (4K\text{-}18)$$

It will be clear from the definition of $s^{\star}$ that, where the power method determines the largest absolute value of $s^{\star}$, in accordance with our objective now the smallest s is found.
For the generalized problem the iterative equation similar to equation (4K-3) reads:

$$\underline{x}_{n+1} = |A|^{-1} \, |B| \, \underline{x}_n \qquad (4K\text{-}19)$$

or after some transformation:

$$|A| \, \underline{x}_{n+1} = |B| \, \underline{x}_n = \underline{r} \qquad (4K\text{-}20)$$

The latter equation shows clearly that each next iteration results from the solution of a system of linear equations where the right hand side $\underline{r}$ varies but the coefficient matrix $|A|$ remains the same.
Due to the different structure of the transposed problem, defined by:

$$|C|^{T} \, \underline{w} = s^{\star} \, \underline{w} \qquad (4K\text{-}21)$$

it requires its own iterative scheme.

Combination of equations (4K-14) and (4K-18) yields:

$$\{ |A|^{-1} |B| \}^T \underline{w} = s^{\star} \underline{w} \qquad (4K\text{-}22)$$

which after some transformation reads:

$$|B|^T \{ |A|^{-1} \}^T \underline{w} = s^{\star} \underline{w} \qquad (4K\text{-}23)$$

The iterative equation for this case reads:

$$\underline{y}_{n+1} = |B|^T \{ |A|^{-1} \}^T \underline{y}_n \qquad (4K\text{-}24)$$

Solution of this equation can be separated into two stages by introduction of a new variable defined as:

$$\underline{z} = (|A|^{-1})^T \underline{y}_n \qquad (4K\text{-}25)$$

Rearrangement of this equations yields:

$$|A|^T \underline{z} = \underline{y}_n \qquad (4K\text{-}26)$$

The new iterate is subsequently computed from:

$$\underline{y}_{n+1} = |B|^T \underline{z} \qquad (4K\text{-}27)$$

Again the solutional procedure is centered around the repeated solution of a set of linear equations with different r.h.s. vectors but unchanged coefficient matrix, viz. $|A|^T$.
This requirement for repeated solution called for the reduction of the amount of operations required for each subsequent solution through appropriate matrix manipulation to obtain reduction of CPU-time. Matrix inversion while reducing solution of the set of equations to a simple multiplication of this inverse and the right hand side vectors, was unsuitable in our case, as the process of inversion loses the band structure and hence the aforementioned economic storage mode. A literature survey yielded a method, the so-called LU-decomposition. Largely possessing the advantages of preliminary matrix preparation while retaining the advantages of the band structure storage mode.
By LU-decomposition a system of linear equations given by:

$$|C| \underline{x} = \underline{r} \qquad (4K\text{-}28)$$

is transformed to:

$$|L| \; |U| \underline{x} = \underline{r} \qquad (4K\text{-}29)$$

where $|L|$ and $|U|$ are two triangular matrices having only zero elements above and below the main diagonal respectively, the product of which is identical to matrix $|C|$. By introducing a new vector $\underline{y}$ defined by:

$$\underline{y} = |U| \underline{x} \qquad (4K\text{-}30)$$

solution of the original set of equations can be replaced by the subsequent solution of two sets, viz.:

$$|L|\ \underline{y} = \underline{r} \qquad \text{(4K-31)}$$

and:

$$|U|\ \underline{x} = \underline{y} \qquad \text{(4K-32)}$$

Due to the very simple structure of the $|L|$ and $|U|$ matrices, the combined solution of equations (4K-28) and (4K-29) requires considerably less CPU-time than direct solution of equation (4K-25). As the CPU-time reduction obtained during repeated solution (up to 60 times) of equations (4K-28) and (4K-29), amply exceeds the CPU-time required for the previous LU-decomposition, application of this method is particularly advantageous in our case. Unfortunately it was found that (cf. IBM-SSP [4K-2], NAG [4K-3], IMSL [K-4] and EISPACK [4K-5]) none of the existing routines was suited for our purpose as all had been designed for application in structural analysis and as such for symmetrical band matrices. Therefore a new routine based on the LU-decomposition (cf. WILKINSON [4K-1]) and adapted for non-symmetrical band matrices, called LUDEC, was developed.
By application of LUDEC the $\underline{v}_1$ and $\underline{w}_1$ eigenvectors associated with the largest eigenvalue s_1 are determined. After cleaning of the starting vector $\underline{\rho}$ from components of $\underline{v}$ and $\underline{w}$ and their congugated counterparts the proces can start again to find $\underline{v}_2$ and $\underline{w}_2$ and so on. The process described above is performed by calling subroutine EIGVEC.

REFERENCES PERTAINING TO APPENDICES

REFERENCES APPENDIX 2A

2A-1 COHEN, S.I., e.a.
A physical Property summary for ANP Fluoride mixtures.
ORNL 2150 (1958).

2A-2 EWING, C.T., e.a.
Radiant Transfer of Heat and the Thermal Conductivity of FLiNaK (Salt A).
US Naval Research Laboratory Report - NRL-5568, Washington D.C. (1960).

2A-3 EWING, C.T. e.a.
Radiant Transfer of Heat in Molten Inorganic Compounds at High Temperatures.
Journal of Chem. & Eng. Data: 7, 246-250 (1962).

2A-4 COOKE, J.W.
Estimation of the Thermal Conductivity of Molten Salt Mixtures.
ORNL Program Report MSR-68-28 (1968).

2A-5 COOKE, J.W.
Improved Method for Calculating the Ionic Number for Estimating the Thermal Conductivity of Molten Salts.
ORNL Program Report MSR-68-43 (1968).

2A-6 DEBOIS-BLANC, D.R.
Ebasco Services, Inc., New York, USA.
Private comminication.

REFERENCES APPENDIX 4B

4B-1. BANKOFF, S.G.
Avariable density single fluid model for two-phase flow with particular reference to steam-water flow.
Journal of Heat Transfer, November (1960).

4B-2. JONES, A.B.
Hydrodynamic stability of a boiling channel.
KAPL-2170, October (1961).

4B-3. HINZE, I.O.
Turbulence.
McGraw-Hill (1975).

REFERENCES APPENDIX 4G

4G-1. ROUTH, E.J.
Stabilization of Motion.
Taylor & Francis Ltd. London (1975).

4G-2. PORTER, B.
Stability Criteria for linear dynamical systems.
Oliver & Boyd, Edinburgh/London (1967).

REFERENCES APPENDIX 4K

4K-1. WILKINSON, J.H.
The algebraic eigenvalue problem.
Academic Press, New York (1966).

4K-2. System/360 Scientific Subroutine Package.
Programmers Manual, IBM GH 20-02.

4K-3. NAG. Library Manual, Mark 5.
Numerical Algorithms Group, Oxford, U.K. (1976).

4K-4. IMSL Library, Edition 6.
International Mathematical Statistical Libraries,
Inc. Houston, U.S.A. (1977).

4K-5. SMITH, B.T., BOYLE, J.M. and GARBOW, B.S.
Matrix Eigensystem Routines.
Springer, Berlin (1974).

STELLINGEN

1. Door de toename van specialistische kennis bij de industrie, zal de nadruk bij de inbreng door ingenieursbureau's in de toekomst minder op kennis en meer op projektorganisatie en -beheer komen te liggen.

2. Ten onrechte veronderstelt Van Vonderen, dat de oorzaak van density-wave instabiliteit ligt in een lokale terugkoppeling tussen dampgehalte en massastroom en dat een fase-verschuiving van 180^0 tussen deze grootheden voorwaarde is voor het ontstaan van oscillaties.
A.C.M. van Vonderen,
On the behaviour of parallel boiling water channels,
proefschrift TH-Eindhoven, 1971.

3. In verhouding tot het grote belang van warmteopslag voor het dynamisch op elkaar afstemmen van warmte- en krachtvraag bij gekombineerde opwekking worden de technische mogelijkheden hiertoe nog onvoldoende onderzocht.

4. Bij wetenschappelijk onderzoek aan universitaire instituten ontbreekt het veelal aan een systematische projektbegeleiding.

5. Er dienen op korte termijn dwingende voorschriften te komen voor adequate geluidsisolatie van woningen, teneinde verdere schade aan de volksgezondheid te voorkomen.

6. De moeilijkheid van wetenschappelijk onderzoek ligt niet zo zeer in het vinden van een verklaring voor waargenomen verschijnselen, als in het verwerpen van deze verklaring wanneer latere experimentele resultaten daarmee in tegenspraak zijn.

7. Het zou van te waarderen aandacht voor het geboren kind getuigen, wanneer politieke partijen zouden bevorderen, dat ook het dragen van veiligheidsgordels achterin auto's verplicht gesteld wordt.

8. De misvatting, dat een voltooide akademische studie een voldoende voorwaarde zou zijn voor het goed ontwerpen en programmeren van komputerprogramma's geeft blijk van ernstige onderschatting van de hiervoor vereiste vakbekwaamheid en ervaring. Dit resulteert in verspilling van programmeer- en komputertijd en in een groot aantal weinig efficiente programma's.

9. De vervanging van handberekeningen door komputerprogramma's bij het ontwerpen van komponenten en installaties blijkt veelal gepaard te gaan aan een verlegging van de verantwoordelijkheid voor het resultaat naar medewerkers met een lager opleidingsniveau. Deze ontwikkeling leidt tot vergroting van het risico van onjuiste of onjuist geïnterpreteerde resultaten.

10. Het meer en meer negeren van verkeerslichten zou sterk worden tegengegaan, door uitschakeling ervan bij gering verkeersaanbod.

11. Wanneer niet op korte termijn maatregelen worden genomen om aan de stijgende energiebehoefte te voldoen, kán de soep in de toekomst niet eens meer heet worden gegeten.

ASPECTS OF MOLTEN FLUORIDES AS HEAT TRANSFER AGENTS FOR POWER GENERATION

FIGURES AND TABLES

B. VRIESEMA

ASPECTS OF MOLTEN FLUORIDES AS HEAT TRANSFER AGENTS FOR POWER GENERATION

FIGURES AND TABLES

B. VRIESEMA

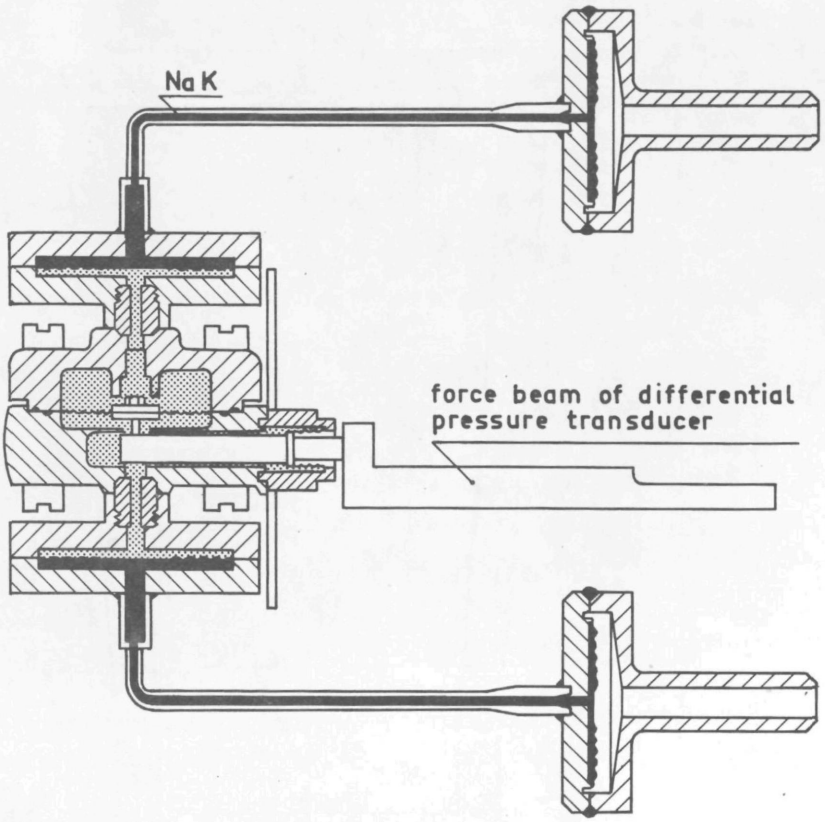

FIGURE 2.2-1.

NaK filled dp-transmitter.

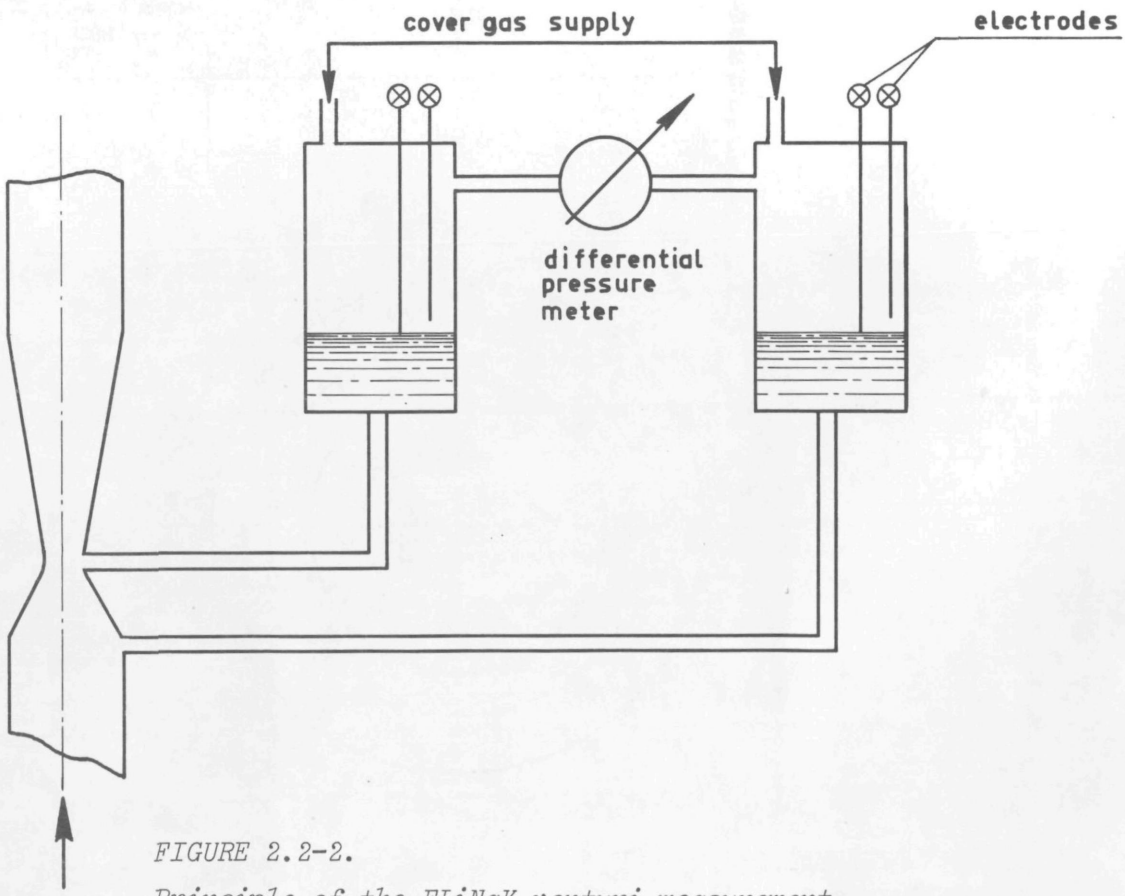

FIGURE 2.2-2.

Principle of the FLiNaK venturi measurement.

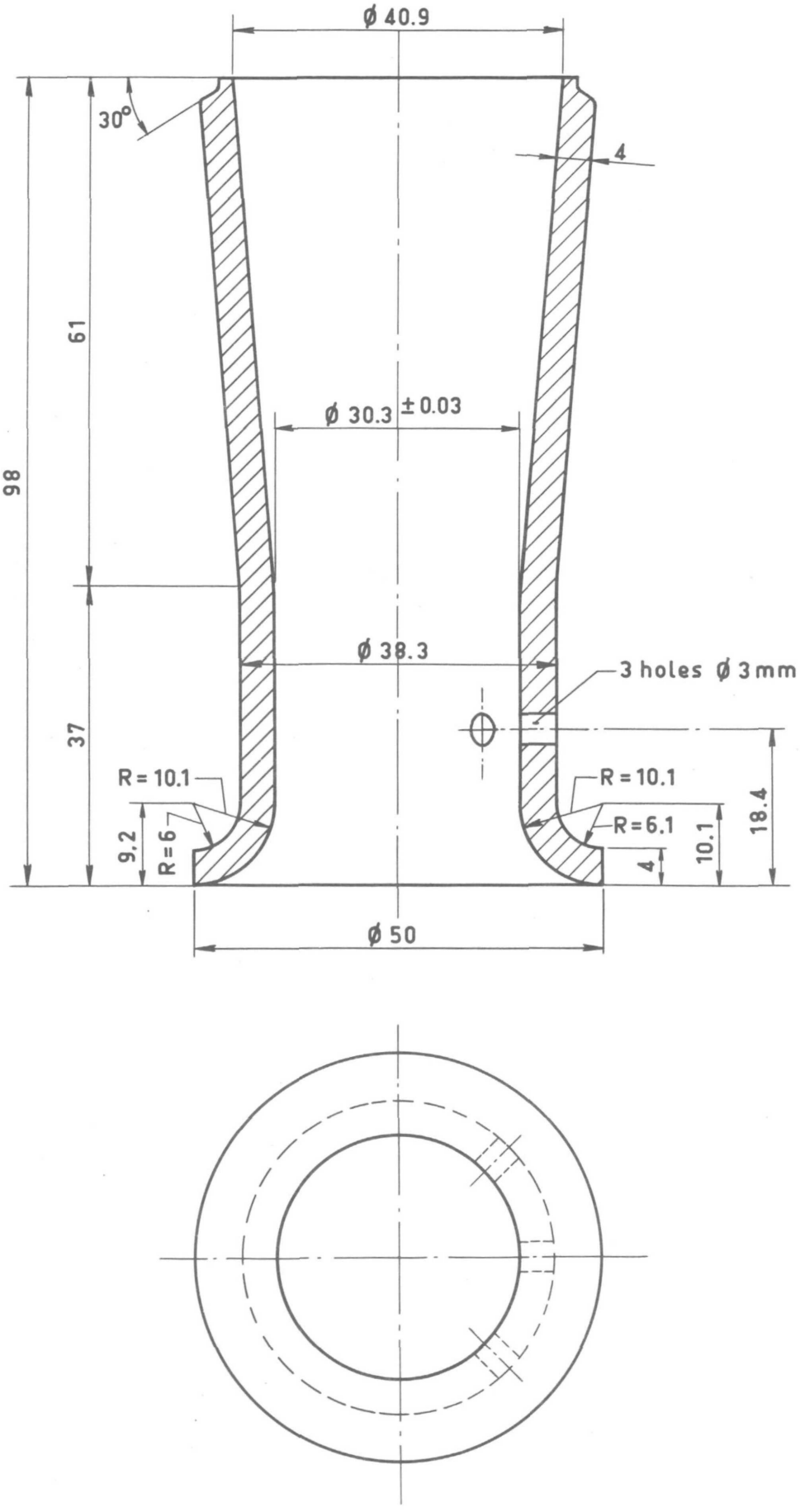

FIGURE 2.2-3.

The venturi as applied in the experiments.

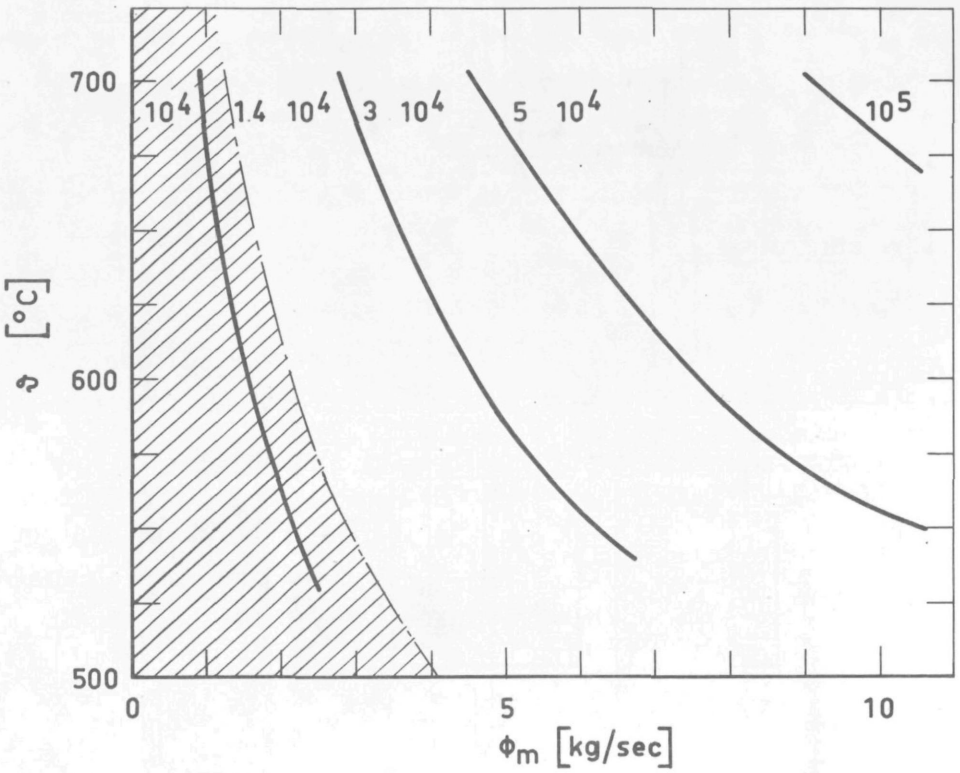

FIGURE 2.2-4.

The Re-number in the venturi as a function of mass flow rate and temperature (in the non-shaded area the accuracy of equation (2.1-1) is better than 1.2%).

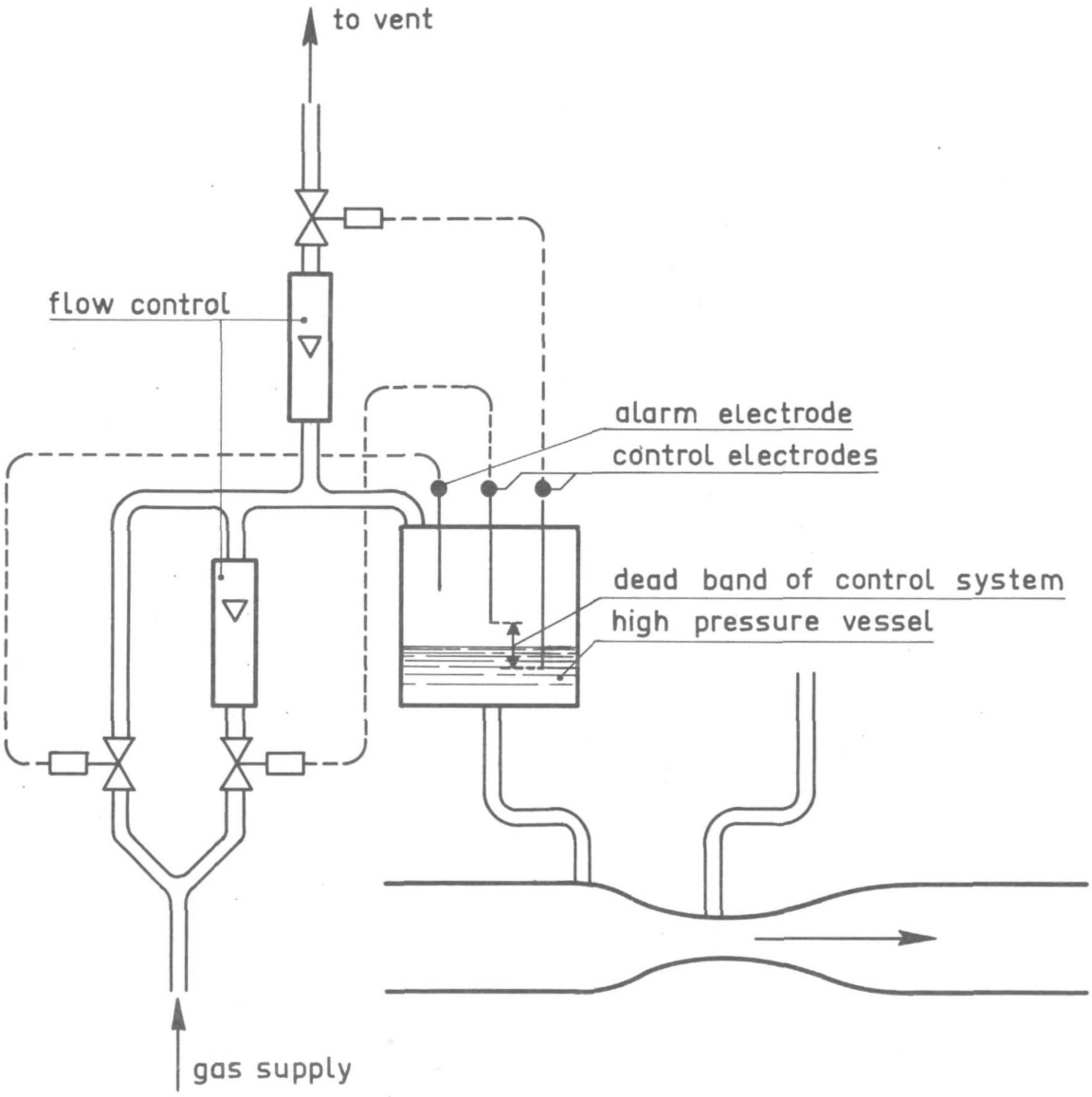

FIGURE 2.2-5.

Diagram of the two-electrode control system.

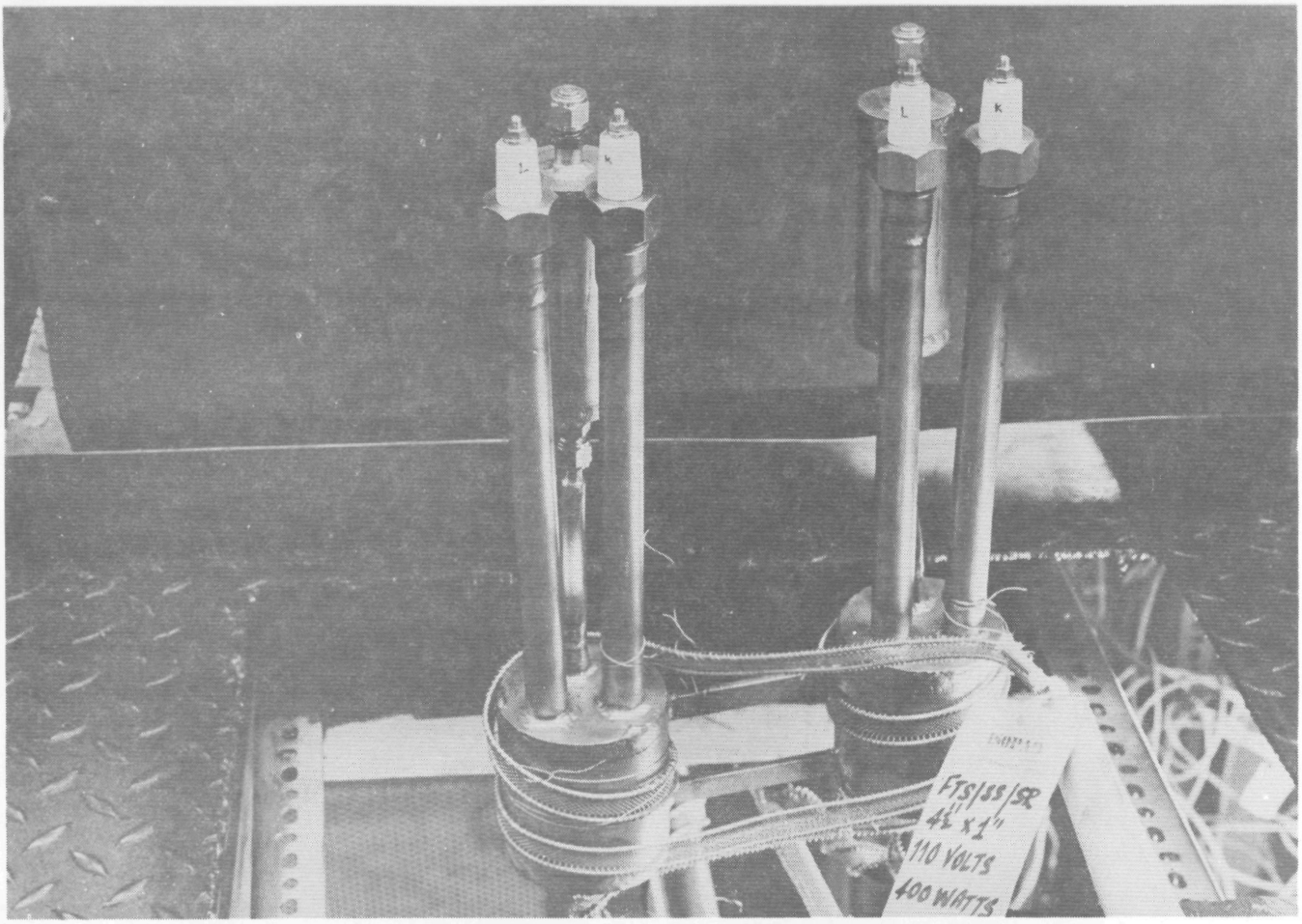

FIGURE 2.2-6.

Photograph of the two venturi vessels showing the ceramic insulators for the electrodes.

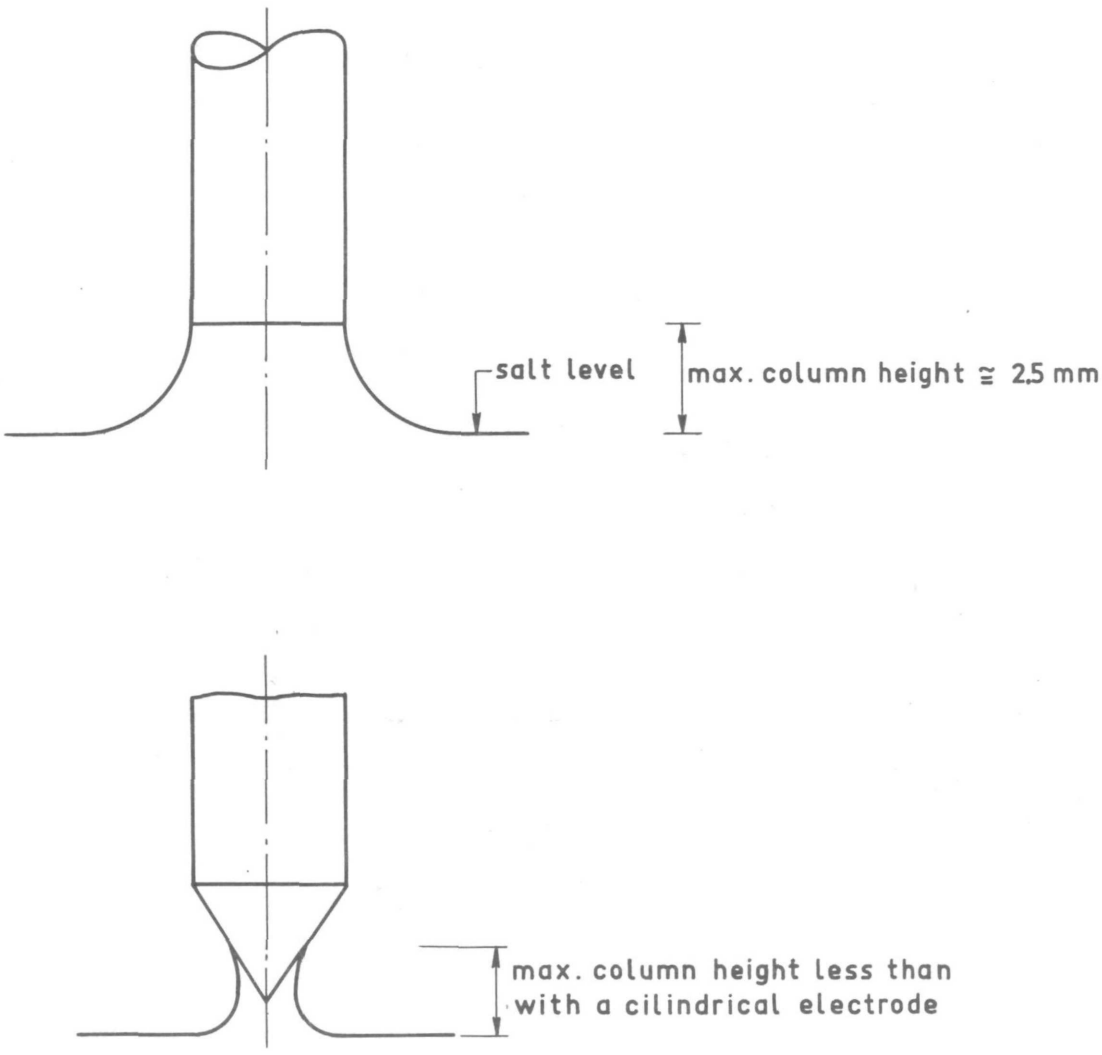

FIGURE 2.2-7.

Salt column under an electrode dipped in the fluid and raised subsequently.

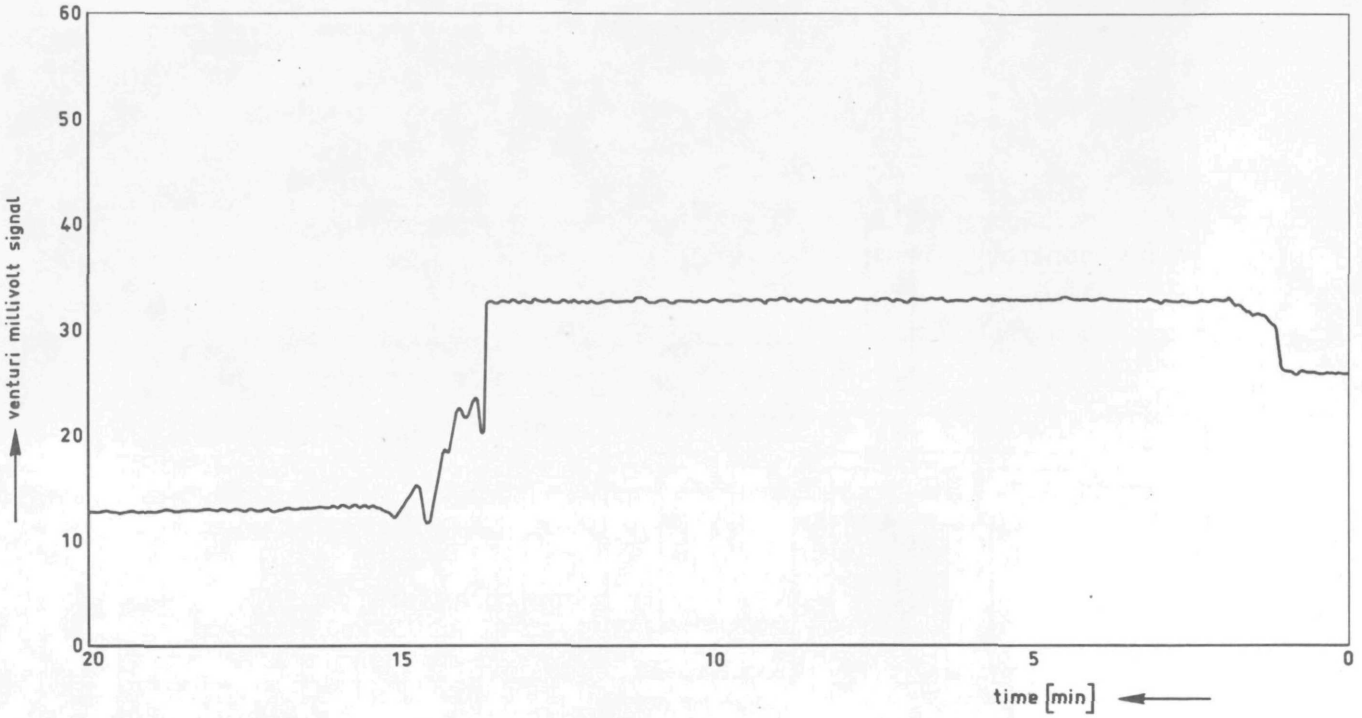

FIGURE 2.2-8.

Dynamic response of the venturi reading to a stepwise change in FLiNaK flow rate (two electrode control system).

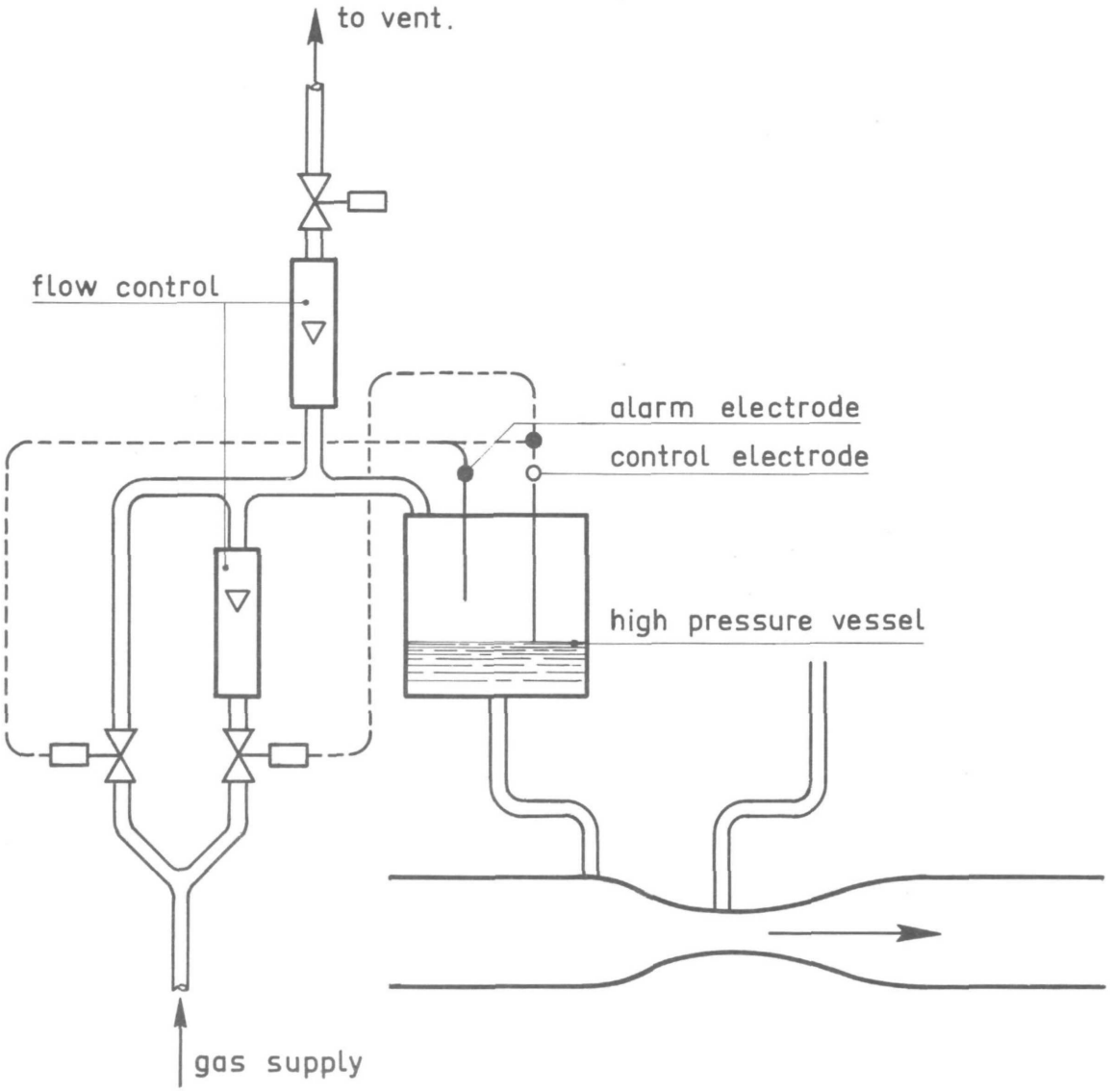

FIGURE 2.2-9.

Diagram of single electrode control sustem.

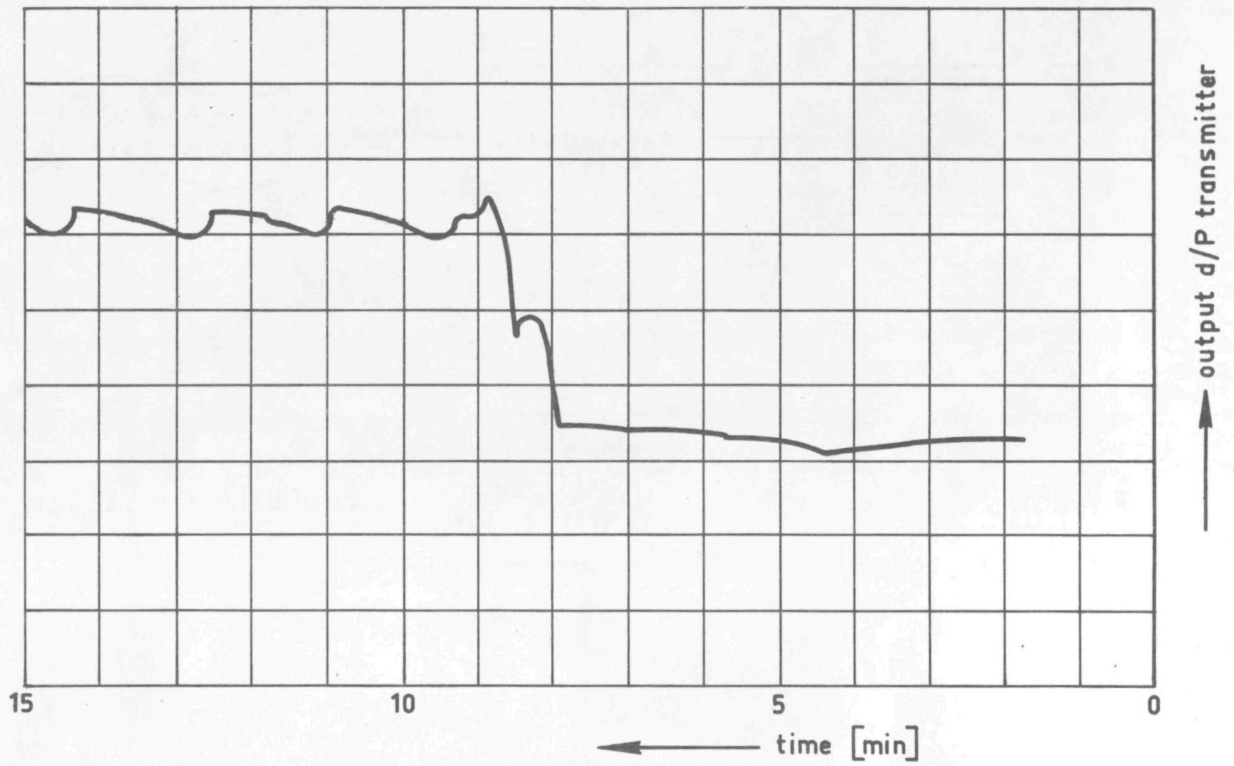

FIGURE 2.2-10.

Reading of the venturi flow meter with single electrode control system.

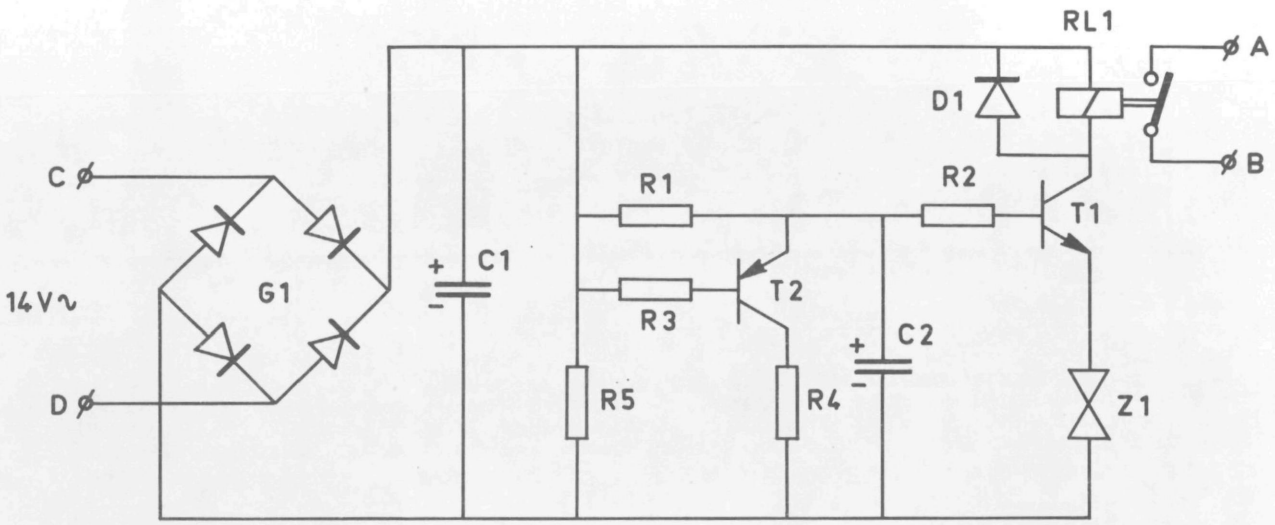

FIGURE 2.2-11.

Delayed action relais applied to avoid rattling of the magnetic valves.

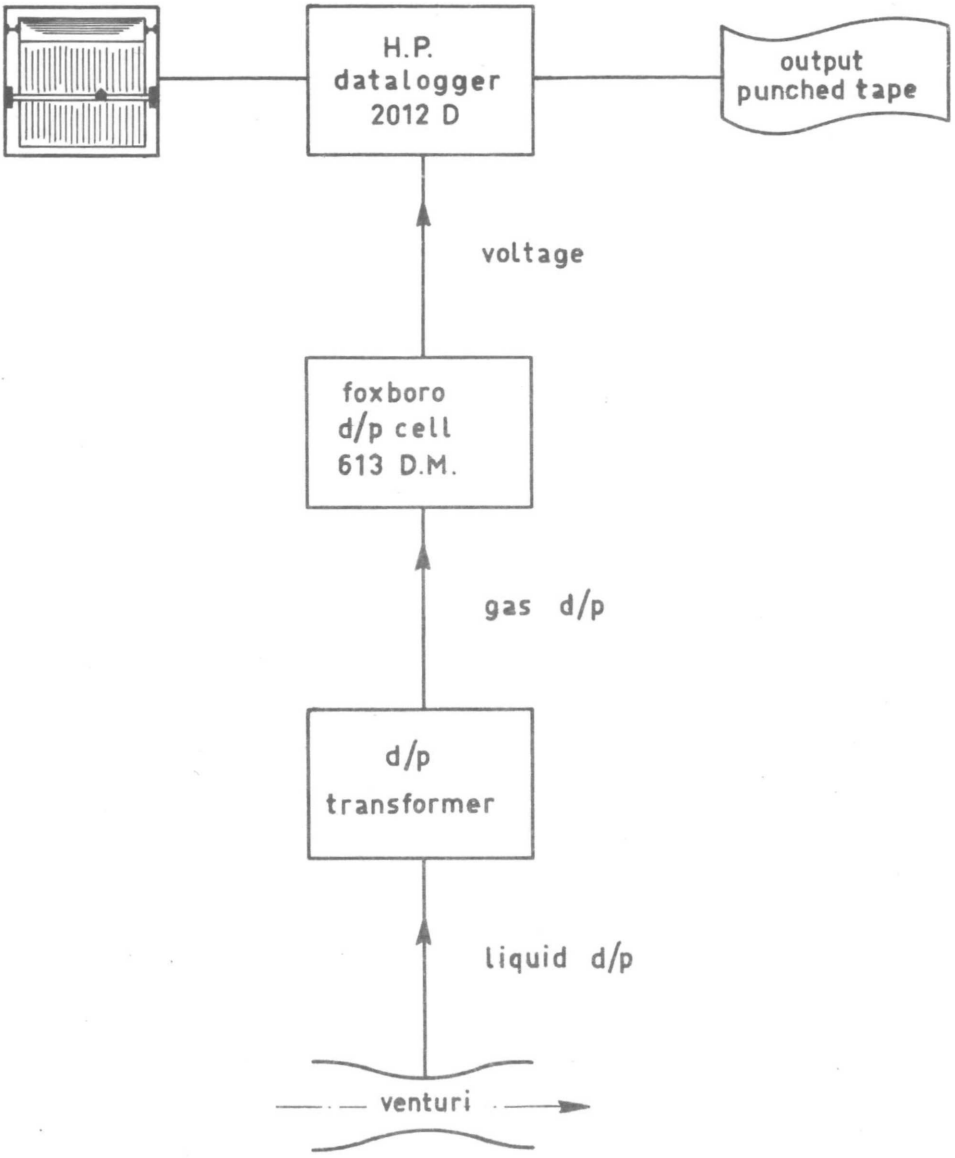

FIGURE 2.2-12.

Instrumentation of the venturi flow meter.

composition	mol %	NaF 11.5 KF 42.0 LiF 46.5	acc.	ref.
composition	weight %	NaF 11.70 KF 59.09 LiF 29.21		2.2-5
melting point	^0C	454		
Liquid state density (T = temp. in ^0C)	kg/m^3	2530 - 0.73 T	10%	
specific heat	kJ/kg ^0C	1.89	5%	
thermal conductivity	W/m ^0C	1.30	?	APP. 2A
kinematic viscosity	m^2/s	at 500 ^0C $3.90\ 10^{-6}$ at 600 ^0C $2.63\ 10^{-6}$ at 700 ^0C $1.95\ 10^{-6}$ at 800 ^0C $1.23\ 10^{-6}$	2%	2.2-6

FIGURE 2.2-13.

Physical properties of FLiNaK.

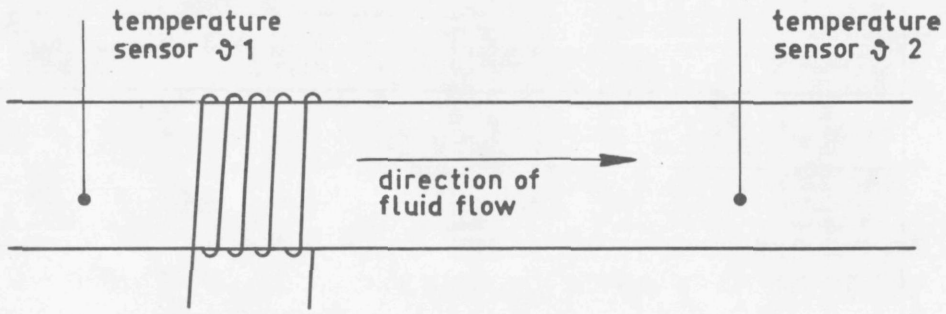

FIGURE 2.3-1.

Principle of the first type of thermal flow meters.

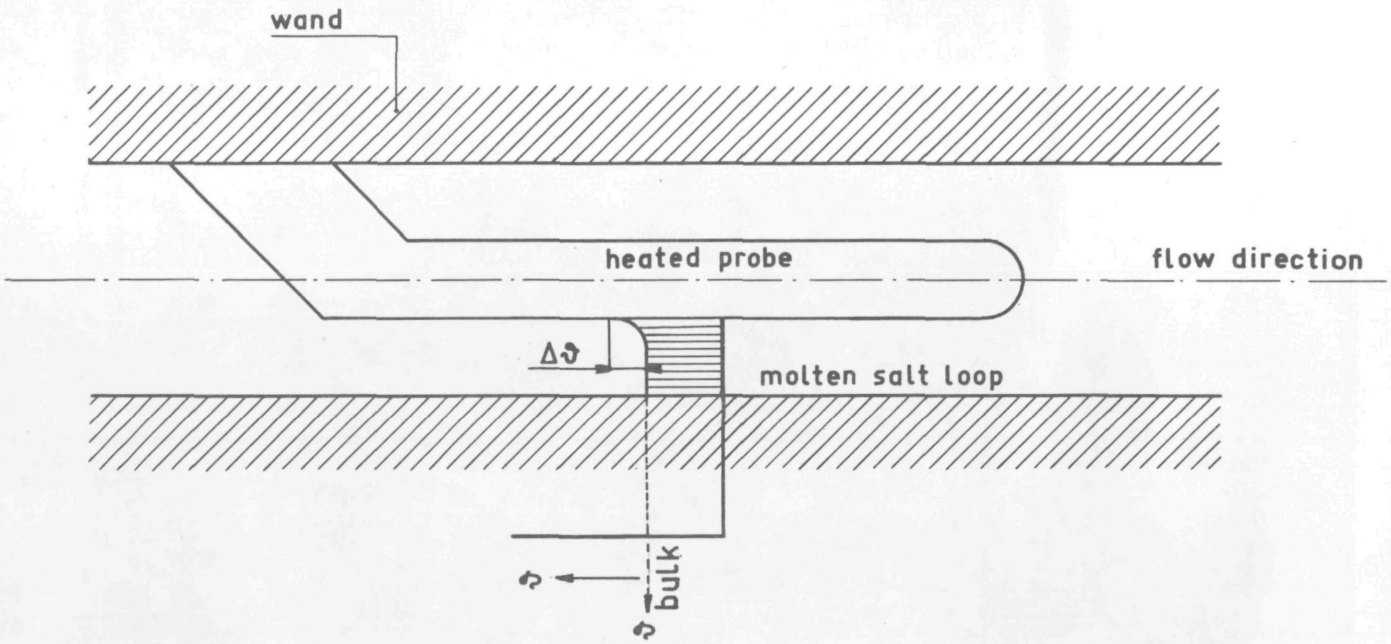

FIGURE 2.3-2.

Principle of the second type of thermal flow meters.

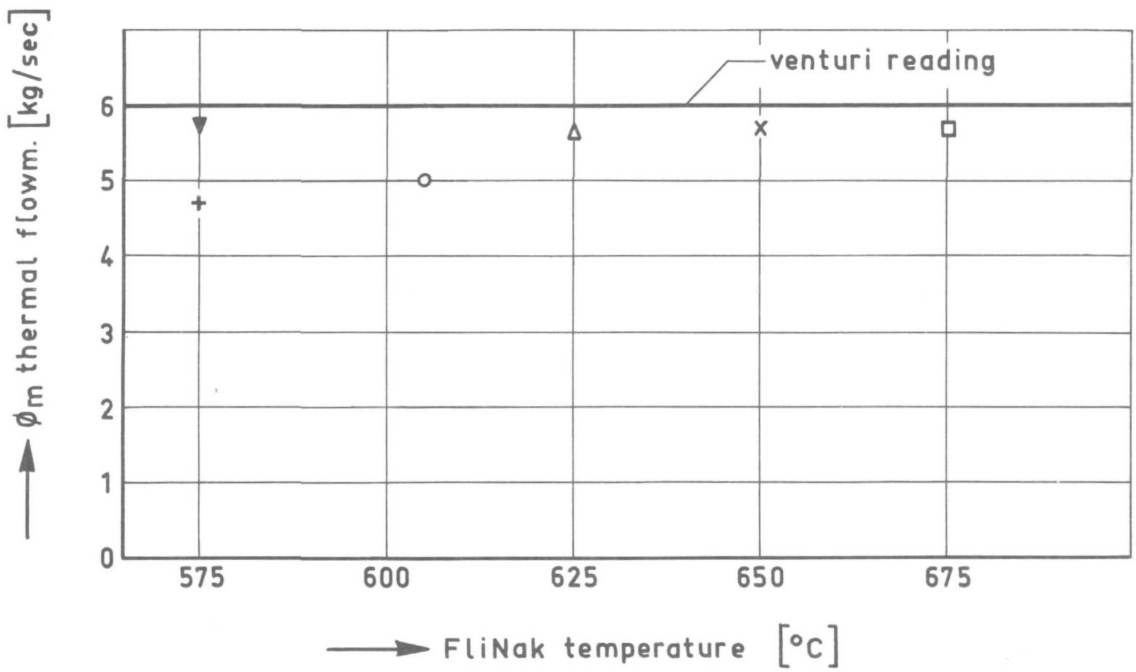

FIGURE 2.3-3.

Temperature dependence of thermal flow meter output (obtained at a corresponding venturi reading of 6 kg/s).

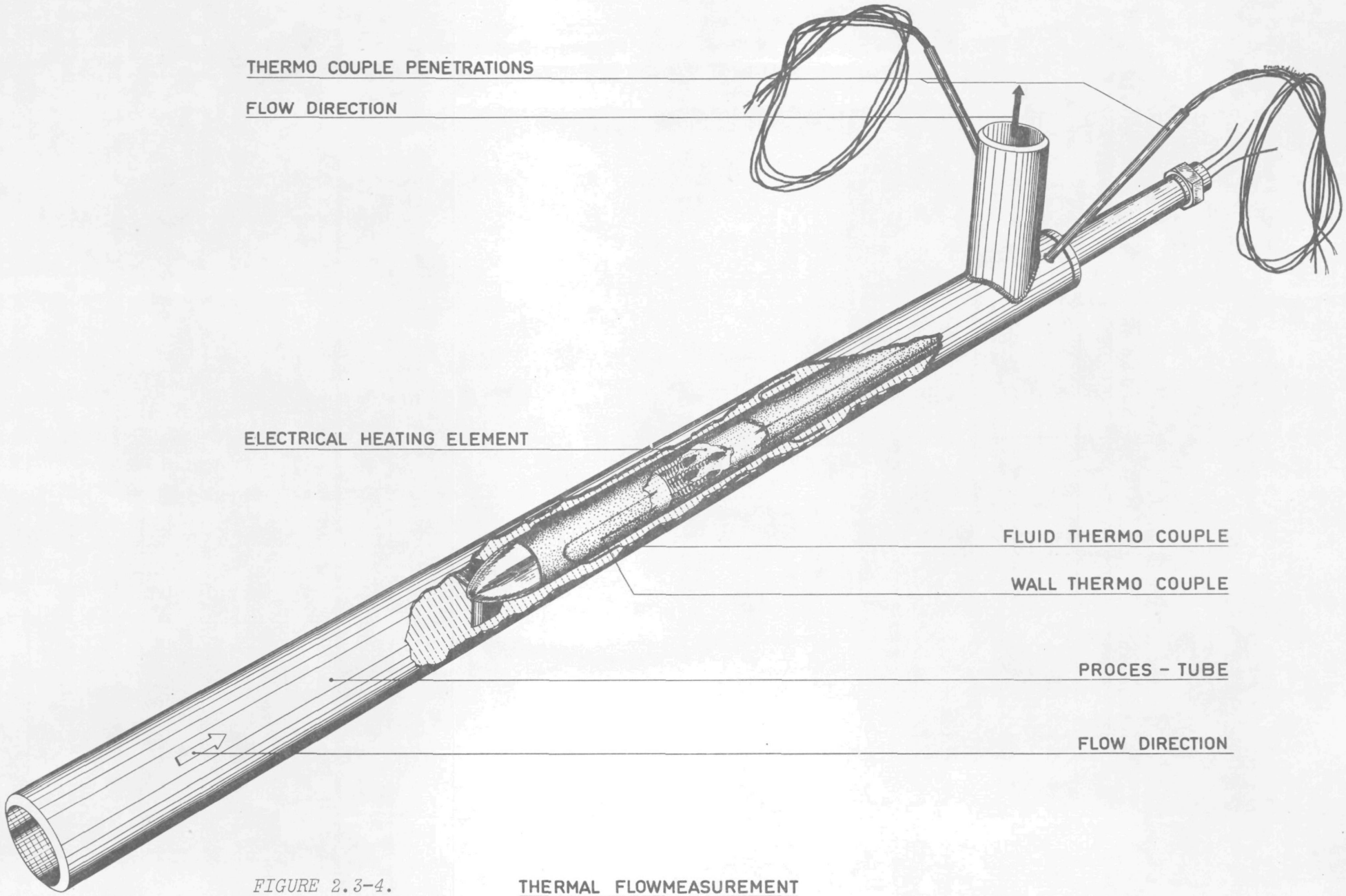

FIGURE 2.3-4.
Thermal flow meter.

THERMAL FLOWMEASUREMENT

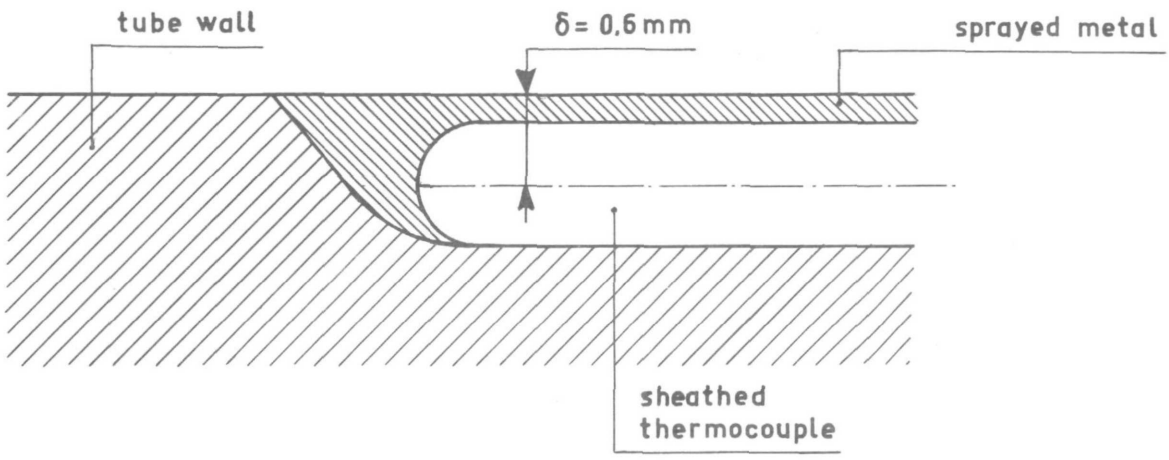

FIGURE 2.3-5.

Location of thermo-couples in the probe wall.

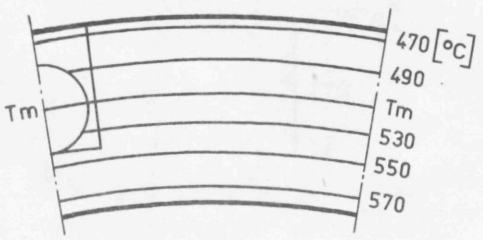

Average surface heat flux	300 Watt / cm^2
Ni-braze thermal conductivity	λ equal to that of Incoloy 800
BN electrical insulation	λ_{BN} = 0,24 J / (m.K.s)
BN t/c insulation	λ_{BN} = 0,24 J / (m.K.s)
t/c contact heat transfer contact heat transfer between electrical	$(\alpha_K)_{BN} = 20 * 10^4$ (m^2.K.s)
insulation and electrode or sheath	$(\alpha_K)_{BN} = 25 * 10^4$ (m^2.K.s)
minimum clearance of t/c in slot	0,01 mm

FIGURE 2.3-6.

Temperature field using Ni-braze for surface embedded thermocouples. [2.3-2.]

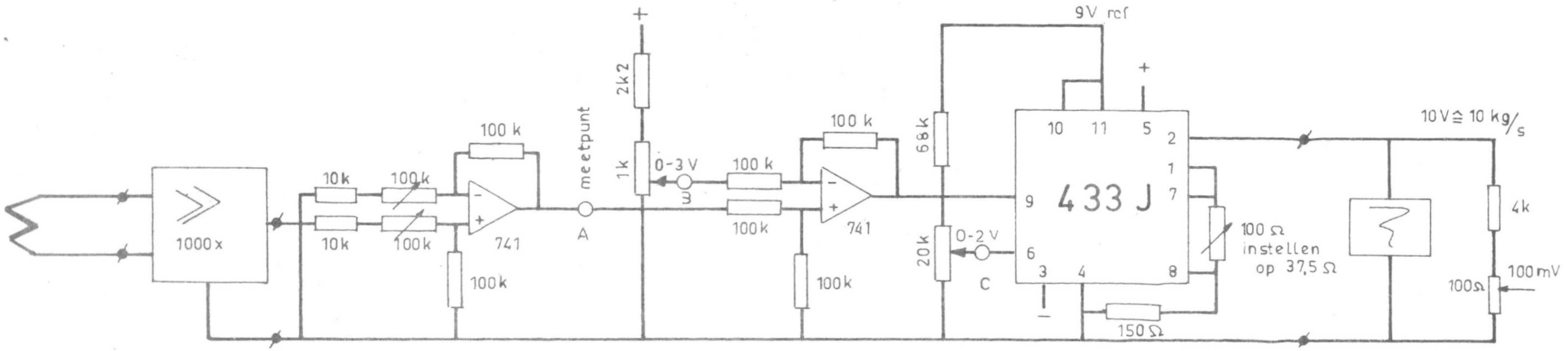

VOEDINGSSPANNING	+15 V −15 V
UITGANGSSPANNING	0 10 V
WEERSTANDEN	5%-¼ W
POTMETERS	20%

MEETGEDEELTE THERMISCHE FLOWMETER III

FIGURE 2.3-7.

Design of an electronic device for linearization of the reading of the thermal flow-meter.

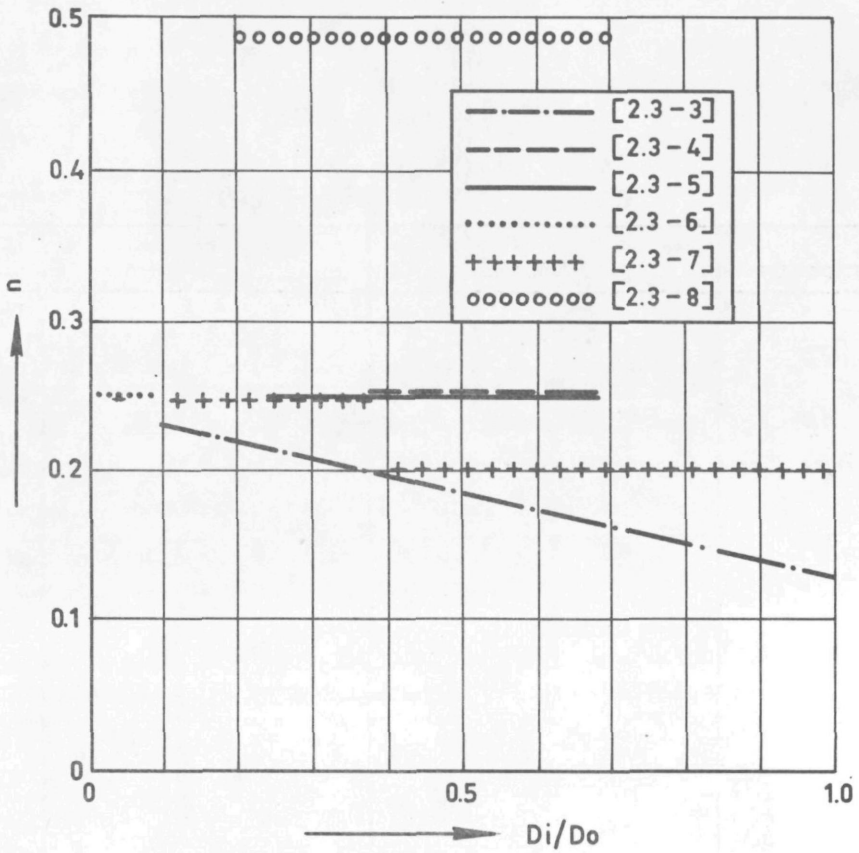

FIGURE 2.3-8.

Literature survey of values of the exponent n of the annular flow correction on the Dittus-Boelter heat transfer correlation.

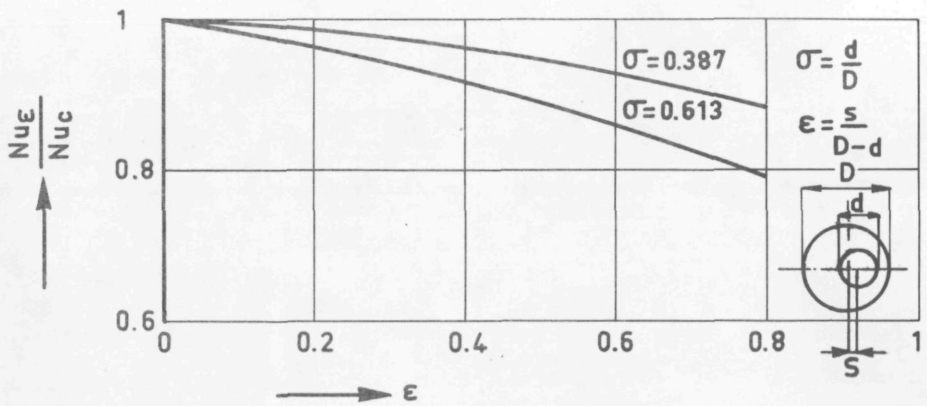

FIGURE 2.3-9.

Effect of the eccentricity of an annular channel on the average Nusselt number according to LEE and BARROW [2.3-8].

Property	Value		Error
A_c	$0.967\ 10^{-3}$	$[m^2]$	5%
ϕ_{w_r}	$\cong 3.0\ 10^{3}$	$[J\ s^{-1}]$	2%
A_h	0.0235	$[m^2]$	0.5%
λ_F		$[J\ m^{-1}\ {}^0C^{-1}]$	
ν_F	cf. figure 2.213	$[m^2\ s^{-1}]$	10%
ρ_F		$[kg\ m^{-3}]$	5%
C_F		$[J\ kg^{-1}\ {}^0C^{-1}]$	10%
D_i	$21.0\ 10^{-3}$	[mm]	0.5%
D_o	$40.9\ 10^{-3}$	[mm]	0.25%
$\Delta\theta_m$	10 - 25	$[{}^0C]$	2%
C_θ		$[m^2\ {}^0C\ W^{-1}]$	10%

FIGURE 2.3-10.

List of properties appearing in equation (2.3-5) and their inaccuracies.

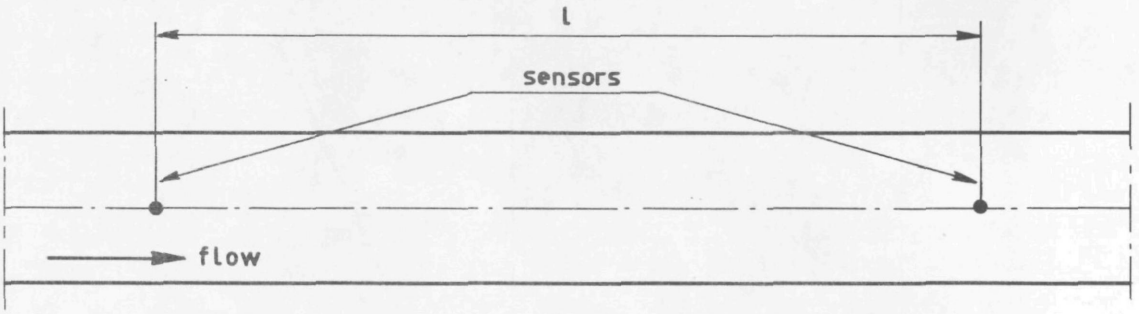

FIGURE 2.4-1.

Principle of correlation flow measurement.

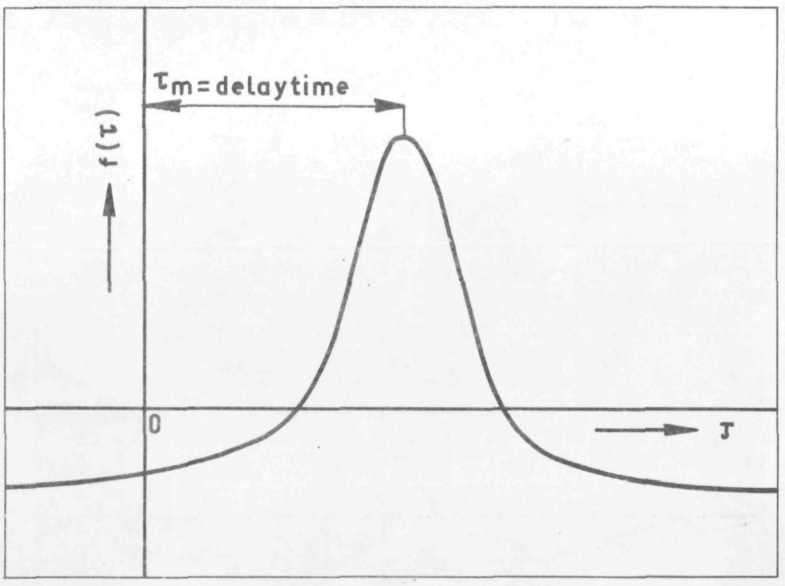

FIGURE 2.4.2.

Example of correlation function to two signals, one of which is delayed by τ_m seconds.

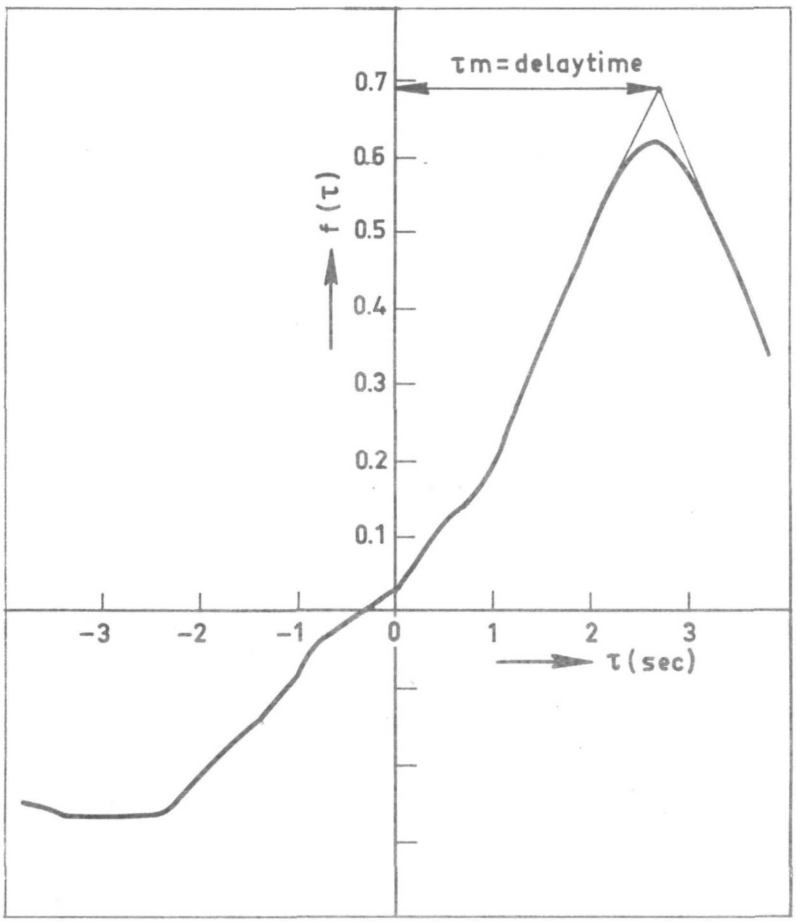

FIGURE 2.4-3.

Example of a correlation function of two sensors at a distance of 3200 mm.

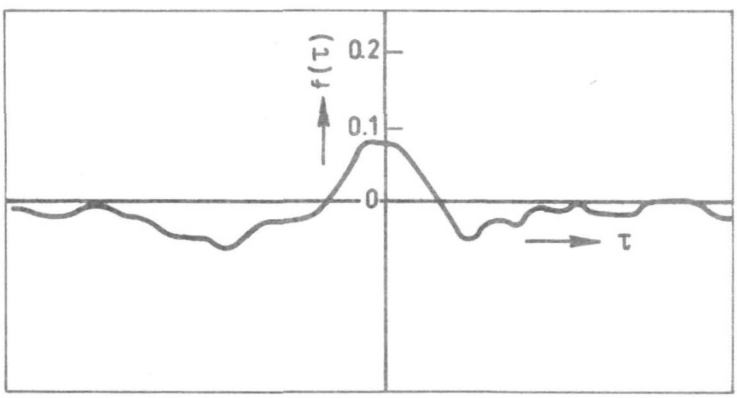

FIGURE 2.4-4.

Example of a correlation function of two sensors at a distance of 200 mm.

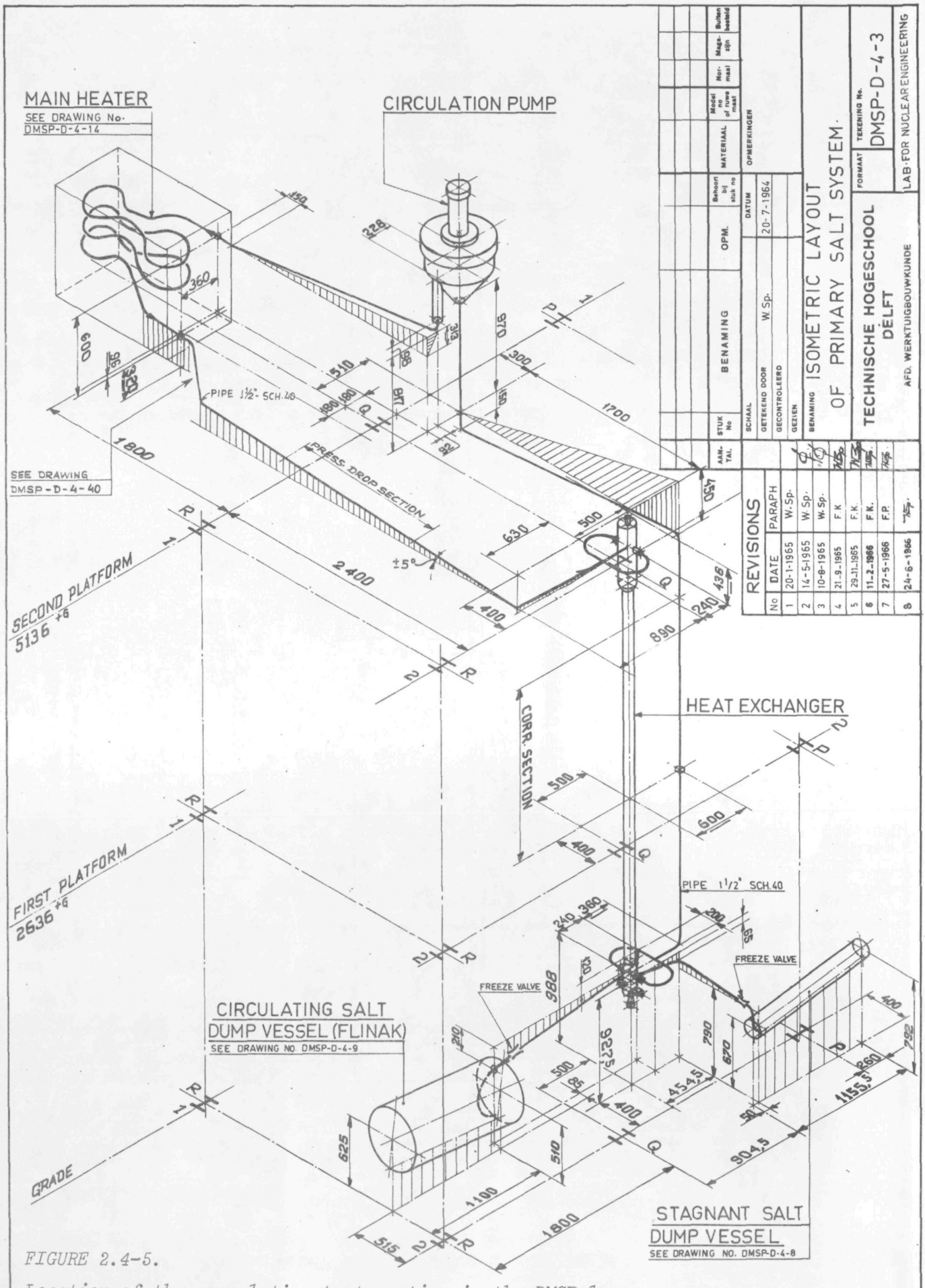

FIGURE 2.4-5.

Location of the correlation test section in the DMSP loop.

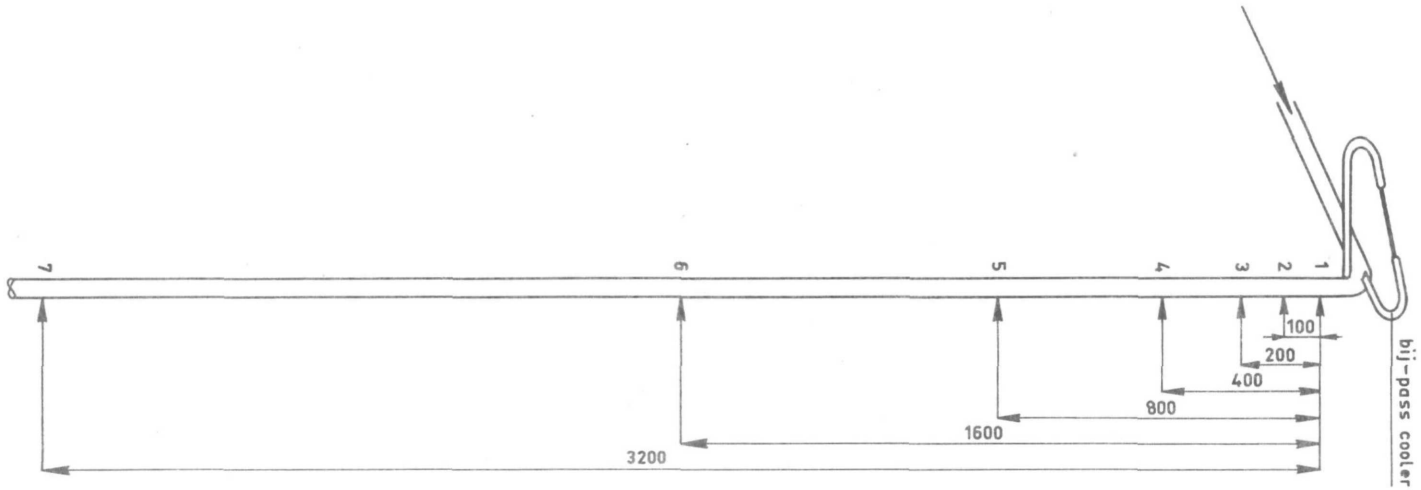

FIGURE 2.4-6.

Correlation section showing position of sensors.

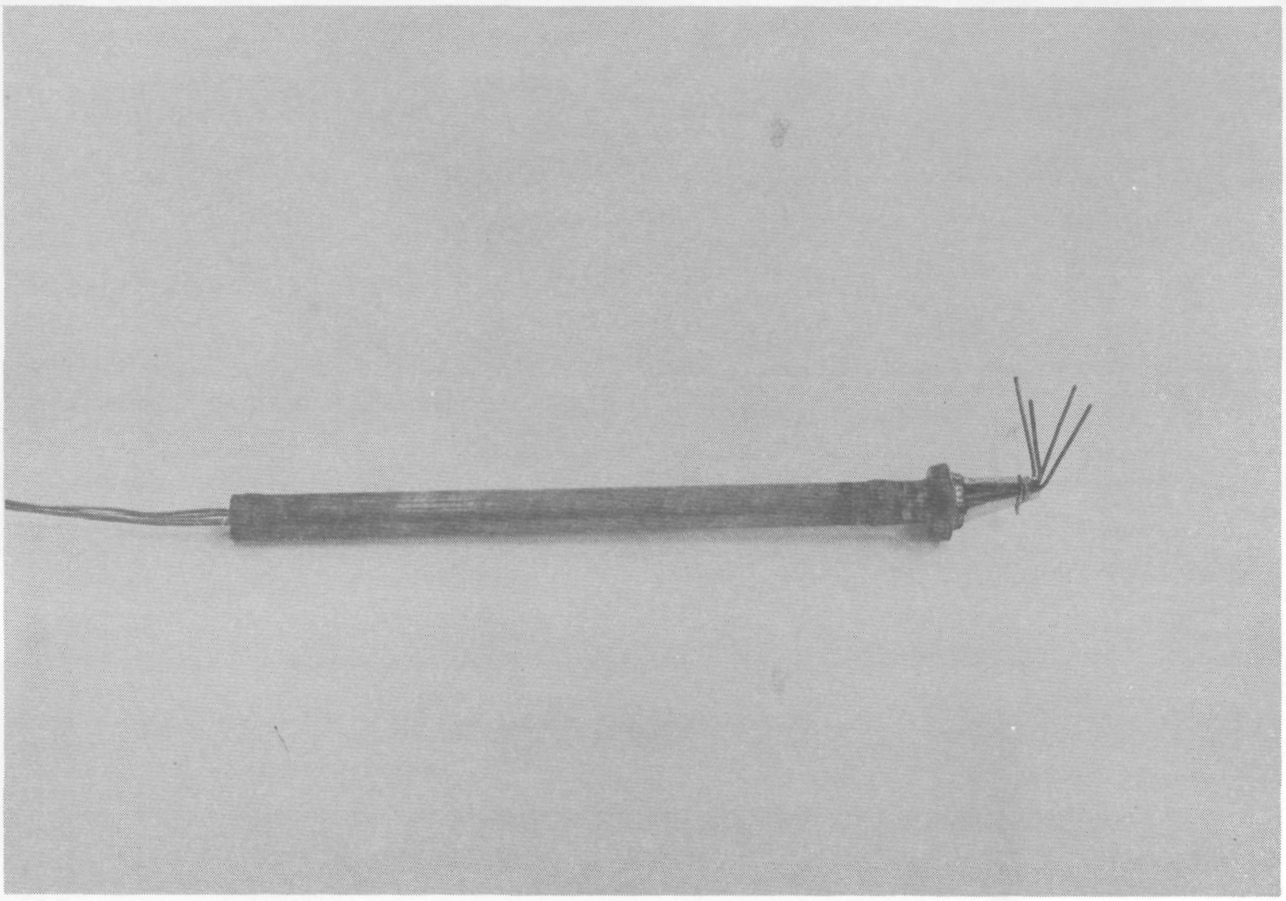

FIGURE 2.4-7.

Thermo-couple sensor and wall penetration.

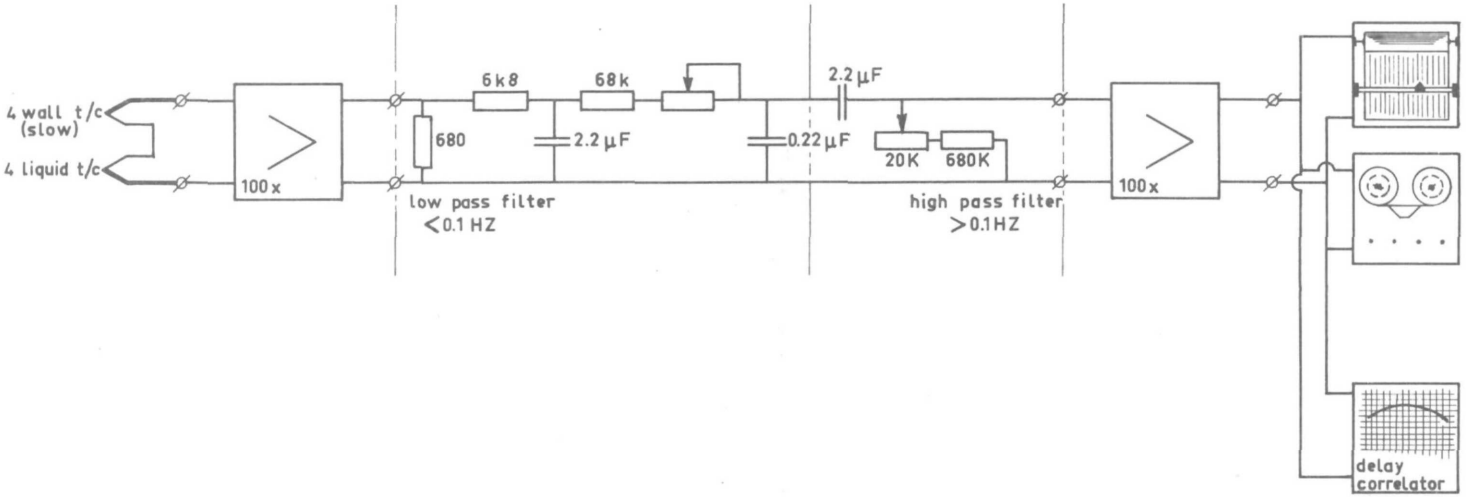

FIGURE 2.4-8.

Diagram of measuring equipment (per sensor).

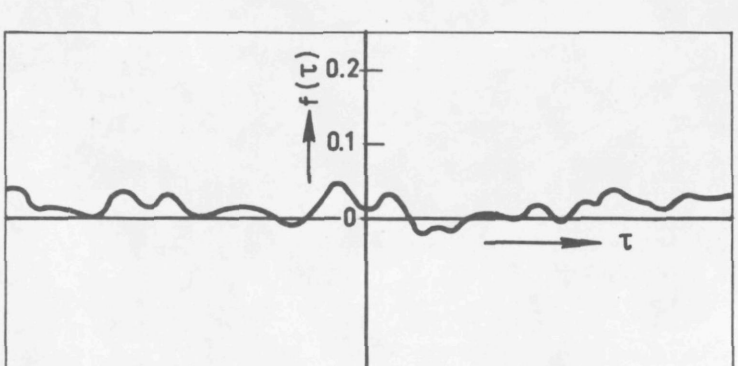

FIGURE 2.4-9.

Correlation function for natural noise signals (sensor spacing 100 mm apart).

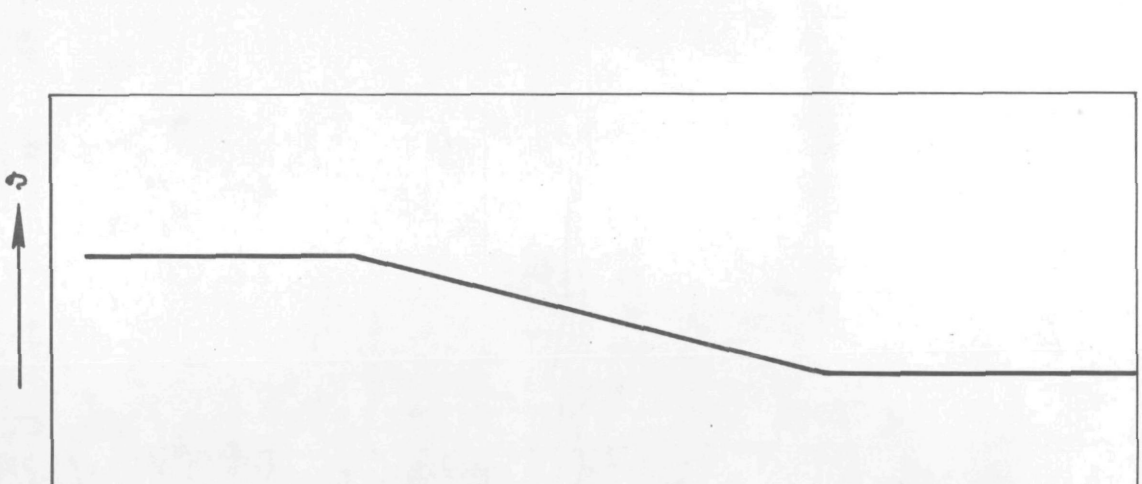

FIGURE 2.4-10.

Temperature profile in the primary loop as a result of a stepwise increase of main heater power.

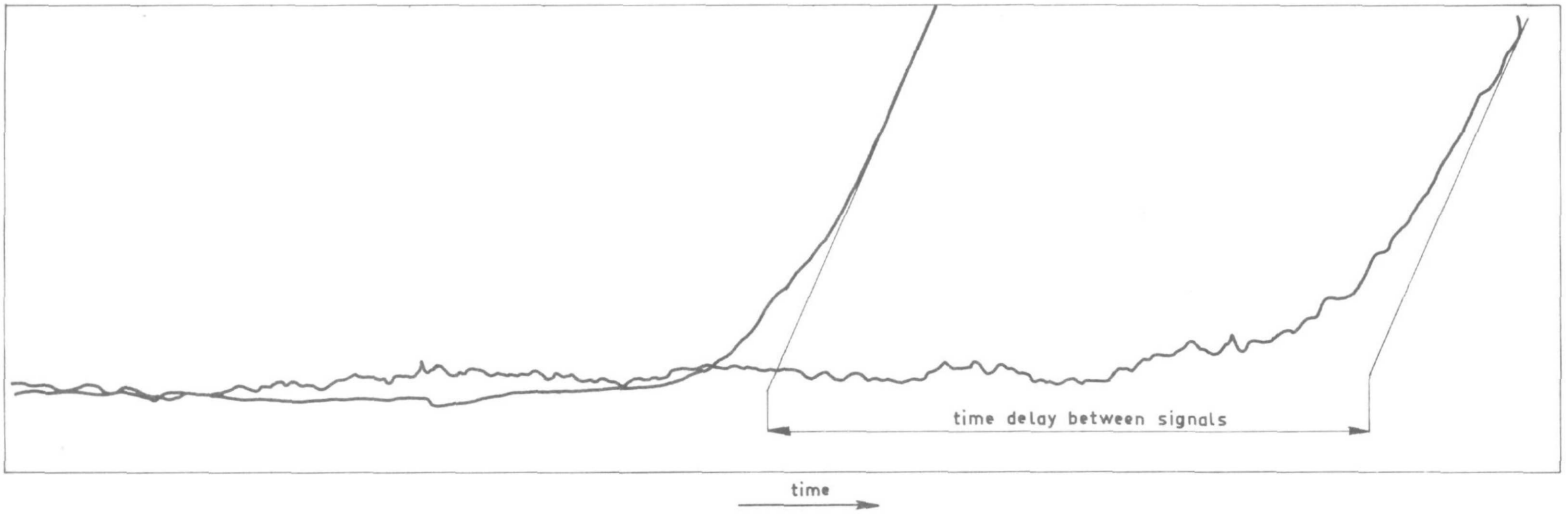

FIGURE 2.4-11.

Signals from the two sensors 3200 mm apart after a stepwise increase in main heater power.

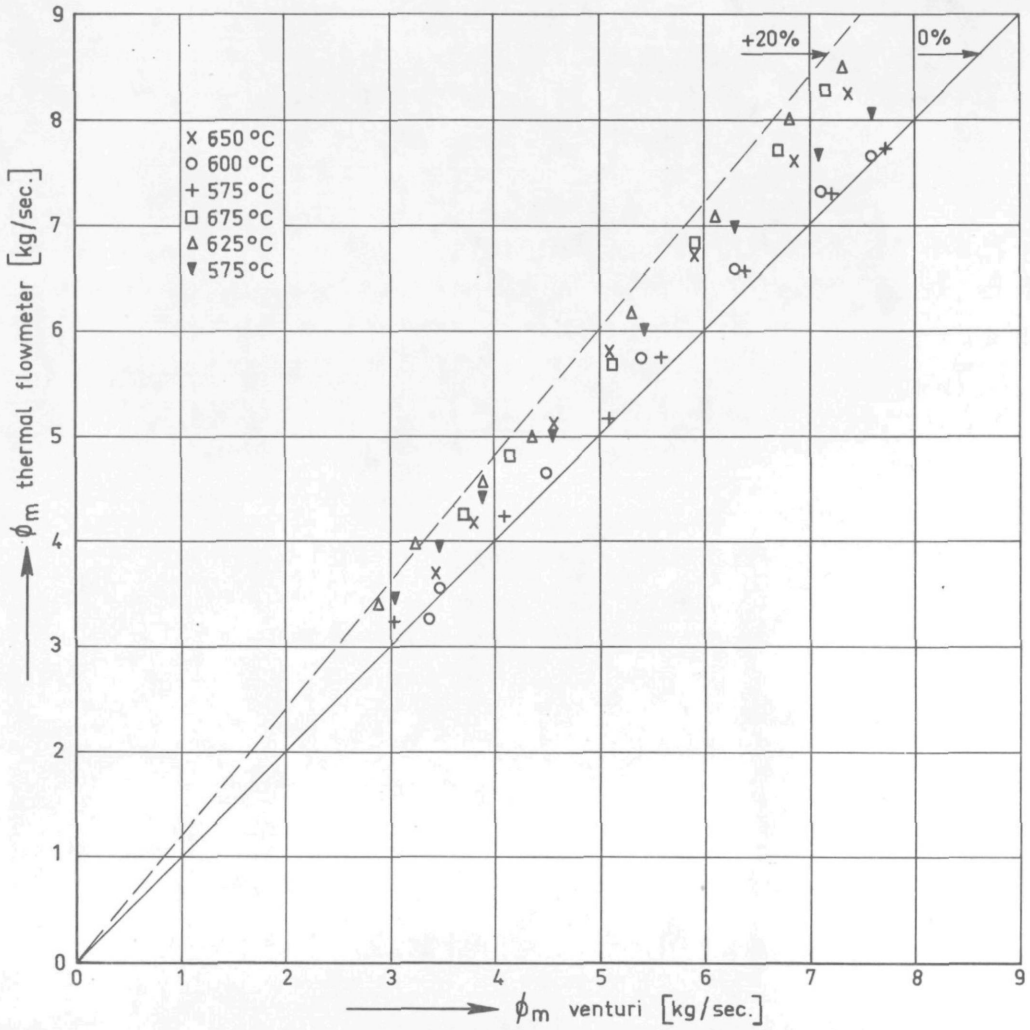

FIGURE 2.6-1.

Results of thermal flow measurements.

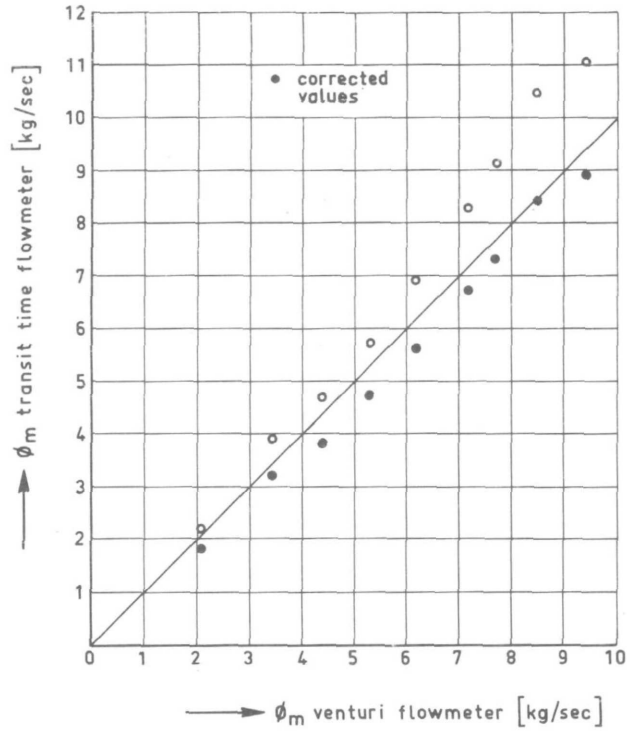

FIGURE 2.6-2.

Results of the thermal shock "correlation" flow measurement at a FLiNaK temperature of 575 ^0C.

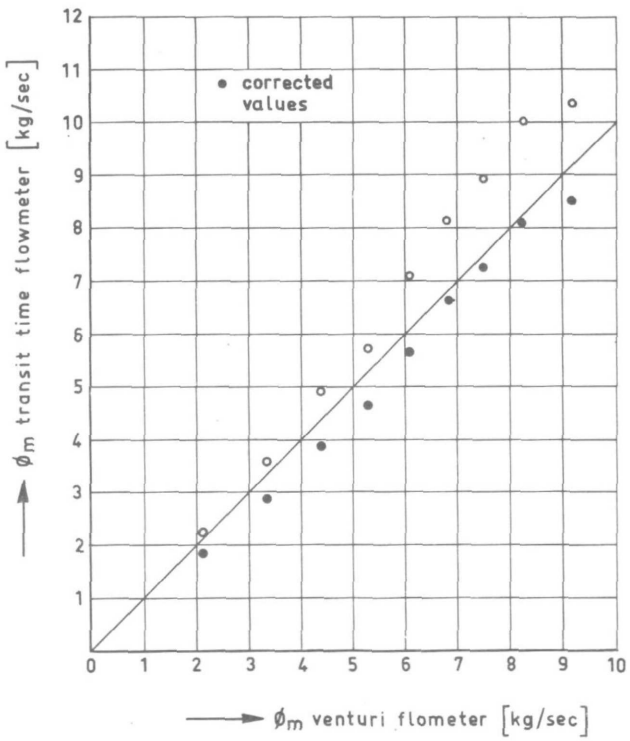

FIGURE 2.6-3.

Results of the thermal shock "correlation" flow measurements at a temperature of 625 ^0C.

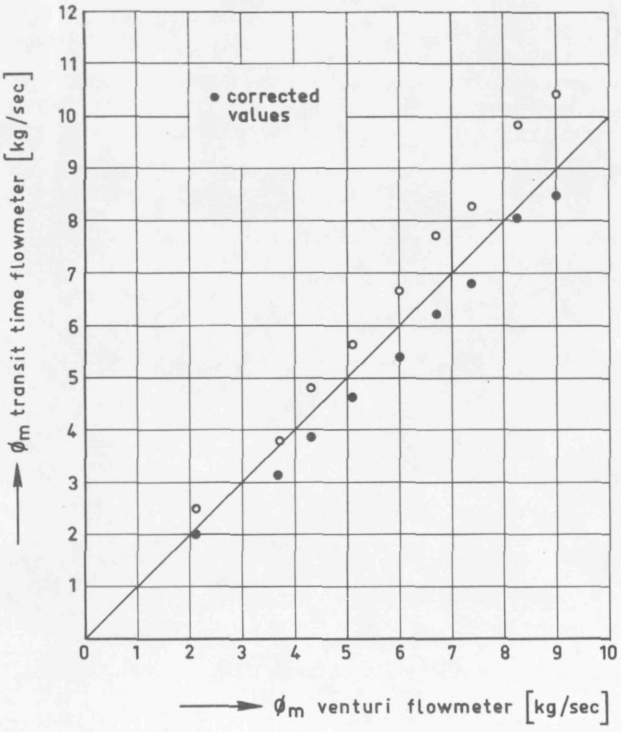

FIGURE 2.6-4.

Results of the thermal shock "correlation" flow measurements at a FLiNaK temperature of 675 ^{0}C.

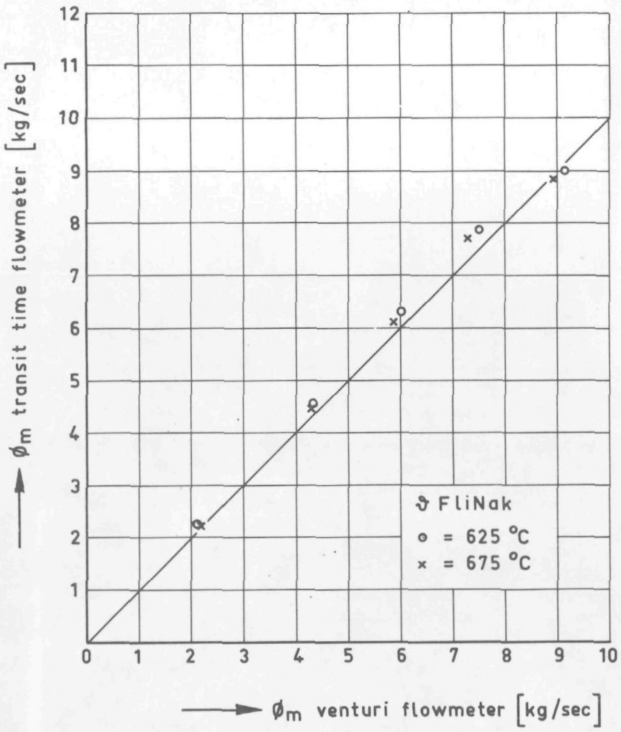

FIGURE 2.6-5.

Results of the "artificial noise" correlation flow measurements.

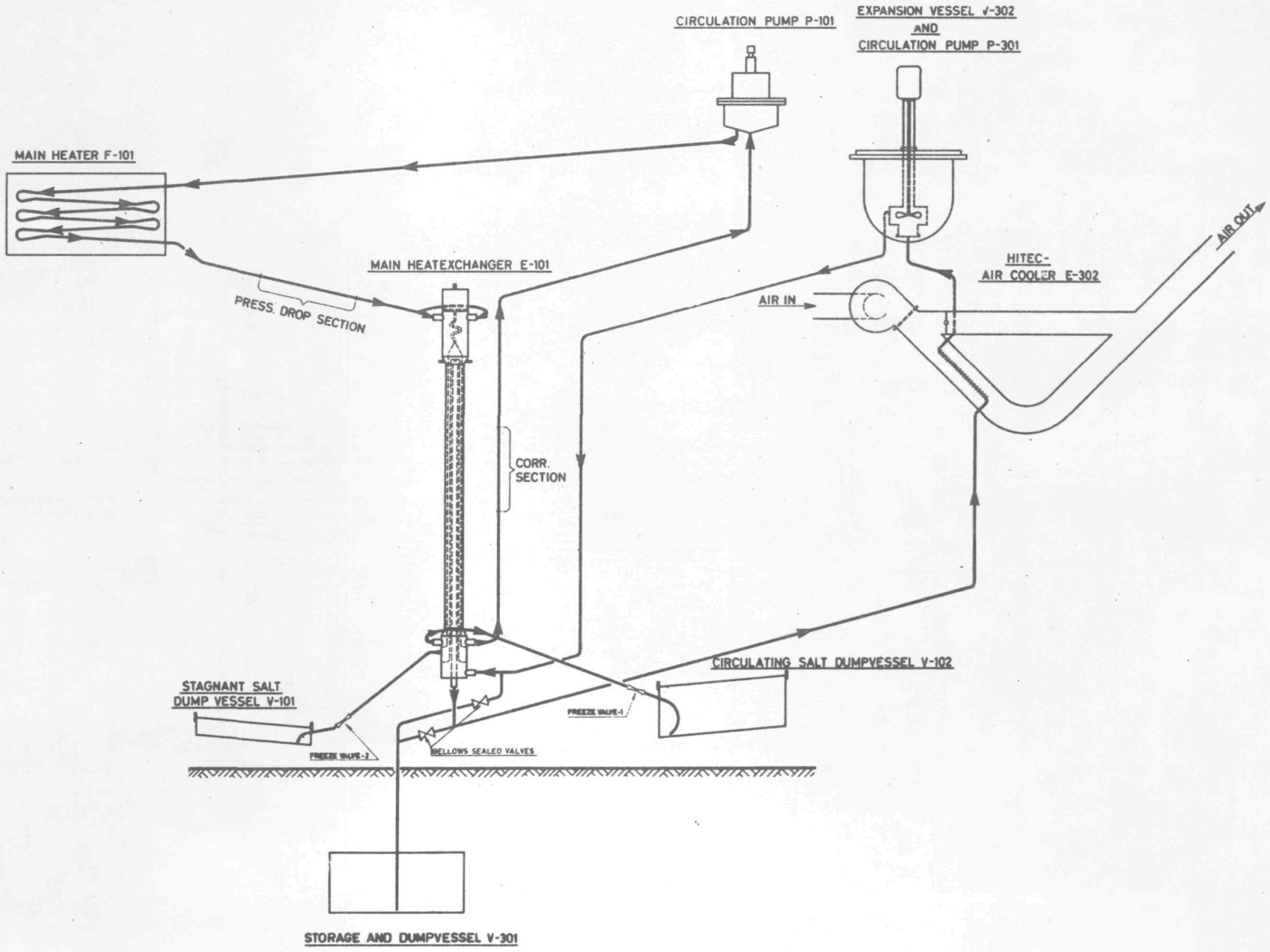

FIGURE 3.2-1.

Flow sheet of the original Delft Molten Salt Project.

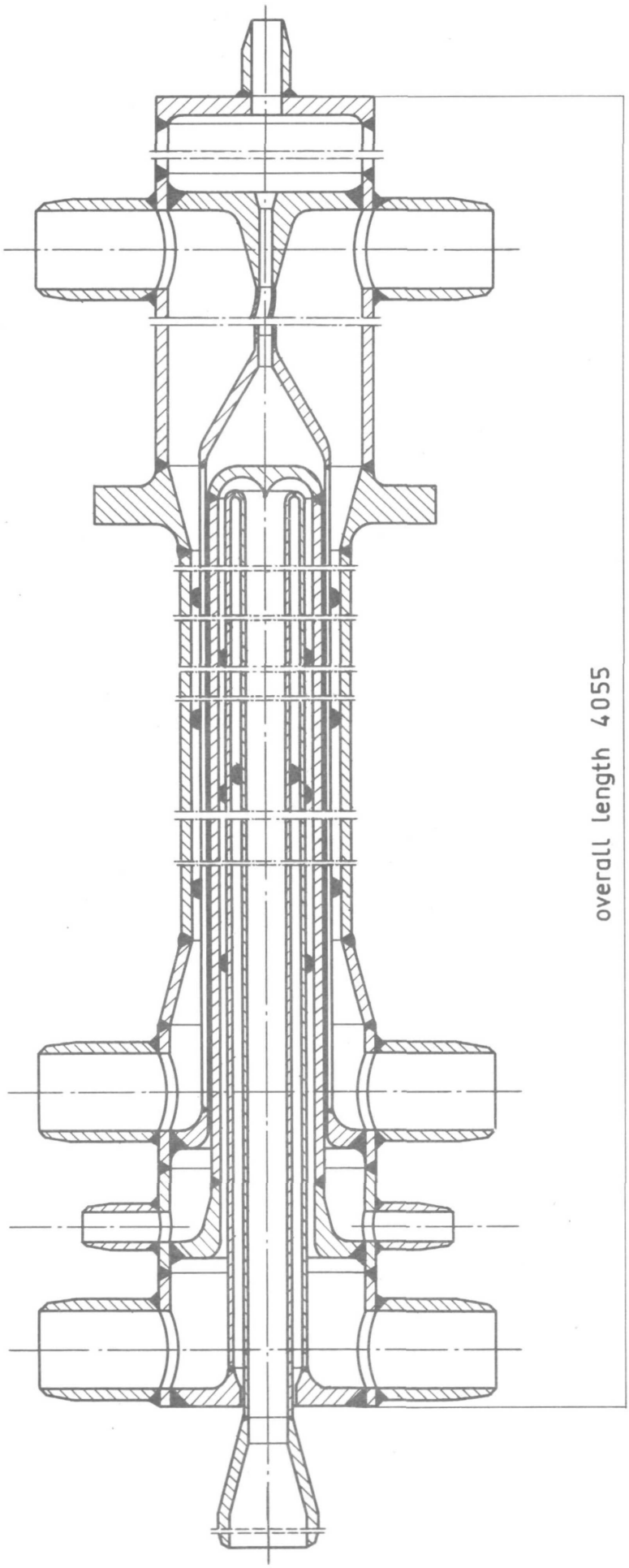

FIGURE 3.2-2.

Cross section of the salt-to-salt heat exchanger.

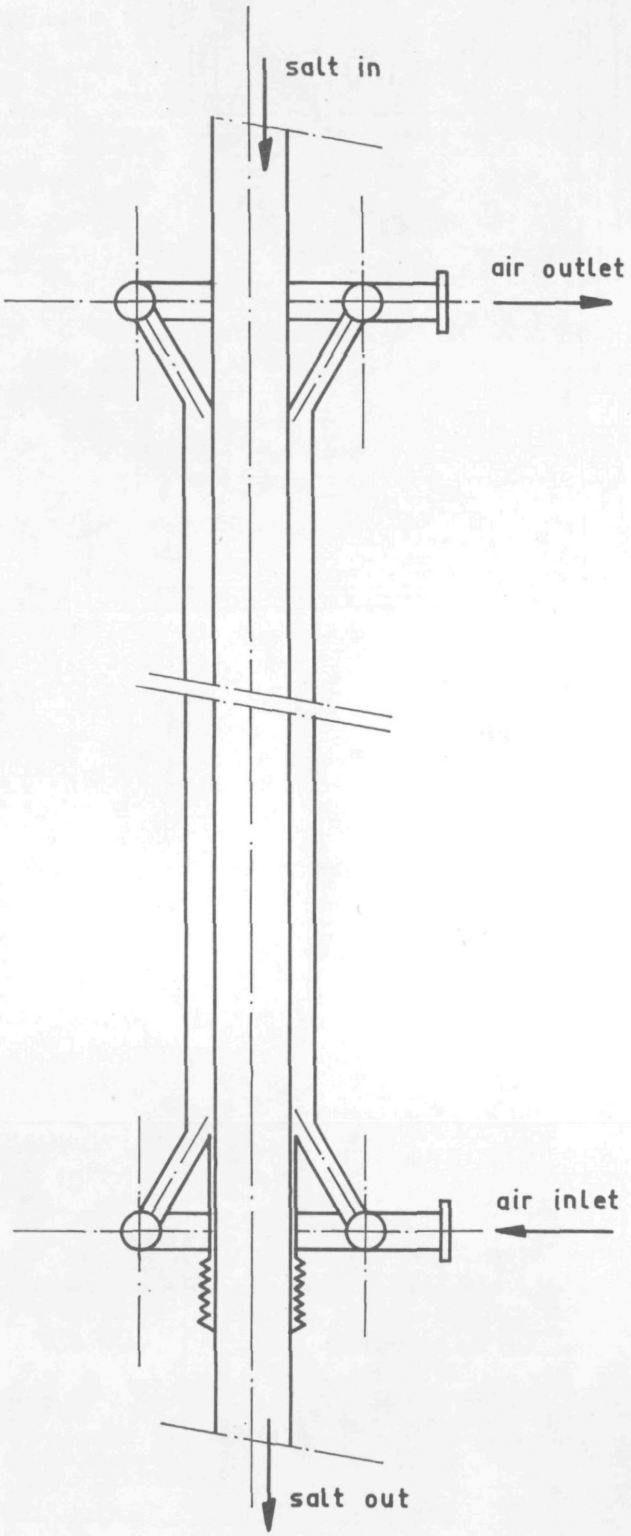

FIGURE 3.2-3.

Basic geometry of the salt-to-air heat exchanger.

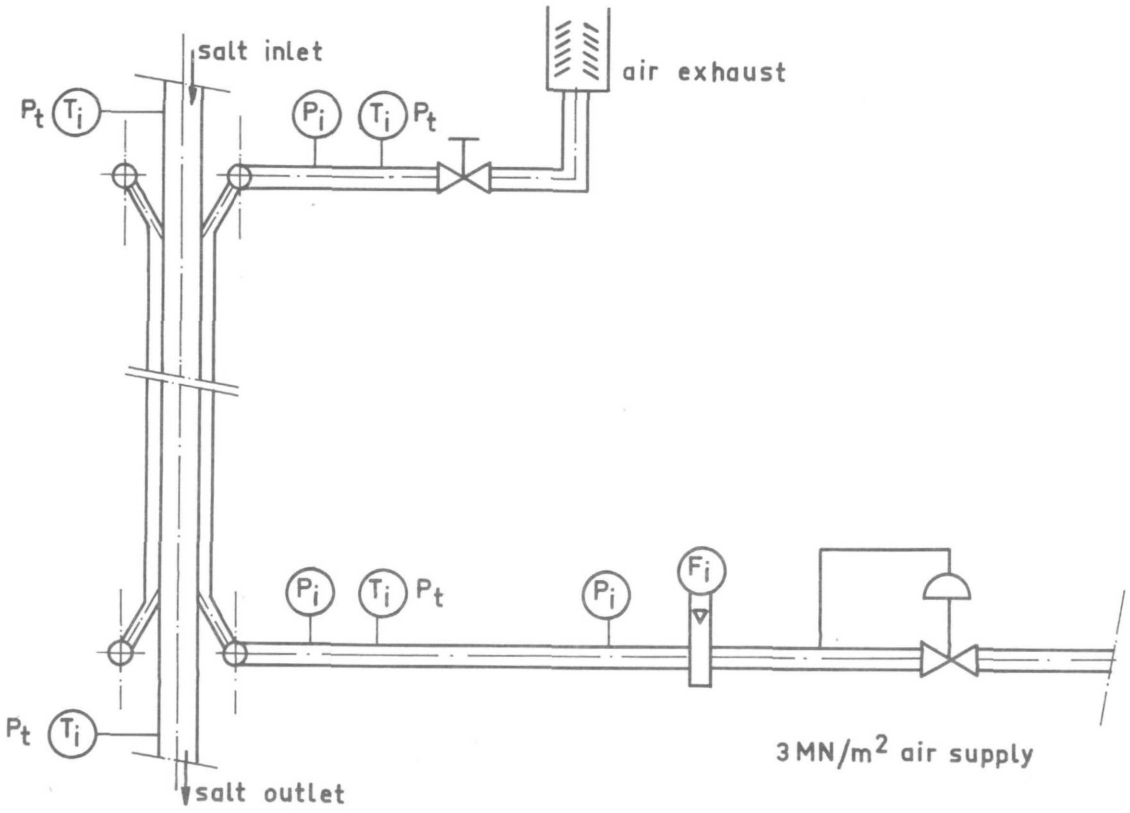

FIGURE 3.2-4.

Flow sheet of the secondary side of the FLiNaK to air heat exchanger test rig.

FLiNaK inlet temperature	575 - 675 ^{0}C
FLiNaK temperature drop	< 5 ^{0}C
FLiNaK mass flow rate	2.3 - 9.5 kg s^{-1}
Air inlet temperature	25 ^{0}C
Air outlet temperature	430 - 630 ^{0}C
Air inlet pressure	0.5 MN m^{-2}
Air pressure drop	0.002 - 0.02 MN m^{-2}
Air mass flow	0.05 - 0.16 kg s^{-1}

FIGURE 3.2-5.

Process conditions of the FLiNaK-to-air heat exchanger.

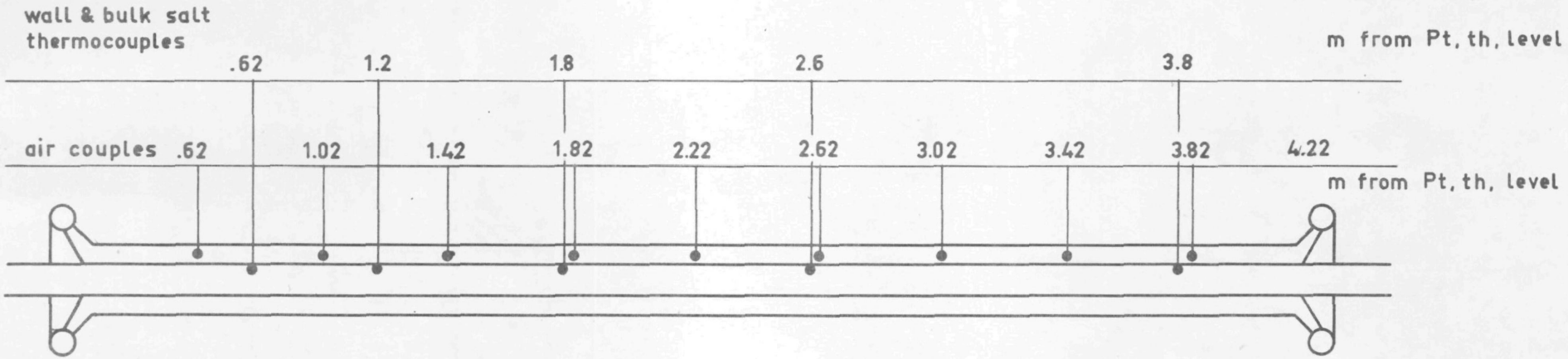

FIGURE 3.2-6.

Positions of the thermo-couples in the FLiNaK-to-air heat exchanger.

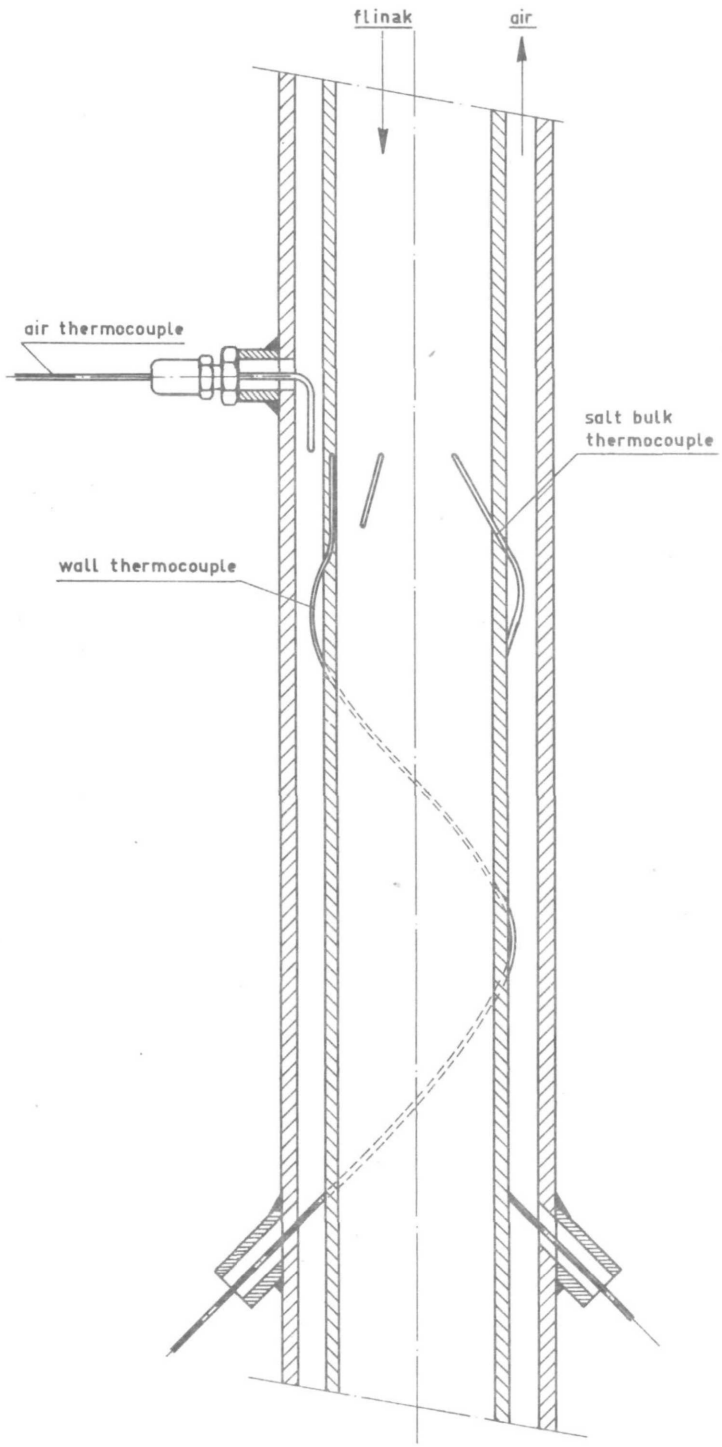

FIGURE 3.2-7.
Details of thermocouple penetrations.

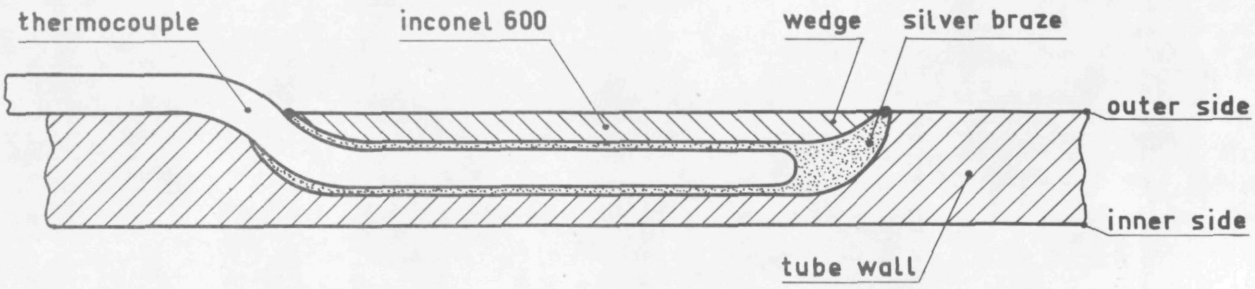

FIGURE 3.2-8.

Imbedding of thermo-couples in the wall of the FLiNaK channel.

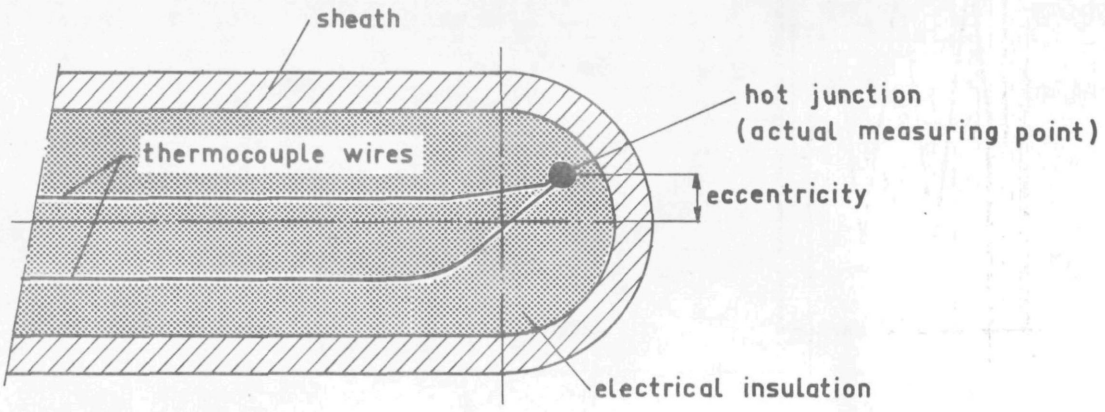

FIGURE 3.2-9.

Non-symmetrical position of the hot junction in a sheated thermo-couple.

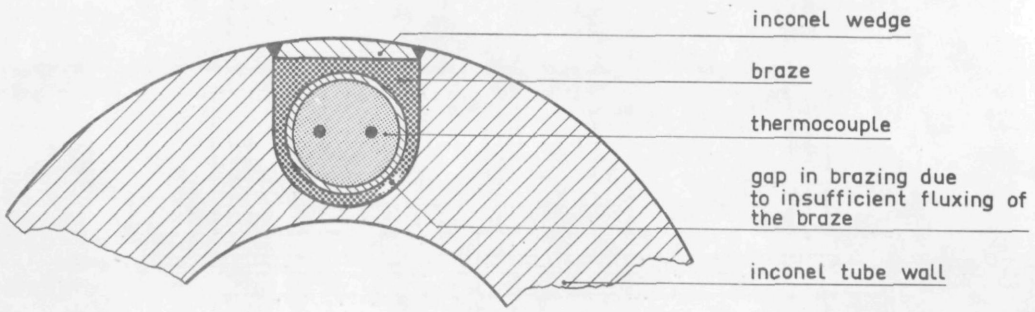

FIGURE 3.2-10.

Example of imperfect brazing of thermocouple in tube wall.

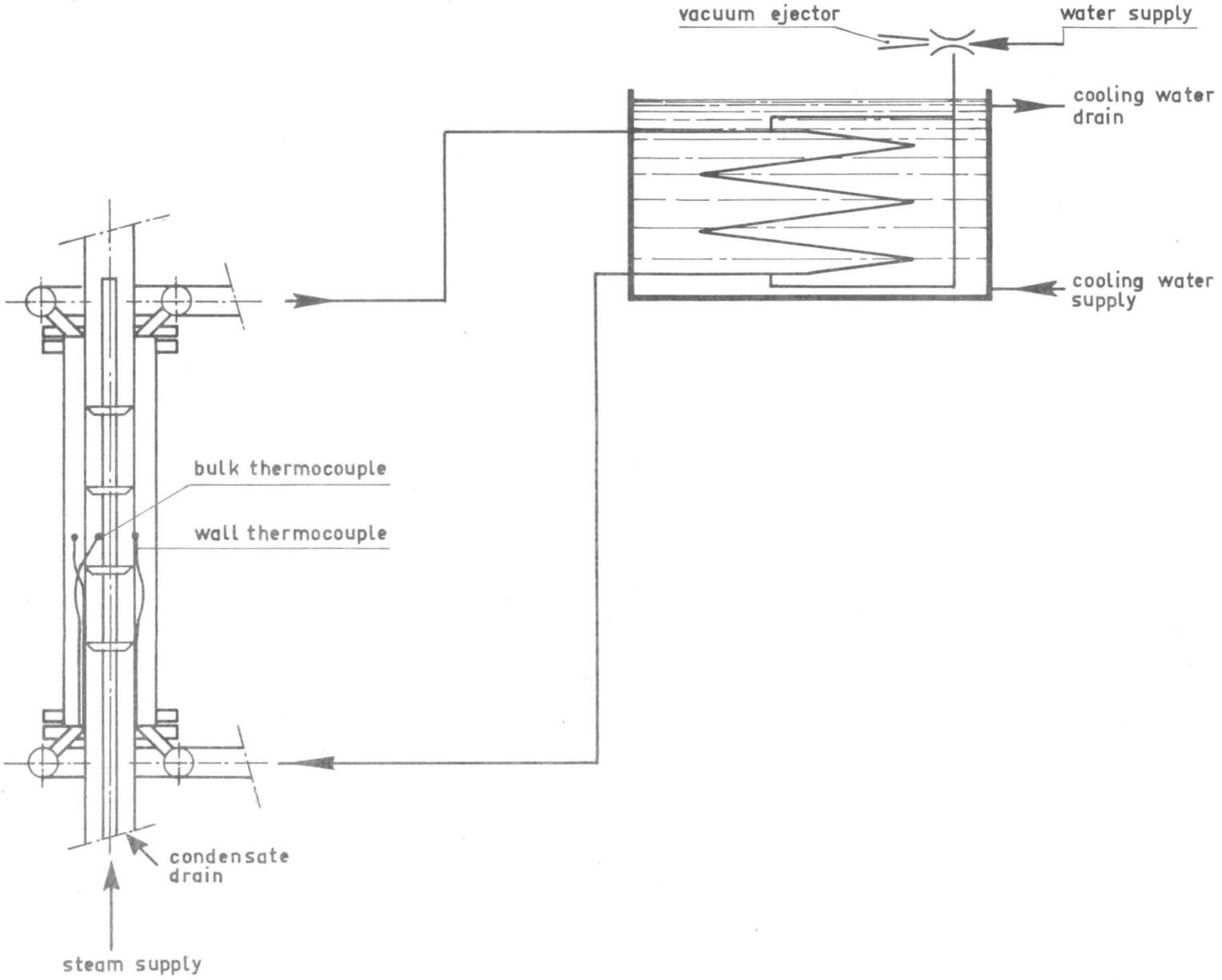

FIGURE 3.2-11.

Simplified flow sheet of test facility for measuring equivalent thermo-couple location.

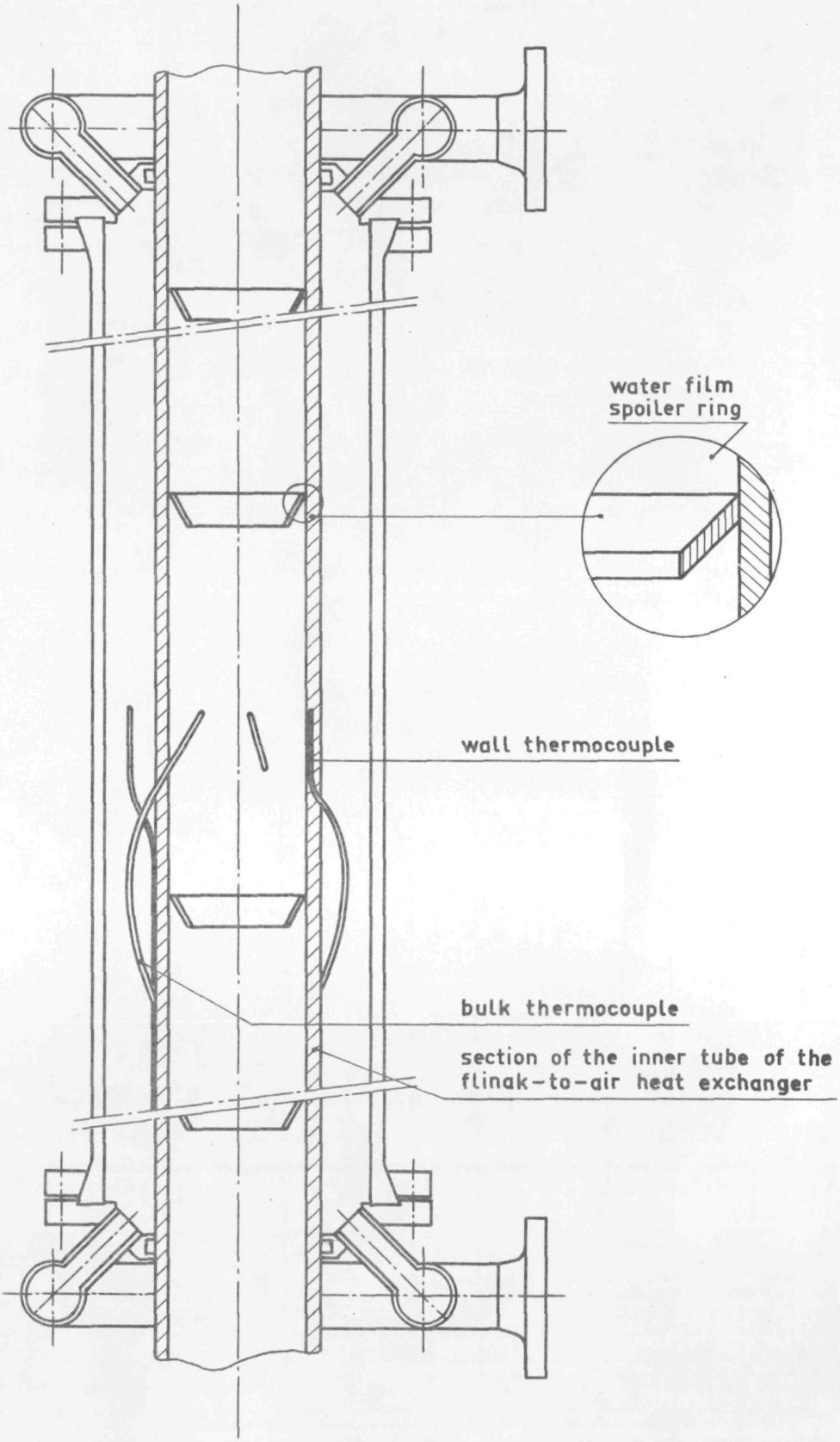

FIGURE 3.2-12.

Special heat exchanger for calibrating purpose.

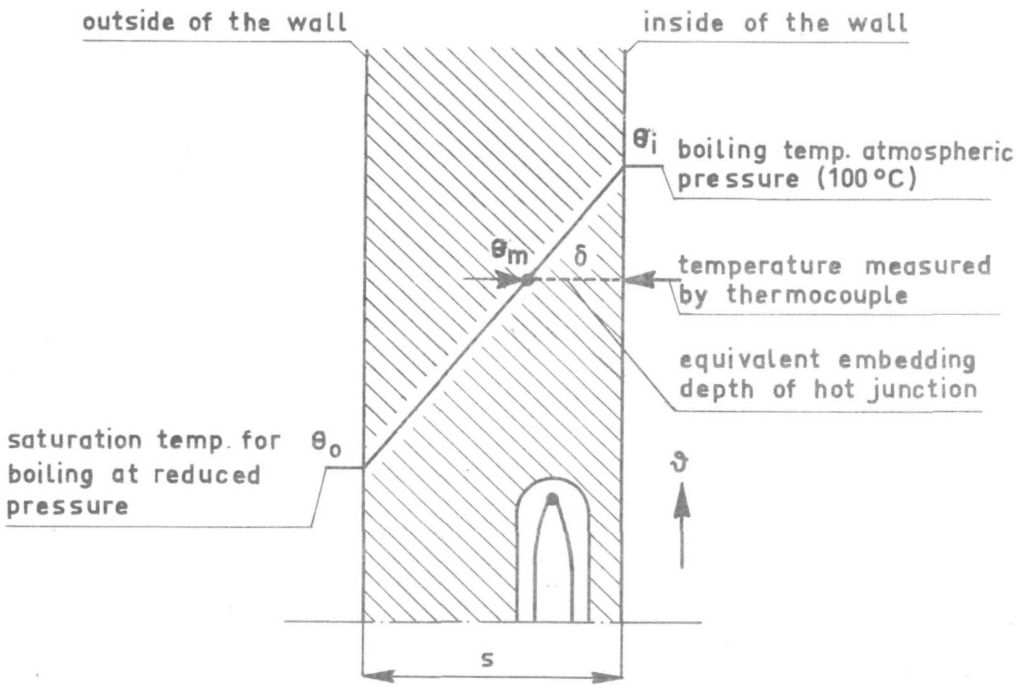

FIGURE 3.2-13.

Method for deriving the equivalent embedding depth of thermo-couples.

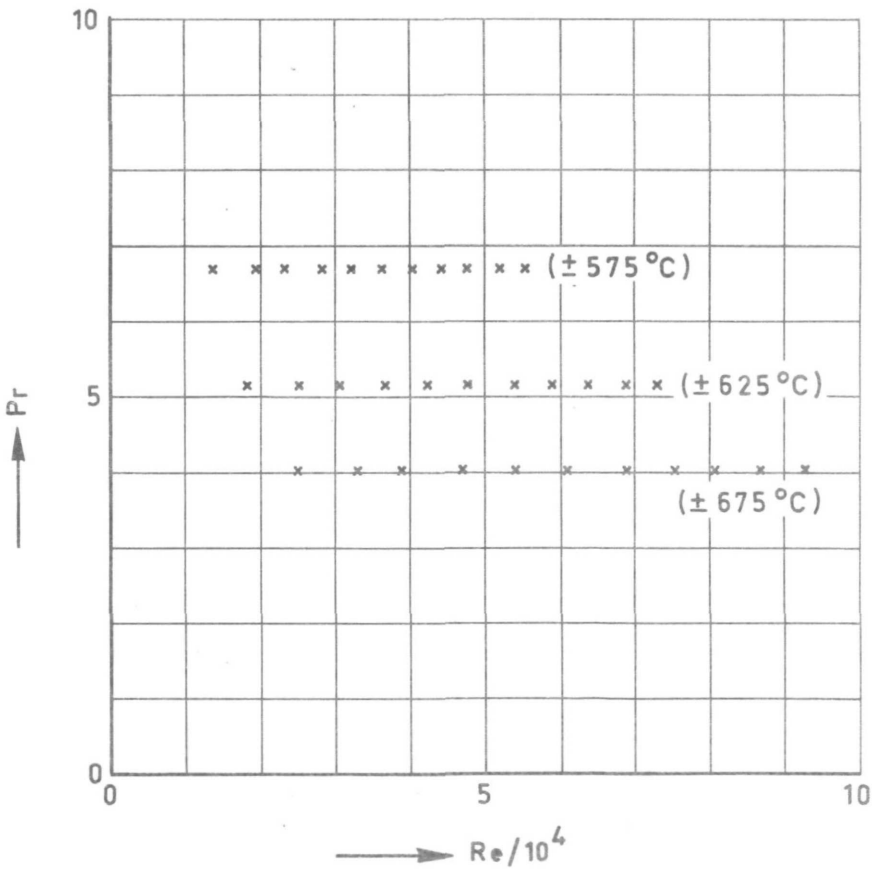

FIGURE 3.2-14.

Test conditions of FLiNaK heat transfer measurements.

$NUSS = 0.0137 * RE^{0.8311} * PR^{0.4106}$

REYNOLDS	PRANDTL	NUSSELT	NUSS	ABS DEV	REL DEV	ALPHA (measured)	ALPHA (computed)
25041.19	4.6449	119.0223	116.9280	2.0943	1.7596%	3792.38	3725.65
33040.65	4.6614	147.0028	147.4399	-0.4371	-0.2973%	4683.91	4697.84
39344.66	4.6425	169.6733	170.1857	-0.5123	-0.3019%	5406.26	5422.58
47396.03	4.6590	198.8708	198.9565	-0.0857	-0.0431%	6336.57	6339.30
54491.82	4.6828	220.4564	223.8834	-3.4270	-1.5545%	7024.35	7133.54
61320.67	4.6638	241.2881	246.5552	-5.2671	-2.1829%	7688.10	7856.93
69113.74	4.6496	266.3374	271.9915	-5.6541	-2.1229%	8486.24	8666.40
75323.46	4.6780	289.2431	292.8853	-3.6422	-1.2592%	9216.08	9332.13
81666.48	4.6614	311.2134	312.7864	-1.5729	-0.5054%	9916.11	9966.23
87622.95	4.6780	338.1457	332.1185	6.0272	1.7824%	10774.25	10582.21
93078.18	4.6899	354.0941	349.5805	4.5136	1.2747%	11282.41	11138.60
13956.33	7.8462	90.7421	89.2038	1.5383	1.6953%	2891.29	2842.28
19396.62	7.8306	117.1327	117.1775	-0.0448	-0.0383%	3732.17	3733.60
23276.89	7.8843	136.7394	136.7375	0.0019	0.0014%	4356.89	4356.83
28272.69	7.8486	159.6043	160.4213	-0.8169	-0.5118%	5085.43	5111.46
32471.76	7.8452	176.8231	179.9567	-3.1336	-1.7721%	5634.07	5733.91
36258.15	7.8437	195.0819	197.2178	-2.1359	-1.0949%	6215.84	6283.90
40675.84	7.9064	215.6868	217.7029	-2.0161	-0.9347%	6872.37	6936.61
44465.25	7.9207	233.2201	234.6054	-1.3852	-0.5940%	7431.03	7475.17
47751.94	7.9842	249.0213	249.7476	-0.7263	-0.2917%	7934.50	7957.64
52495.92	7.8814	272.5989	268.7691	3.8298	1.4049%	8685.75	8563.72
55405.71	7.9414	279.0539	281.9721	-2.9182	-1.0457%	8891.42	8984.40
18485.11	6.0087	103.0114	100.9833	2.0281	1.9688%	3282.23	3217.61
25314.34	6.0009	131.5173	131.0703	0.4470	0.3399%	4190.50	4176.26
30388.73	5.9958	151.1797	152.5107	-1.3310	-0.8804%	4817.00	4859.41
36990.77	5.9693	177.9107	179.2569	-1.3463	-0.7567%	5668.72	5711.62
42499.36	6.0199	197.5966	201.8784	-4.2818	-2.1669%	6295.97	6432.40
47740.36	6.0196	219.9911	222.3590	-2.3679	-1.0764%	7009.52	7084.97
53908.95	5.9822	245.7051	245.3615	0.3436	0.1398%	7828.84	7817.89
58812.31	6.0162	265.5239	264.3870	1.1369	0.4282%	8460.32	8424.10
63557.97	6.0306	286.5018	282.2773	4.2244	1.4745%	9128.73	8994.13
68909.59	6.0196	311.4283	301.6706	9.7577	3.1332%	9922.96	9612.05
73435.08	5.9998	329.7338	317.6185	12.1153	3.6743%	10506.22	10120.20

MEAN RELATIVE ERROR= 1.17 %

FIGURE 3.2-15.

Table of experimental heat transfer data and best fit of general form $Nu = C\ Re^n\ Pr^n$.

$NUSS = 0.0195 * RE^{0.8000} * PR^{0.4000}$

REYNOLDS	PRANDTL	NUSSELT	NUSS	ABS DEV	REL DEV	ALPHA (measured)	ALPHA (computed)
25041.19	4.6449	119.0223	119.2718	-0.2495	-0.2096%	3792.38	3800.33
33040.65	4.6614	147.0028	149.0971	-2.0944	-1.4247%	4683.91	4750.64
39344.66	4.6425	169.6733	171.1727	-1.4994	-0.8837%	5406.26	5454.03
47396.03	4.6590	198.8708	198.9463	-0.0755	-0.0380%	6336.57	6338.98
54491.62	4.6626	220.4564	222.8896	-2.4332	-1.1037%	7024.35	7101.87
61320.67	4.6638	241.2681	244.5705	-3.2824	-1.3604%	7688.10	7792.69
69113.74	4.6496	266.3374	268.8076	-2.4701	-0.9274%	8486.24	8564.95
75323.46	4.6780	289.2431	288.6638	0.5793	0.2003%	9216.08	9197.62
81666.48	4.6614	311.2134	307.5145	3.6990	1.1886%	9916.11	9798.25
87622.95	4.6780	338.1457	325.7935	12.3522	3.6529%	10774.25	10380.68
93078.18	4.6899	354.0941	342.2695	11.8246	3.3394%	11282.41	10905.65
13956.33	7.8462	90.7421	92.1520	-1.4099	-1.5537%	2891.29	2936.21
19396.62	7.8305	117.1327	119.8184	-2.6857	-2.2929%	3732.17	3817.74
23276.89	7.8643	136.7394	139.0175	-2.2781	-1.6660%	4356.89	4429.48
28272.69	7.8486	159.6043	162.1195	-2.5152	-1.5759%	5085.43	5165.57
32471.76	7.8452	176.8231	181.0801	-4.2570	-2.4075%	5634.07	5769.71
36258.15	7.8437	195.0619	197.7690	-2.6871	-1.3774%	6215.84	6301.46
40675.84	7.9064	215.6868	217.5130	-1.8262	-0.8467%	6872.37	6930.56
44465.25	7.9207	233.2201	233.7470	-0.5269	-0.2259%	7431.03	7447.82
47751.94	7.9842	249.0213	248.2611	0.7603	0.3053%	7934.50	7910.28
52495.92	7.8614	272.5989	266.4190	6.1799	2.2670%	8685.75	8488.84
55405.71	7.9414	279.0539	279.0151	0.0388	0.0139%	8891.42	8890.19
18485.11	5.0087	103.0114	103.7036	-0.6922	-0.6719%	3282.23	3304.28
25314.34	5.0009	131.5173	133.2917	-1.7743	-1.3491%	4190.50	4247.04
30388.73	5.9958	151.1797	154.2169	-3.0373	-2.0090%	4817.00	4913.77
36990.77	5.9695	177.9107	180.1646	-2.2540	-1.2669%	5668.72	5740.54
42499.36	6.0199	197.5966	202.0074	-4.4109	-2.2323%	6295.97	6436.51
47740.36	6.0196	219.9911	221.6971	-1.7060	-0.7755%	7009.52	7063.88
53908.95	5.9822	245.7051	243.7233	1.9818	0.8066%	7828.84	7765.69
58812.31	6.0182	265.5239	261.8952	3.6287	1.3666%	8460.32	8344.70
63557.97	6.0306	286.5018	278.9351	7.5667	2.6411%	9128.73	8887.64
68909.59	6.0196	311.4283	297.3550	14.0733	4.5190%	9922.96	9474.55
73435.08	5.9996	329.7338	312.4661	17.2676	5.2368%	10506.22	9956.03

MEAN RELATIVE ERROR= 1.57 %

FIGURE 3.2-16.

Table of experimental heat transfer data and best fit of general form $Nu = C\ Re^{0.8}\ Pr^{0.4}$.

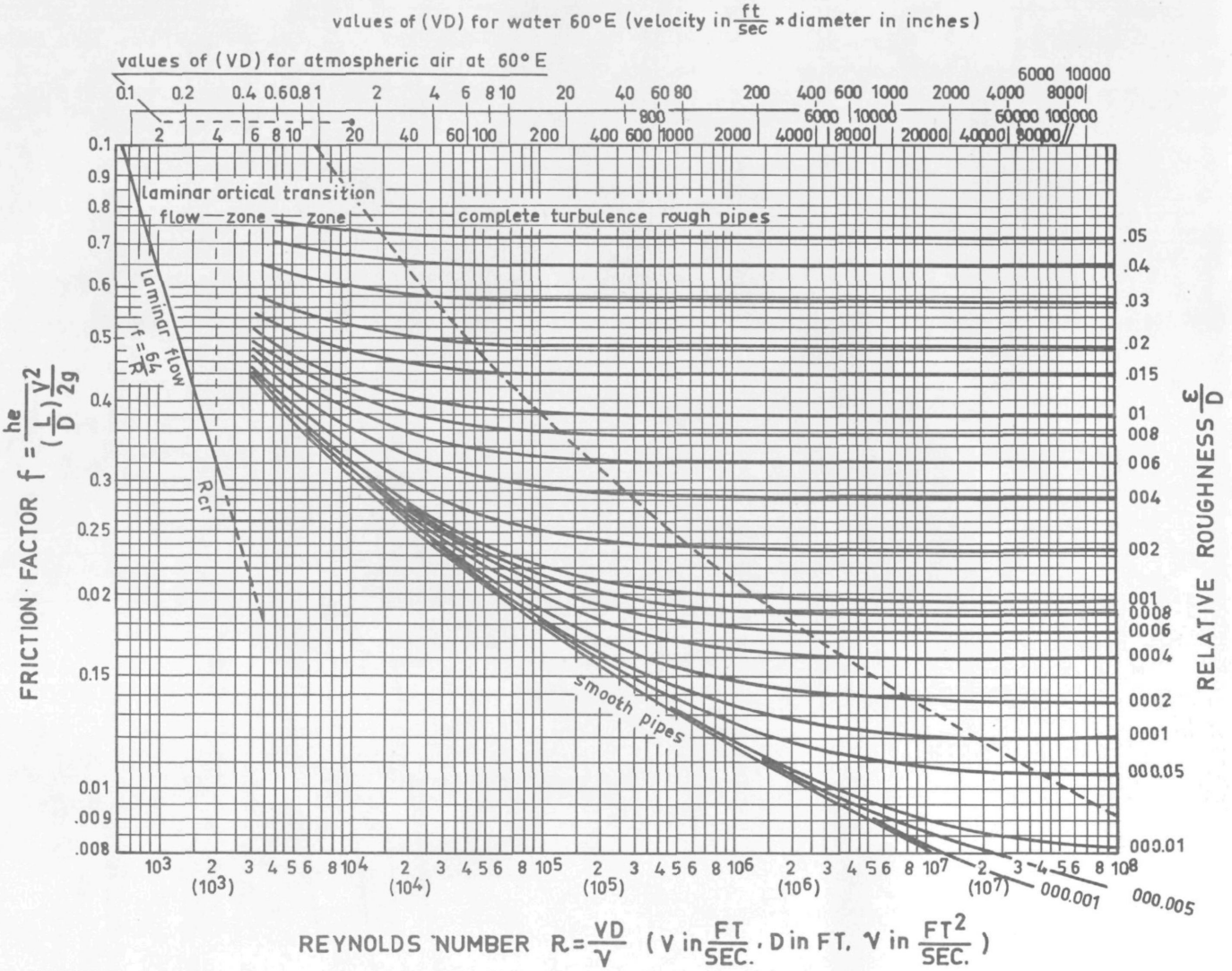

FIGURE 3.3-1.

Moody diagram.

FIGURE 3.3-2.

The location of the pressure drop section in the test loop is shown in figure 2.4-5.

test tube: $1\frac{1}{2}$" sched. 40

D_o = 48.3 mm

D_i = { 40.9 mm (standard)
{ 41.25 mm (after being ground internally)

material: inconel 600

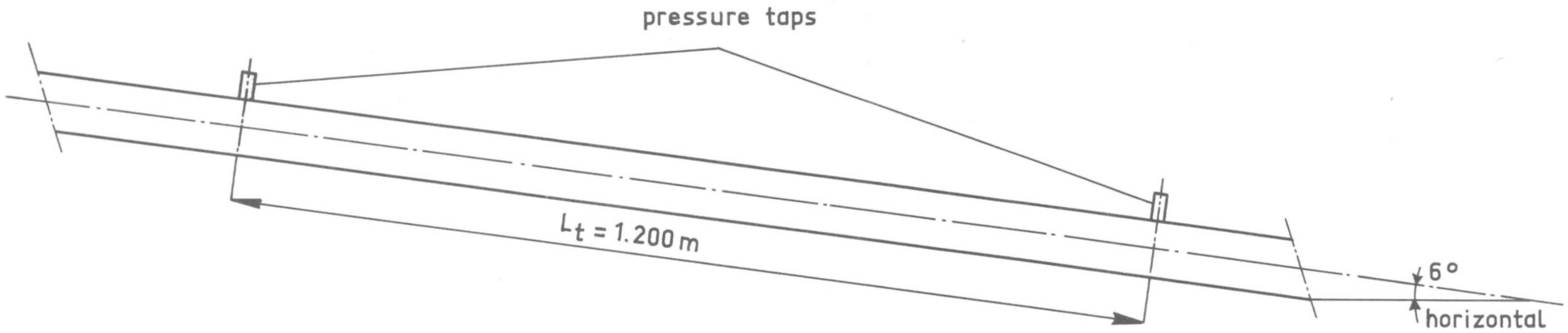

FIGURE 3.3-3.

Test tube for frictional pressure drop measurements.

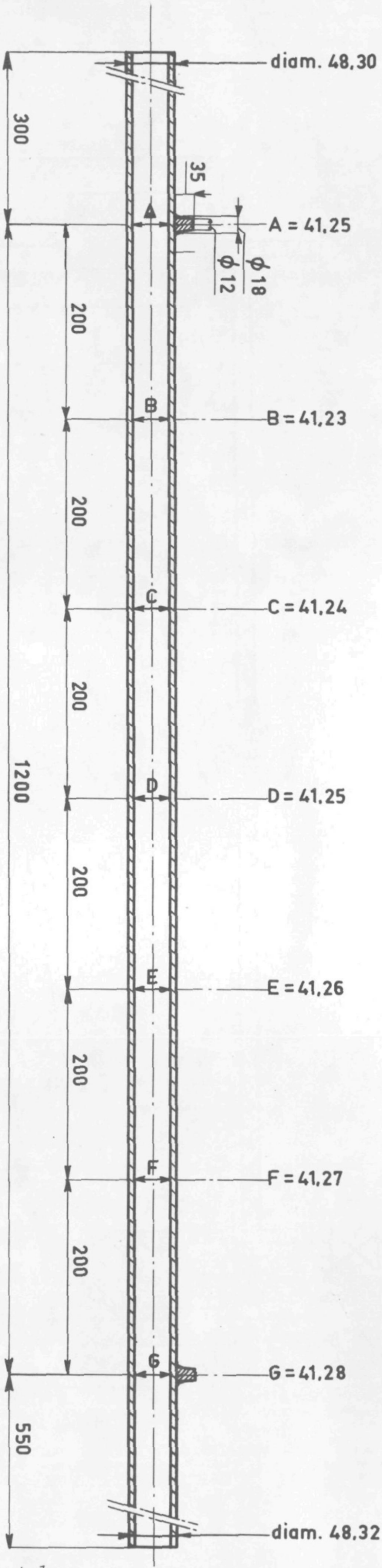

FIGURE 3.3-4.

Dimensions of the test tube.

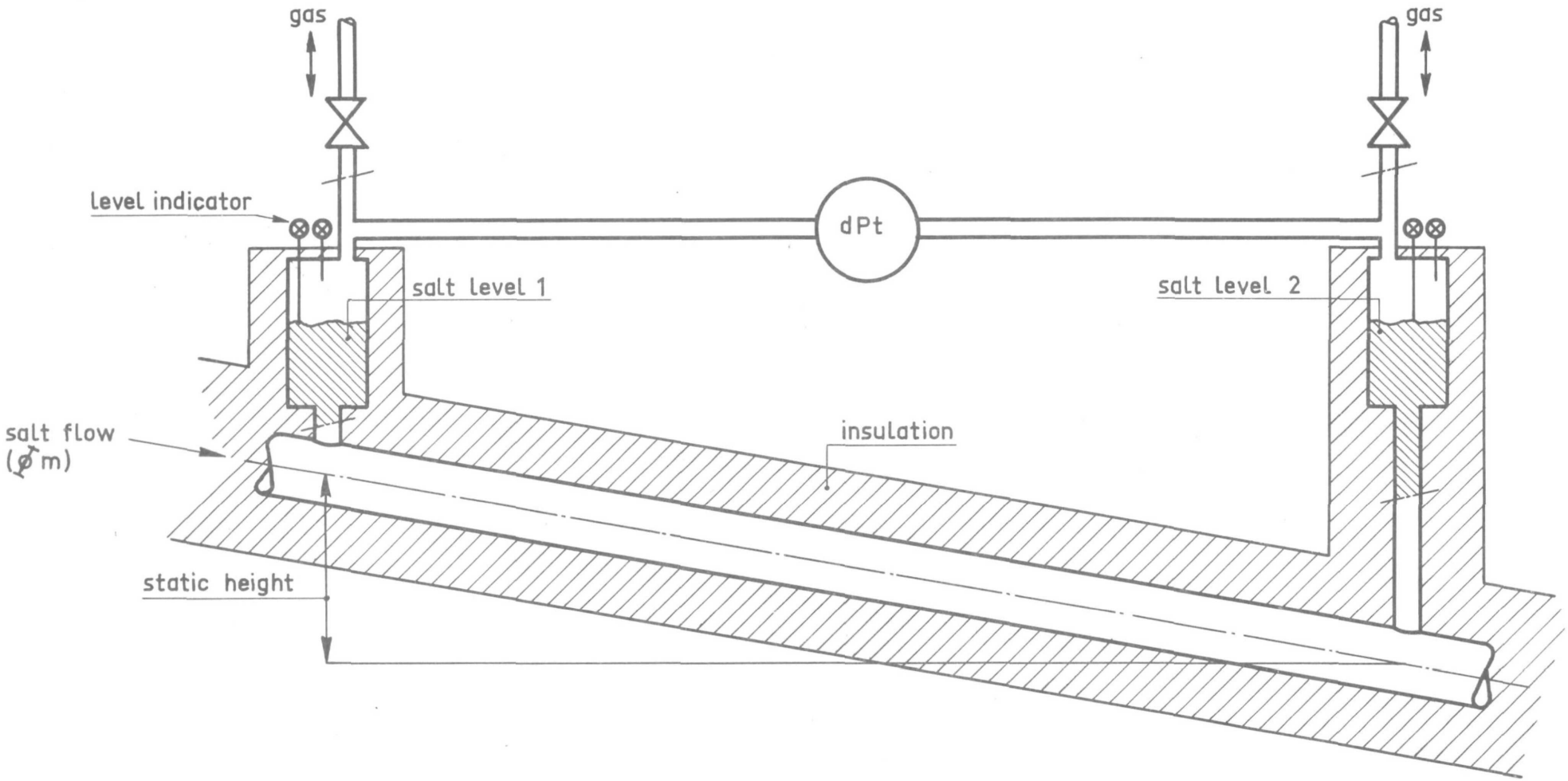

FIGURE 3.3-5.

Principle of frictional pressure drop measurement.

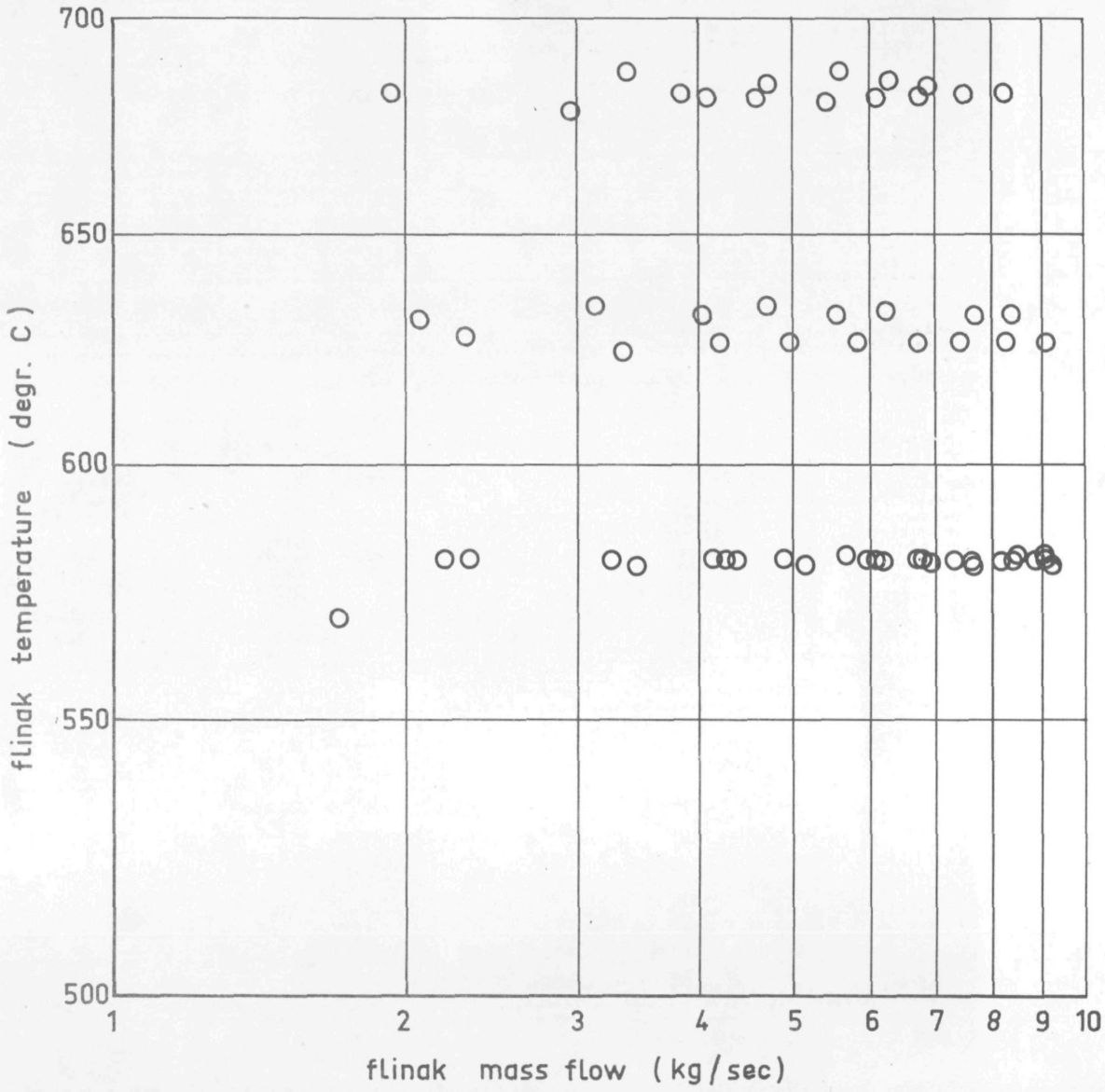

FIGURE 3.3-6.

Summary of test conditions for frictional pressure drop measurements.

FLINAK FRICTION FACTOR MEASUREMENT

MEASUREMENT IDENTIFICATION 1-8-72

DELTA P. VENTURI BAR	DELTA P. FRICTION BAR	MASS FL. FLINAK KG/SEC	TEMP. FLINAK DEGR. C	RE /10**4	FRICTION FACTOR TEST	FRICTION FACTOR BLASIUS	DIFF. TEST-BLAS ABS	DIFF. TEST-BLAS REL % OF MEA.
0.0030	0.022	2.03	684	2.04	0.0181	0.0265	0.0084	-47
0.0125	0.062	3.39	687	3.46	0.0271	0.0232	0.0039	14
0.0195	0.090	4.09	681	4.05	0.0291	0.0223	0.0068	23
0.0265	0.121	4.74	684	4.75	0.0294	0.0214	0.0080	27
0.0360	0.170	5.61	687	5.73	0.0284	0.0205	0.0080	28
0.0460	0.214	6.30	685	6.35	0.0288	0.0199	0.0089	31
0.0550	0.258	6.92	684	6.94	0.0286	0.0195	0.0091	32

MEASUREMENT IDENTIFICATION 3-8-72/1

DELTA P. VENTURI BAR	DELTA P. FRICTION BAR	MASS FL. FLINAK KG/SEC	TEMP. FLINAK DEGR. C	RE /10**4	FRICTION FACTOR TEST	FRICTION FACTOR BLASIUS	DIFF. TEST-BLAS ABS	DIFF. TEST-BLAS REL % OF MEA.
0.0053	0.020	1.93	682	1.92	0.0356	0.0269	0.0087	24
0.0120	0.047	2.97	678	2.91	0.0339	0.0242	0.0097	29
0.0180	0.080	3.85	682	3.84	0.0302	0.0226	0.0076	25
0.0250	0.114	4.60	681	4.56	0.0294	0.0217	0.0078	26
0.0330	0.158	5.42	680	5.34	0.0280	0.0208	0.0072	26
0.0490	0.200	6.10	681	6.04	0.0329	0.0202	0.0127	39
0.0535	0.245	6.75	681	6.68	0.0293	0.0197	0.0096	33
0.0680	0.305	7.53	682	7.50	0.0299	0.0191	0.0108	36
0.0770	0.368	8.27	682	8.24	0.0281	0.0187	0.0094	33

MEASUREMENT IDENTIFICATION 3-8-72/2

DELTA P. VENTURI BAR	DELTA P. FRICTION BAR	MASS FL. FLINAK KG/SEC	TEMP. FLINAK DEGR. C	RE /10**4	FRICTION FACTOR TEST	FRICTION FACTOR BLASIUS	DIFF. TEST-BLAS ABS	DIFF. TEST-BLAS REL % OF MEA.
0.0065	0.022	2.06	631	1.58	0.0388	0.0282	0.0106	27
0.0137	0.052	3.13	634	2.45	0.0354	0.0253	0.0101	29
0.0200	0.086	4.03	632	3.12	0.0312	0.0238	0.0074	24
0.0260	0.117	4.70	634	3.68	0.0298	0.0228	0.0070	23
0.0360	0.163	5.55	632	4.29	0.0296	0.0220	0.0077	26
0.0465	0.207	6.25	633	4.86	0.0301	0.0213	0.0088	29
0.0690	0.315	7.72	632	5.96	0.0294	0.0202	0.0092	31
0.0775	0.375	8.42	632	6.51	0.0277	0.0198	0.0079	29

FIGURE 3.3-7[a].

Experimental data of frictional pressure drop measurements.

MEASUREMENT IDENTIFICATION 10-8-72/1

DELTA P. VENTURI BAR	DELTA P. FRICTION BAR	MASS FL. FLINAK KG/SEC	TEMP. FLINAK DEGR. C	RE /1000A	FRICTION FACTOR TEST	FRICTION FACTOR BLASIUS	DIFF. TEST-BLAS ABS	DIFF. TEST-BLAS REL % OF MEA.
0.0040	0.015	1.70	569	0.91	0.0358	0.0324	0.0034	10
0.0130	0.055	3.25	581	1.88	0.0317	0.0270	0.0047	15
0.0210	0.090	4.16	581	2.41	0.0313	0.0254	0.0059	19
0.0278	0.125	4.90	581	2.83	0.0298	0.0244	0.0055	18
0.0365	0.167	5.67	582	3.30	0.0293	0.0235	0.0059	20
0.0465	0.200	6.20	581	3.59	0.0312	0.0230	0.0082	26
0.0590	0.240	6.80	581	3.93	0.0330	0.0225	0.0105	32
0.0710	0.305	7.66	581	4.43	0.0312	0.0218	0.0094	30
0.0775	0.380	8.55	582	4.98	0.0274	0.0212	0.0062	23
0.0810	0.430	9.09	582	5.30	0.0253	0.0209	0.0044	17

MEASUREMENT IDENTIFICATION 10-8-72/2

DELTA P. VENTURI BAR	DELTA P. FRICTION BAR	MASS FL. FLINAK KG/SEC	TEMP. FLINAK DEGR. C	RE /1000A	FRICTION FACTOR TEST	FRICTION FACTOR BLASIUS	DIFF. TEST-BLAS ABS	DIFF. TEST-BLAS REL % OF MEA.
0.0810	0.430	9.10	581	5.26	0.0253	0.0209	0.0044	17
0.0800	0.410	8.88	581	5.13	0.0262	0.0210	0.0052	20
0.0745	0.350	8.21	581	4.74	0.0286	0.0214	0.0071	25
0.0630	0.280	7.34	581	4.24	0.0302	0.0220	0.0082	27
0.0535	0.235	6.72	581	3.89	0.0306	0.0225	0.0080	26
0.0440	0.185	5.97	581	3.45	0.0319	0.0232	0.0087	27
0.0320	0.125	4.90	581	2.83	0.0344	0.0244	0.0100	29
0.0255	0.095	4.28	581	2.47	0.0360	0.0252	0.0108	30
0.0170	0.055	3.25	581	1.88	0.0415	0.0270	0.0145	35
0.0105	0.025	2.19	581	1.27	0.0564	0.0298	0.0266	47

MEASUREMENT IDENTIFICATION 8-9-72/1

DELTA P. VENTURI BAR	DELTA P. FRICTION BAR	MASS FL. FLINAK KG/SEC	TEMP. FLINAK DEGR. C	RE /1000A	FRICTION FACTOR TEST	FRICTION FACTOR BLASIUS	DIFF. TEST-BLAS ABS	DIFF. TEST-BLAS REL % OF MEA.
0.0065	0.028	2.30	627	1.73	0.0312	0.0276	0.0036	11
0.0145	0.059	3.34	624	2.48	0.0330	0.0252	0.0078	24
0.0215	0.094	4.22	626	3.15	0.0307	0.0237	0.0070	23
0.0285	0.130	4.96	626	3.71	0.0294	0.0228	0.0066	23
0.0410	0.180	5.84	626	4.36	0.0306	0.0219	0.0087	28
0.0520	0.240	6.74	626	5.04	0.0291	0.0211	0.0080	27
0.0610	0.293	7.45	626	5.57	0.0279	0.0206	0.0073	26
0.0740	0.365	8.32	626	6.21	0.0272	0.0200	0.0072	26
0.0805	0.439	9.12	626	6.81	0.0246	0.0196	0.0050	20

MEASUREMENT IDENTIFICATION 8-9-72/2

DELTA P. VENTURI BAR	DELTA P. FRICTION BAR	MASS FL. FLINAK KG/SEC	TEMP. FLINAK DEGR. C	RE /1000A	FRICTION FACTOR TEST	FRICTION FACTOR BLASIUS	DIFF. TEST-BLAS ABS	DIFF. TEST-BLAS REL % OF MEA.
0.0810	0.441	9.21	580	5.29	0.0247	0.0209	0.0038	15
0.0760	0.372	8.46	581	4.89	0.0274	0.0213	0.0061	22
0.0630	0.306	7.68	580	4.40	0.0276	0.0218	0.0058	21
0.0535	0.249	6.92	580	3.97	0.0288	0.0224	0.0064	22
0.0380	0.194	6.11	581	3.53	0.0263	0.0231	0.0032	12
0.0320	0.138	5.15	580	2.96	0.0311	0.0241	0.0070	22
0.0225	0.100	4.39	581	2.54	0.0302	0.0251	0.0051	17
0.0150	0.062	3.45	580	1.98	0.0325	0.0267	0.0058	18
0.0050	0.028	2.32	581	1.34	0.0240	0.0294	0.0054	-23

FIGURE 3.3-7b.

Experimental data of frictional pressure drop measurements.

$$F\_FR = 0.2657 * RE^{-0.2058}$$

RE	F_FR(MEAS)	F_FR(CORL)	ABS ERROR	REL. ERROR
-34591.00	0.027060	0.030927	0.003867	14.29
40499.00	0.029080	0.029940	0.000860	2.96
47503.00	0.029390	0.028973	-0.000417	-1.42
57279.00	0.028420	0.027878	-0.000542	-1.91
63536.00	0.028850	0.027290	-0.001560	-5.41
69364.00	0.028610	0.026801	-0.001809	-6.32
19202.00	0.035570	0.034909	-0.000661	-1.86
29082.00	0.033910	0.032051	-0.001859	-5.48
38404.00	0.030200	0.030269	0.000069	0.23
45580.00	0.029430	0.029220	-0.000210	-0.71
53350.00	0.028030	0.028289	0.000259	0.92
-60372.00	0.032880	0.027578	-0.005302	-16.13
66820.00	0.029310	0.027008	-0.002302	-7.85
74985.00	0.029920	0.026375	-0.003545	-11.85
82367.00	0.028080	0.025870	-0.002210	-7.87
15831.00	0.038770	0.036324	-0.002446	-6.31
24541.00	0.035360	0.033191	-0.002169	-6.13
31153.00	0.031210	0.031601	0.000391	1.25
36811.00	0.029820	0.030534	0.000714	2.39
42889.00	0.029640	0.029588	-0.000052	-0.17
48647.00	0.030150	0.028831	-0.001319	-4.37
59622.00	0.029400	0.027649	-0.001751	-5.96
65053.00	0.027740	0.027157	-0.000583	-2.10
9127.00	0.035790	0.040684	0.004894	13.67
-18802.00	0.031720	0.035061	0.003341	10.53
24051.00	0.031320	0.033329	0.002009	6.41
28345.00	0.029850	0.032221	0.002371	7.94
33000.00	0.029330	0.031228	0.001898	6.47
35854.00	0.031200	0.030700	-0.000500	-1.60
39276.00	0.032990	0.030129	-0.002861	-8.67
44276.00	0.031240	0.029395	-0.001845	-5.91
49779.00	0.027370	0.028695	0.001325	4.84
52952.00	0.025280	0.028332	0.003052	12.07
52572.00	0.025280	0.028374	0.003094	12.24
51335.00	0.026190	0.028514	0.002324	8.87
47430.00	0.028570	0.028982	0.000412	1.44
42423.00	0.030200	0.029655	-0.000545	-1.80
38865.00	0.030550	0.030194	-0.000356	-1.16
34511.00	0.031870	0.030942	-0.000928	-2.91
28345.00	0.034360	0.032221	-0.002139	-6.23
24710.00	0.036030	0.033144	-0.002886	-8.01
-18802.00	0.041480	0.035061	-0.006419	-15.47
-12676.00	0.056370	0.038024	-0.018346	-32.55
17317.00	0.031160	0.035660	0.004500	14.44
24808.00	0.032980	0.033117	0.000137	0.42
31521.00	0.030700	0.031524	0.000824	2.69
37068.00	0.029420	0.030490	0.001070	3.64
43618.00	0.030570	0.029486	-0.001084	-3.55
50366.00	0.029080	0.028626	-0.000454	-1.56
55650.00	0.027940	0.028044	0.000104	0.37
62113.00	0.027210	0.027417	0.000207	0.76
68119.00	0.024610	0.026901	0.002291	9.31
52857.00	0.024650	0.028343	0.003693	14.98
48898.00	0.027420	0.028801	0.001381	5.04
44029.00	0.027630	0.029429	0.001799	6.51
39717.00	0.028840	0.030060	0.001220	4.23
35312.00	0.026290	0.030796	0.004506	17.14
29568.00	0.031120	0.031942	0.000822	2.64
25352.00	0.030200	0.032969	0.002769	9.17
19819.00	0.032470	0.034683	0.002213	6.82

MEAN RELATIVE ERROR= 6.43 %

FIGURE 3.3-8

Least squares approximation of experimental data.

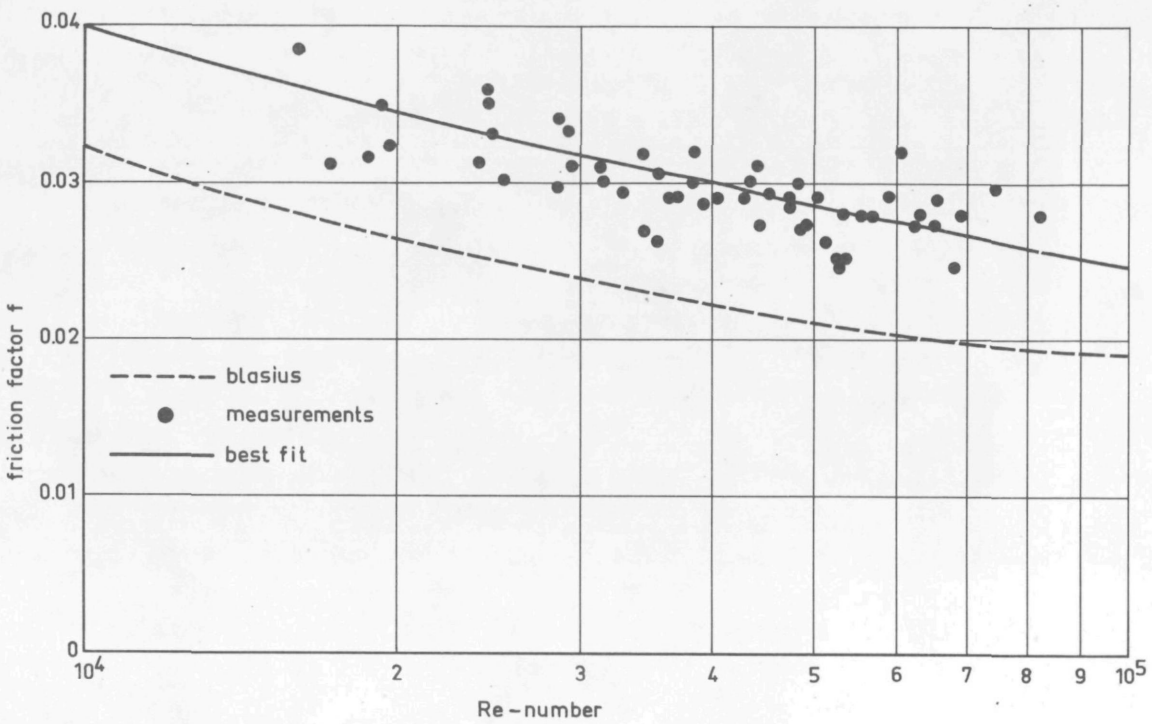

FIGURE 3.3-9.

Experimental data of frictional pressure drop measurments, best fit and Blasius formula.

variable	value	abs. error	relative error [% of max. value]	source
L	1200 [mm]	1	0.08 %	fig. 3.3-3
D	41.25 [mm]	0.5	0.1 %	fig. 3.3-3
c_{re}	$9.55\ 10^{-4}$ [m^2]		1.2 %	ref. 2.2-3
ρ , ν }	cf. figure 2.2-13			
ΔP_v			2%	subsection 2.2-3
ΔP_f			3%	Appendix 3A

FIGURE 3.3-10.

Accuracies of properties appearing in equation (3.3-6).

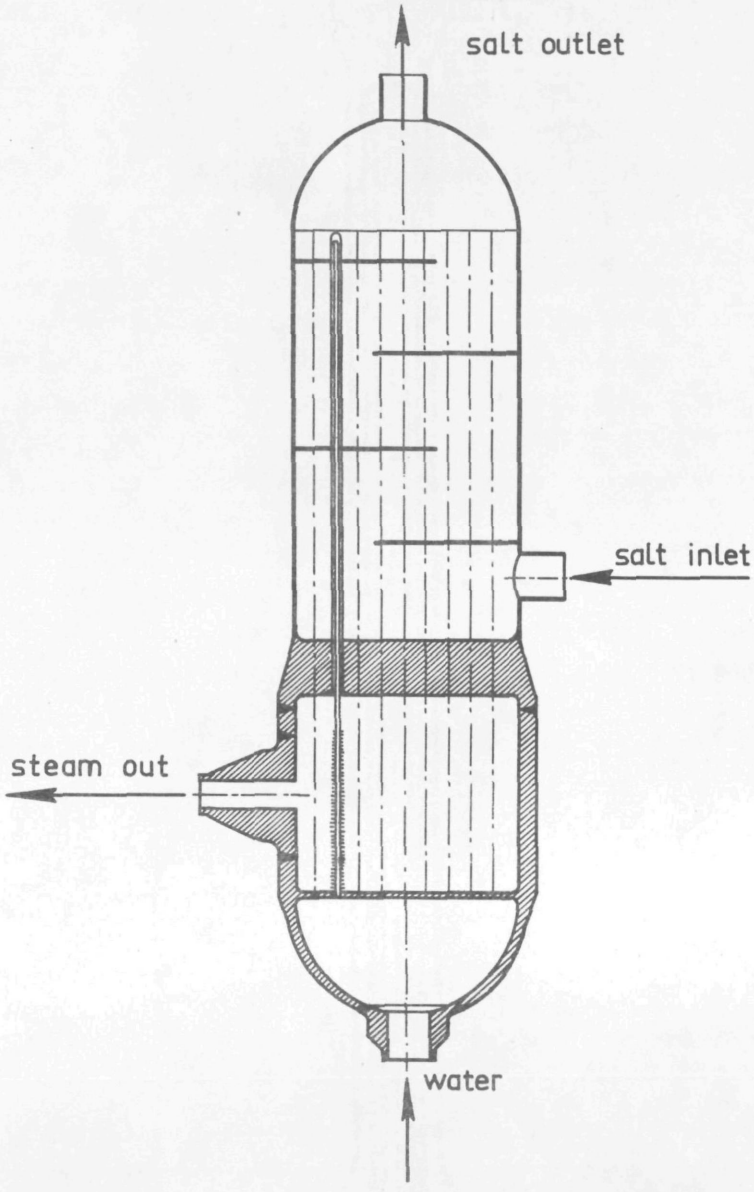

FIGURE 4.1-1.

Cross-section of a full-size bayonet tube steam generator.

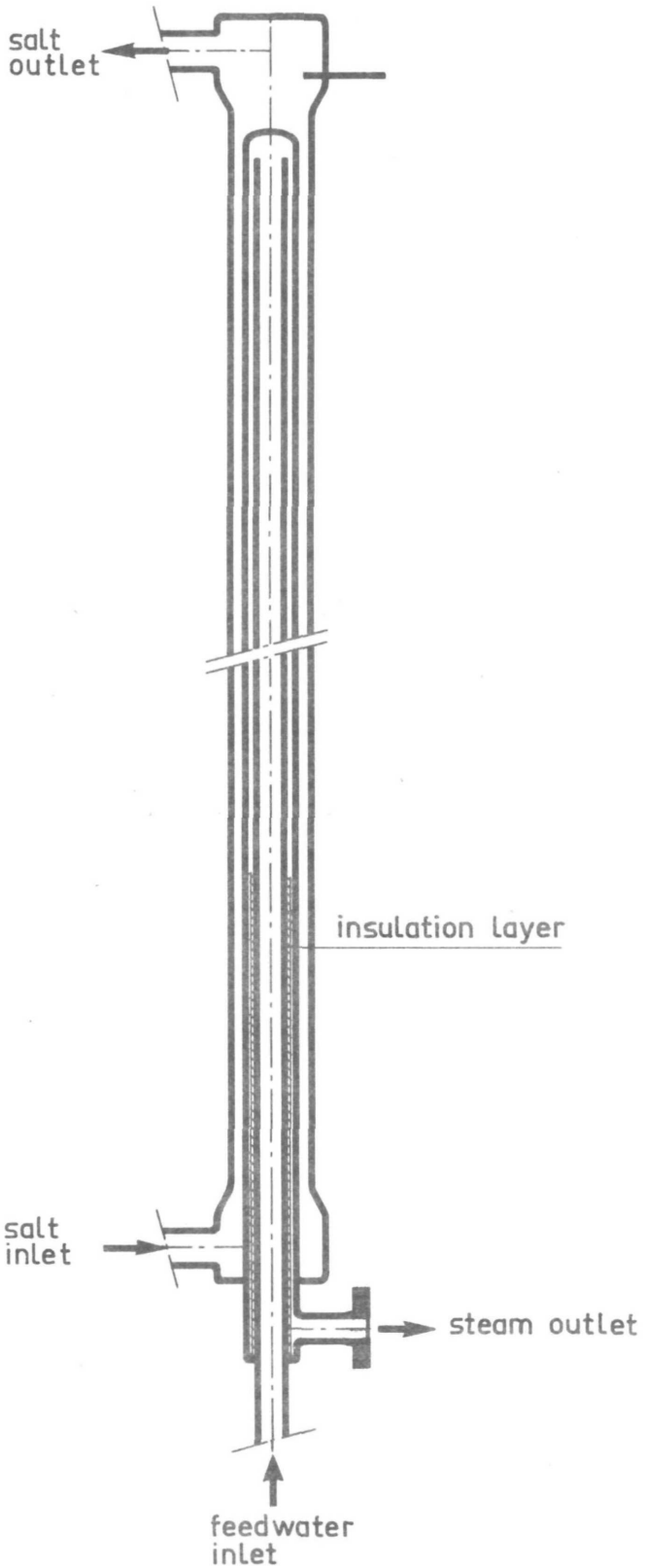

FIGURE 4.1-2.

Cross-section of the bayonet tube test module.

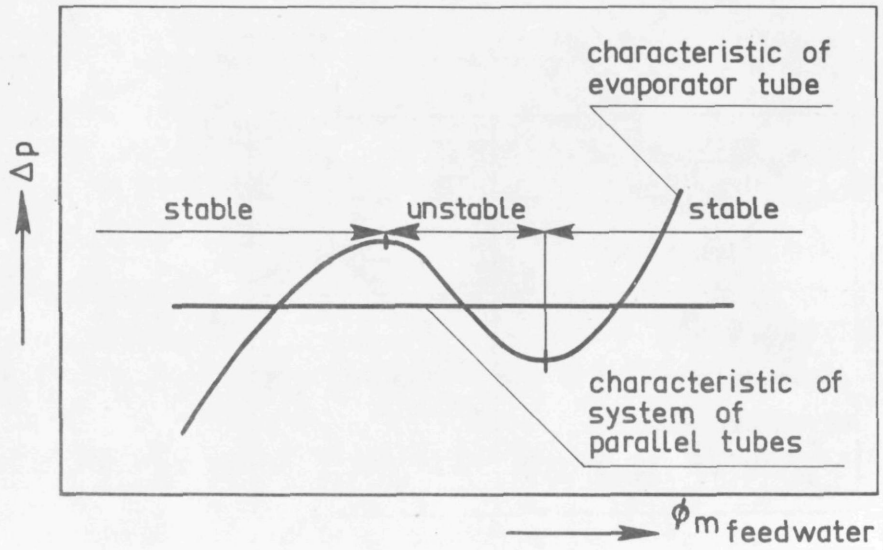

FIGURE 4.1-3.

Region of static instability in parallel tubes.

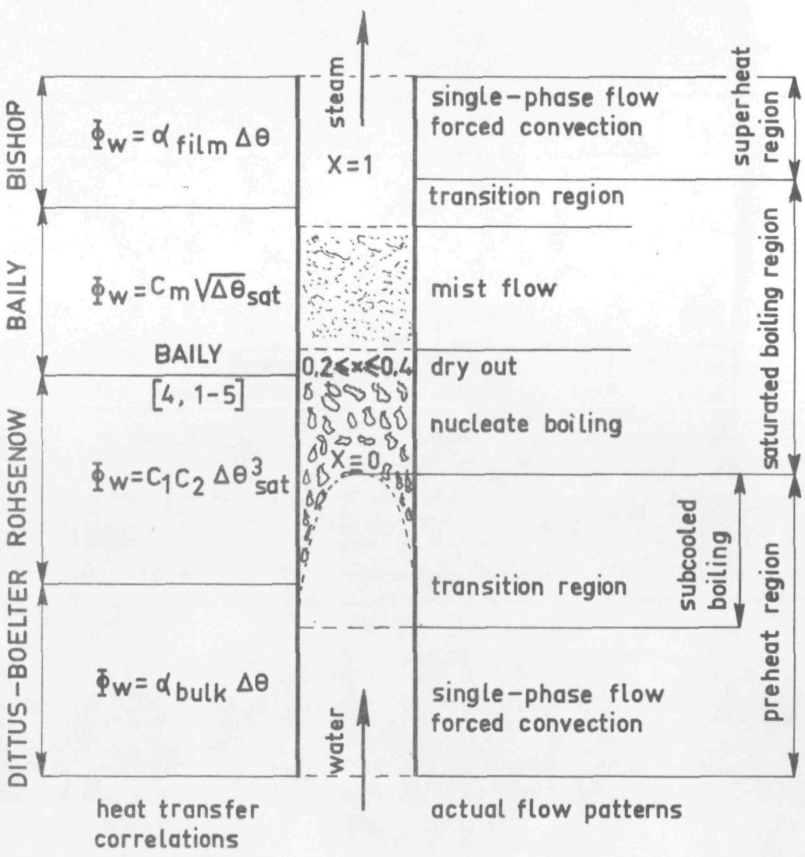

FIGURE 4.2-1.

Secondary side flow patterns and heat transfer correlations.

Temp. FLiNaK in	625 ^{0}C
Temp. FLiNaK out	614 ^{0}C
Mass flow FLiNaK	6.8 kg/s
Temp. feedwater in	280 ^{0}C
Temp. steam out	540 ^{0}C
Pressure steam out	18 MN/m^2
Mass flow feedwater	0.065 kg/s

FIGURE 4.3-1.

Table of process conditions at full load.

Lenght	9.1 m	
tube diameters		
evaporator tube		
top 6.7 m	17.2/12.6 mm	CR Mo 910
lower 2.4 m (insul.)	15.2/10.6 mm	
pressure tube	26.0/20.8 mm	Inconel 600
outer tube	60.3/52.5 mm	
insulation layer		
app. thickness	1.5 mm	ZO_2 oxide
heat resistance	1.0 m^2 ^{0}C/kW	

FIGURE 4.3-2.

Dimensions and materials of test module.

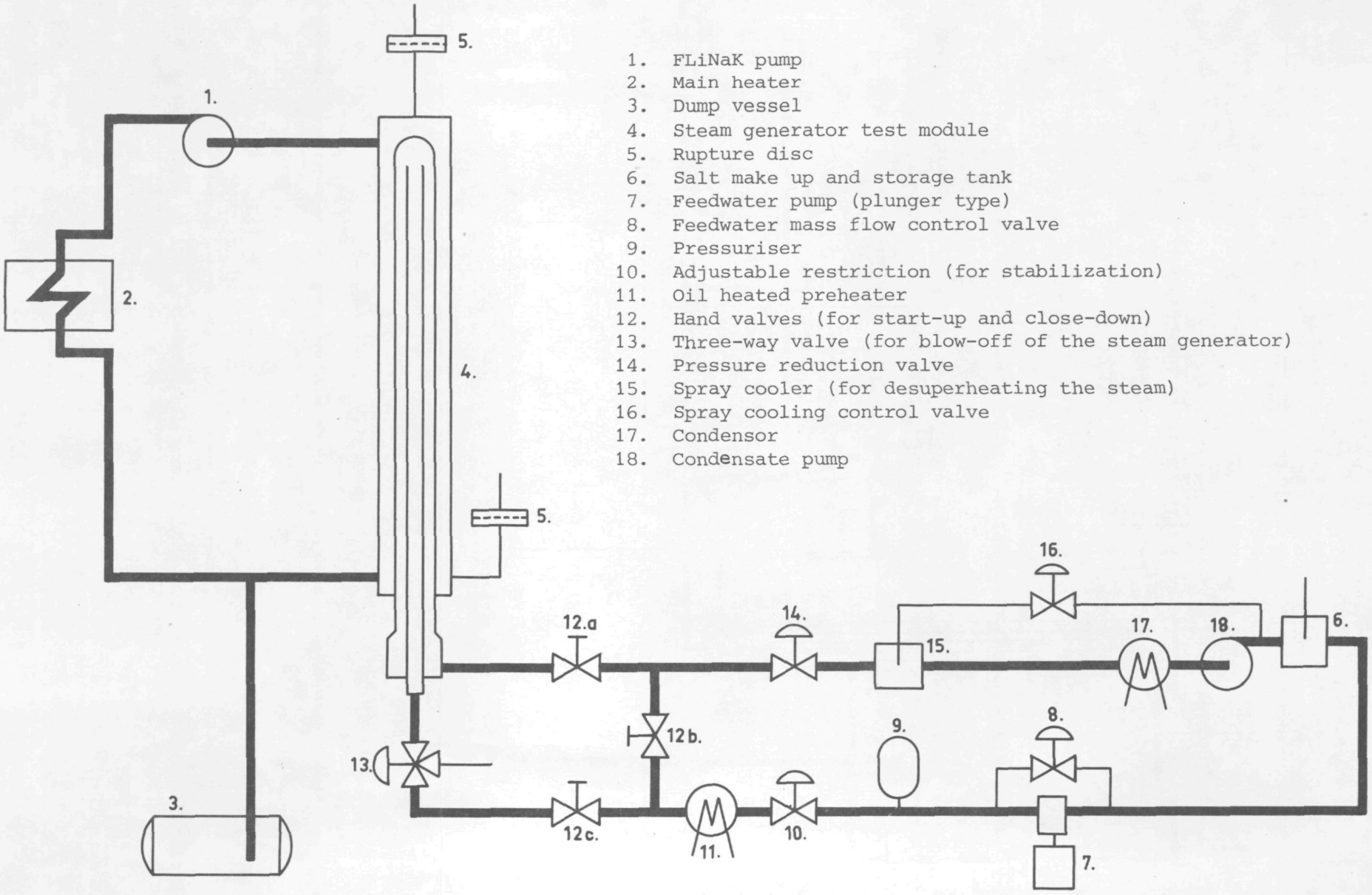

1. FLiNaK pump
2. Main heater
3. Dump vessel
4. Steam generator test module
5. Rupture disc
6. Salt make up and storage tank
7. Feedwater pump (plunger type)
8. Feedwater mass flow control valve
9. Pressuriser
10. Adjustable restriction (for stabilization)
11. Oil heated preheater
12. Hand valves (for start-up and close-down)
13. Three-way valve (for blow-off of the steam generator)
14. Pressure reduction valve
15. Spray cooler (for desuperheating the steam)
16. Spray cooling control valve
17. Condensor
18. Condensate pump

FIGURE 4.3-3.

Flowsheet of bayonet tube steam generator test facility.

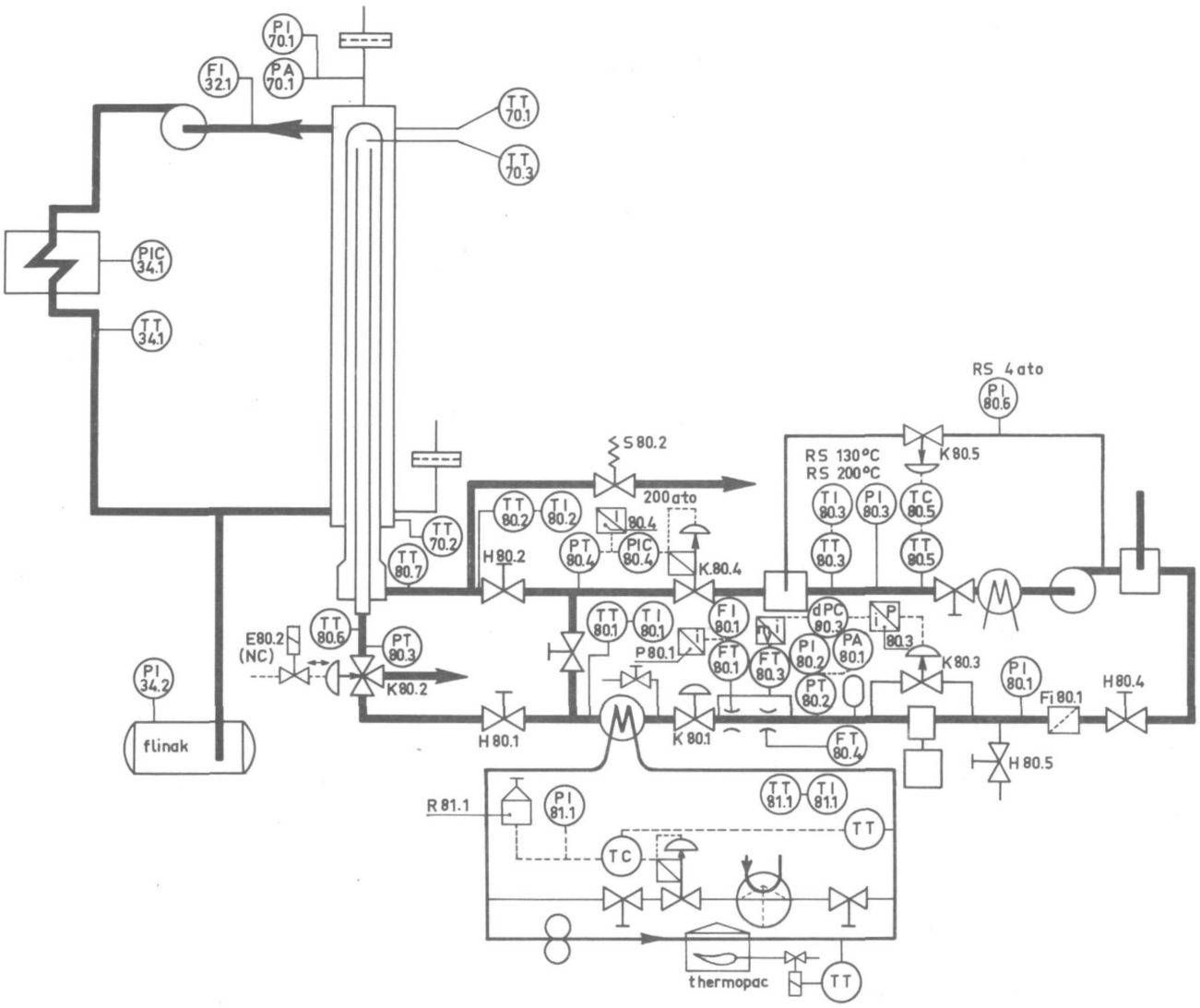

FIGURE 4.3-4.

Instrumentation diagram of bayonet tube test facility.

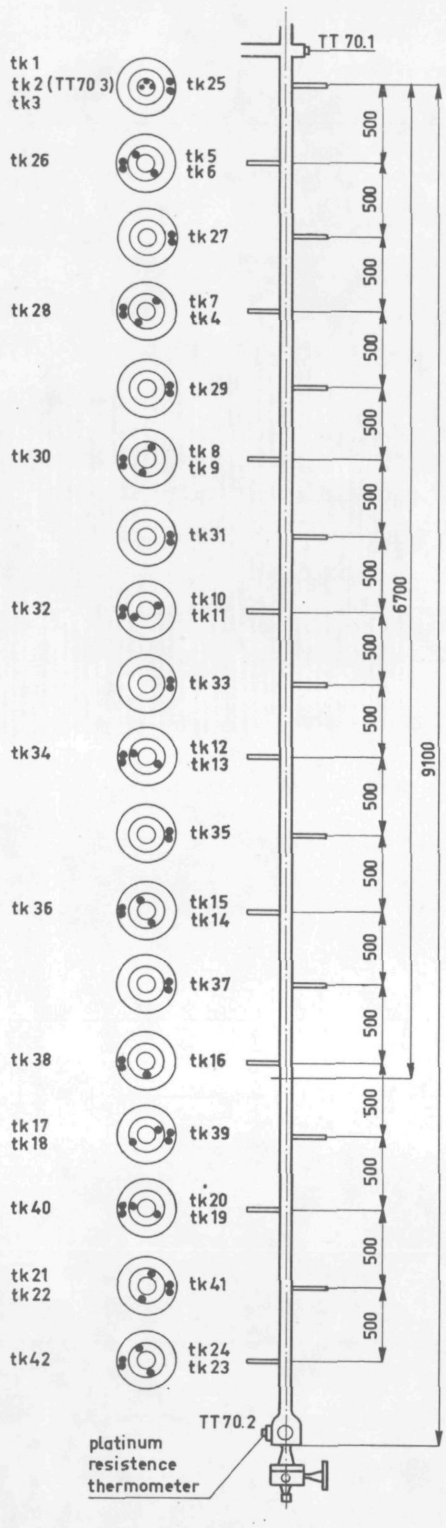

FIGURE 4.3-5.

Thermo-couple locations in the test module.

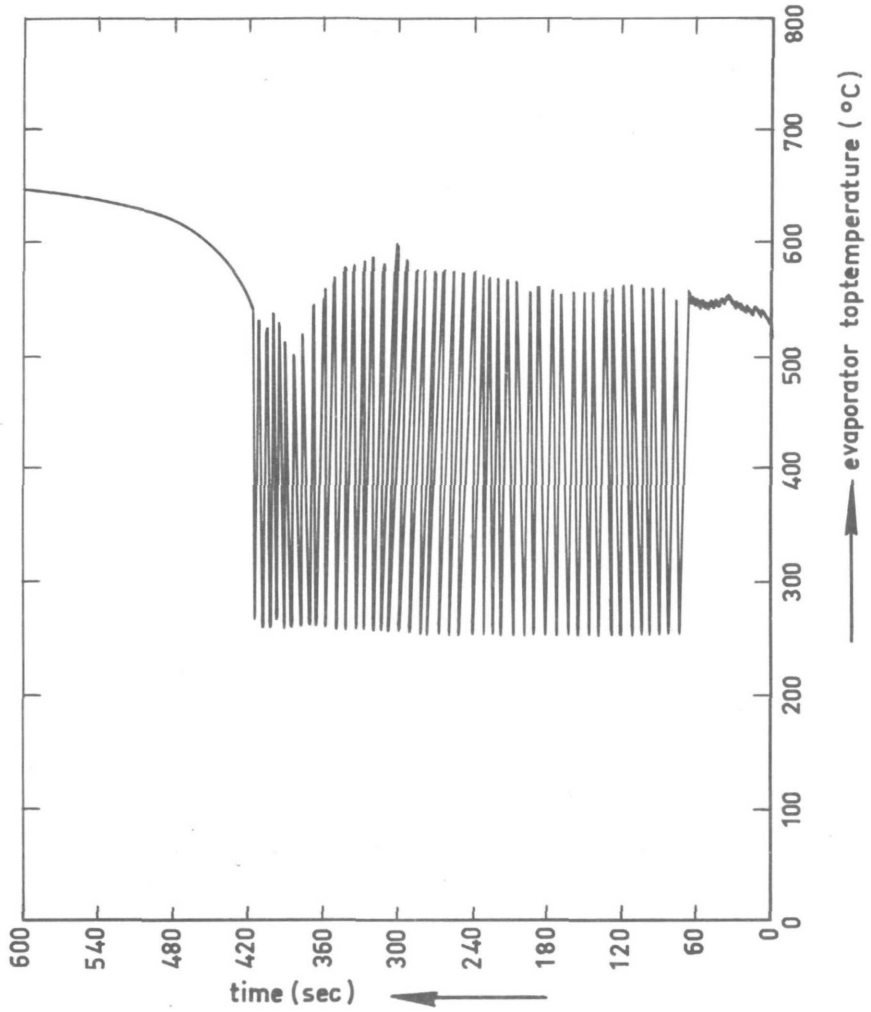

FIGURE 4.3-6.

Top temperature during shut-down instability.

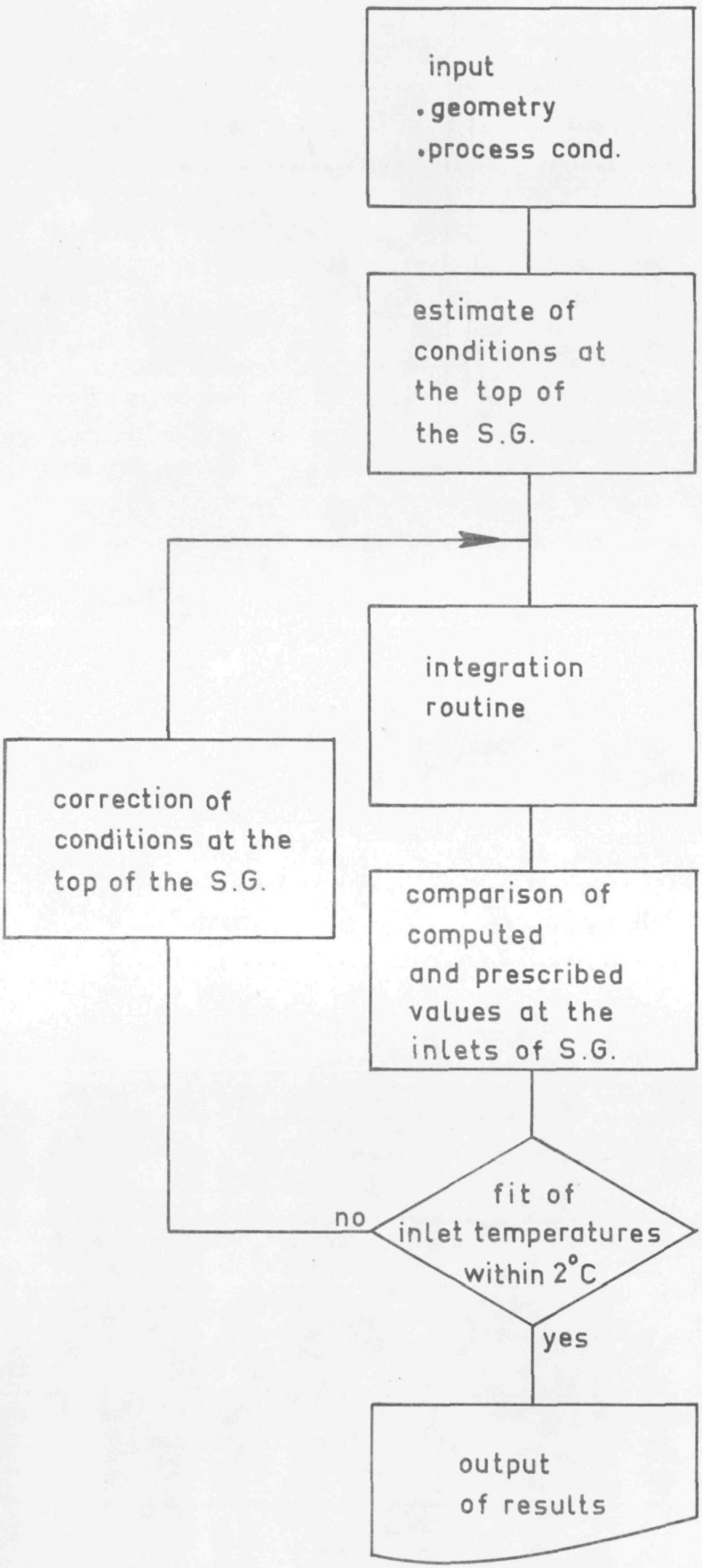

FIGURE 4.4-1.

Structure of steady state program.

```
**********************************************************
*                                                        *
*          METING 2        INPUT DATA          BASTA     *
*                                                        *
**********************************************************
```

TOTAL LENGTH	9.10	M
PIPE DIAMETER 1	0.0603	M
PIPE DIAMETER 2	0.0525	M
PIPE DIAMETER 3	0.0250	M
PIPE DIAMETER 4	0.0206	M
PIPE DIAMETER 5	0.0172	M
PIPE DIAMETER 6	0.0126	M
HEAT RESISTANCE OF INSULATION	0.0010	CM**2/W
INSULATING LENGTH	2.40	M
SALT IN TEMP	586.2	C
MASSFLOW SALT	0.9	KG/S
STEAM PRESSURE	177.0	BAR
FEEDWATER TEMP	275.3	C
MASSFLOW FEEDWATER	0.056	KG/S
STEAM_TOP ENT	2647.548	KJ/KG

```
**********************************************************
*                                                        *
*          METING 2 OVERALL OUTPUT DATA       BASTA      *
*                                                        *
**********************************************************
```

TRANSMITTED POWER	121.8	KW
SALT IN TEMP	586.1	C
SALT OUT TEMP	574.3	C
MASSFLOW SALT	0.9	KG/S
FEEDWATER TEMP	274.0	C
SATURATION TEMP	355.57	C
TOP TEMP	362.95	C
STEAM OUT TEMP	508.7	C
MASSFLOW FEEDWATER	0.056	KG/S
STEAM PRESSURE	177.0	BAR

FIGURE 4.4-2.

Sample output of "BASTA".

Z	TSALT	TWALL SALTSIDE	TWALL STEAMSIDE	TSTEAM	TWALL STEAMSIDE	TWALL WATERSIDE	TWATER	DELTAZ	QUALITY X
0.000000	574.3328	504.2342	454.9224	362.9505	362.9505	362.9505	362.9505	0.000000	1.000000
0.150000	574.7188	510.4828	465.4164	371.9246	365.9352	368.0352	362.6667		
0.300000	575.1050	515.1504	473.2266	380.8983	374.7664	371.3557	362.4225	0.300000	1.000000
0.450000	575.4346	520.6868	482.5254	390.9773	381.7256	376.4302	361.7336		
0.600000	575.7642	524.6959	489.2332	401.0563	386.3350	379.5582	361.0448	0.300000	1.000000
0.750000	576.0474	529.0506	496.5114	410.3056	392.1413	383.7429	360.0910		
0.900000	576.3306	532.1649	501.6901	419.5550	395.8658	386.1998	359.1372	0.300000	1.000000
0.915000	576.3571	533.4948	502.2382	420.4152	396.2969	386.4988	359.0368		
0.930000	576.3835	532.8151	502.7701	421.2755	396.7120	386.7845	358.9364	0.030000	1.000000
0.945000	576.4096	533.1356	503.3023	422.0907	395.1918	384.3581	358.8281		
0.960000	576.4357	533.4268	503.7842	422.9059	397.4958	387.3160	358.7198	0.030000	1.000000
1.110000	576.6777	536.5473	508.9538	430.0862	400.1871	388.1581	357.7067		
1.260000	576.9198	538.6054	512.3325	437.2664	401.0952	387.5635	356.6935	0.300000	1.000000
1.410000	577.1598	540.8250	515.9602	442.8706	404.8067	390.6137	356.1331		
1.560000	577.3582	542.4674	518.6237	448.4749	407.5210	392.8764	355.5726	0.300000	0.585027
1.710000	577.5598	544.1964	521.4270	453.0216	410.8766	395.8266	355.5726		
1.860000	577.7613	545.5156	523.5433	457.5682	413.4732	398.1724	355.5726	0.300000	0.526517
2.010000	577.9496	546.8979	525.7618	461.2766	416.3553	400.8428	355.5726		
2.160000	578.1367	547.9735	527.4672	464.9849	418.7280	403.0269	355.5726	0.300000	0.866694
2.310000	578.3134	549.0966	529.2500	468.0325	421.3156	405.4775	355.5726		
2.460000	578.4901	549.9914	530.6518	471.0801	423.4517	407.5435	355.5726	0.300000	0.805988
2.610000	578.6579	550.9216	532.1114	473.6201	425.7557	409.8345	355.5726		
2.760000	578.8257	551.6830	533.2903	476.1601	427.7844	411.8231	355.5726	0.300000	0.745003
2.910000	578.9863	552.4704	534.5116	478.3187	429.9524	414.0072	355.5726		
3.060000	579.1468	553.1343	535.5283	480.4774	431.8478	415.9544	355.5726	0.300000	0.684216
3.210000	579.3012	553.8170	536.5756	482.3561	433.8551	418.0776	355.5726		
3.360000	579.4556	554.4105	537.4760	434.2347	435.7429	420.0158	355.5726	0.300000	0.624012
3.510000	579.6046	555.0173	538.3980	485.9133	437.7268	422.1168	355.5726		
3.660000	579.7536	555.5611	539.2168	487.5918	439.5536	424.0733	355.5726	0.300000	0.564701
3.810000	579.8979	556.1125	540.0504	489.1326	441.5101	426.1844	355.5726		
3.960000	580.0421	556.6234	540.8139	490.6733	443.3462	428.1819	355.5726	0.300000	0.506543
4.110000	580.1819	557.1388	541.5870	492.1246	445.3096	430.3294	355.5726		
4.260000	580.3217	557.6259	542.3151	493.5759	447.1818	432.3867	355.5726	0.300000	0.449758
4.410000	580.4573	558.1164	543.0488	494.9750	448.9732	434.5921	355.5726		
4.560000	580.5929	558.5859	543.7365	496.3741	451.0982	436.7241	355.5726	0.300000	0.394537
4.710000	580.7244	559.0651	544.4667	497.7495	453.1405	439.0040	355.5726		
4.860000	580.8560	559.5318	545.1354	499.1249	455.1314	441.2223	355.5726	0.300000	0.341048
4.875000	580.8699	559.5784	545.2352	499.2616	455.3368	441.4521	355.5726		
4.890000	580.8818	559.6250	545.3049	499.3983	455.5417	441.6814	355.5726	0.030000	0.326312
4.903000	580.8947	559.6716	545.3747	499.5350	455.7478	441.9122	355.5726		
4.920000	580.9076	559.7181	545.4444	499.6716	455.9534	442.1424	355.5726	0.030000	0.331488
4.935000	580.9205	559.7647	545.5141	499.8084	456.1603	442.3741	355.5726		
4.950000	580.9333	559.8112	545.5837	499.9451	456.3667	442.6052	355.5726	0.030000	0.326284
4.965000	580.9461	559.8577	545.6534	500.0818	456.5742	442.8378	355.5726		
4.980000	580.9589	559.9041	545.7230	500.2186	456.7814	443.0695	355.5726	0.030000	0.321098
4.995000	580.9717	559.9506	545.7927	500.3554	456.9857	443.3034	355.5726		
5.010000	580.9845	559.9970	545.8623	500.4922	457.1976	443.5365	355.5726	0.030000	0.315931
5.025000	580.9972	560.0435	545.9319	500.6290	457.4066	443.7710	355.5726		
5.040000	581.0099	560.0899	546.0015	500.7659	457.6153	444.0049	355.5726	0.030000	0.310784
5.055000	581.0226	560.1363	546.0711	500.9029	457.8252	444.2404	355.5726		
5.070000	581.0353	560.1827	546.1406	501.0398	458.0346	444.4753	355.5726	0.030000	0.305657

FIGURE 4.4-2.

Sample output of "BASTA" (continued).

5.085000	581.0480	560.2291	546.2102	501.1769	458.2452	444.7117	355.5726		
5.100000	581.0636	560.2755	546.2793	501.3140	458.4554	444.9476	355.5726	C.030000	0.300549
5.115000	581.0732	560.3219	546.3494	501.4511	458.6665	445.1850	355.5726		
5.130000	581.0858	560.3683	546.4190	501.5882	458.8779	445.4219	355.5726	C.030000	0.295461
5.145000	581.0984	560.4147	546.4886	501.7256	459.0901	445.6602	355.5726		
5.160000	581.1110	560.4610	546.5582	501.8630	459.3019	445.8981	355.5726	C.030000	0.290393
5.175000	581.1235	560.5074	546.6278	502.0004	459.5145	446.1374	355.5726		
5.190000	581.1360	560.5537	546.6974	502.1379	459.7275	446.3762	355.5726	C.030000	0.285346
5.205000	581.1485	560.6001	546.7670	502.2755	459.9414	446.6166	355.5726		
5.220000	581.1610	560.6465	546.8367	502.4131	460.1548	446.8564	355.5726	C.030000	0.280318
5.235000	581.1734	560.6928	546.9063	502.5505	460.3694	447.0977	355.5726		
5.250000	581.1859	560.7392	546.9760	502.6887	460.5837	447.3385	355.5726	C.030000	0.275311
5.265000	581.1983	560.7856	547.0457	502.8267	460.7992	447.5808	355.5726		
5.280000	581.2107	560.8319	547.1154	502.9647	461.0142	447.8226	355.5726	C.030000	0.270324
5.295000	581.2231	560.8783	547.1851	503.1029	461.2305	448.0659	355.5726		
5.310000	581.2354	560.9247	547.2549	503.2411	461.4464	448.3087	355.5726	C.030000	0.265358
5.325000	581.2477	560.9711	547.3247	503.3795	461.6633	448.5530	355.5726		
5.340000	581.2601	561.0175	547.3945	503.5179	461.8803	448.7968	355.5726	C.030000	0.260413
5.355000	581.2723	561.0639	547.4643	503.6565	462.0983	449.0421	355.5726		
5.370000	581.2846	561.1103	547.5342	503.7952	462.3159	449.2869	355.5726	C.030000	0.255485
5.385000	581.2969	561.1567	547.6040	503.9338	428.1161	403.2859	355.5726		
5.400000	581.3091	561.2031	547.6740	504.0727	393.9194	357.2816	355.5726	C.030000	0.250585
5.550000	581.4505	561.6674	547.7440	504.1116	391.6688	357.2527	355.5726		
5.700000	581.5919	562.1318	547.8140	504.1505	391.4451	357.2355	355.5726	C.030000	0.245800
5.850000	581.7332	562.5962	547.8840	504.1894	391.2230	357.2155	355.5726		
6.000000	581.8746	563.0605	547.9540	504.2284	391.0008	357.1955	355.5726	C.030000	0.241000
6.150000	582.0160	563.5249	548.0240	504.2673	390.7787	357.1755	355.5726		
6.300000	582.1573	563.9893	548.0940	504.3063	390.5565	357.1555	355.5726	C.030000	0.236200
6.450000	582.2987	564.4537	548.1640	504.3452	390.3344	357.1355	355.5726		
6.600000	582.4401	564.9180	548.2340	504.3842	390.1122	357.1155	355.5726	C.030000	0.231400
6.650000	582.4814	565.0724	548.2595	504.3971	390.0381	357.1088	355.5726		
6.700000	582.5228	565.2268	548.2850	504.4101	390.0381	357.1088	355.5726	C.030000	0.226600
6.850000	582.6642	565.6912	548.3550	504.4490	389.8160	357.0888	355.5726		
7.000000	582.8055	566.1556	548.4250	504.4880	389.5938	357.0688	355.5726	C.030000	0.221800
7.150000	582.9469	566.6199	548.4950	504.5269	389.3717	357.0488	355.5726		
7.300000	583.0883	567.0843	548.5650	504.5659	389.1495	357.0288	355.5726	C.030000	0.217000
7.451000	583.2297	567.5487	548.6350	504.6048	388.9274	357.0088	355.5726		
7.601000	583.3711	568.0131	548.7050	504.6438	388.7052	356.9888	355.5726	C.030000	0.212200
7.751000	583.5125	568.4774	548.7750	504.6827	388.4831	356.9688	355.5726		
7.901000	583.6538	568.9418	548.8450	504.7217	388.2609	356.9488	355.5726	C.030000	0.207400
8.051000	583.7952	569.4062	548.9150	504.7606	388.0388	356.9288	355.5726		
8.201000	583.9366	569.8706	548.9850	504.7996	387.8166	356.9088	355.5726	C.030000	0.202600
8.351000	584.0780	570.3349	549.0550	504.8385	387.5945	356.8888	355.5726		
8.501000	584.2193	570.7993	549.1250	504.8775	387.3723	356.8688	355.5726	C.030000	0.197800
8.651000	584.3607	571.2637	549.1950	504.9164	387.1502	356.8488	355.5726		
8.801000	584.5021	571.7281	549.2650	504.9554	386.9280	356.8288	355.5726	C.030000	0.193000
8.955000	584.6435	572.2044	549.3371	504.9943	386.7059	356.8088	355.5726		
9.110000	584.7848			505.0333	386.4837	356.7888	355.5726	C.030000	0.188200

FIGURE 4.4-2.

Sample output of "BASTA" (continued).

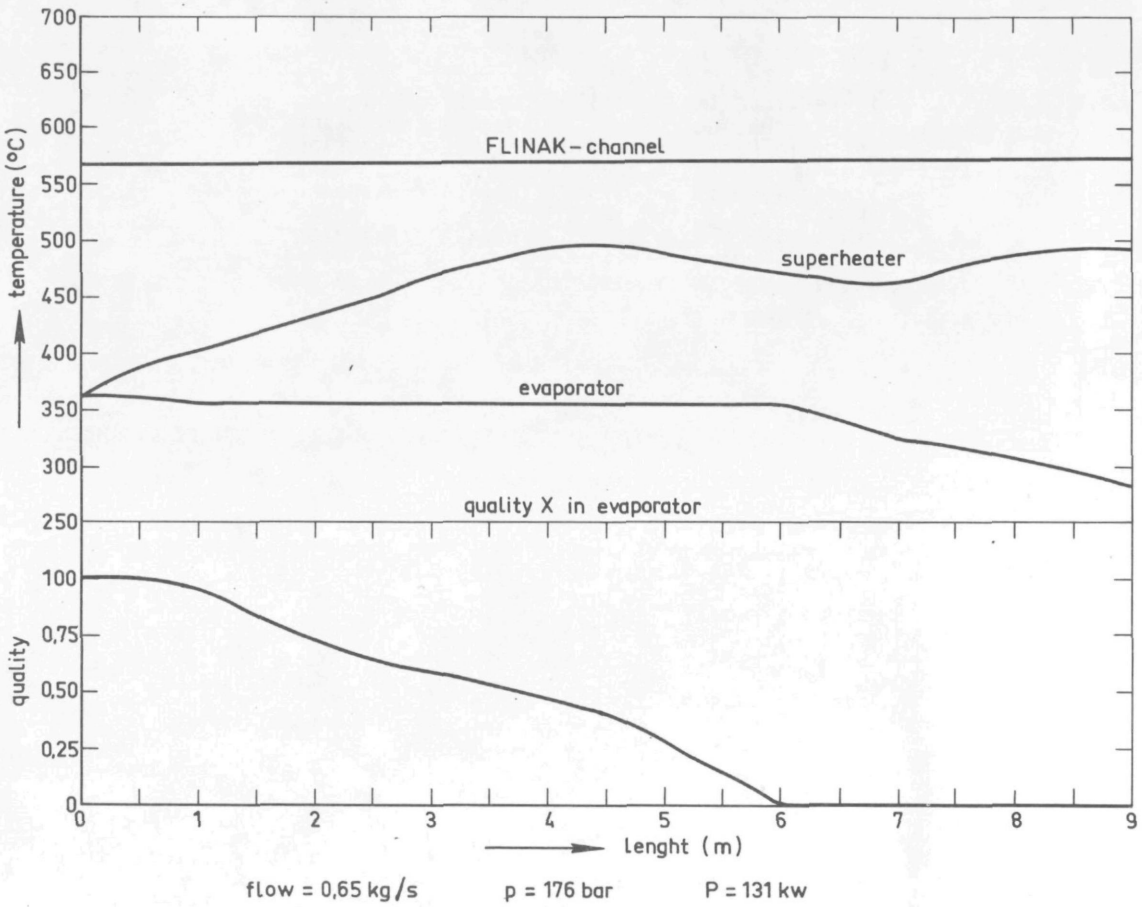

FIGURE 4.4-3.

Sample plot output of "BASTA".

METING 2 SERIE 180 09-3-75

FLINAK	FLOW	= 6.94	KG/S
	TEMPERATURE IN	= 586	DEGREE CENTIGRADE
	TEMPERATURE OUT	= 577	DEGREE CENTIGRADE
	SPECIFIC HEAT	= 2.02KJ/KG*DEGREECENTIGRADE	
WATER	FLOW	=.0580	KG/S
	TEMPERATURE IN	= 275	DEGREE CENTIGRADE
	PRESSURE IN	= 179	BAR
STEAM	TEMPERATURE OUT	= 501	DEGREE CENTIGRADE
	PRESSURE OUT	= 177	BAR
POWER	DELIVERED	= 120	KW

TEMPERATURE-, QUALITY —AND HEAT_RESISTANCE DISTRIBUTION IN STEAMGENERATOR

LENGTH (M)	T_FLINAK (C)	T_STEAM (C)	T_WATER (C)	QUALITY	R FL/ST (M**2*C/KW)	R ST/W
0.00	576.0	362.8	362.8	1.00		
0.25					0.576	-0.140
0.50	576.5	403.7	368.4	1.00		
0.75					0.625	0.155
1.00	577.0	414.4	357.4	1.00		
1.25					0.643	0.231
1.50	577.6	425.0	356.3	0.87		
1.75					0.661	0.301
2.00	578.1	435.6	356.4	0.72		
2.25					0.677	0.383
2.50	578.7	446.2	356.4	0.59		
2.75					0.699	1.612
3.00	579.2	472.4	356.4	0.55		
3.25					0.719	1.150
3.50	579.7	487.1	356.4	0.49		
3.75					0.728	1.744
4.00	580.2	501.9	356.4	0.44		
4.25					0.732	1.073
4.50	580.6	505.2	356.4	0.36		
4.75					0.732	0.839
5.00	581.1	502.6	356.4	0.26		
5.25					0.731	0.794
5.50	581.6	499.9	356.4	0.15		
5.75					0.728	0.515
6.00	582.0	487.3	355.9	0.00		
6.25					0.720	0.444
6.50	582.2	474.7	340.5	0.00		
6.75					0.714	0.562
7.00	582.4	471.7	322.8	0.00		
7.25					0.718	1.267
7.50	582.6	485.0	312.8	0.00		
7.75					0.727	1.827
8.00	582.7	498.3	304.5	0.00		
8.25					0.731	1.315
8.50	582.9	501.1	291.1	0.00		
8.75					0.731	1.263
9.00	586.2	501.1	275.3	0.00		

FIGURE 4.4-4.

Sample print output of "SMEBT".

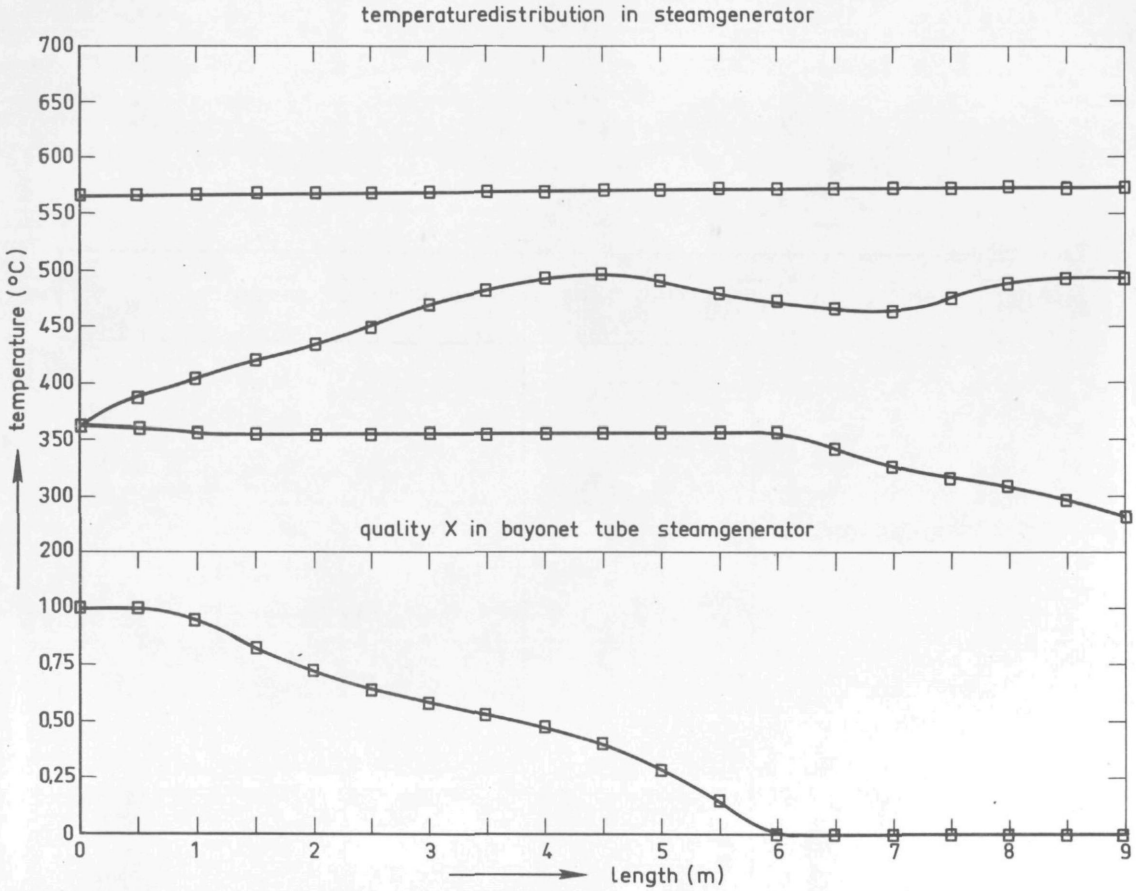

FIGURE 4.4-5.

Sample plot output of "SMEBT".

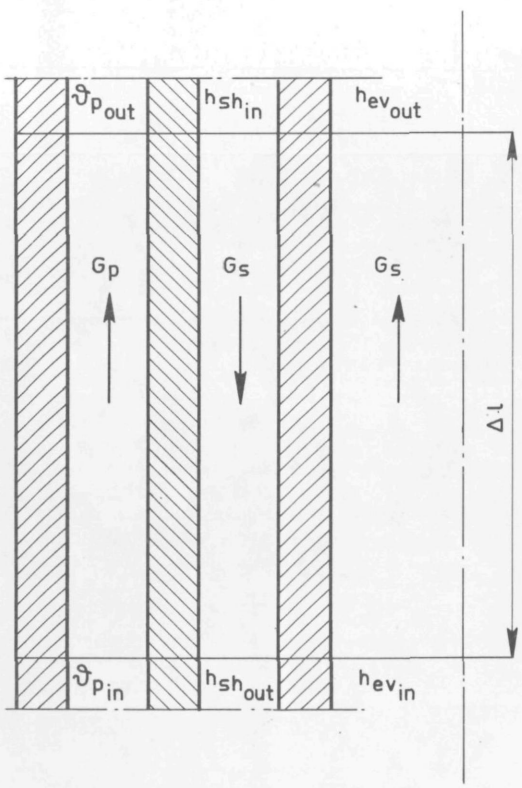

FIGURE 4.4-6.

Steam generator section covered by energy balance equation (4.4-14).

P-MEAS (kW)	P-CAL (kW)	ERROR (% of measured P)	
56.00	54.45	-2.76	
72.00	69.24	-3.84	
120.00	119.48	-0.43	
98.00	98.88	0.89	
79.00	79.13	0.17	
80.00	77.83	-2.71	for:
97.00	96.01	-1.02	a = 3.42
119.00	118.40	-0.50	b = 0.308
119.00	115.76	-2.73	
51.00	50.20	-1.57	
54.00	53.57	-0.79	
56.00	54.50	-2.68	
26.00	23.16	-10.93	
74.00	77.85	5.21	
78.00	82.34	5.57	
97.00	97.68	0.71	
98.00	102.47	4.57	

FIGURE 4.4-7.

Results of the least squares fitting of a number of steady state measurements by equation (4.4-21).

Testnumber				1	2	3	4	5	6	7	8	9	10	11
FLiNaK	Flow		[kg/s]	6.82	6.94	6.97	6.58	6.96	6.58	7.62	5.66	5.50	5.50	6.90
	Temp.	in	[^{0}C]	573	586	596	583	586	625	640	600	602	622	600
	Temp.	out	[^{0}C]	564	577	588	575	578	621	635	598	594	620	592
Water	Flow		[kg/s]	0.0648	0.0580	0.0568	0.0493	0.0445	0.039	0.027	0.013	0.045	0.012	0.052
	Temp.	in	[^{0}C]	281	275	276	257	250	271	221	248	261	249	262
	Pressure	in	[bar]	178	179	179	179	178	176	192	183	103	161	138
Steam	Temp.	out	[^{0}C]	493	501	508	496	498	540	525	497	516	516	522
	Pressure	out	[bar]	176	179	179	177	176	174	192	182	161	161	137
Power supplied			[kW]	131	120	119	106	97	90	66	28	98	26	113

FIGURE 4.4-8.

Conditions of reported steady state experiments.

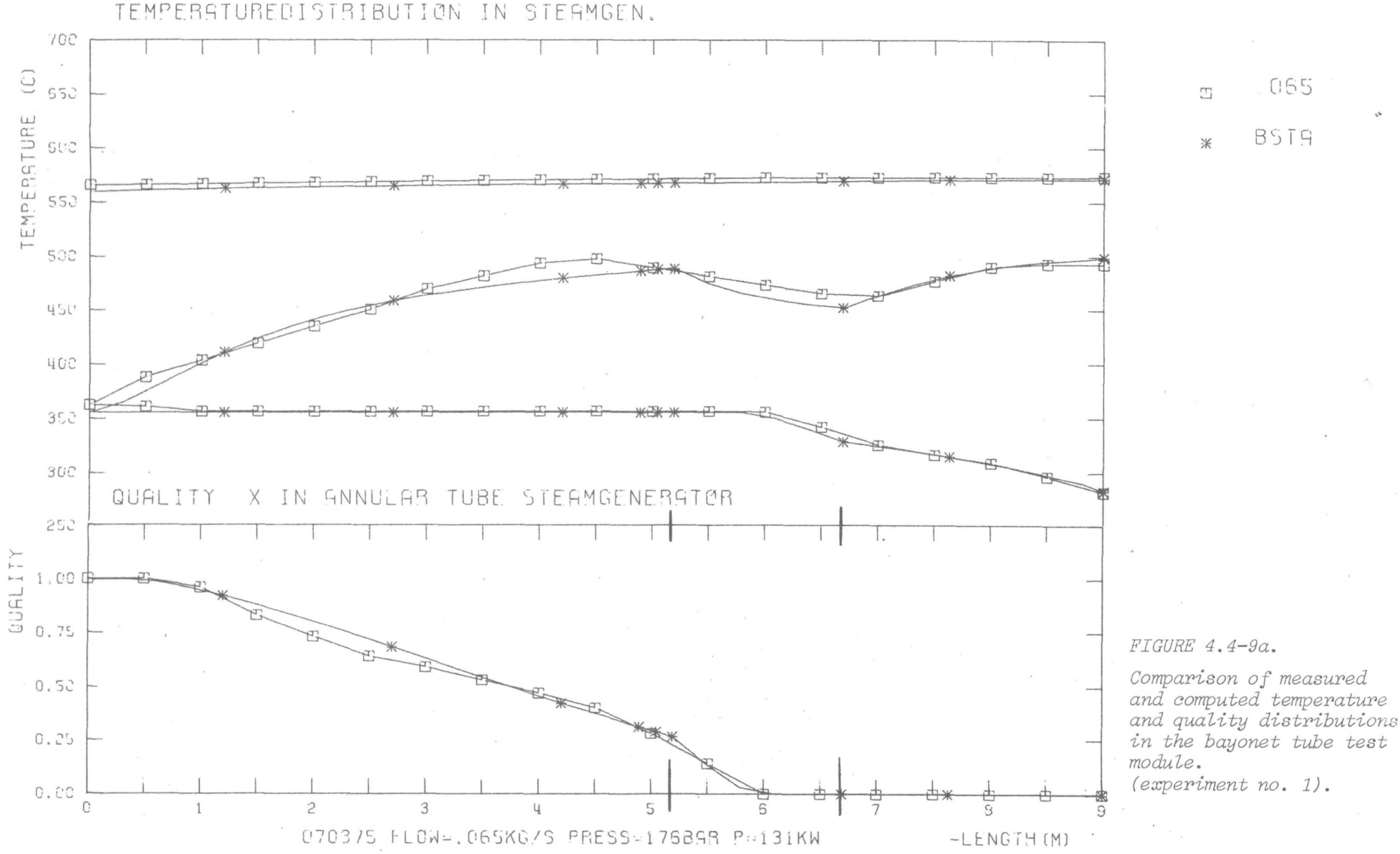

FIGURE 4.4-9a.

Comparison of measured and computed temperature and quality distributions in the bayonet tube test module. (experiment no. 1).

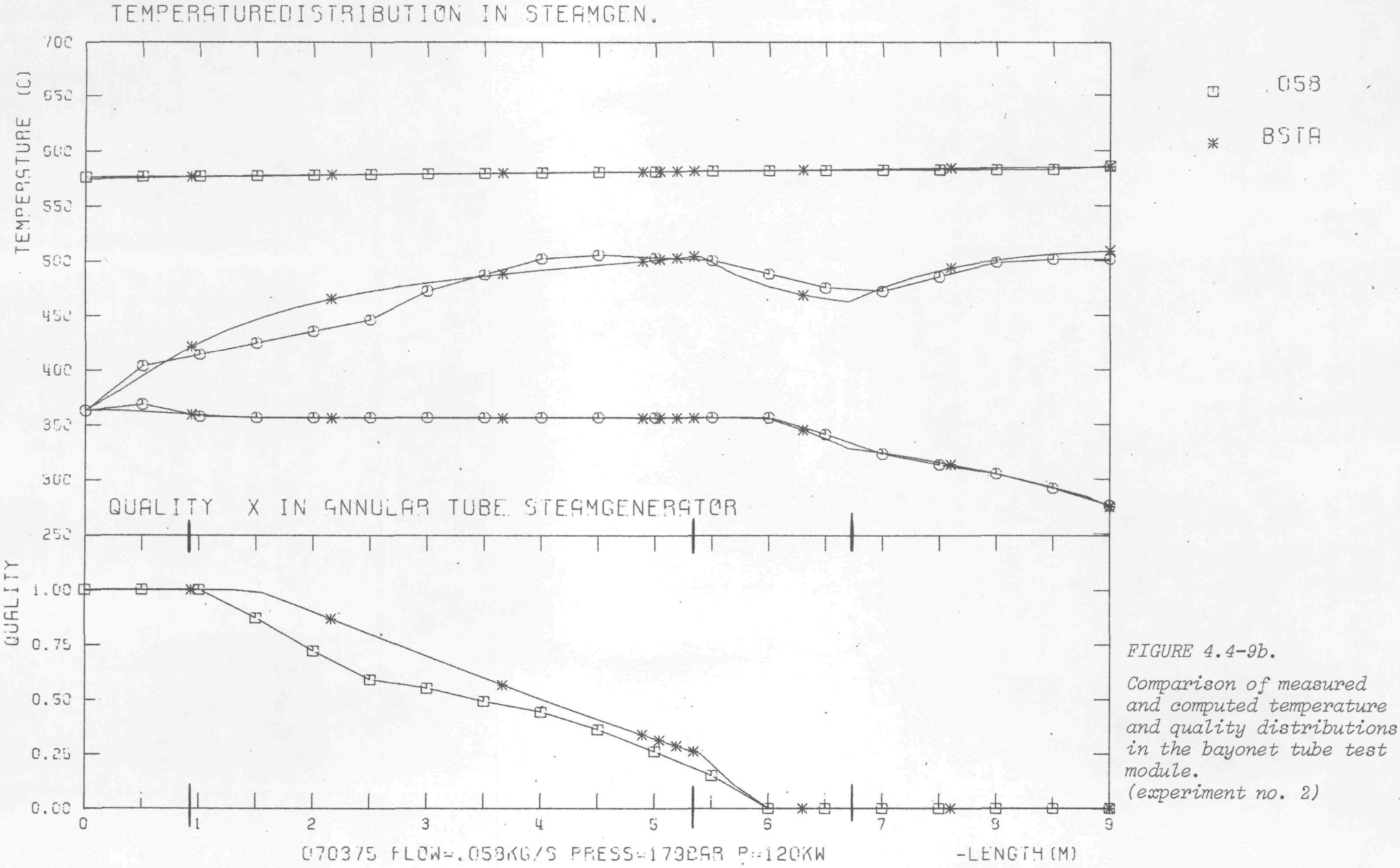

FIGURE 4.4-9b.

Comparison of measured and computed temperature and quality distributions in the bayonet tube test module.
(experiment no. 2)

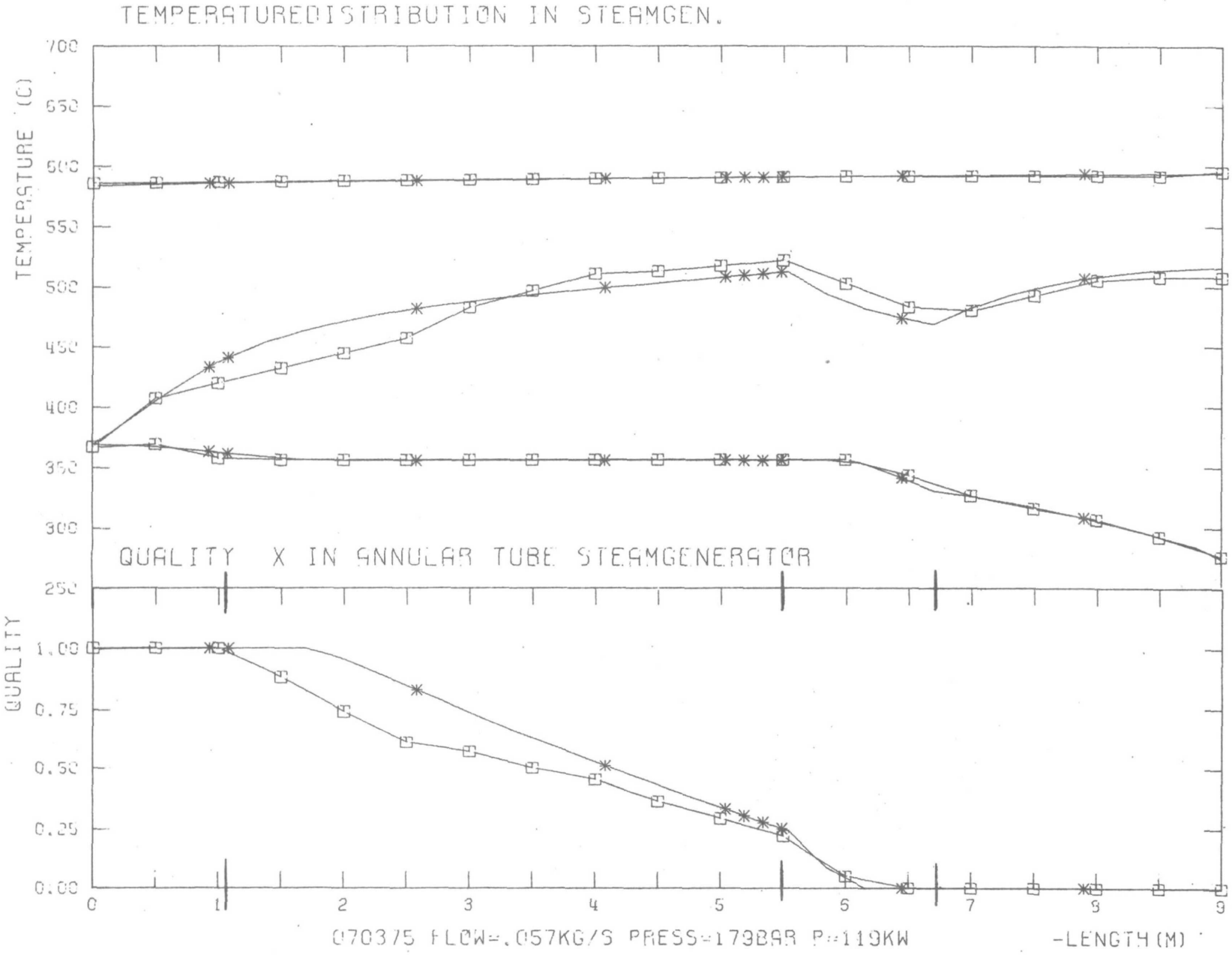

FIGURE 4.4-9c.

Comparison of measured and computed temperature and quality distributions in the bayonet tube test module.
(experiment no. 3)

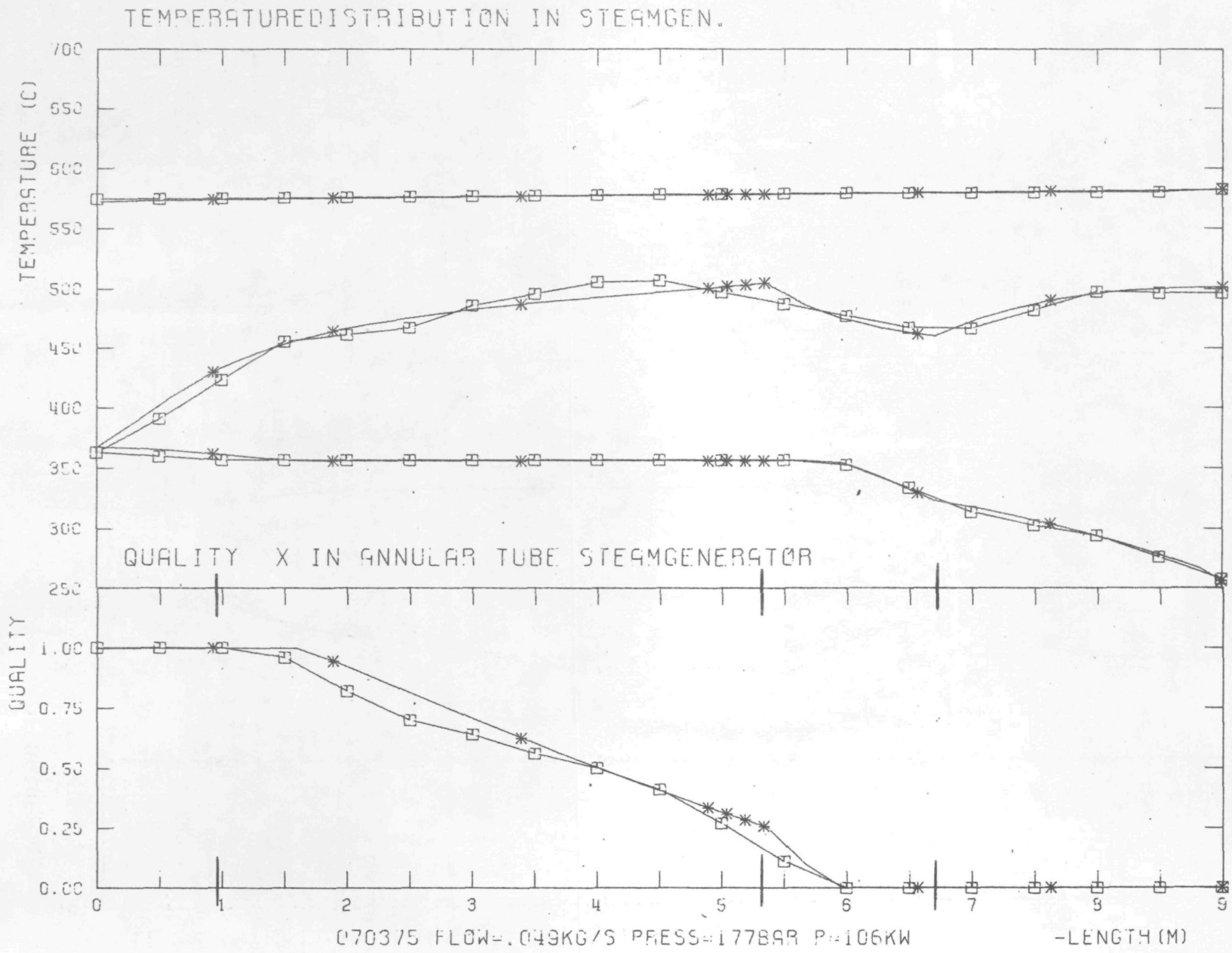

FIGURE 4.4-9d.

Comparison of measured and computed temperature and quality distributions in the bayonet tube test module. (experiment no. 4)

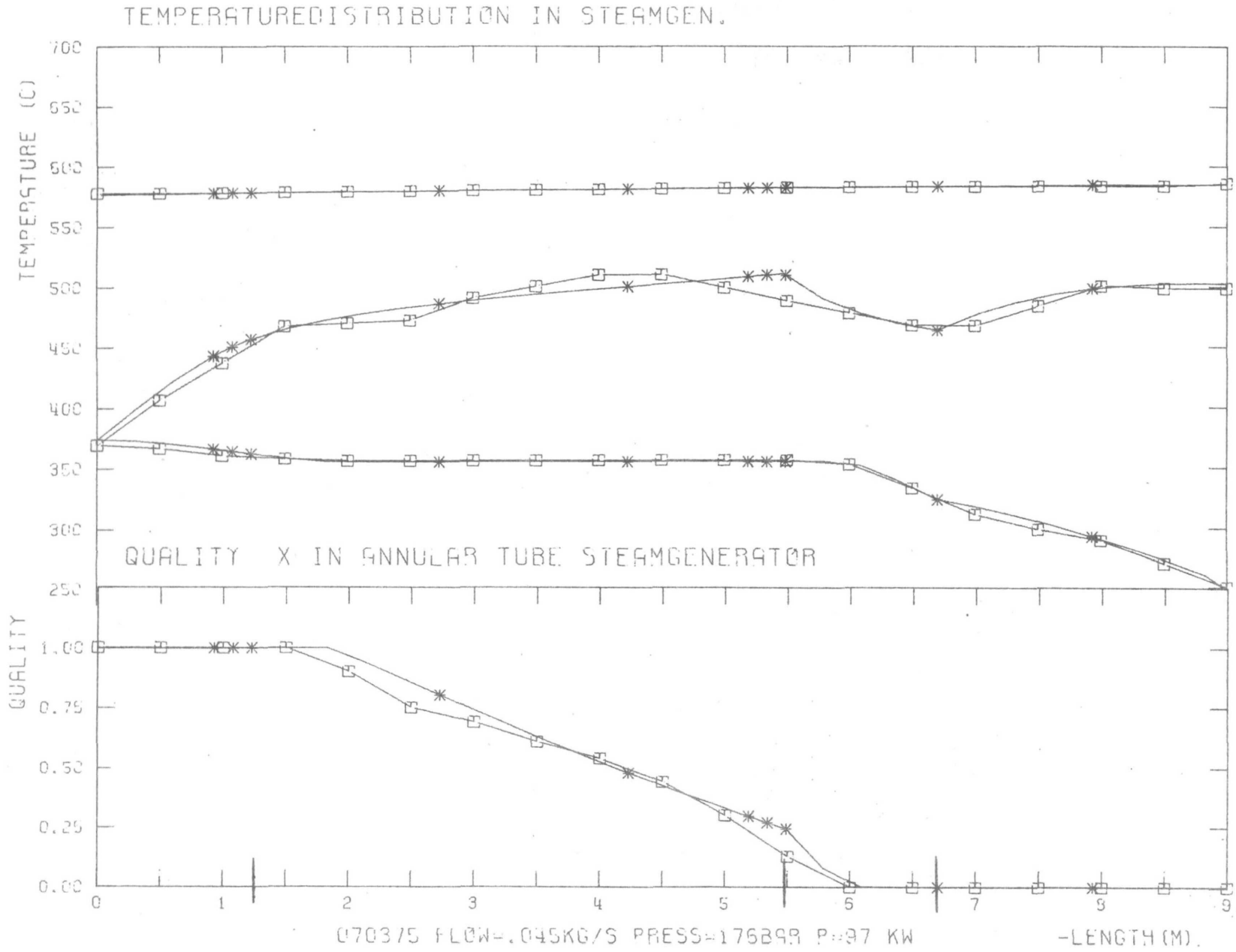

FIGURE 4.4-9e.

Comparison of measured and computed temperature and quality distributions in the bayonet tube test module. (experiment no. 5)

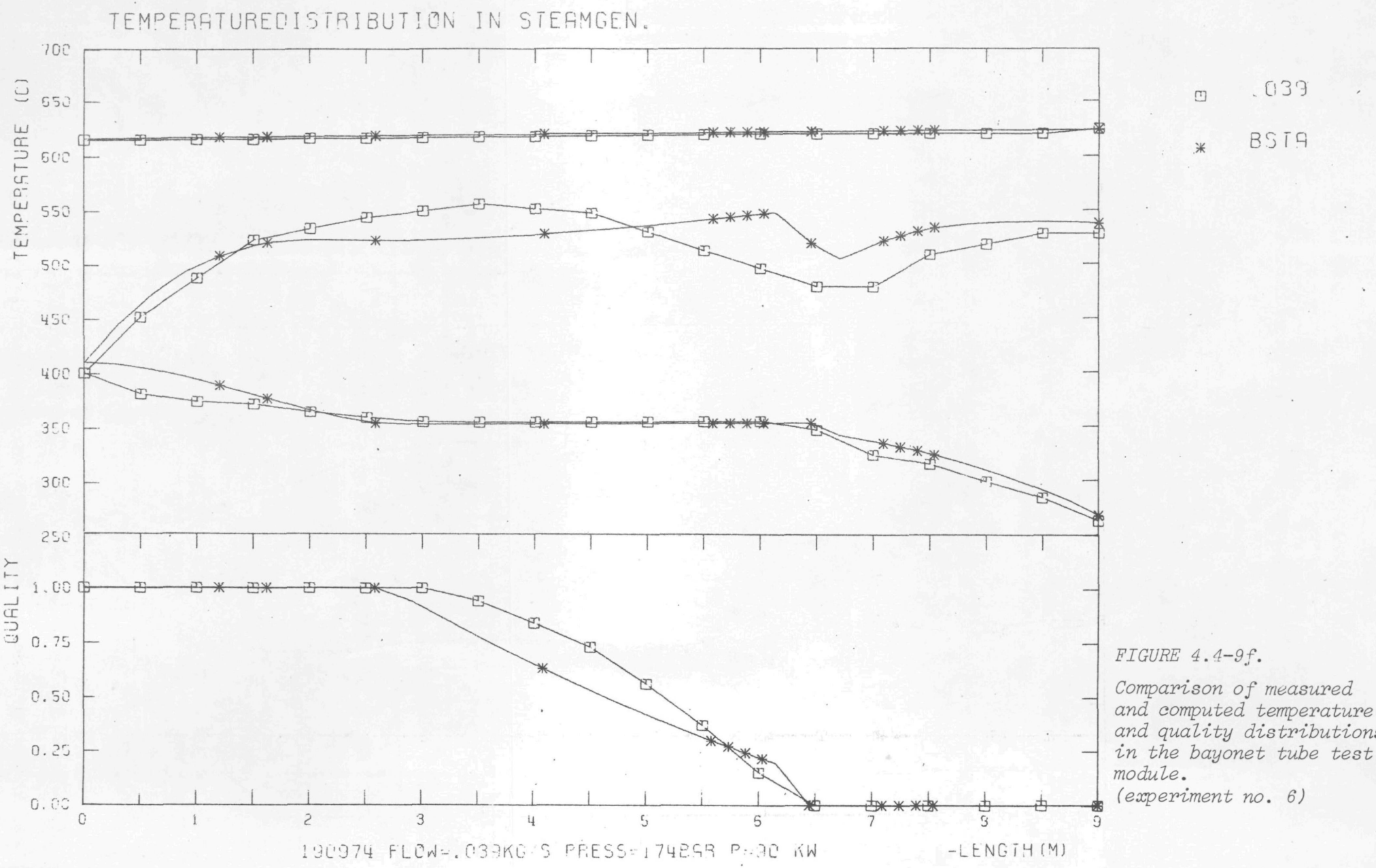

FIGURE 4.4-9f.

Comparison of measured and computed temperature and quality distributions in the bayonet tube test module.
(experiment no. 6)

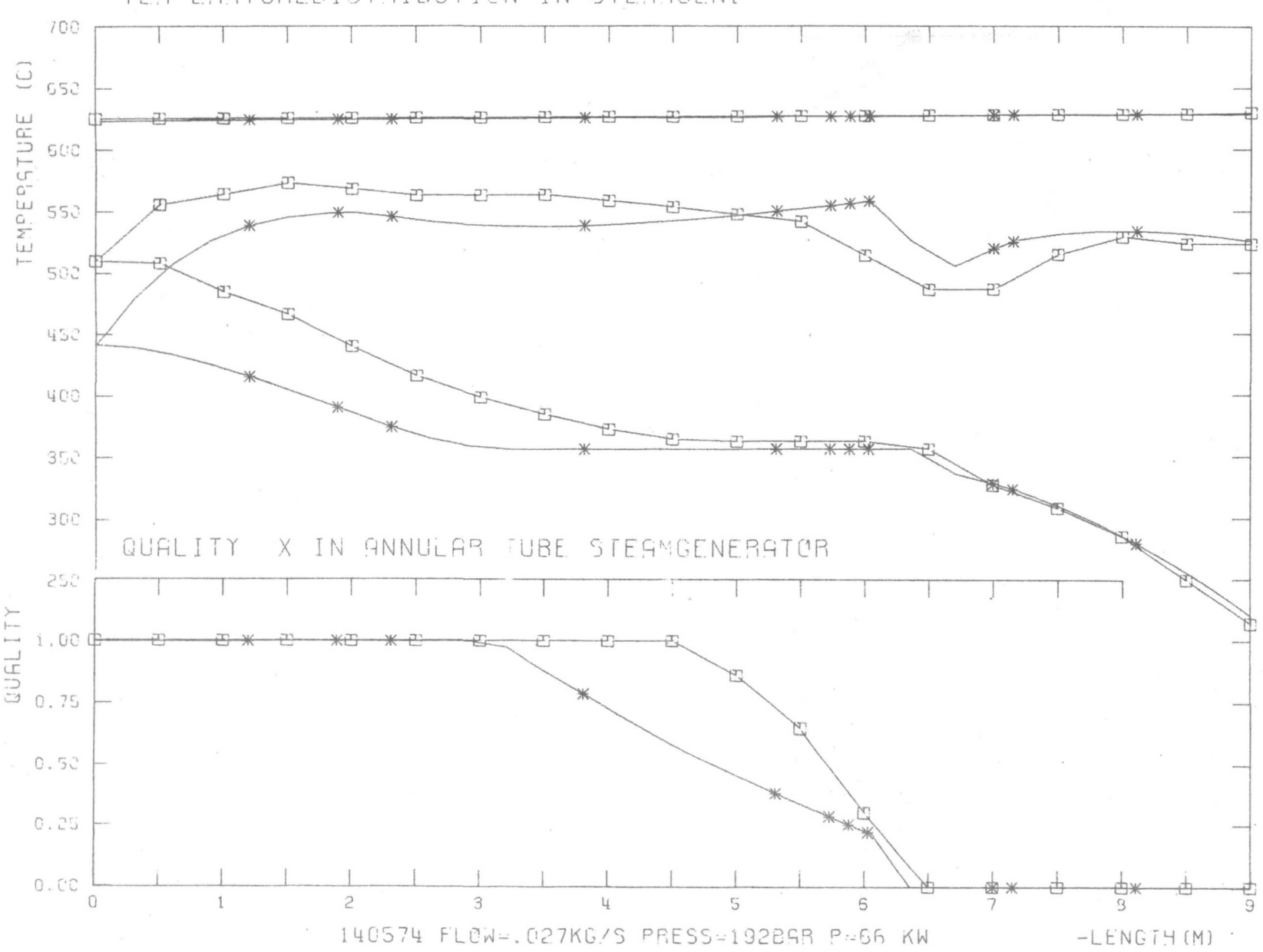

FIGURE 4.4-9g.

Comparison of measured and computed temperature and quality distributions in the bayonet tube test module.
(experiment no. 7)

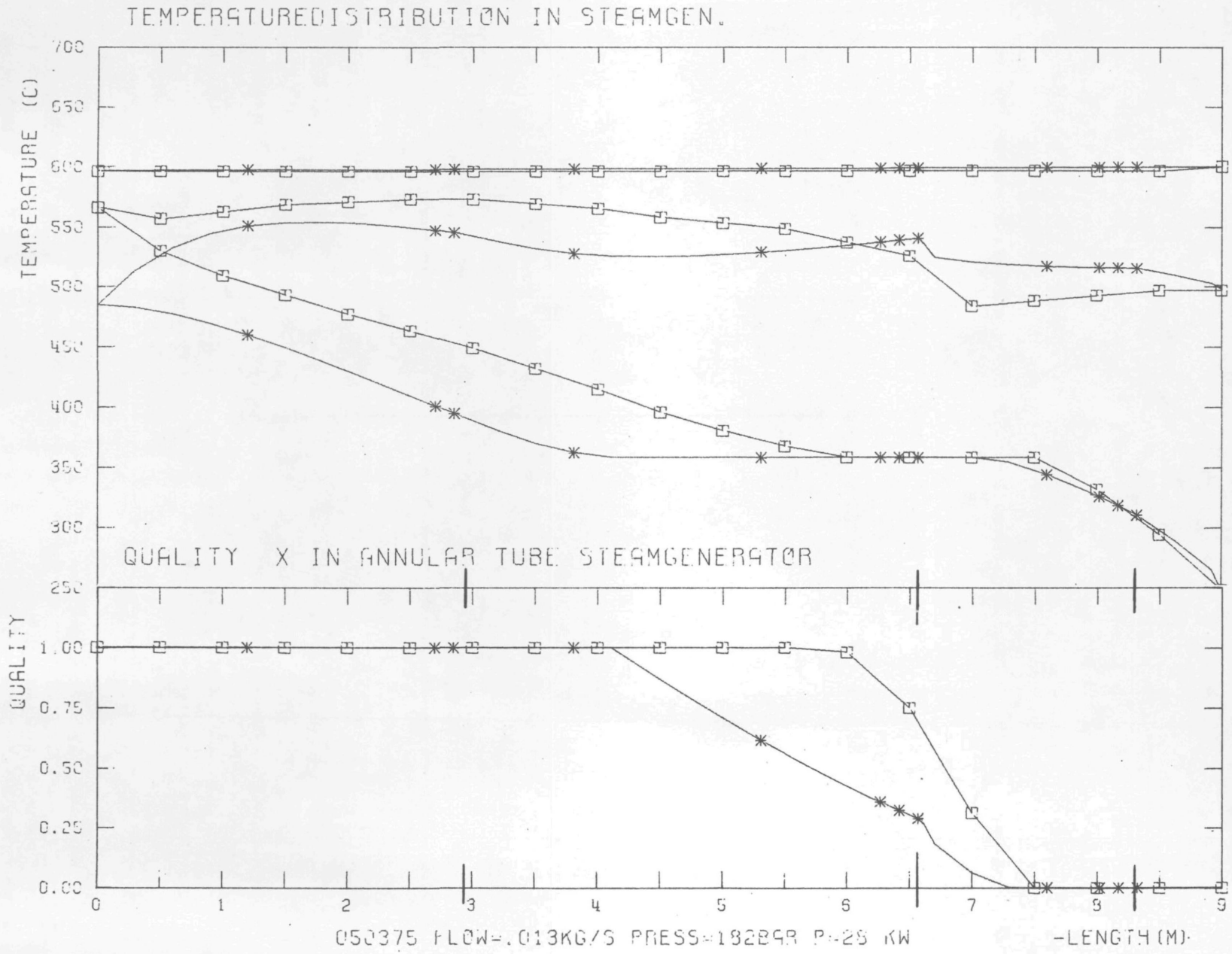

FIGURE 4.4-9h.

Comparison of measured and computed temperature and quality distributions in the bayonet tube test module.
(experiment no. 8)

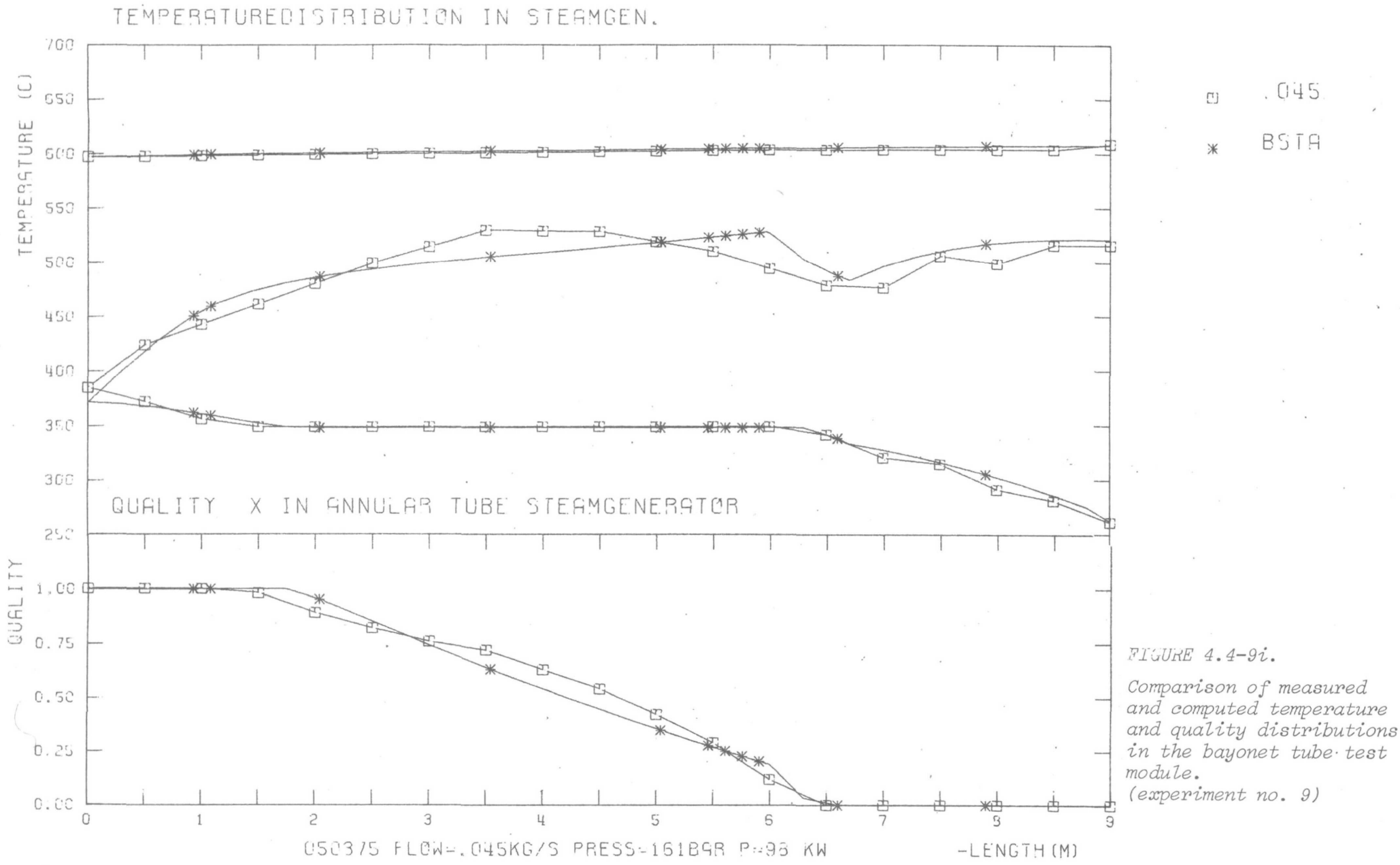

FIGURE 4.4-9i.

Comparison of measured and computed temperature and quality distributions in the bayonet tube test module.
(experiment no. 9)

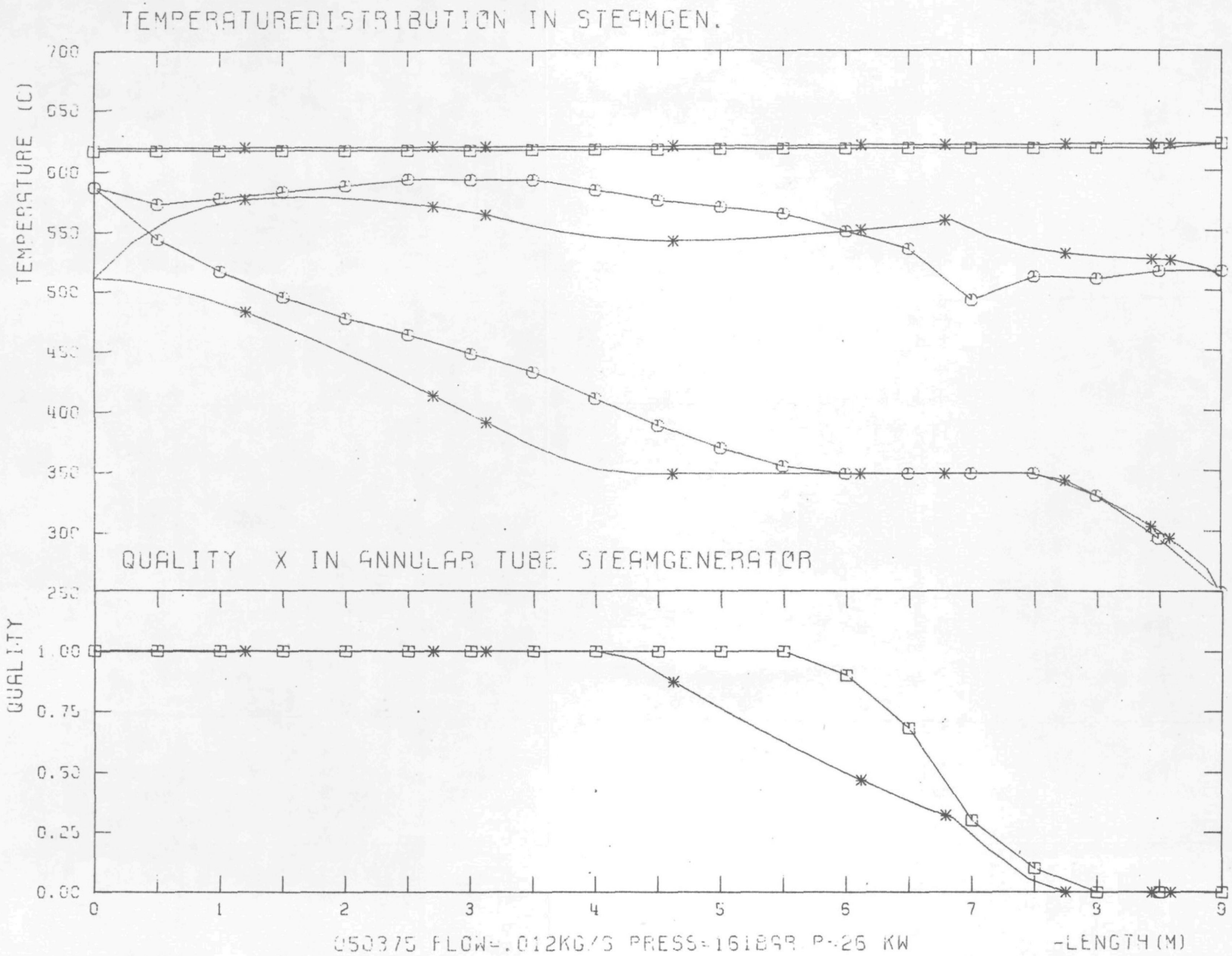

FIGURE 4.4-9j.

Comparison of measured and computed temperature and quality distributions in the bayonet tube test module.
(experiment no. 10)

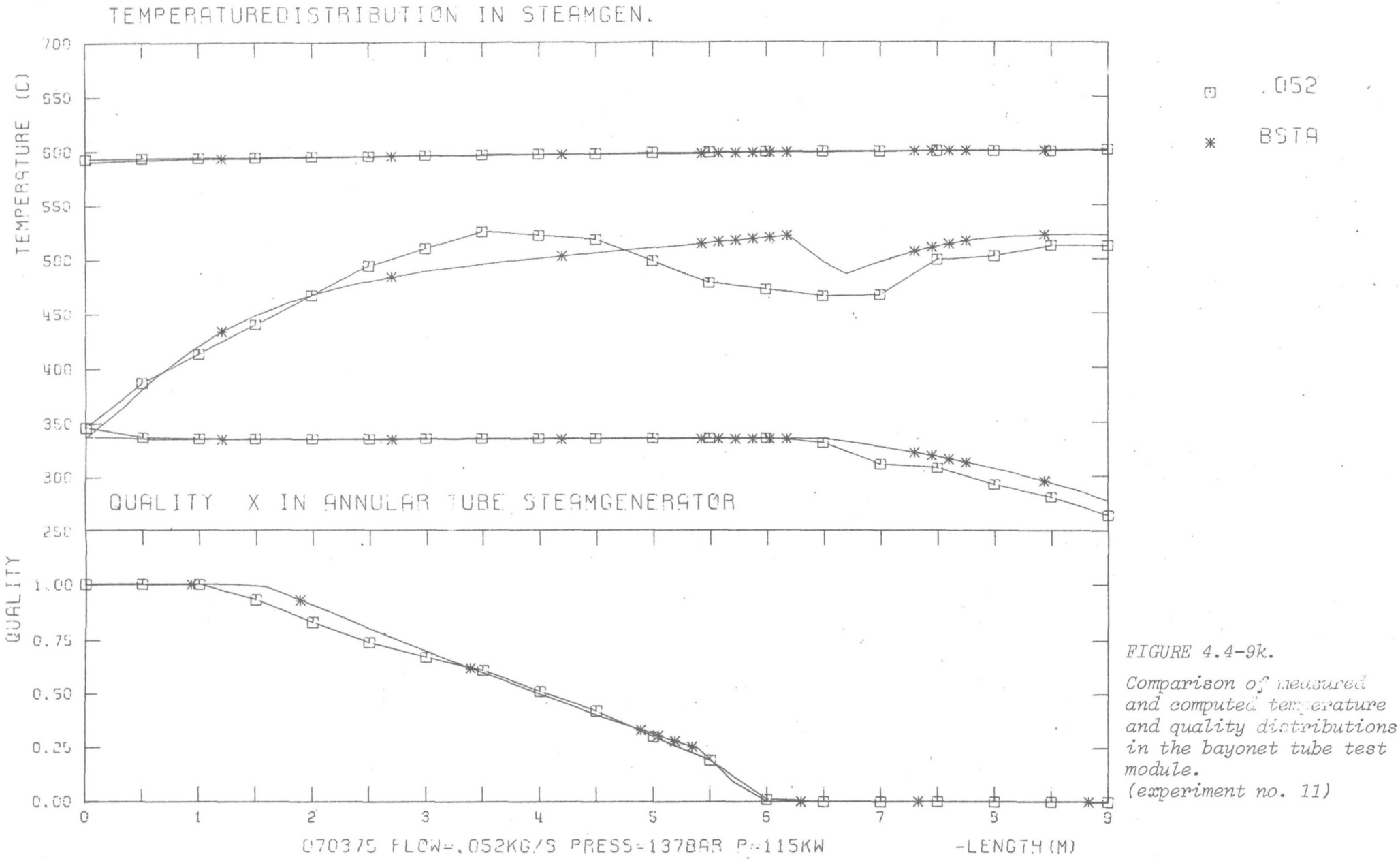

FIGURE 4.4-9k.

Comparison of measured and computed temperature and quality distributions in the bayonet tube test module.
(experiment no. 11)

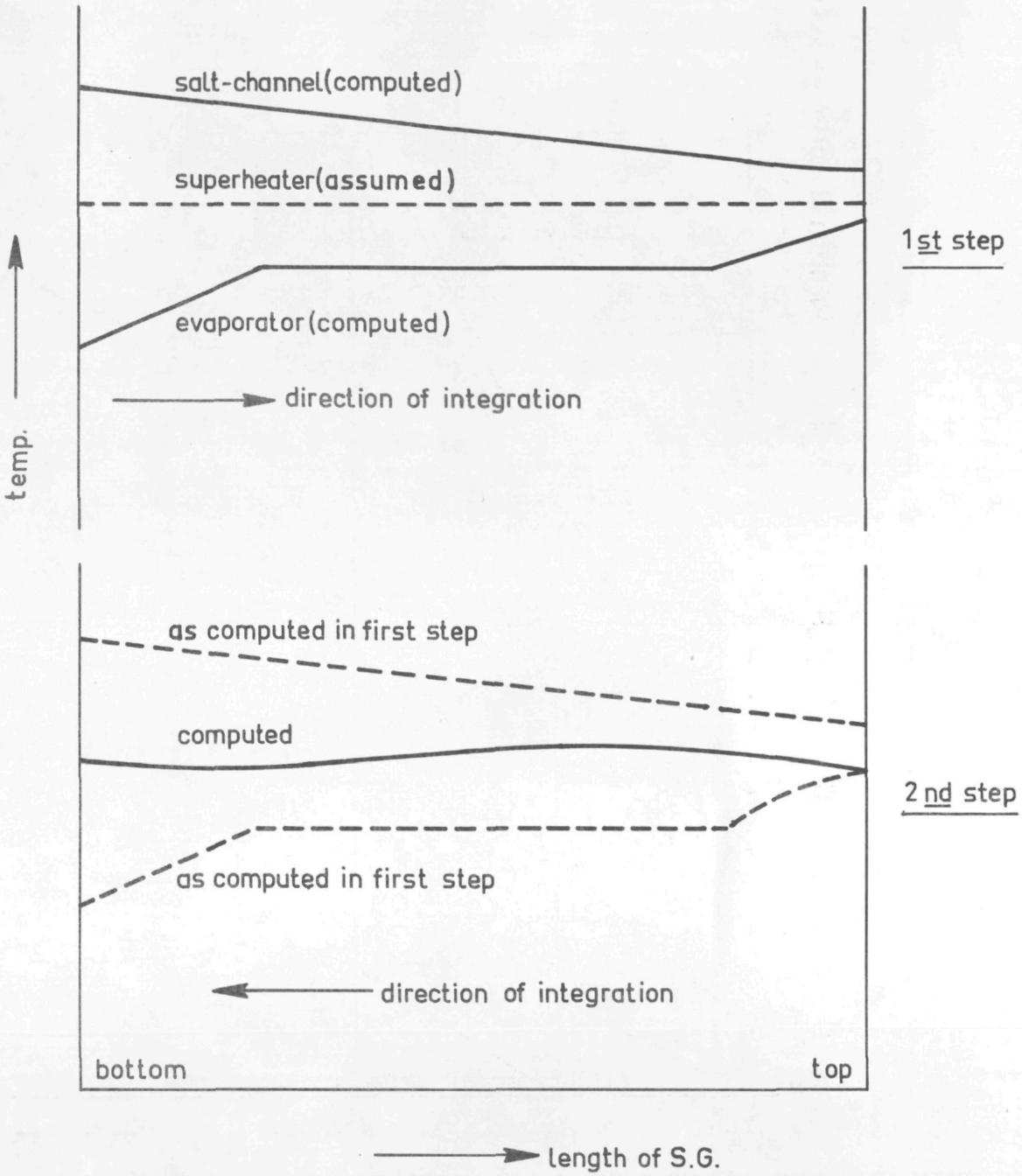

FIGURE 4.5-1.

First two steps in the iterative procedure for determination of the dynamic temperature profiles in the bayonet tube test module.

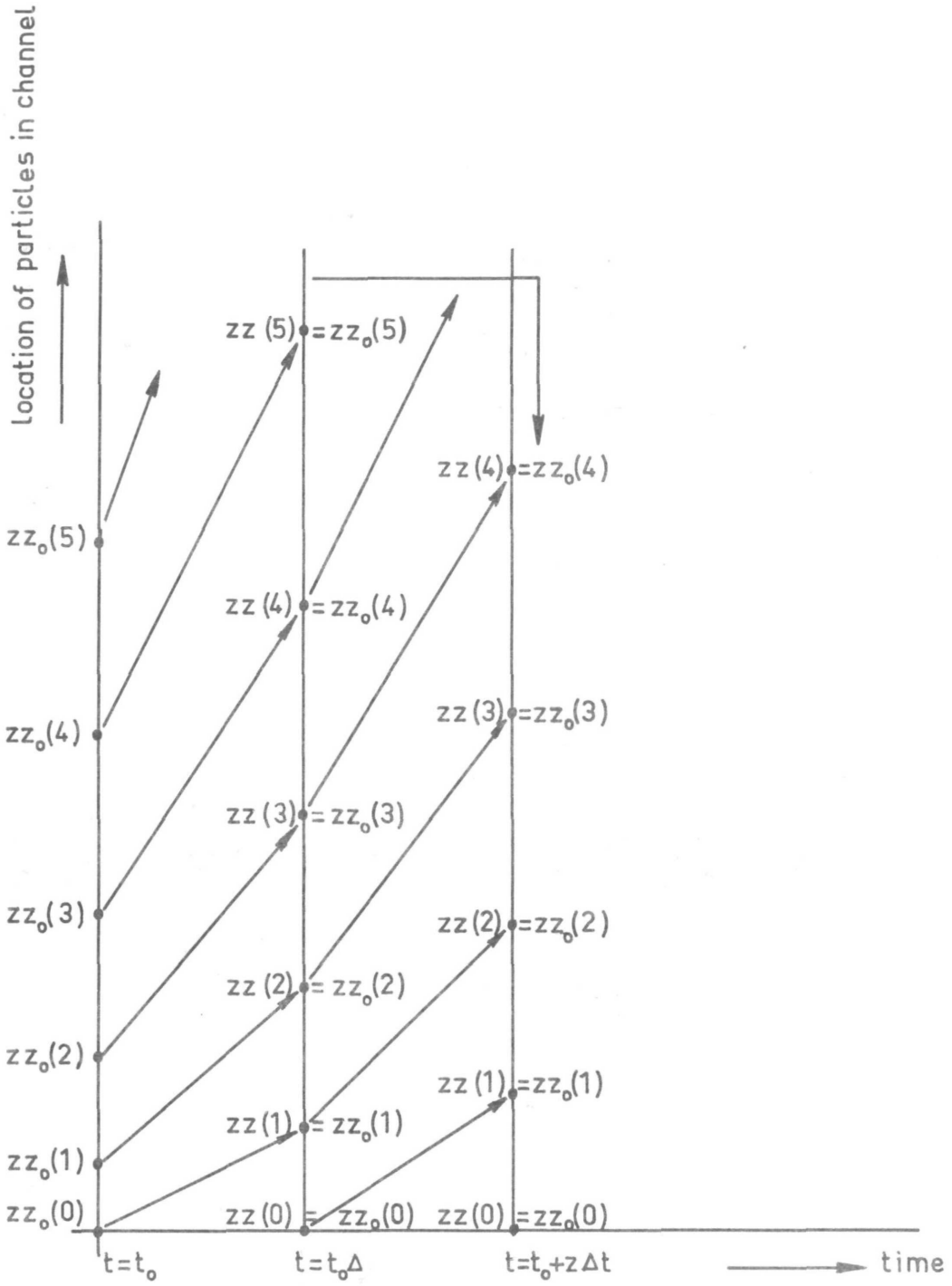

FIGURE 4.5-2.

Dynamic displacement of particles under observation.

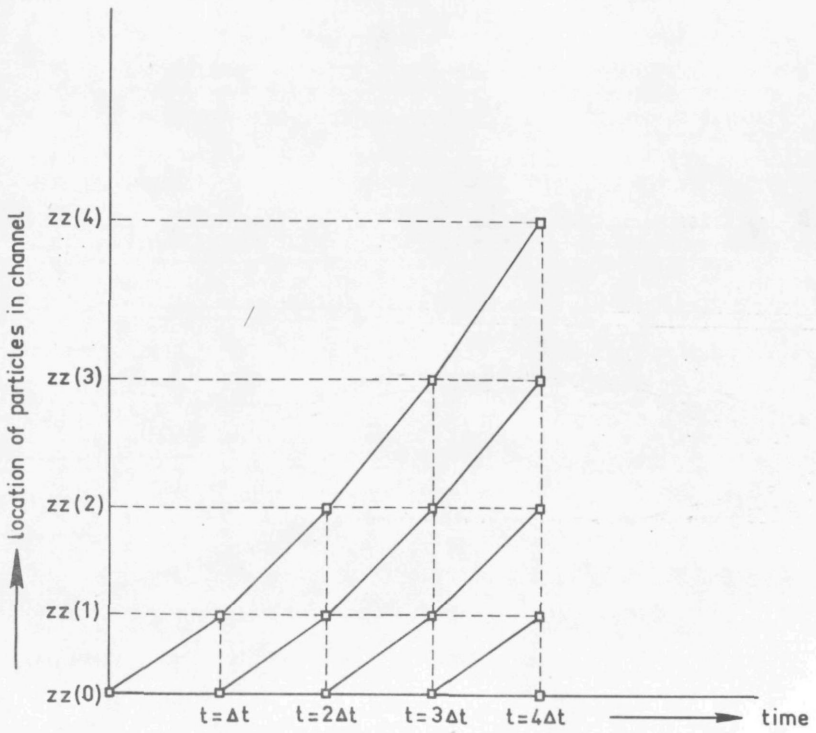

FIGURE 4.5-3.

Displacement of particles under steady state conditions.

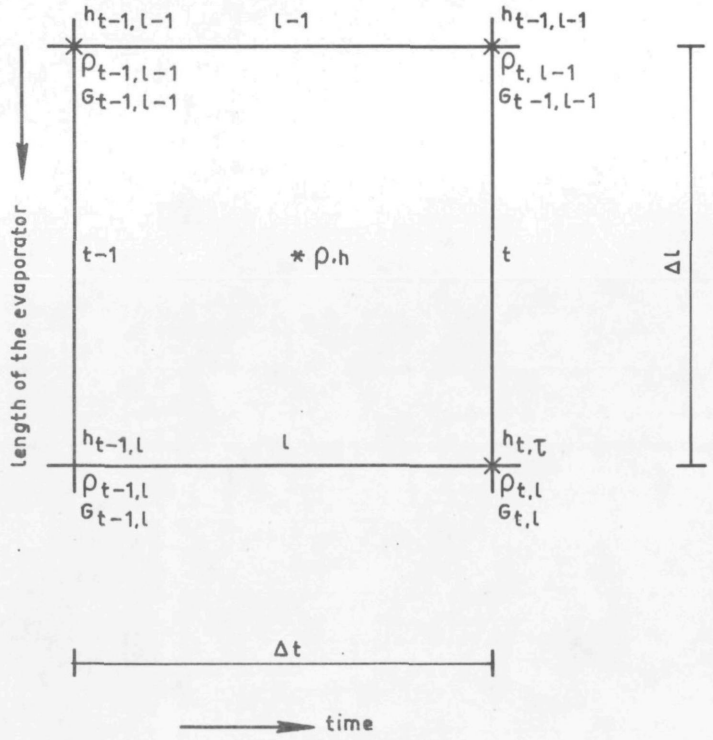

FIGURE 4.5-4.

A time-space representation of the conditions at the boundaries of a channel section of the superheater or the evaporator.

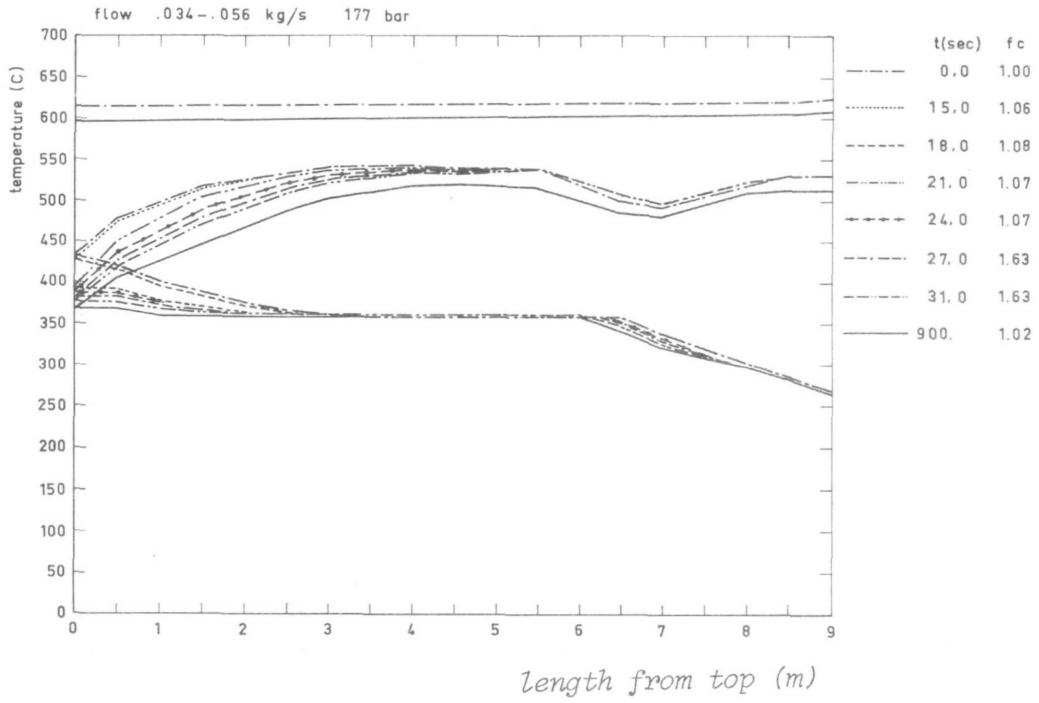

FIGURE 4.5-5.

Temperature profiles in the bayonet tube steam generator following a step in the feedwater mass flow.

Exp. nr.	before transient			after transient		
	feedwater flow	steam pressure	power	feedwater flow	steam pressure	power
	kg/s	MN/m^2	kW	kg/s	MN/m^2	kW
1	0.0312	17.72	69	0.0253	17.59	56
2	0.0251	17.68	56	0.0331	17.66	72
3	0.0335	17.69	74	0.0555	17.79	120
4	0.0552	17.78	118	0.0458	17.70	98
5	0.0468	17.72	100	0.0368	17.70	79
6	0.0373	17.69	81	0.0378	17.61	80
7	0.0376	17.66	80	0.0443	17.71	97
8	0.0447	17.83	95	0.0557	17.70	119
9	0.0467	17.65	103	0.0556	17.60	119
10	0.0553	17.71	121	0.0229	17.64	51
11	0.0250	16.16	56	0.0246	18.28	54
12	0.0264	18.34	59	0.0248	16.14	56
13	0.0117	16.18	26	0.0129	18.25	28
14	0.0159	18.14	35	0.0116	16.06	26
15	0.0341	16.05	76	0.0338	18.43	74
16	0.0337	18.32	75	0.0352	16.11	78
17	0.0447	16.08	99	0.0437	18.21	97
18	0.0445	18.11	96	0.0446	16.09	98

FIGURE 4.5-6.

Conditions of transient experiments.

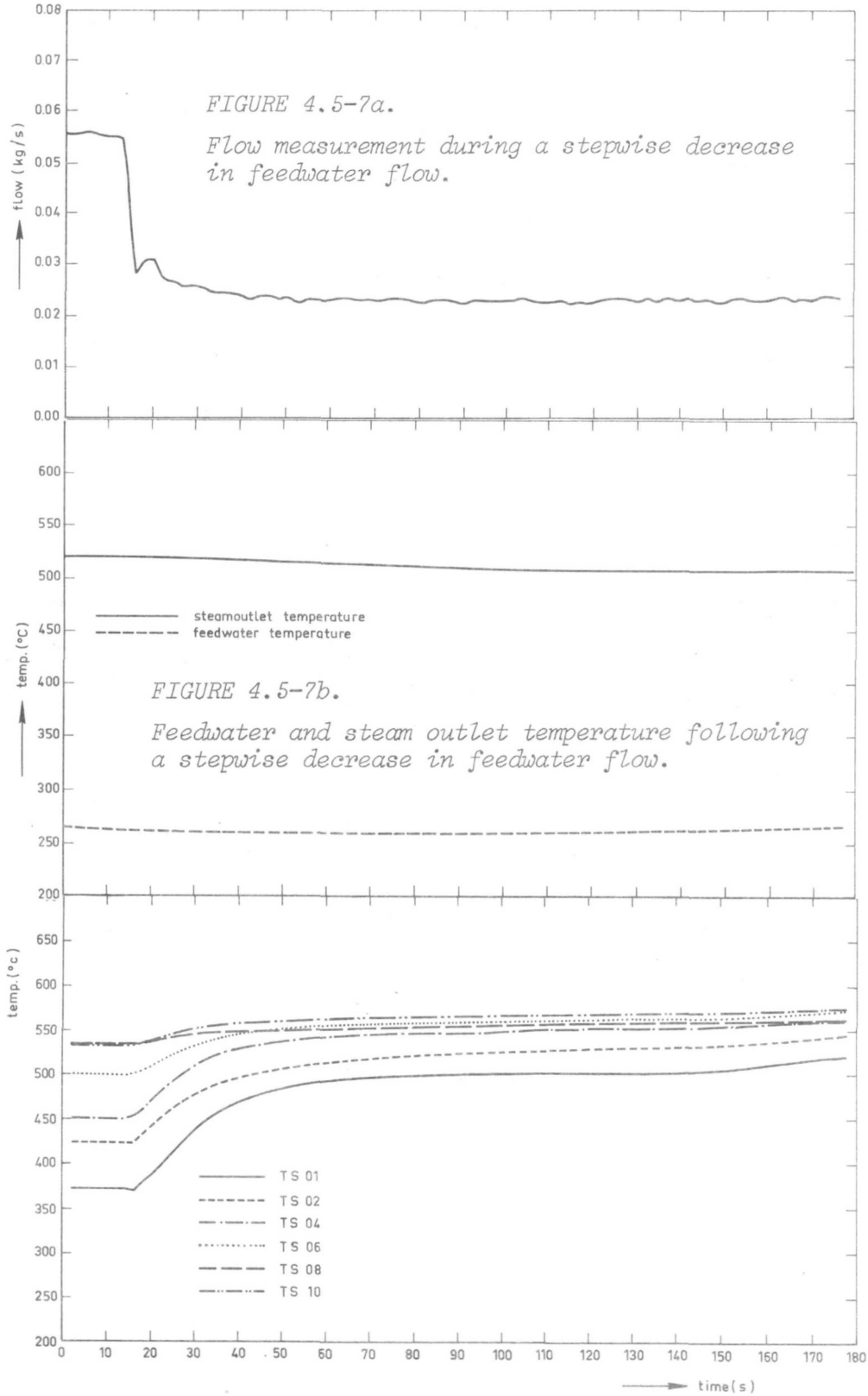

FIGURE 4.5-7a.

Flow measurement during a stepwise decrease in feedwater flow.

FIGURE 4.5-7b.

Feedwater and steam outlet temperature following a stepwise decrease in feedwater flow.

FIGURE 4.5-7c.

Superheater gap temperatures following a stepwise decrease in feedwater flow.

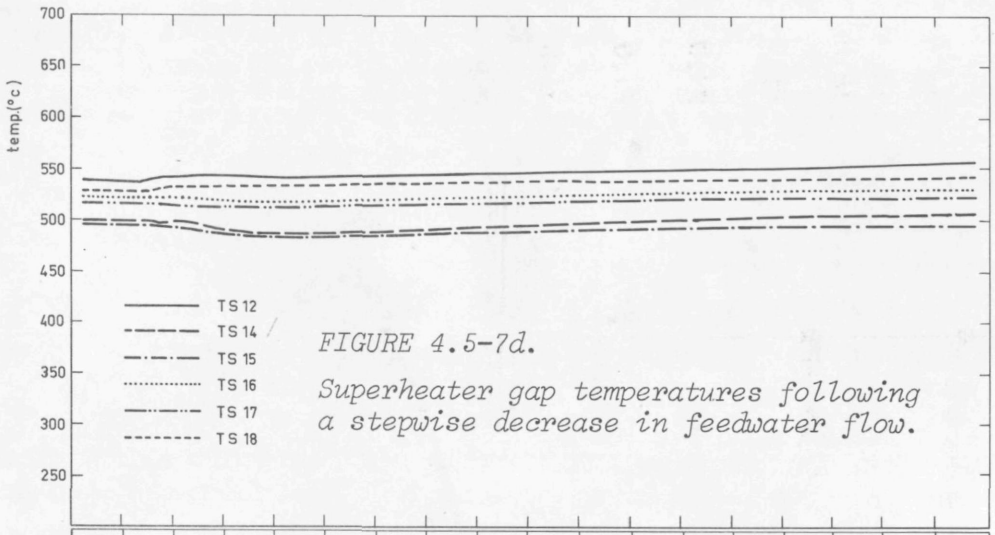

FIGURE 4.5-7d.

Superheater gap temperatures following a stepwise decrease in feedwater flow.

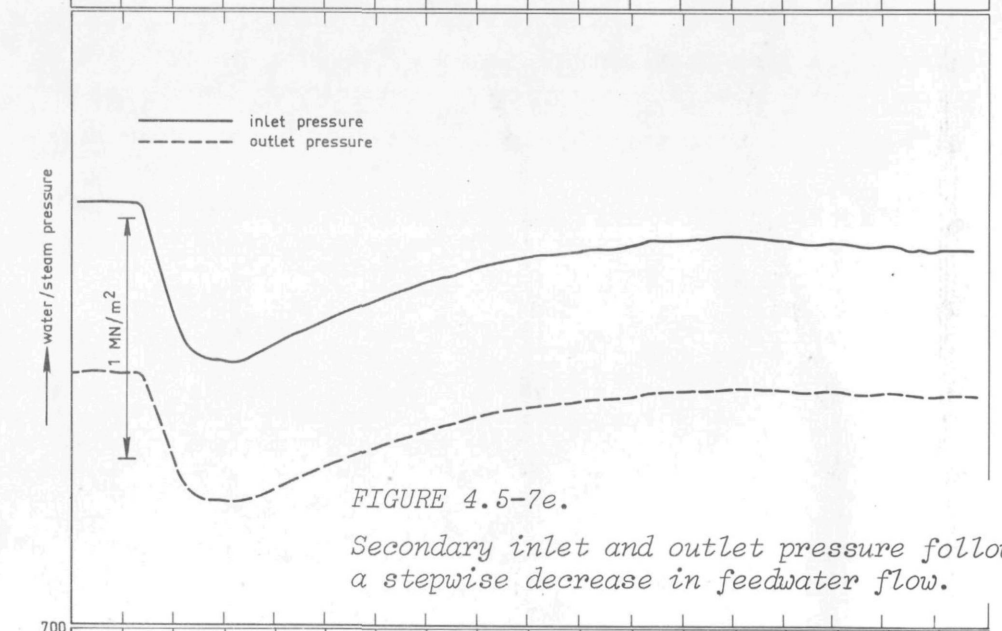

FIGURE 4.5-7e.

Secondary inlet and outlet pressure following a stepwise decrease in feedwater flow.

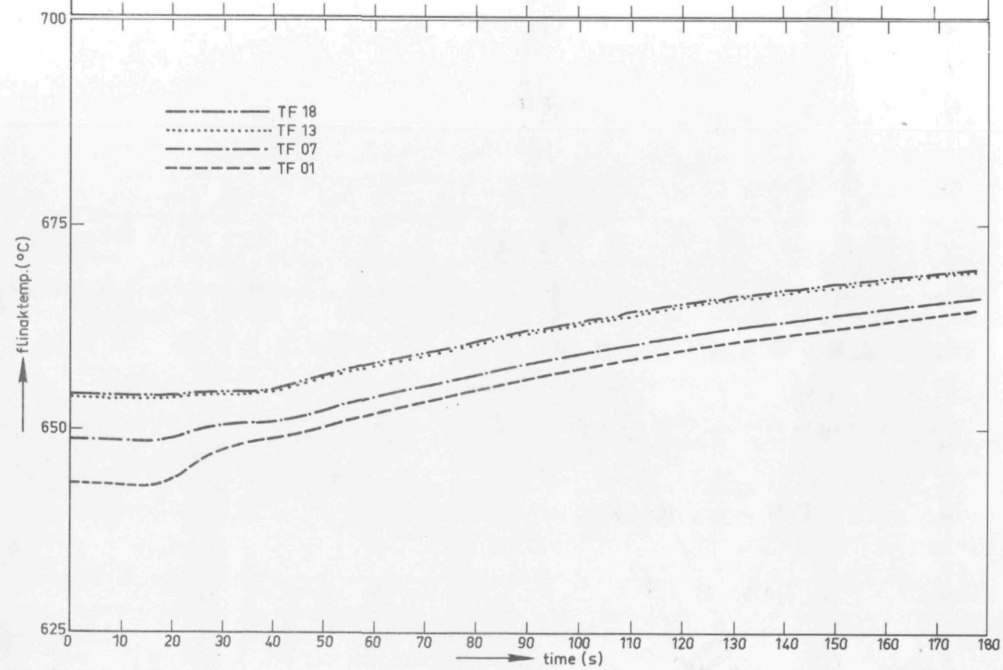

FIGURE 4.5-7f.

FLiNaK temperatures following a stepwise decrease in feedwater flow.

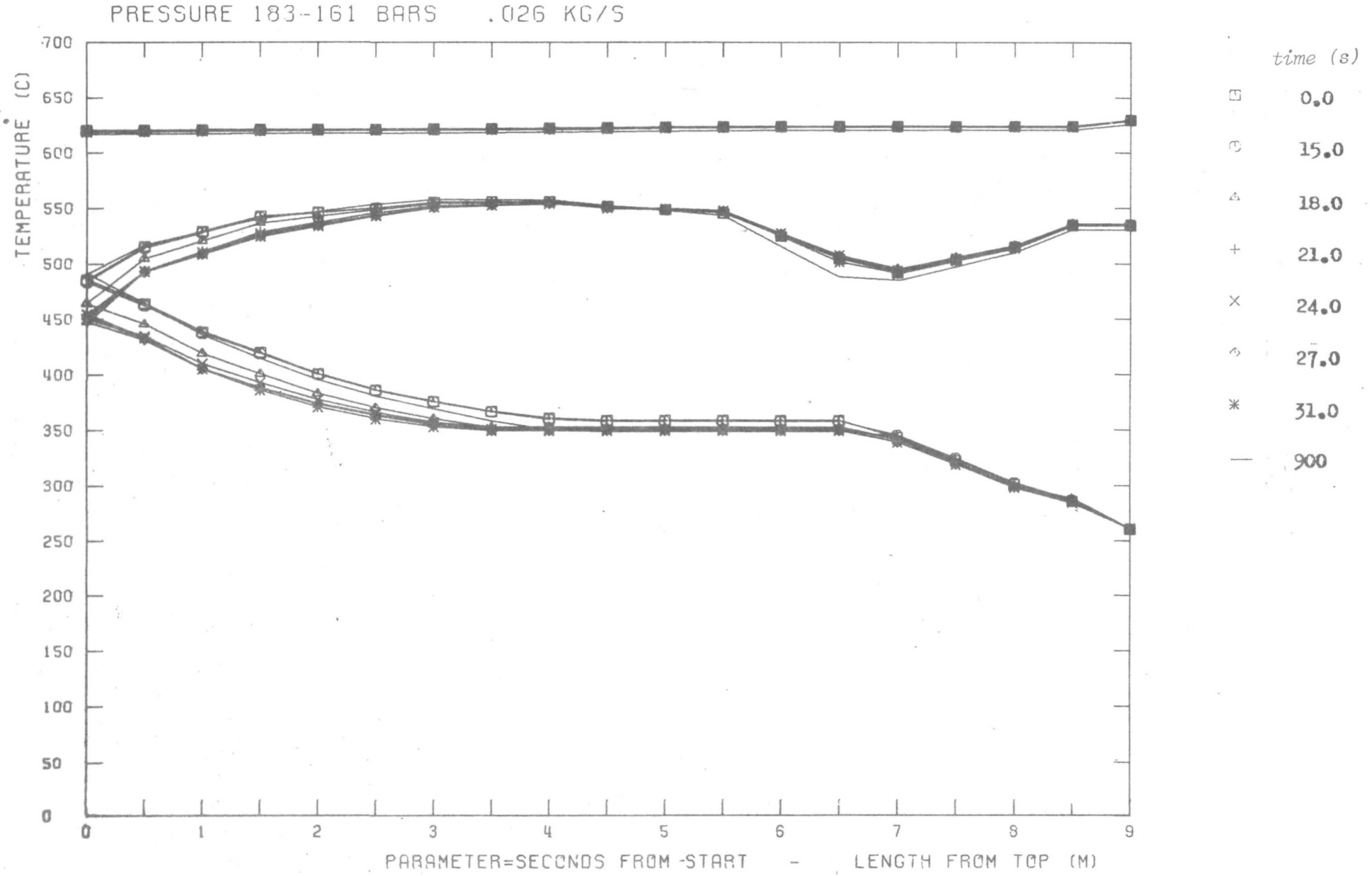

FIGURE 4.5-7g.

Temperature profiles following a stepwise decrease in feedwater flow.

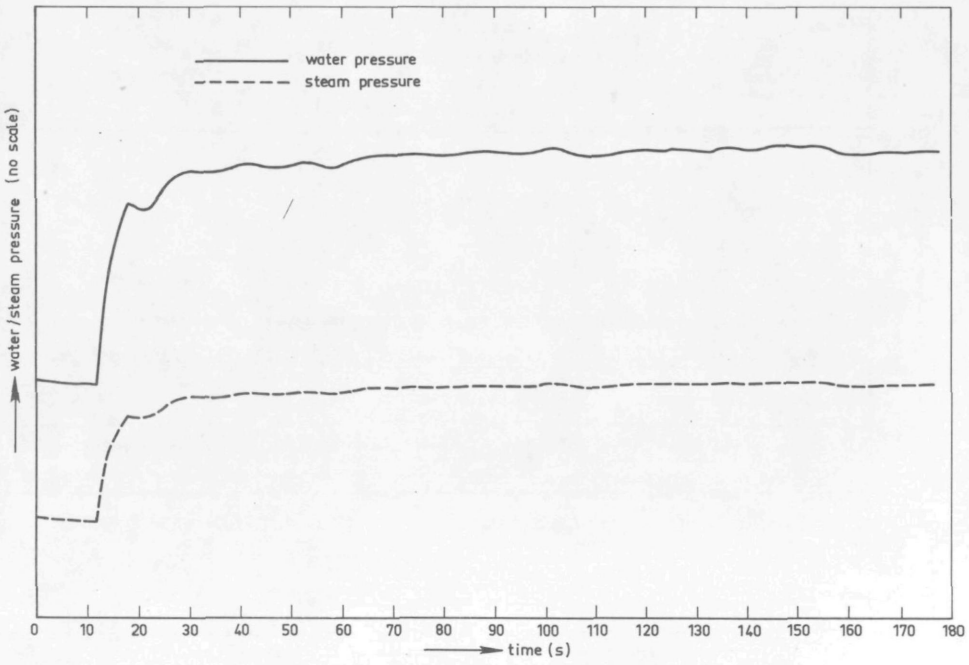

FIGURE 4.5-7h.

Stepwise increase in outlet pressure and response of the inlet pressure.

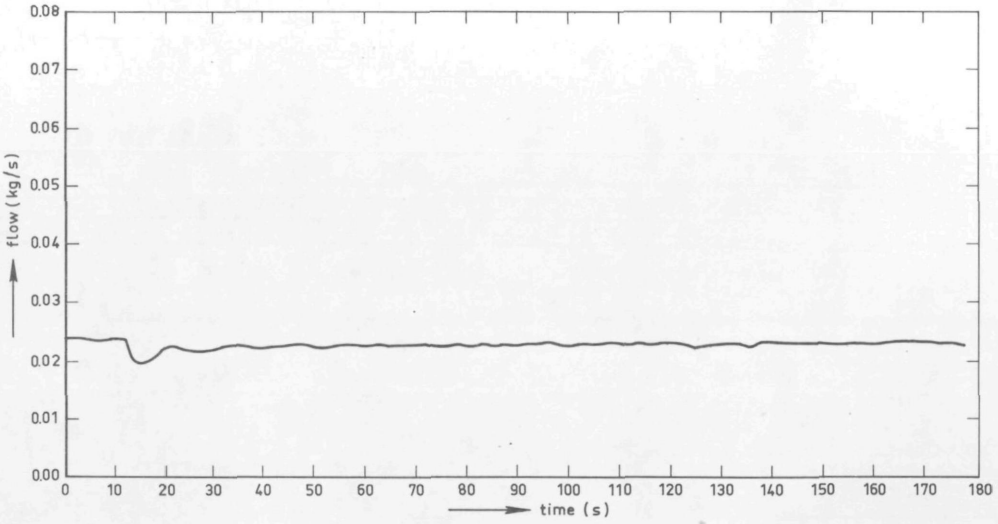

FIGURE 4.5-7i.

Feedwater flow response to a stepwise increase in outlet pressure.

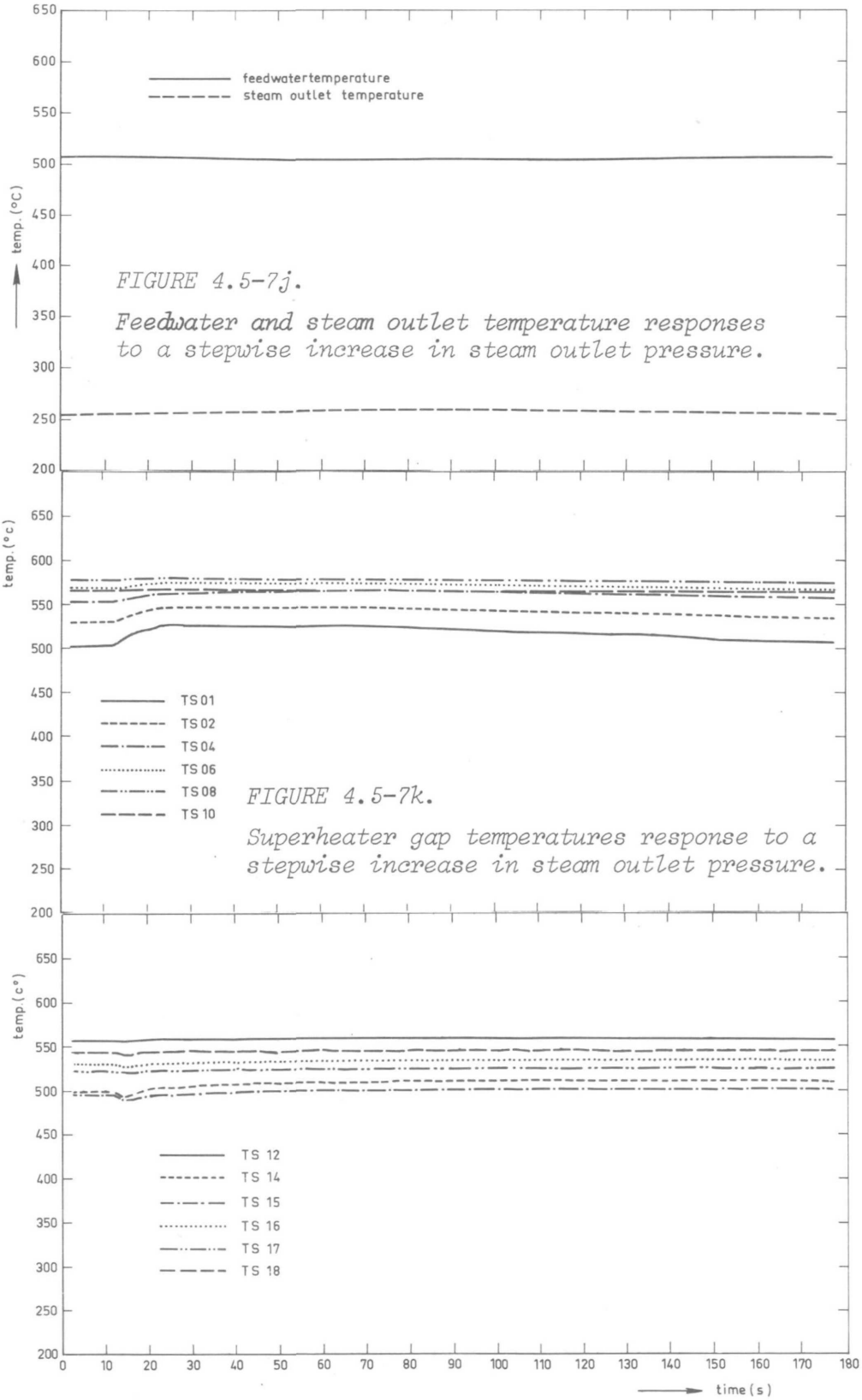

FIGURE 4.5-7j.

Feedwater and steam outlet temperature responses to a stepwise increase in steam outlet pressure.

FIGURE 4.5-7k.

Superheater gap temperatures response to a stepwise increase in steam outlet pressure.

FIGURE 4.5-7l.

Superheater gap temperatures response to stepwise increase in steam outlet pressure.

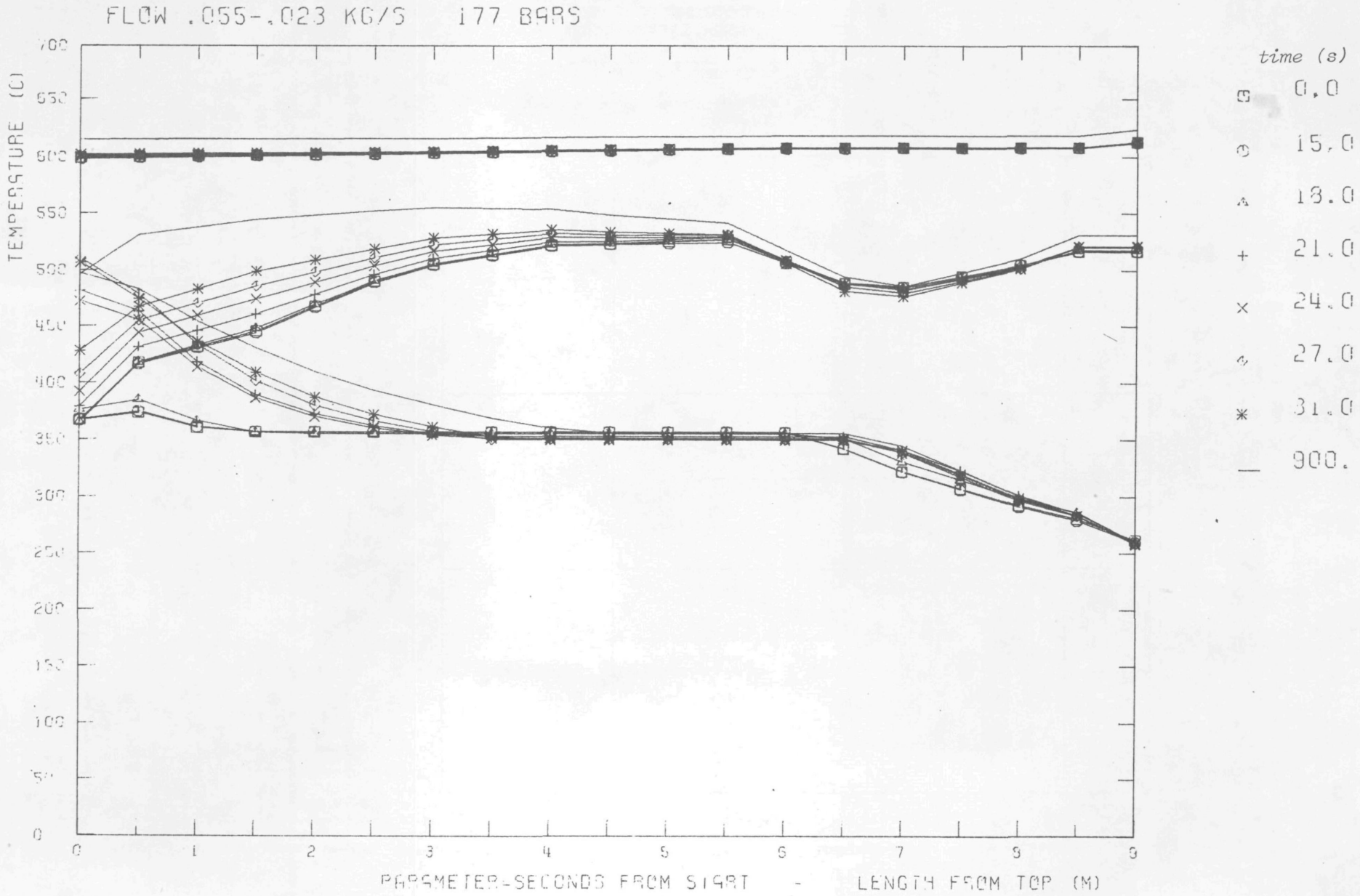

FIGURE 4.5-7m.

Temperature profiles following a stepwise increase in steam outlet pressure.

Property	Plot symbol	Thermocouple nr. cf. figure 3.4-5
Superheater gap temperatures	TS 01	TC 1
	02	5
	04	4
	06	8
	08	10
	10	12
	12	14
	14	16
	15	18
	16	19
	17	22
	18	23
FLiNaK channel temperatures	01	25
	07	31
	13	37
	18	42

FIGURE 4.5-8.

Thermocouple numbers/symbols.

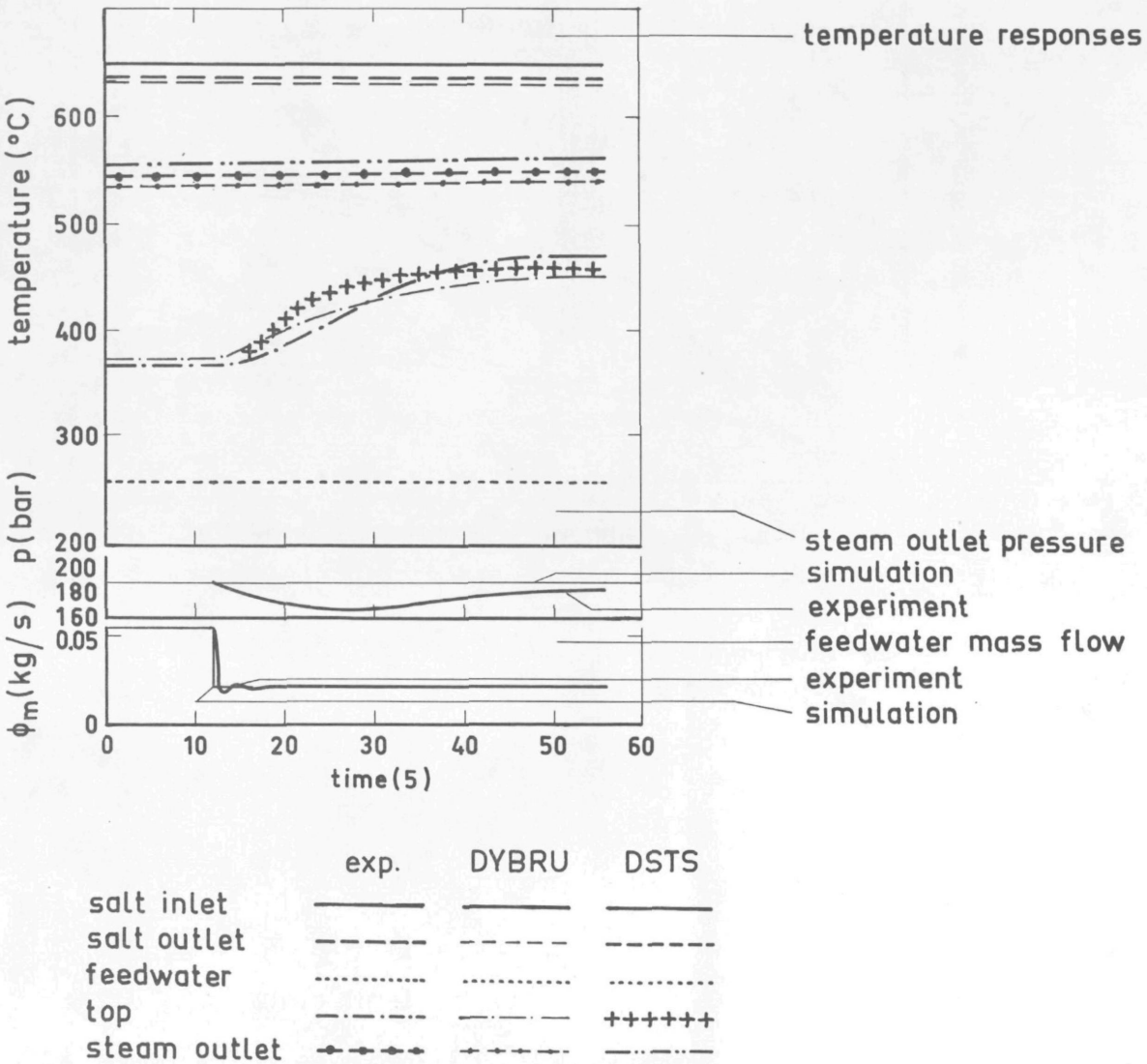

FIGURE 4.5-9.

Bayonet tube steam generator: measured and calculated (DYBRU and DSTS) time-depentent responses following a stepwise decrease in feedwater mass flow from 85% to 35%.

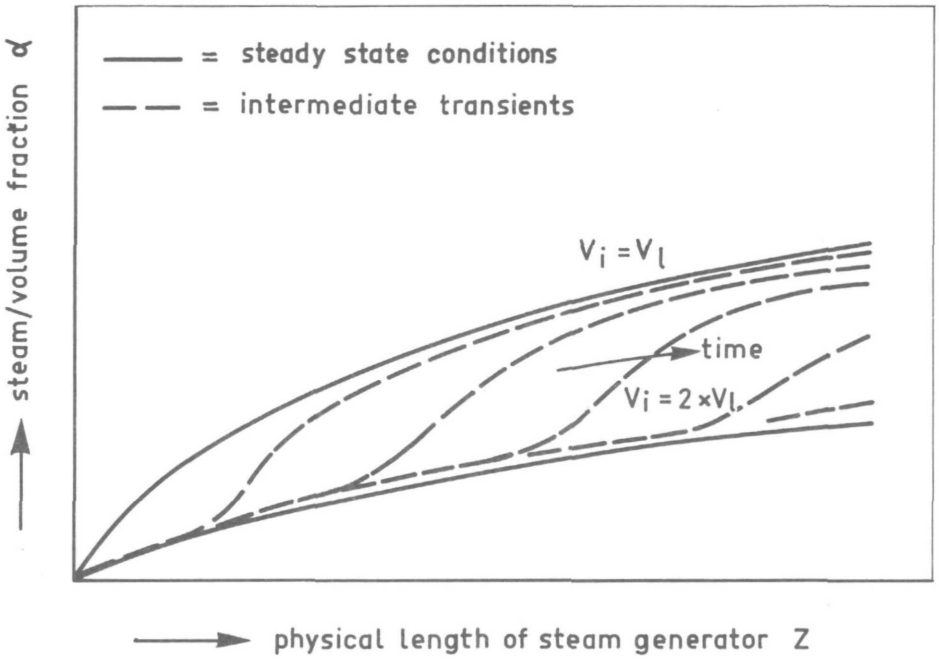

FIGURE 4.6-1.

Dynamic response of void-fraction distribution following a step in the inlet mass flow rate.

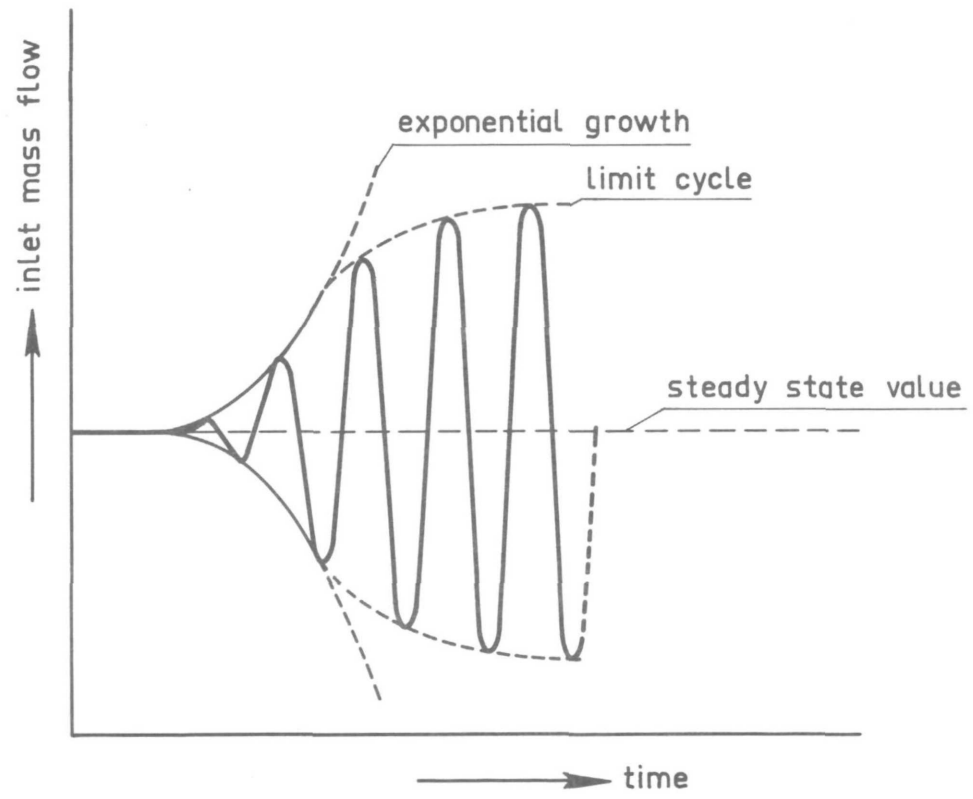

FIGURE 4.6-2.

Growing amplitude of a diverging oscillation resulting in a limit cycle.

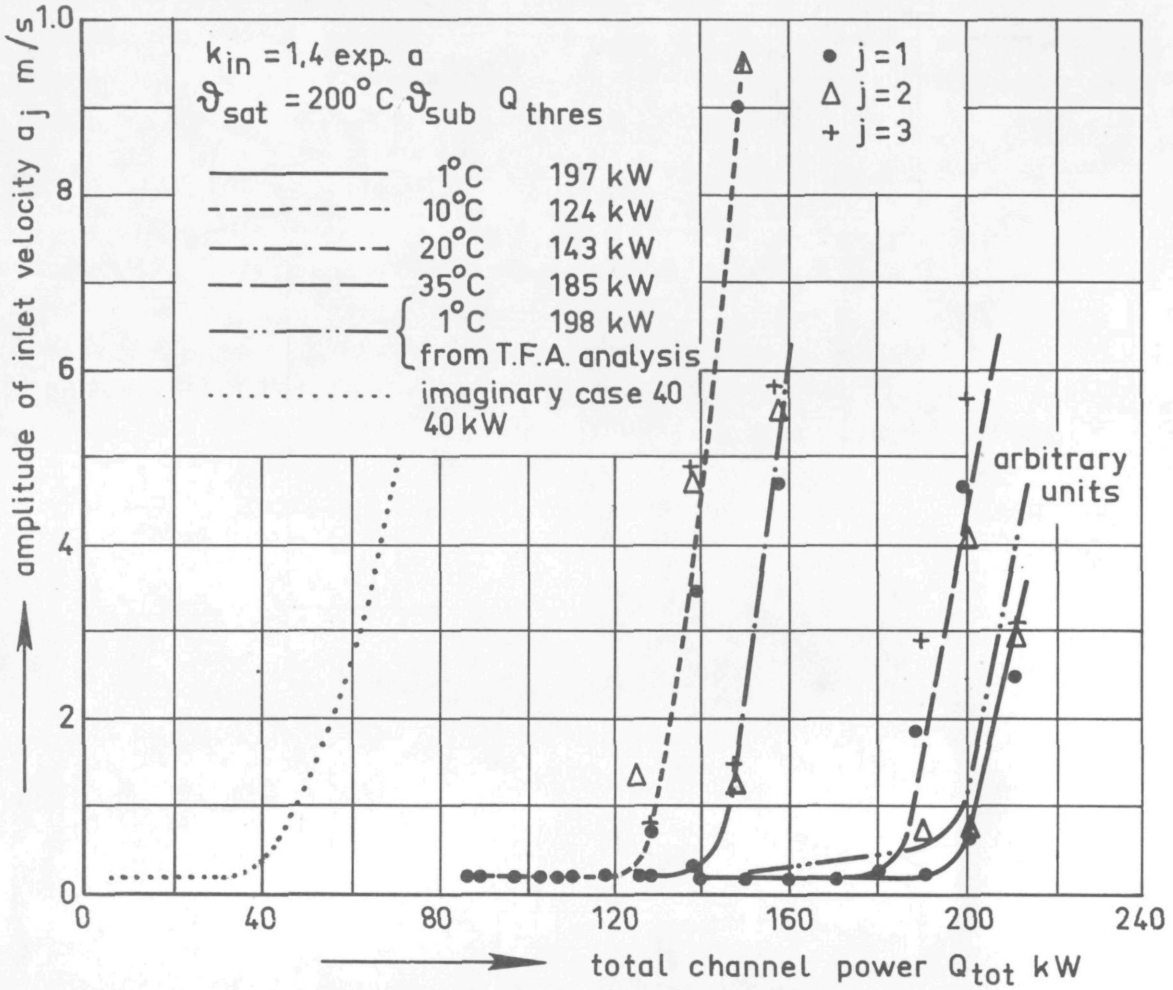

FIGURE 4.6-3.

Oscillation amplitudes versus channel power (taken from VAN VONDEREN [4.6-5]).

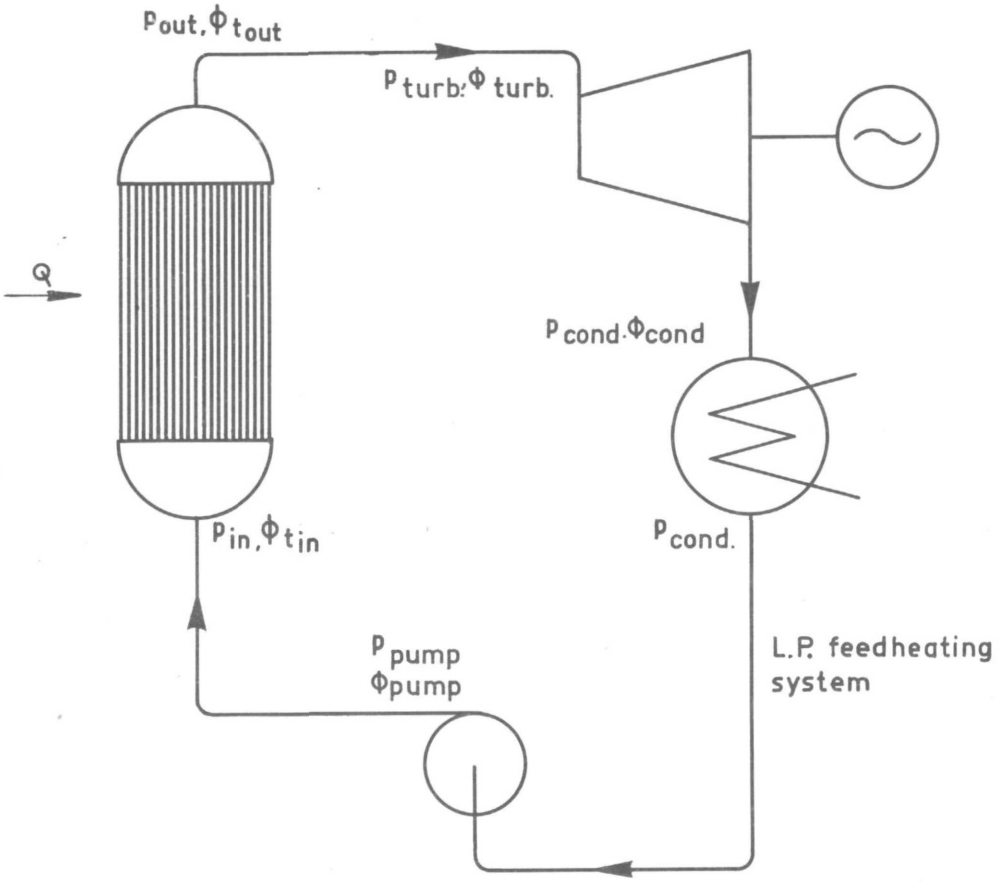

FIGURE 4.6-4.

Simplified diagram of steam generator turbine system.

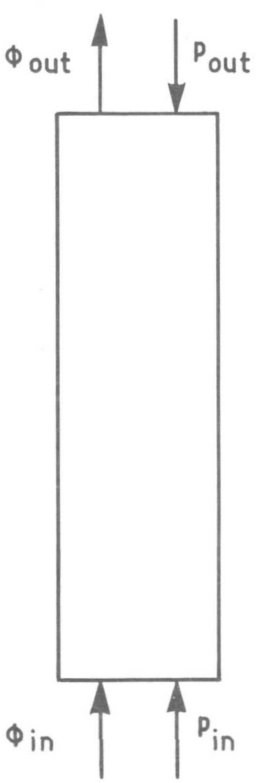

FIGURE 4.6-5.

Four-pole element.

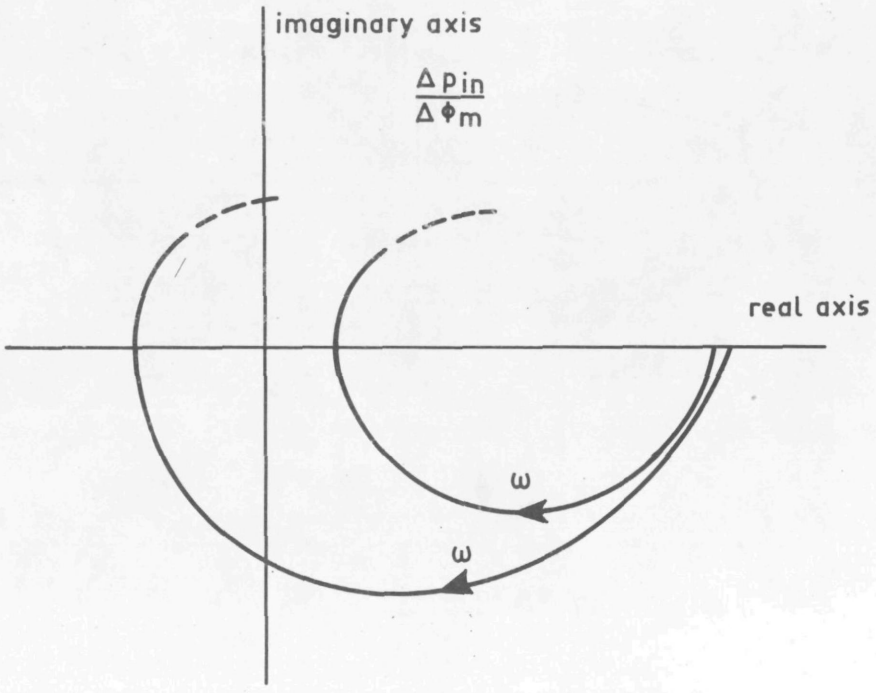

FIGURE 4.6-6.

Idealized shape of the inlet impedance curve of an evaporator channel.

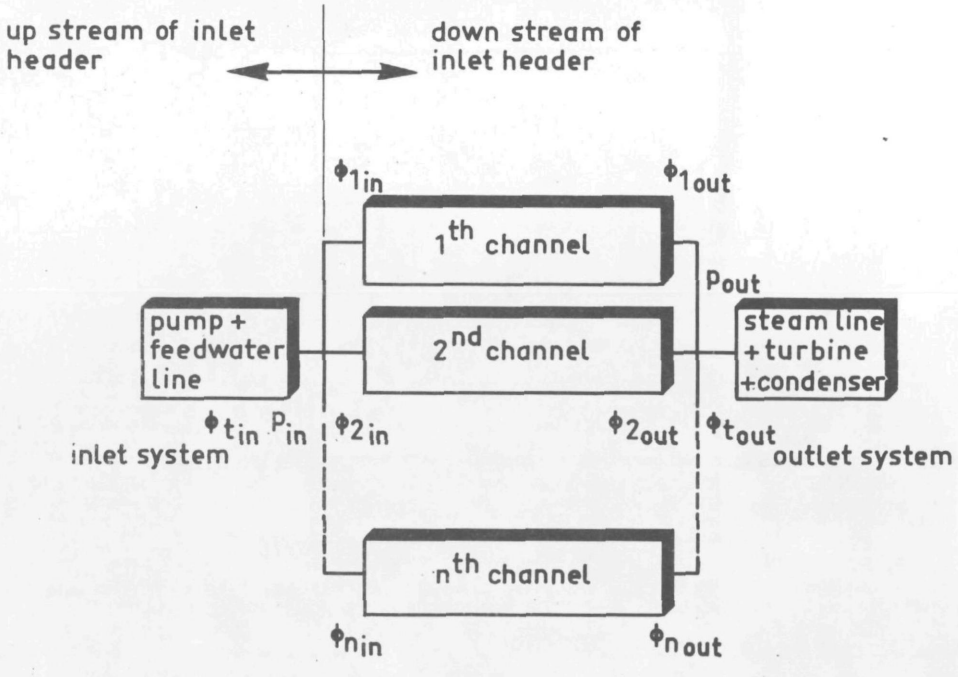

FIGURE 4.6-7.

Block diagram of a steam generator turbine system.

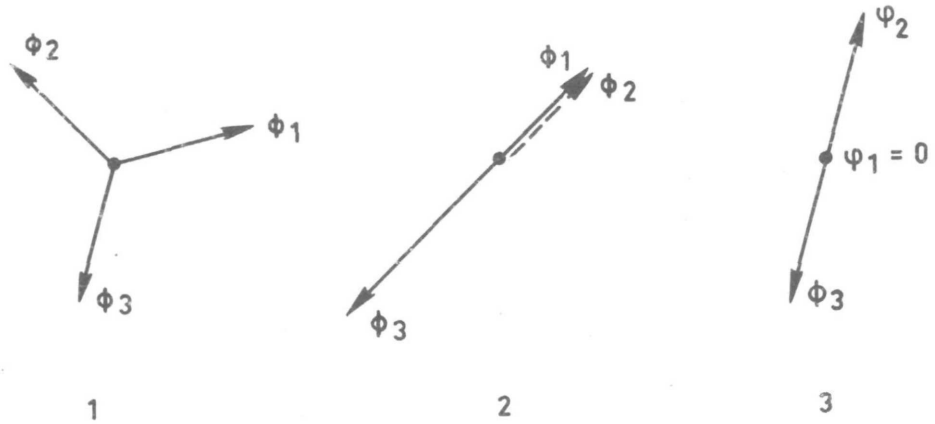

FIGURE 4.6-8.
The three different modes of oscillation observed by VAN VONDEREN [4.2-12].

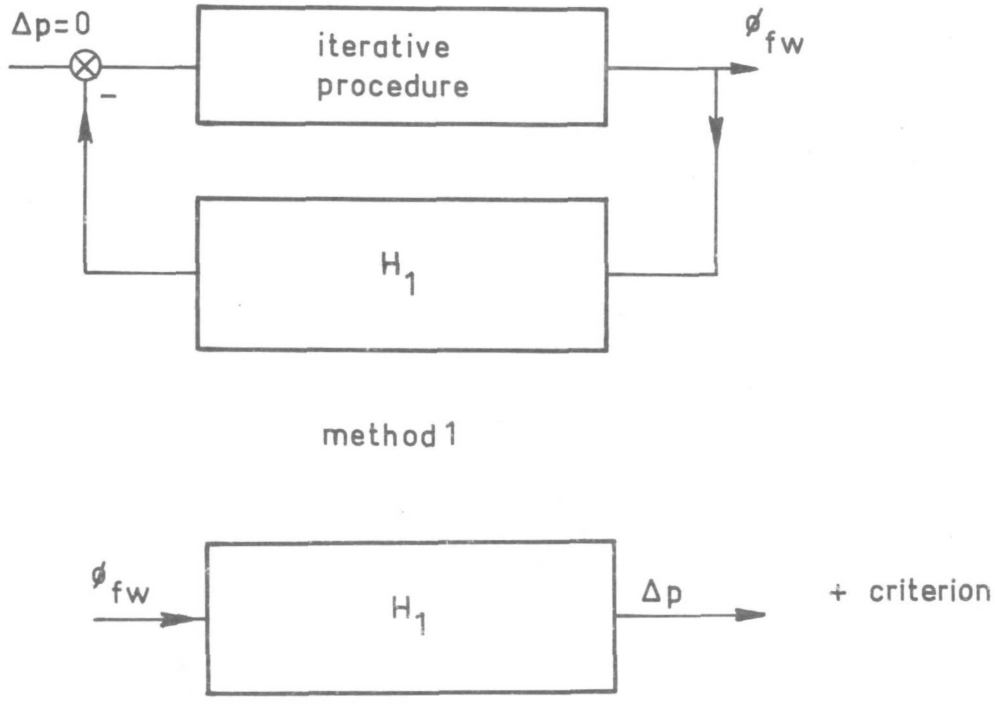

FIGURE 4.6-9.
Two simulation methods stability prediction in the time domain.

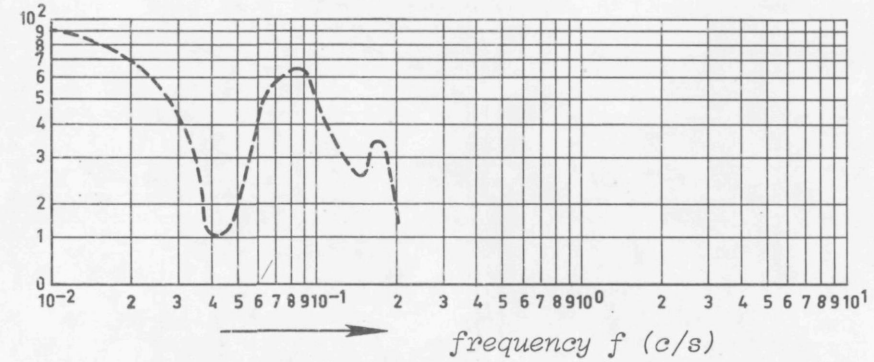

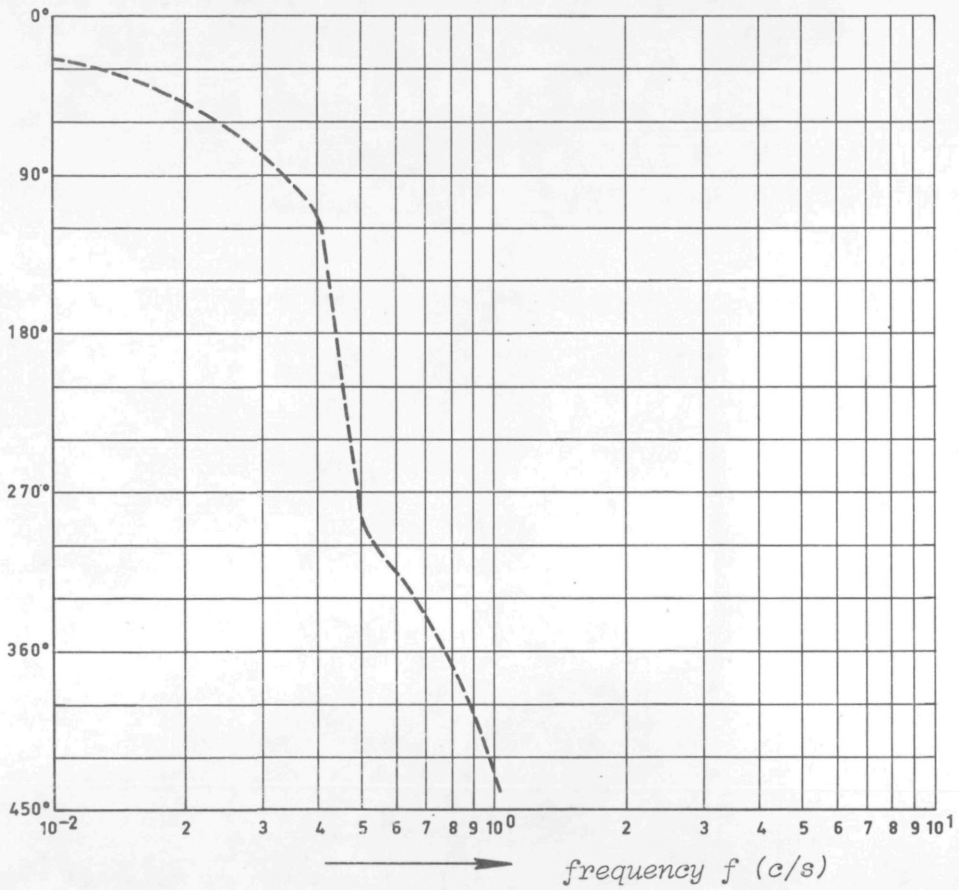

FIGURE 4.6-10.

Sample result of method 2 simulation.

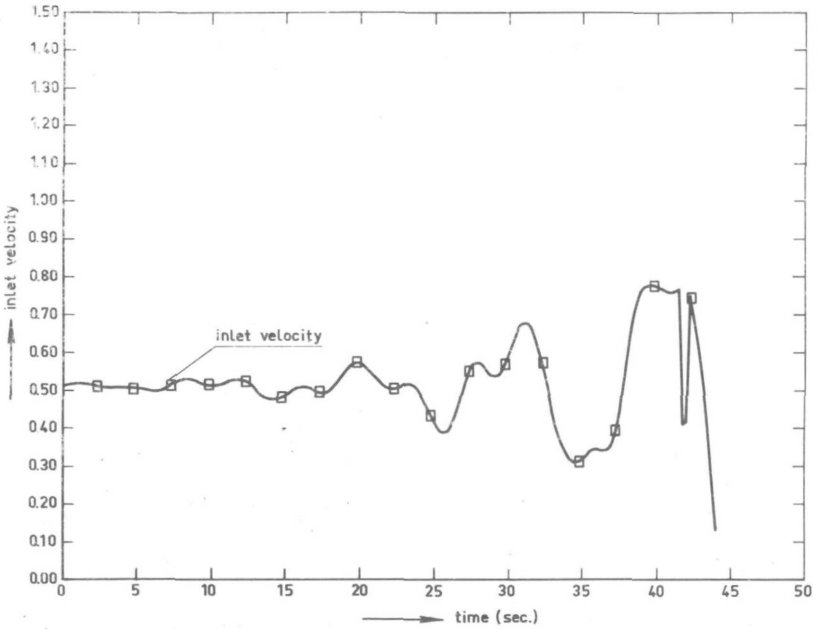

FIGURE 4.6-11.
Sample results of method 1 simulations.

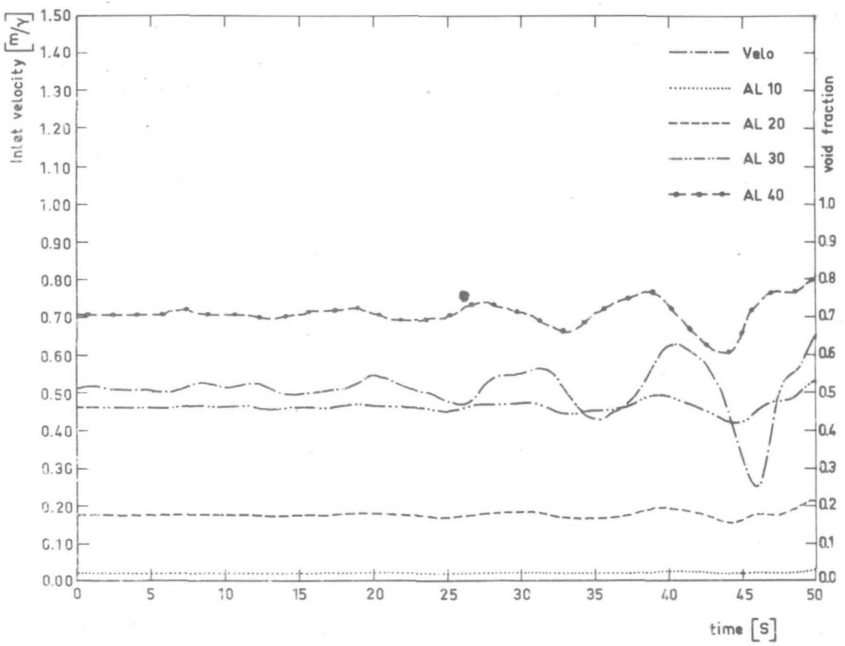

FIGURE 4.6-12.
Sample results of method 1 simulations.

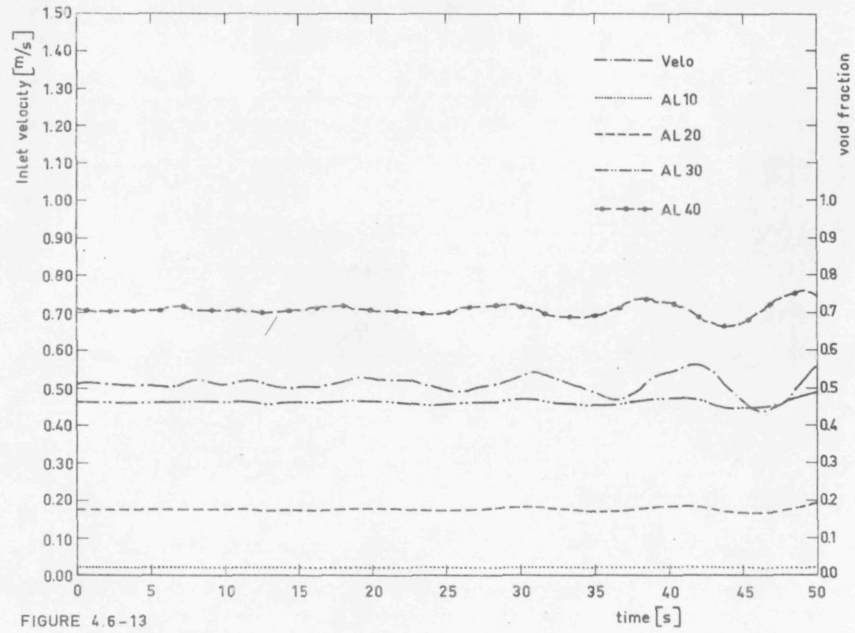

FIGURE 4.6-13

FIGURE 4.6-13.

Sample results of method 1 simulations.

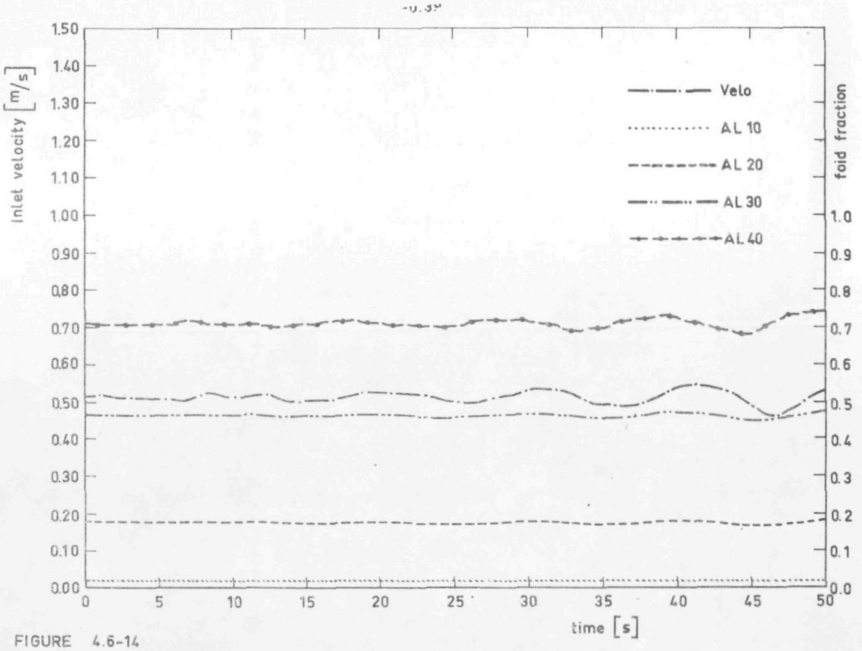

FIGURE 4.6-14

FIGURE 4.6-14.

Sample results of method 1 simulations.

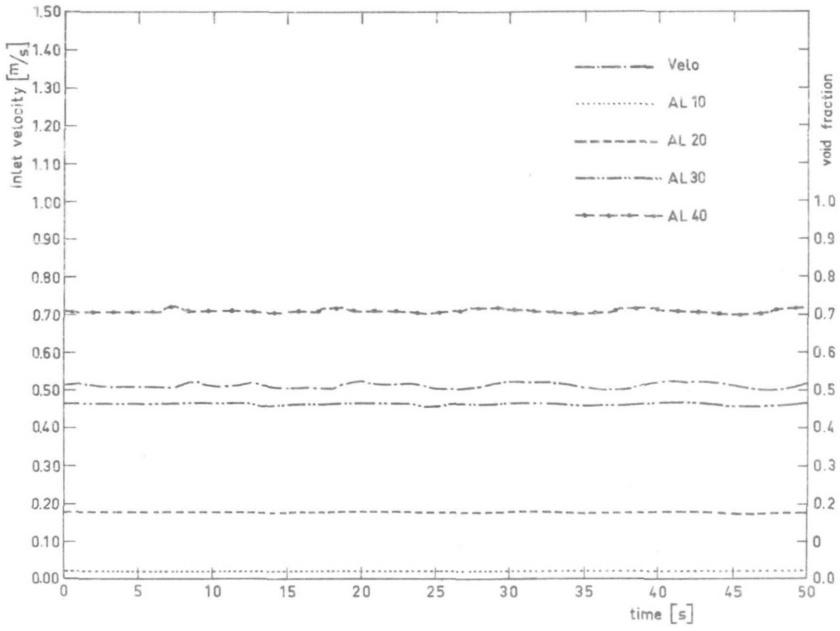

FIGURE 4.6-15.

Sample results of method 1 simulations.

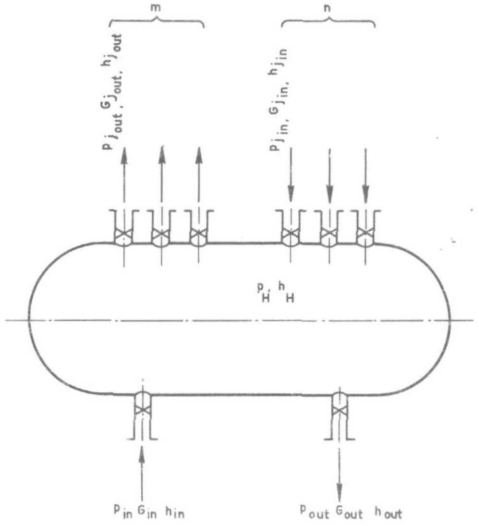

FIGURE 4.6-16.

Schematization of a header.

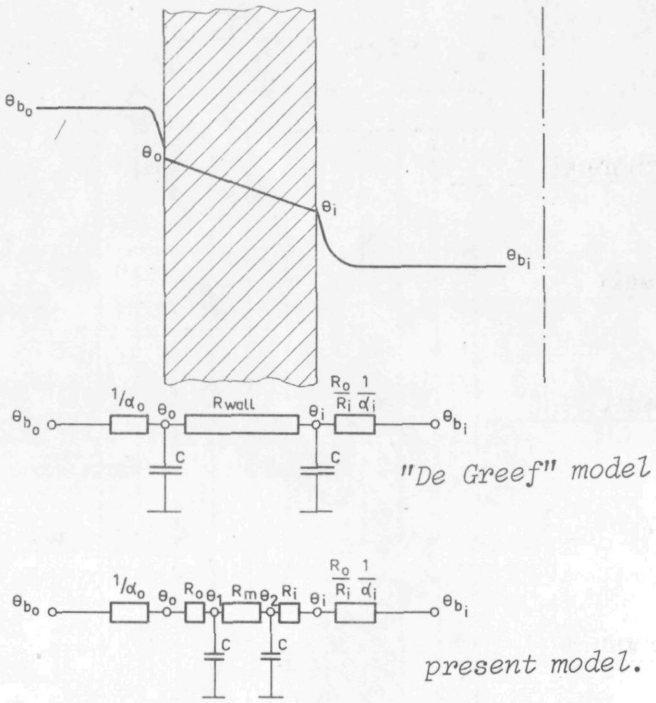

FIGURE 4.6-17.

Modeling of wall dynamics.

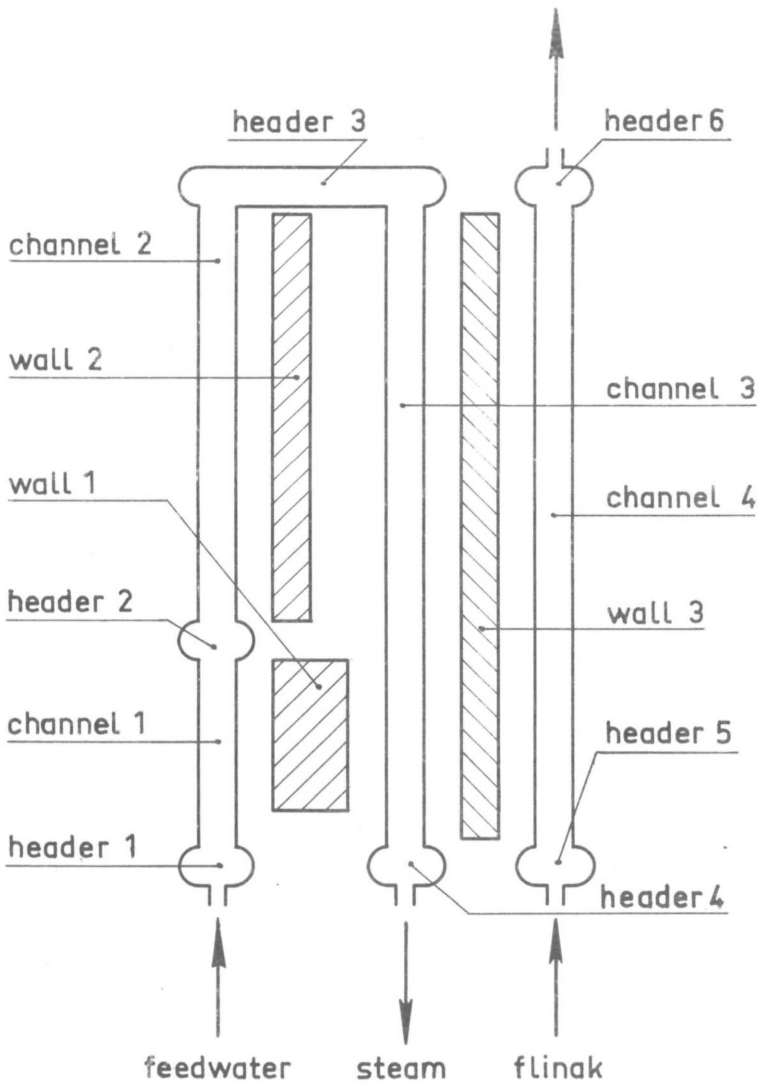

FIGURE 4.6-18.

Schematization of bayonet tube test module.

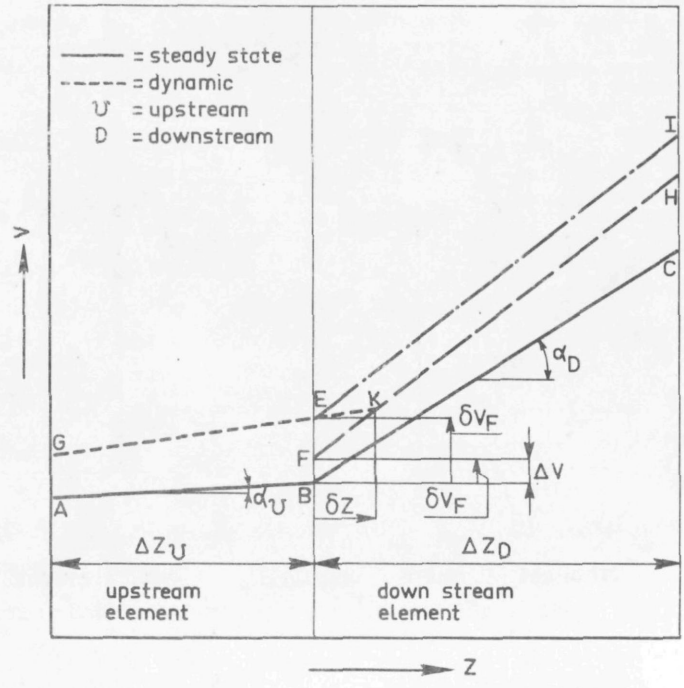

FIGURE 4.6-19.

Approximation of the dynamics of a transition in a frequency domain model.

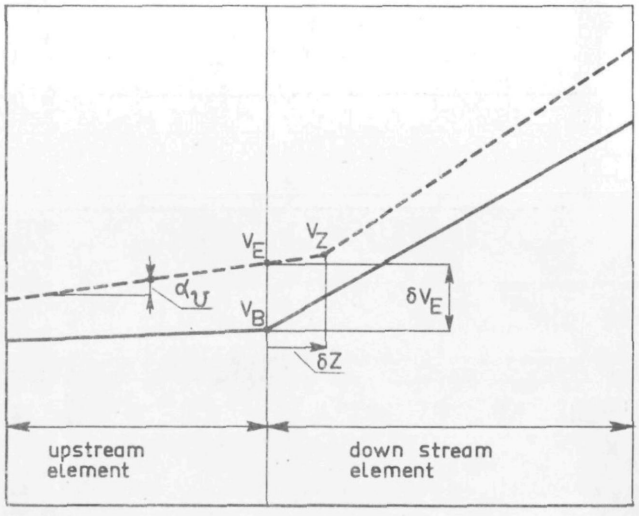

FIGURE 4.6-20.

Determination of local values of the basic variations.

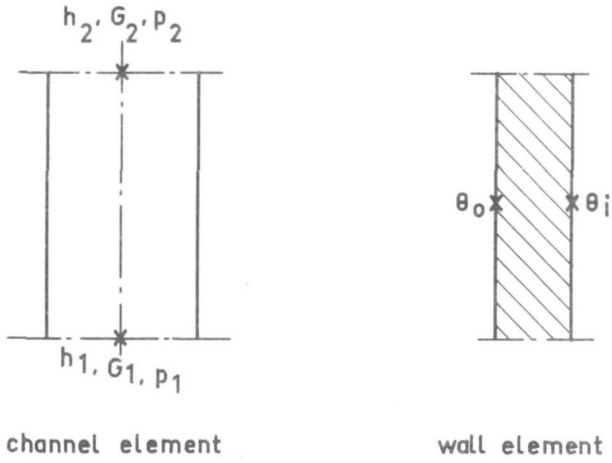

FIGURE 4.6-21.

Location of nodal variables of channel and wall elements.

Key designated to element nr. 04 of channel (type 01) nr. 02, between level 03 and level 04.

FIGURE 4.6-22.

Structure of a key.

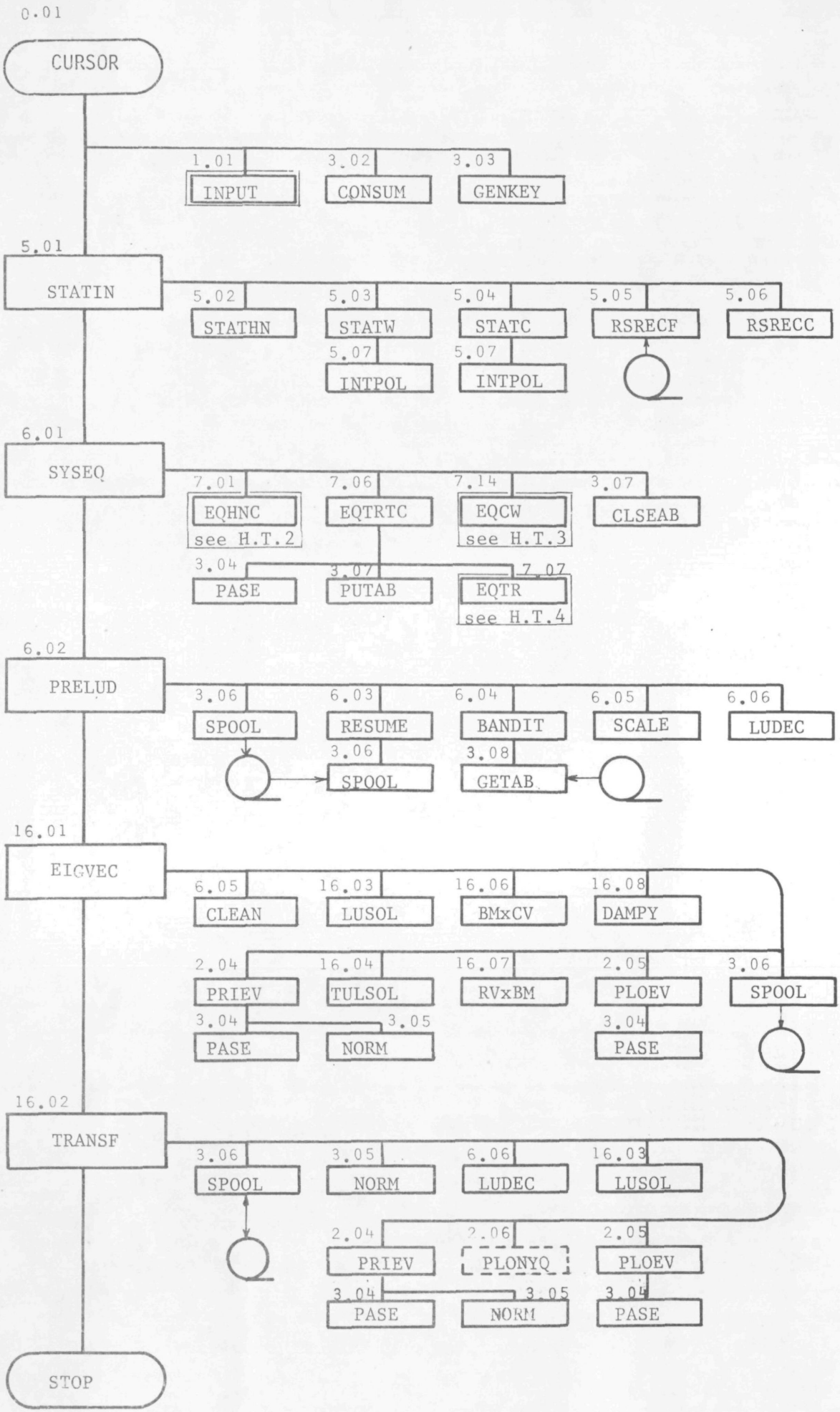

FIGURE 4.6-23.

Hierarchy table of the CURSSE program.

```
     STABILITEITS METING NR. 15  VERJONGD, VERBETERDE ISOLATIE WAND              ..CONTINUED
CHANNEL  3 CONTAINING  1 PHASE FLUID   F R E Q U E N C Y  STEP NR.  3  OMEGA=  .25133      LAMBDA=  .0

 Z          ENTHALPY                    MASSFLOW                    PRESSURE
          AMPLITUD    PHASE          AMPLITUD    PHASE          AMPLITUD    PHASE

 0.0      .618157    -102.838                                   1.10945D-06 -136.945          EXIT  HEADER NR.  4

          .618157    -102.838       3.47107     -139.330        .0           .0               EXIT  NOZZLE

 0.0      .642190    -103.371       3.47107     -139.330        2.19084D-06 -138.945
                                1     .2281        51.39          .1419        57.09
 0.25     .614570    -104.365       3.47021     -139.311        1.01947D-03 -139.071
                                2     .2246        54.00          .1407        59.72
 0.51     .587186    -113.866       3.46967     -139.297        2.04473D-03 -139.120

 0.51     .587186    -113.866       3.46967     -139.297        2.04473D-03 -139.120
                                1     .2223        55.62          .1402        61.36
 0.81     .560773    -113.800       3.46925     -139.283        3.24711D-03 -139.175
                                2     .2175        55.56          .1381        61.21
 1.10     .413578    -114.644       3.46877     -139.268        4.45233D-03 -139.190
                                3     .2111        55.30          .1349        61.26
 1.40     .465540    -116.786       3.46827     -139.256        5.66145D-03 -139.193
                                4     .2024        55.63          .1303        61.68
 1.70     .507785    -120.752       3.46778     -139.231        6.87632D-03 -139.191

 1.70     .507785    -120.752       3.46778     -139.231        6.87632D-03 -139.191
                                1     .1943        56.12          .1259        62.30
 1.84     .527324    -123.408       3.46758     -139.221        7.45867D-03 -139.191
                                2     .1880        56.71          .1223        62.97
 1.98     .531961    -126.284       3.46740     -139.211        8.04375D-03 -139.191
                                3     .1809        57.55          .1182        63.87
 2.13     .549698    -130.366       3.46727     -139.201        8.63155D-03 -139.195
                                4     .1740        59.26          .1144        65.61
 2.27     .456147    -137.911       3.46720     -139.192        9.22268D-03 -139.196
                                5     .1729        61.95          .1141        68.26
 2.41     .294124    -157.396       3.46726     -139.186        9.81726D-03 -139.203

 2.41     .294124    -157.396       3.46726     -139.186        9.81726D-03 -139.203
                                1     .1838        64.50          .1217        70.92
 3.08     .368595    -166.392       3.46805     -139.164        1.26032D-02 -139.252
                                2     .2243        67.23          .1356        73.89
 3.74     .434800     179.992       3.46963     -139.143        1.53473D-02 -139.299
                                3     .2427        69.84          .1610        76.67
 4.41     .541116     169.916       3.47226     -139.152        1.80476D-02 -139.358
                                4     .3610        62.40          .2361        69.55
 5.08    2.55910      33.2618       3.47282     -139.315        2.06701D-02 -139.377

 5.08    2.55910      33.2618       3.47282     -139.315        2.06701D-02 -139.377
                                1     .3966        63.64          .2617        71.97
 6.09    1.48776      67.1378       3.47430     -139.651        2.46322D-02 -139.433
                                2     .2625        77.50          .1826        85.48
 7.09     .897675     93.1234       3.48056     -139.824        2.87994D-02 -139.597
                                3     .2376        95.49          .1703       103.0
 8.10    2.22410     121.379        3.49375     -139.925        3.30335D-02 -139.827
                                4     .3656        82.53          .2486        91.53
 9.11    2.93486      61.6252       3.51068     -140.279        3.68505D-02 -140.064

 9.11    2.93486      61.6252                                   3.68505D-02 -140.064          ENTRY HEADER NR.  3

     STABILITEITS METING NR. 15  VERJONGD, VERBETERDE ISOLATIE WAND              ..CONTINUED
CHANNEL  4 CONTAINING  PRIMARY FLUID   F R E Q U E N C Y  STEP NR.  3  OMEGA=  .25133      LAMBDA=  .0
THIS CHANNEL HAS NO EXTERNAL WALL

 Z          ENTHALPY
          AMPLITUD    PHASE

          .0           .0                                                                  ENTRY NOZZLE

 0.0      .0           .0                                                                  ENTRY HEADER NR.  5

 0.0      .0           .0          1
 0.25    3.75448D-03  58.6354      2
 0.51    7.41110D-03  61.5102

 0.51    7.41110D-03  61.5102      1
 0.81    1.15539D-02  64.4096      2
 1.10    1.56080D-02  66.6634      3
 1.40    1.94480D-02  68.7836      4
 1.70    2.30617D-02  70.8647

 1.70    2.30617D-02  70.8647      1
 1.84    2.46939D-02  71.9602      2
 1.98    2.62574D-02  72.9921      3
 2.13    2.77460D-02  74.1115      4
 2.27    2.91665D-02  75.3167      5
 2.41    3.05714D-02  76.6269

 2.41    3.05714D-02  76.6269      1
 3.08    3.75567D-02  82.6507      2
 3.74    4.50719D-02  88.5154      3
 4.41    5.39476D-02  93.2532      4
 5.08    6.64326D-02  94.9940

 5.08    6.64326D-02  94.9940      1
 6.09    8.63566D-02  98.5519      2
 7.09    9.87921D-02  107.423      3
 8.10    .1099.0      118.116      4
 9.11    .125540      124.246

 9.11    .125464      124.246                                                             EXIT  HEADER NR.  6

         .125464      124.246                                                             EXIT  NOZZLE

THERE ARE  3 PLOTS PREPARED.
. DATA PROCESSING TOOK 12300 MILLISECONDS

# THE COLUMN NUMBER OF THE NOZZLE OF HEADER NR 1 PROPERTY 3 IS=   3
```

FIGURE 4.6-24.

Example of printed output of CURSSE results.

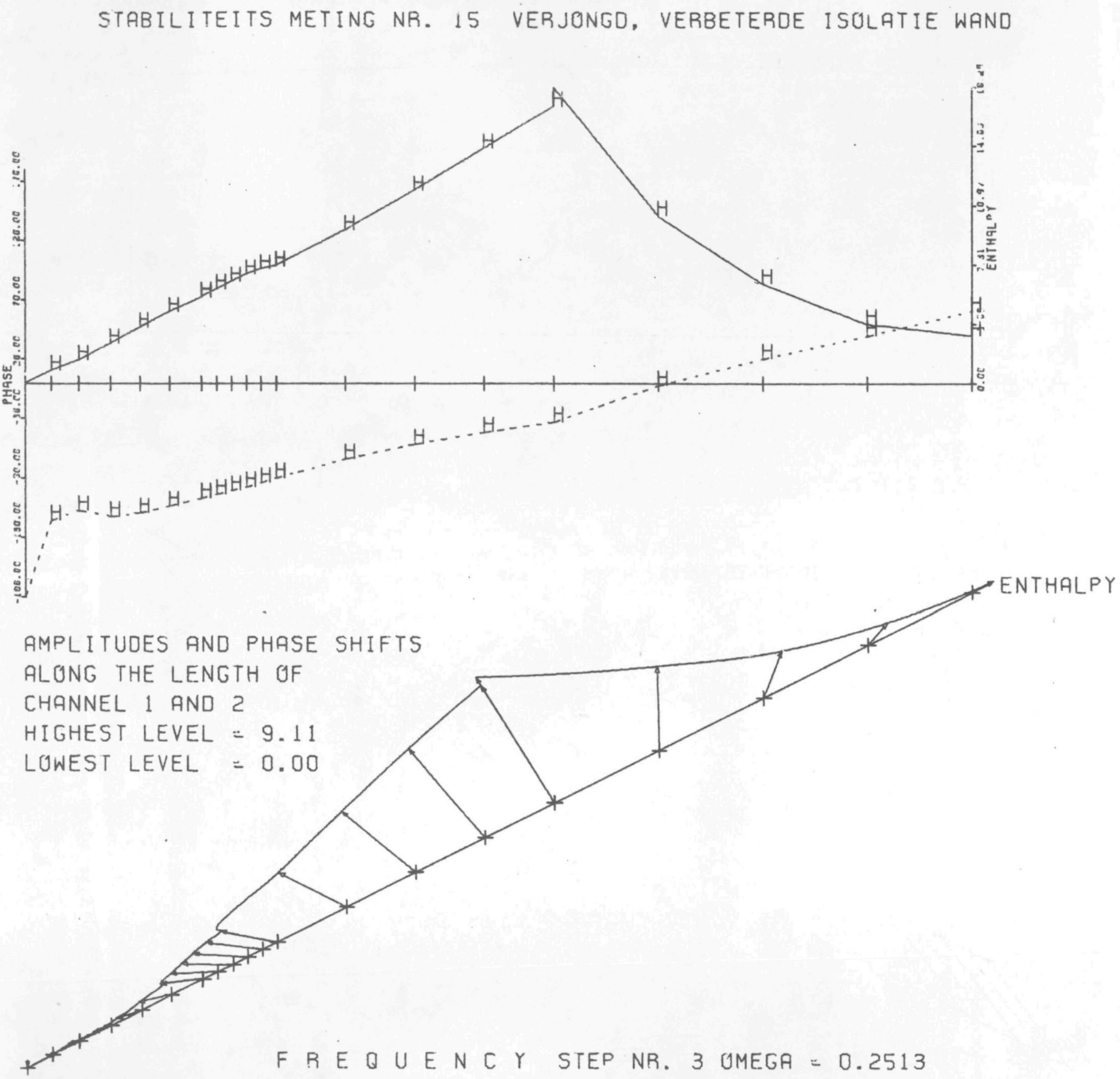

FIGURE 4.6-25a.

Example of plotted output of CURSSE results.

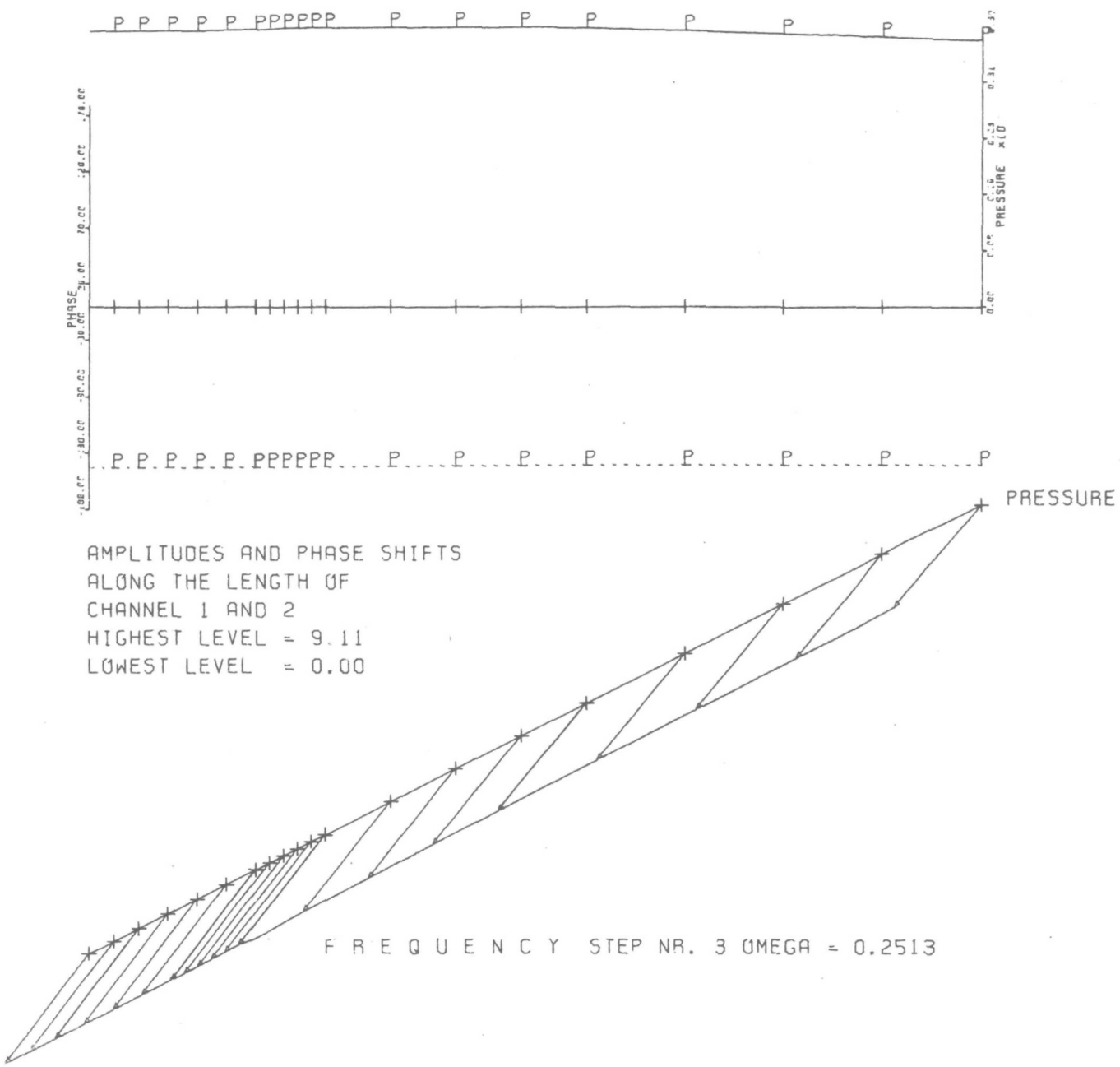

FIGURE 4.6-25b.

Example of plotted output of CURSSE results.

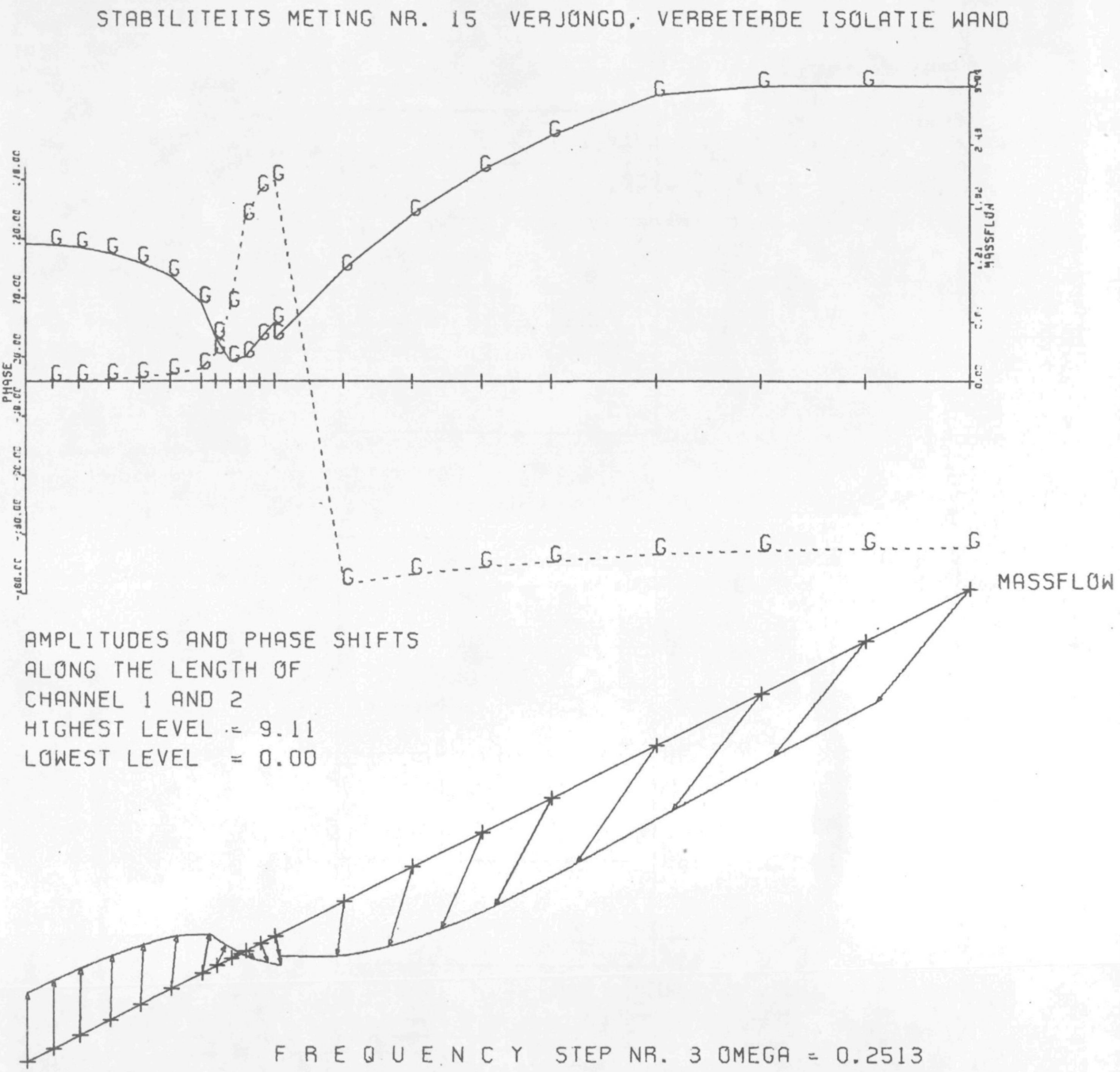

FIGURE 4.6-25c.

Example of plotted output of CURSSE results.

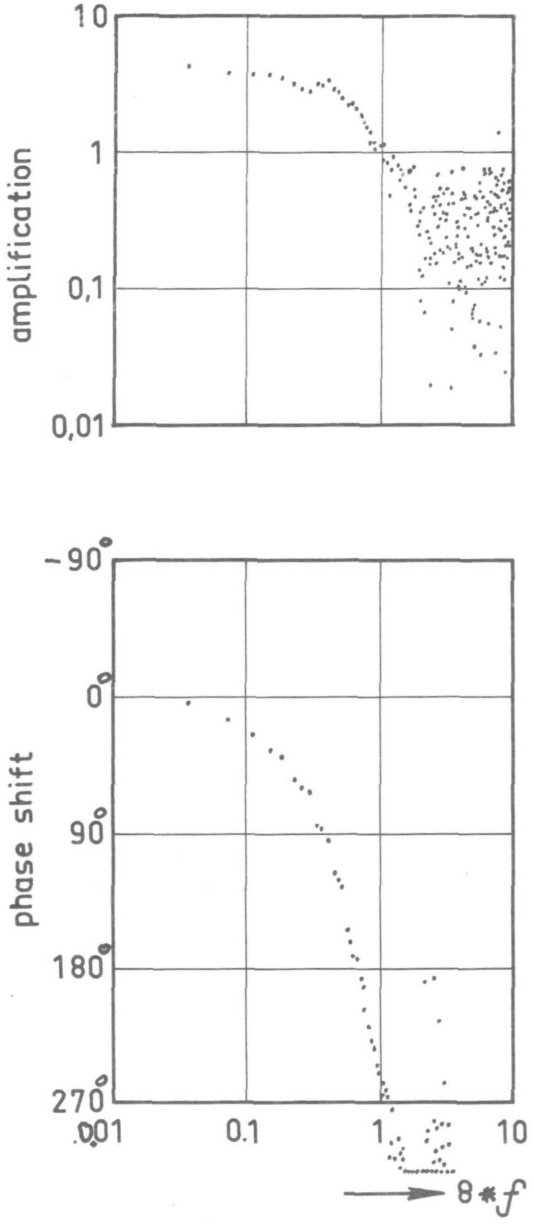

FIGURE 4.6-26.

Example of a Bode-diagram obtained by applying binary noise signals, processed by a PDP-8 computer.

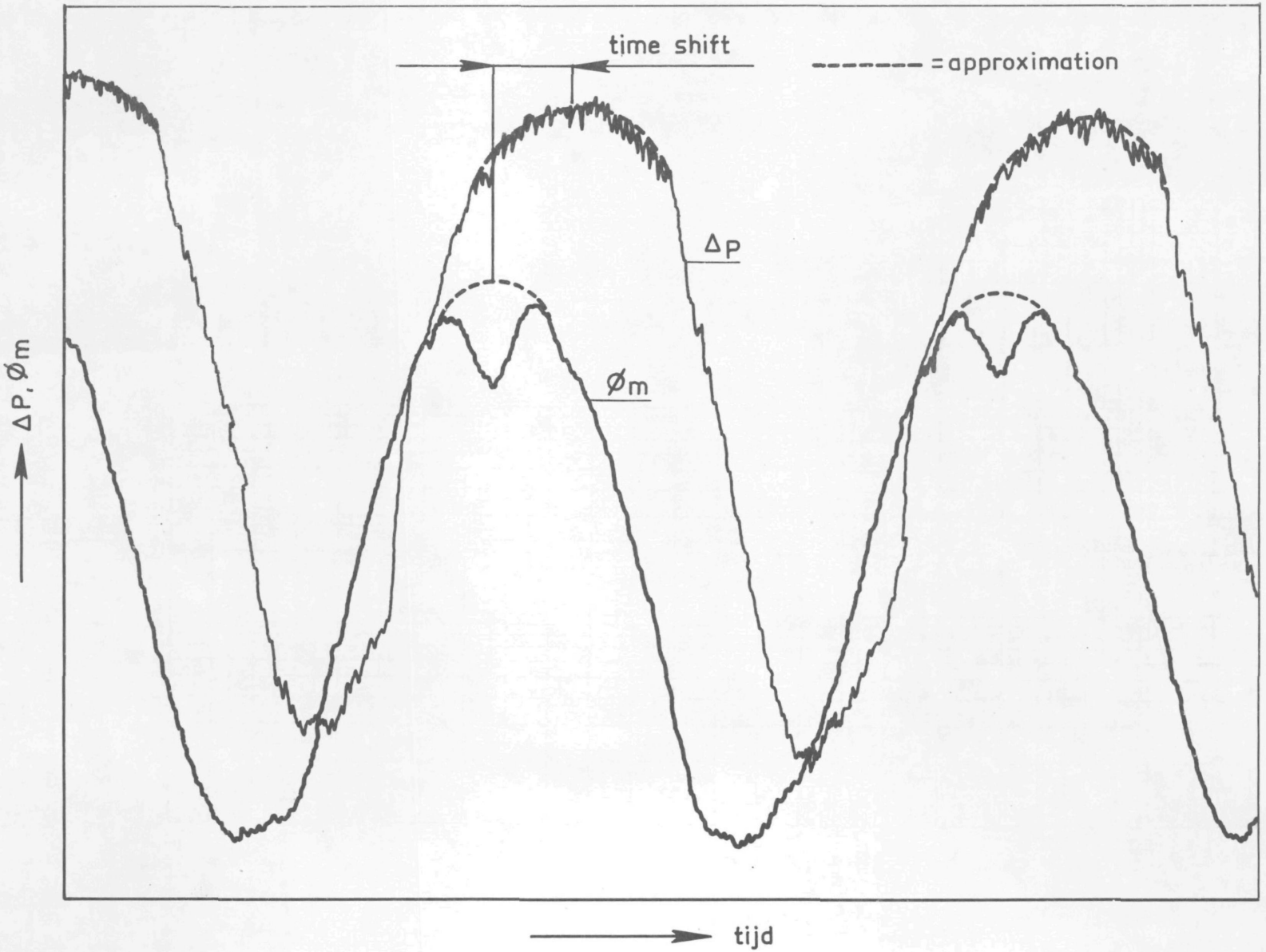

FIGURE 4.6-27.

Example of a recording of flow variation and pressure response in the DMSP bayonet tube steam generator test module.

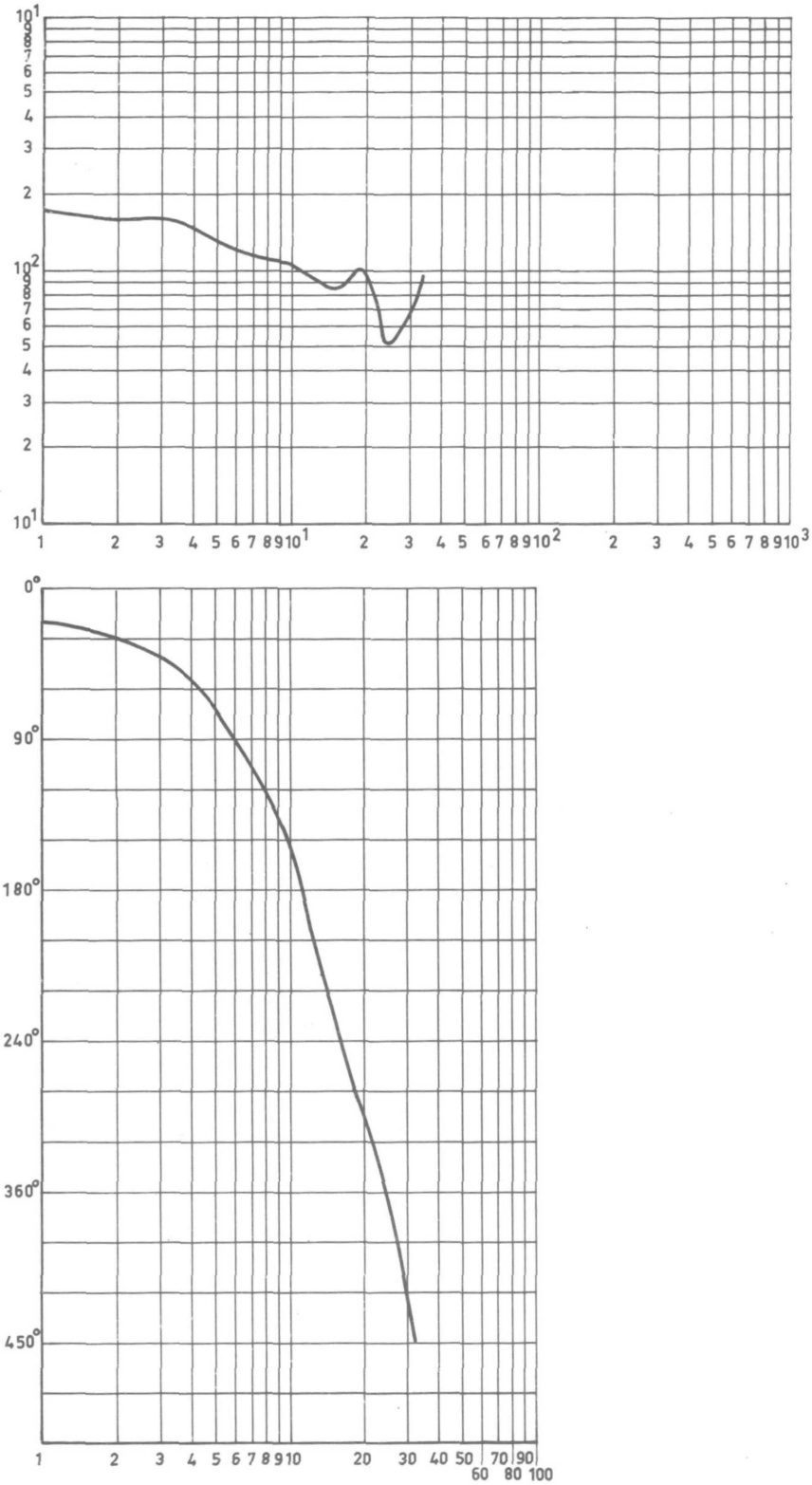

FIGURE 4.6-28.

Amplitude ratio and phase shift of the inlet impedance of the DMSP-steam generator test module.

No	feedwater flow [kg/s]	feedwater temp. ^0C	steam pressure MN/m^2	FLiNaK inlet temp. ^0C
5	79	222	18.5	623
6	142	227	18.5	618
7	145	224	18.5	619
8	144	224	18.5	622
12	147	241	18.0	626
1	75	267	18.0	620
4	77	273	18.5	618
15	76	280	18.0	620
3	134	282	18.0	632
9	142	270	18.8	623
10	146	270	18.7	622
11	145	271	18.4	620
2	201	287	18.0	626
14	145	251	14.0	630
13	145	275	14.0	630
16	142	280	18.0	630
17	146	273	14.5	670

FIGURE 4.6-29.

Conditions of frequency-response stability experiments performed on the DMSP-bayonet tube test module.

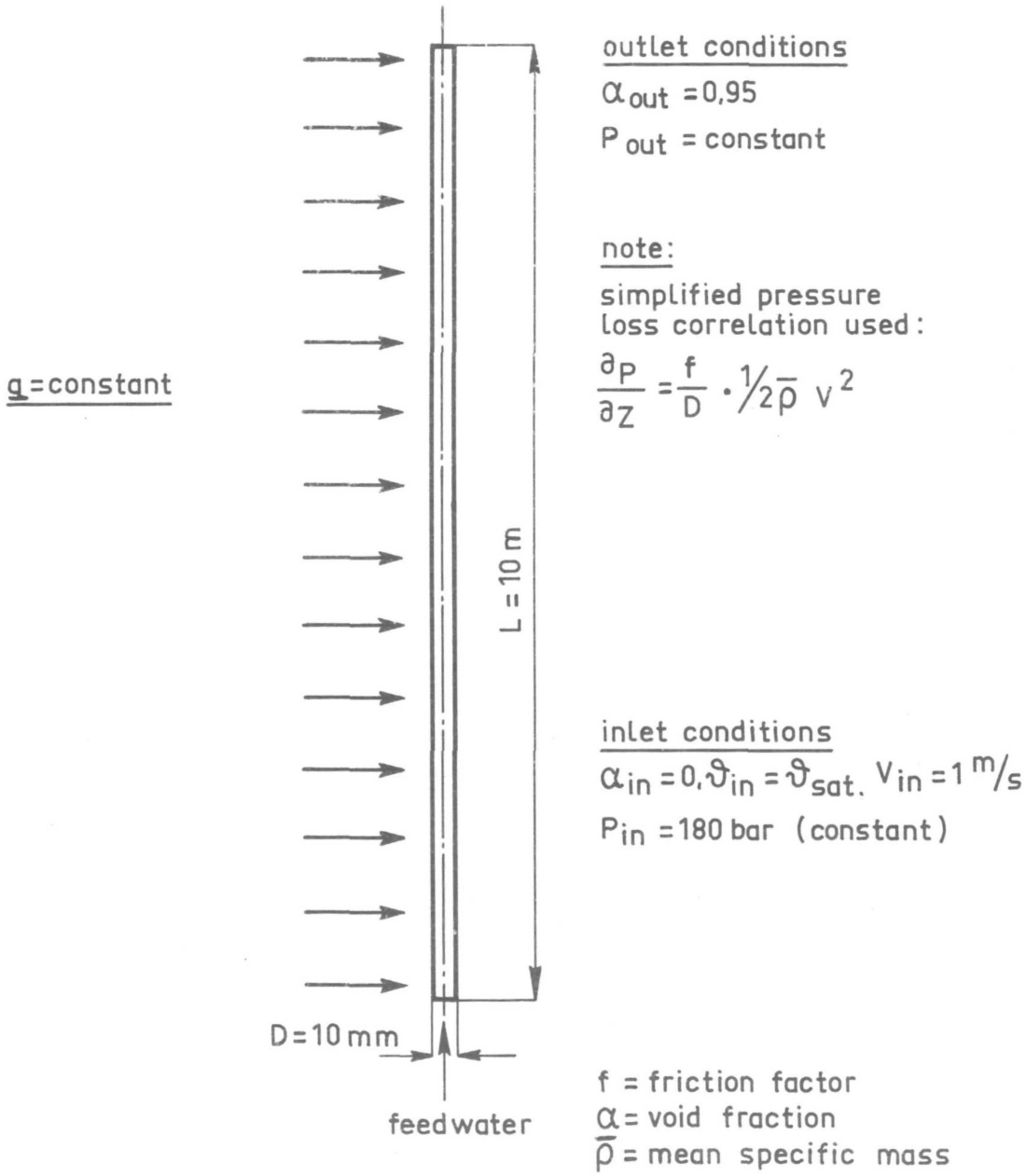

FIGURE 4.6-30.

Geometry and process conditions of the test case.

λ	ω	
	rad/s	(c/s)
- 0.38	1.10	(0.17)
- 1.10	2.37	(0.37)
- 2.71	3.76	(0.59)
- 6.13	4.12	(0.65)

FIGURE 4.6-31.

Data for determining eigenvalues $s = \lambda + i\omega$ obtained by application of the power method/vector deflation on the test-case shown in figure 4.6-30.

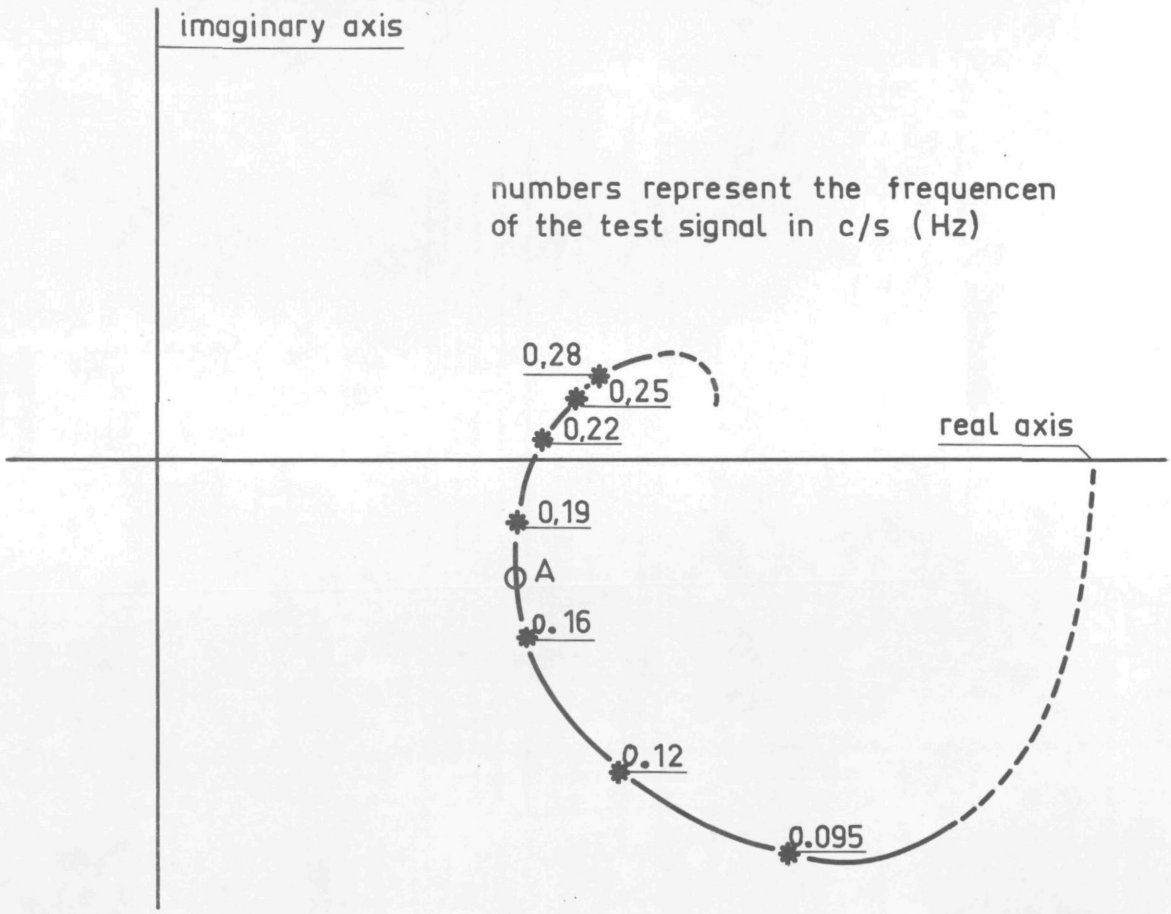

FIGURE 4.6-32.

Polar plot of the inlet impedance of the test case shown in fugyre 4.6-30 as computed by applying the CURSSE program.

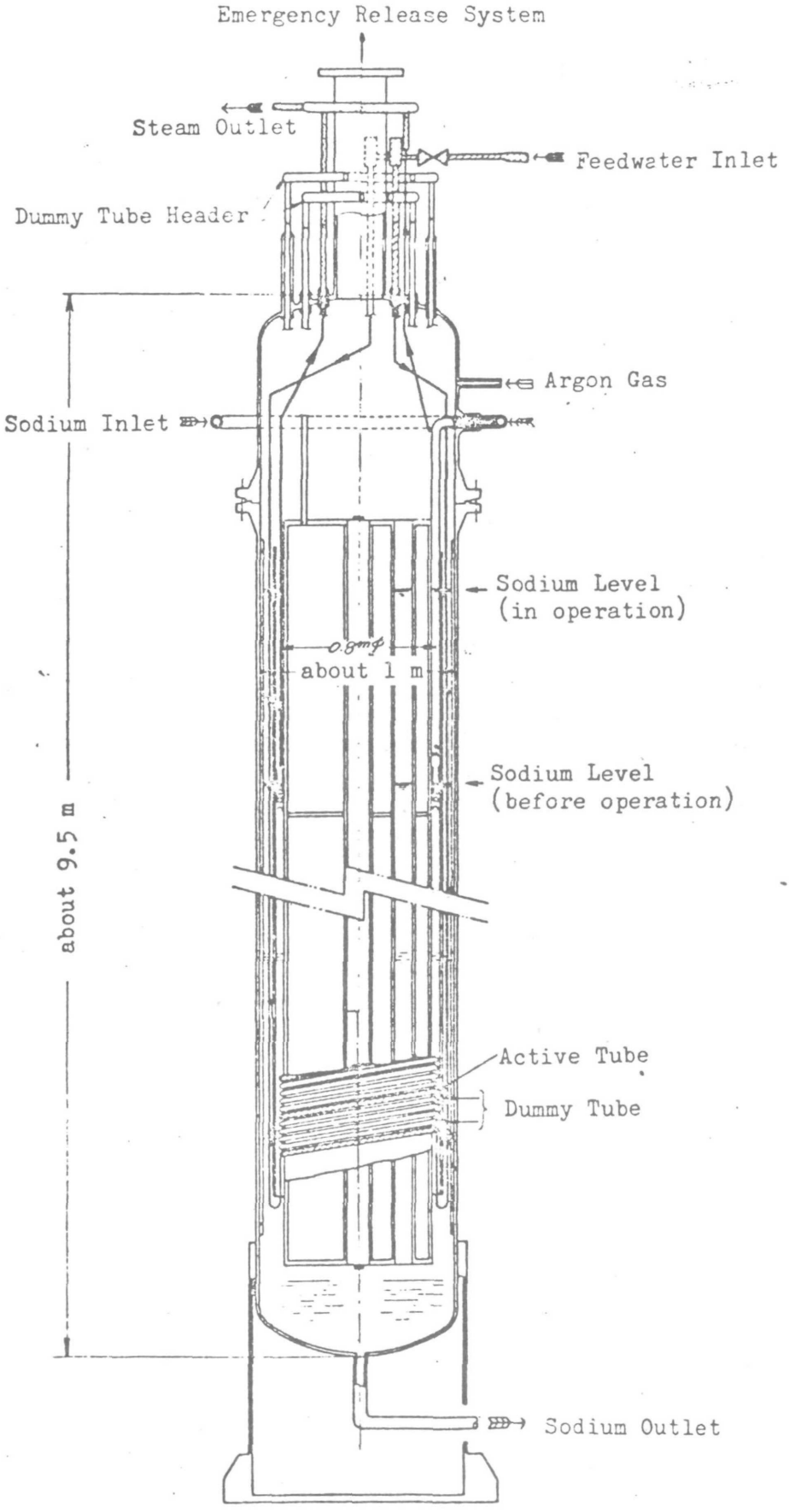

FIGURE 4.6-33.

1 MW_t steam generator-schematic.

Eigenvalues no.:	1	- 0.11709
	2	- 0.11899
	3	- 0.12230
	4	- 0.12654
	5	- 0.13194
	6	- 0.13464

FIGURE 4.6-34.

Table of the first smallest absolute eigenvalues computed for the 1 MW_{th} experiments (full load).

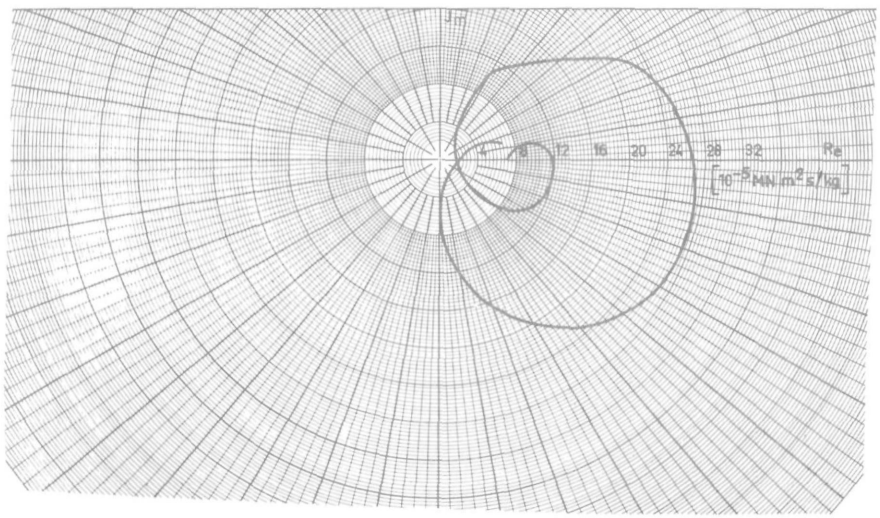

FIGURE a (M1).

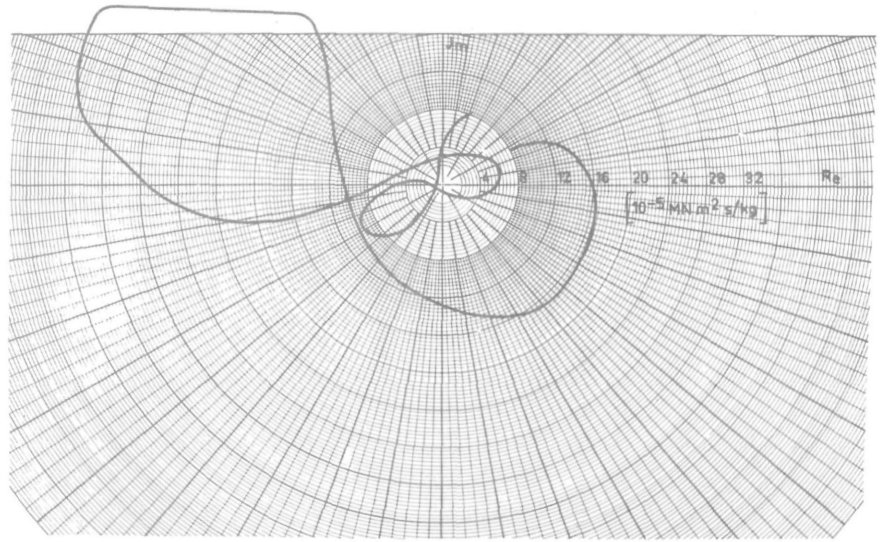

FIGURE b (M2).

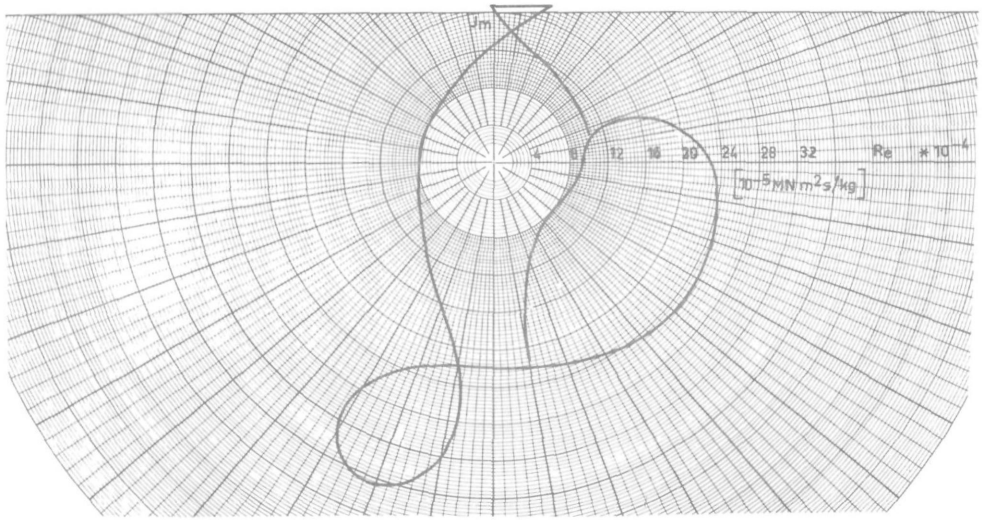

FIGURE c (M3).

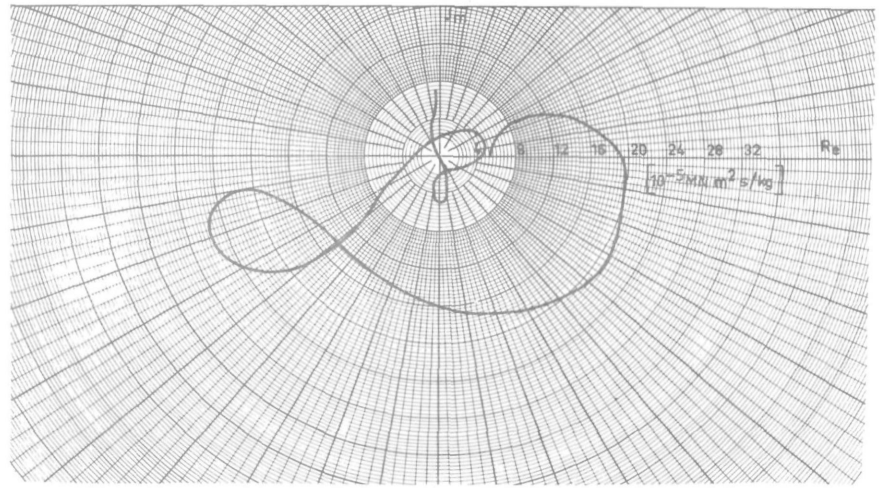

FIGURE d (M4).

FIGURE 4.6-35.

Polar plot of the inlet impedance of the 1 MW_{th} test module.

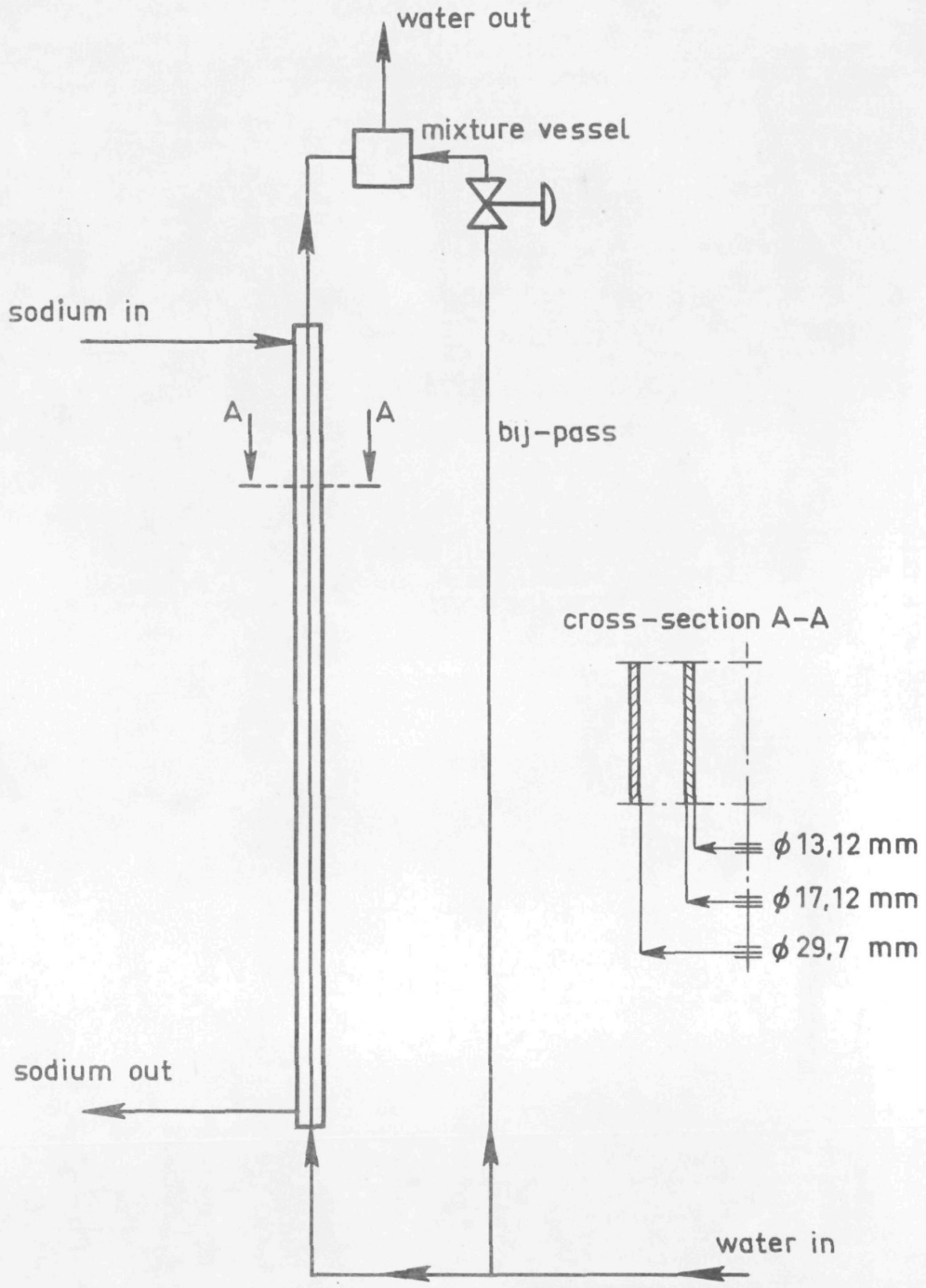

FIGURE 4.6-36.

Geometry of the SWISH test module.

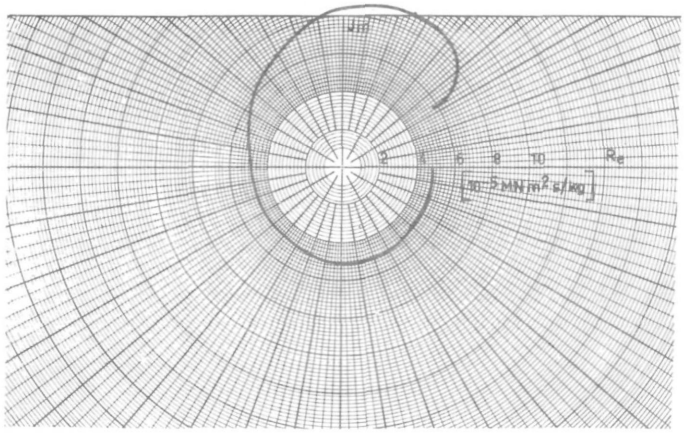

FIGURE a (M1).

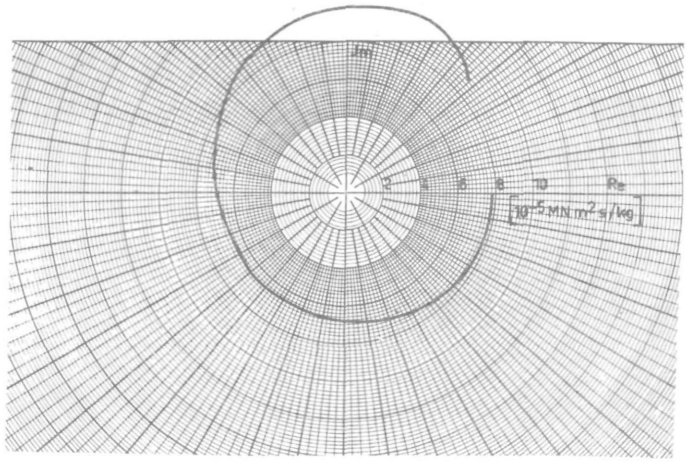

FIGURE b (M2).

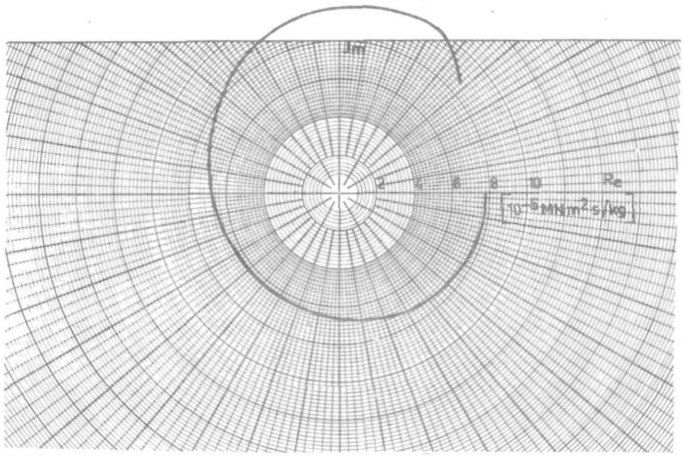

FIGURE c (M3).

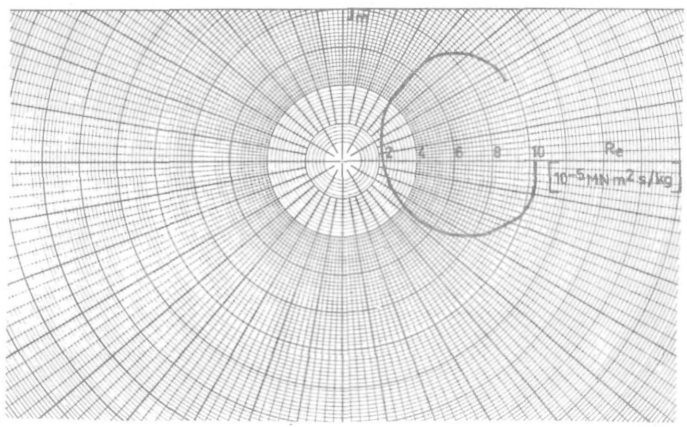

FIGURE d (M4).

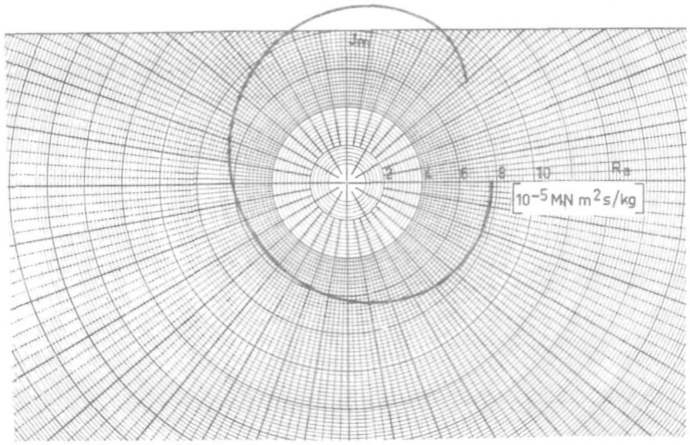

FIGURE e (M5).

FIGURE 4.6-37.

Polar plot of the inlet impedance of the SWISH test module.

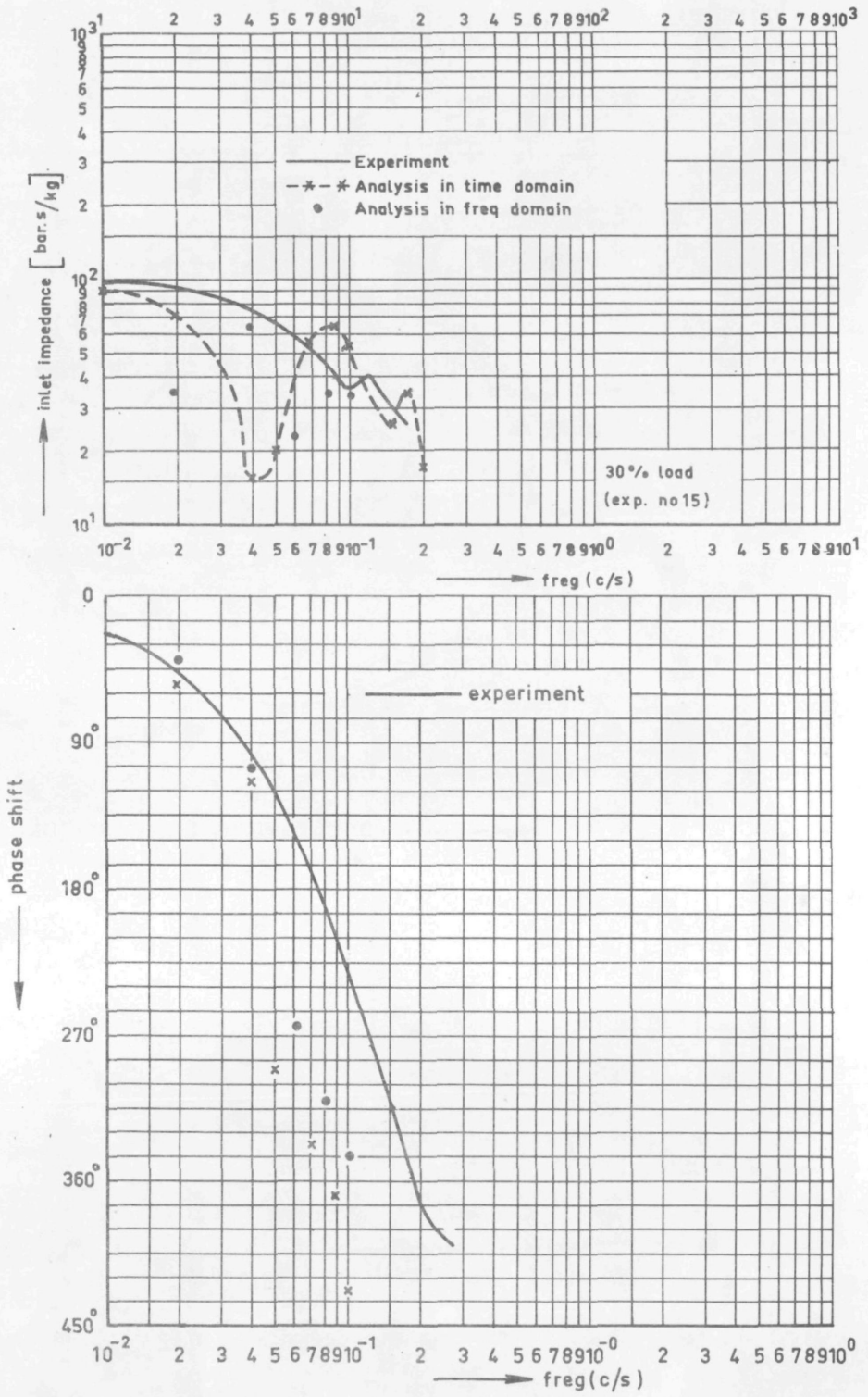

FIGURE 4.6-38 a + b.

Amplitude ratio and phase shift of the inlet impedance of the DMSP bayonet tube steam generator test module (30% load).

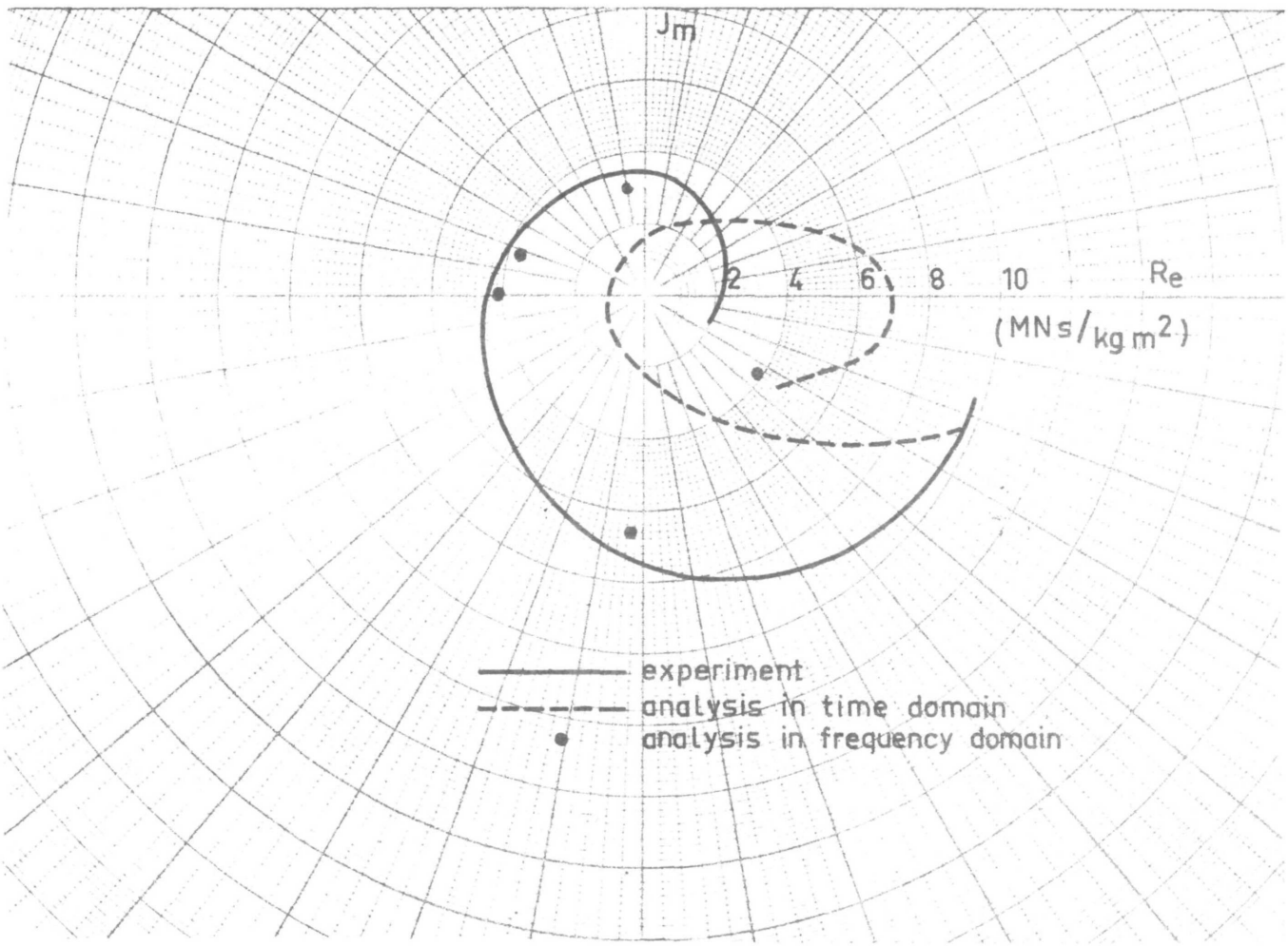

FIGURE 4.6-38c.

Polar plot of the inlet impedance of the DMSP bayonet tube steam generator test module (30% load).

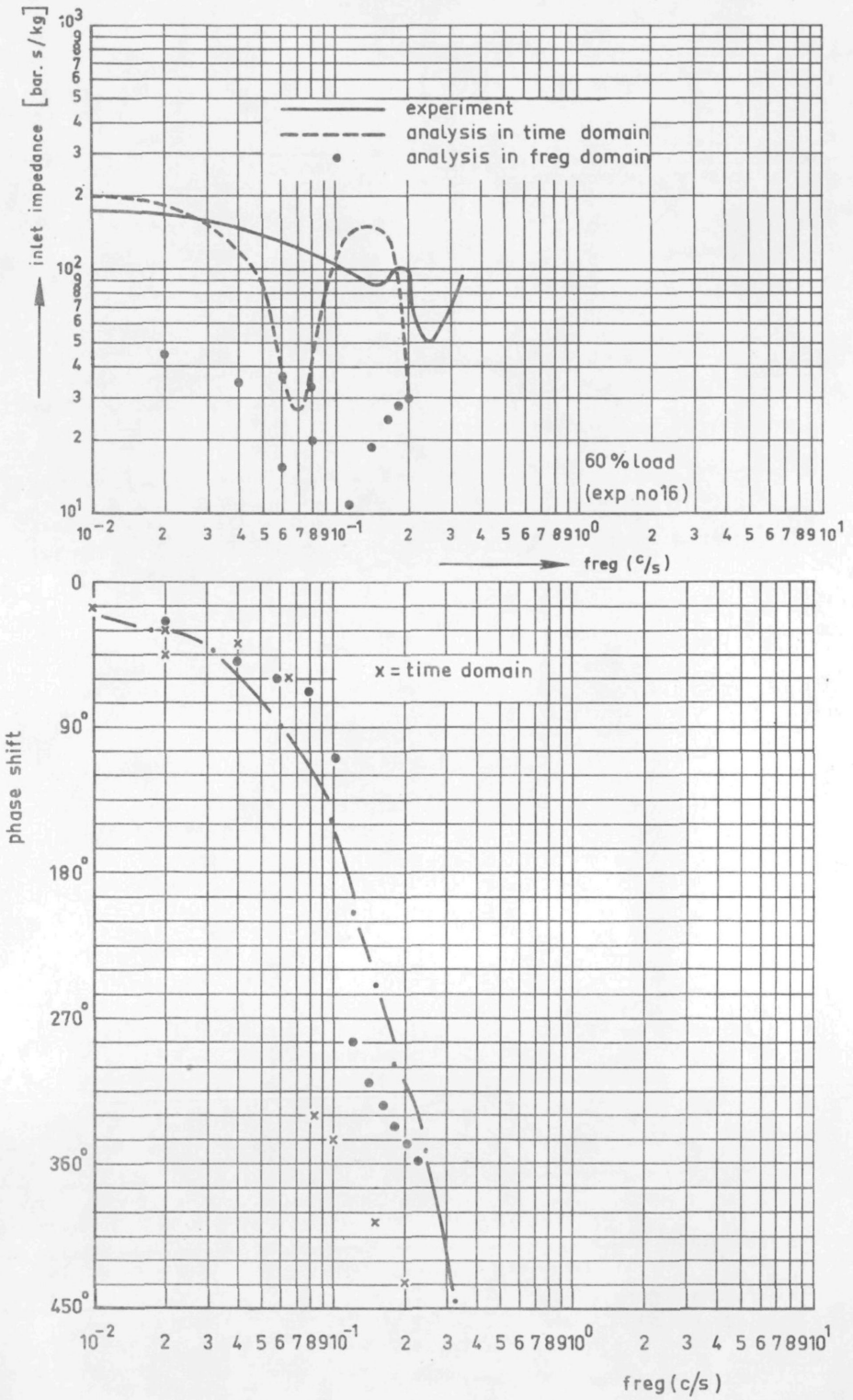

FIGURE 4.6-38 d + e.

Amplitude ratio and phase shift of the inlet impedance of the DMSP-bayonet tube steam generator test module (60% load).

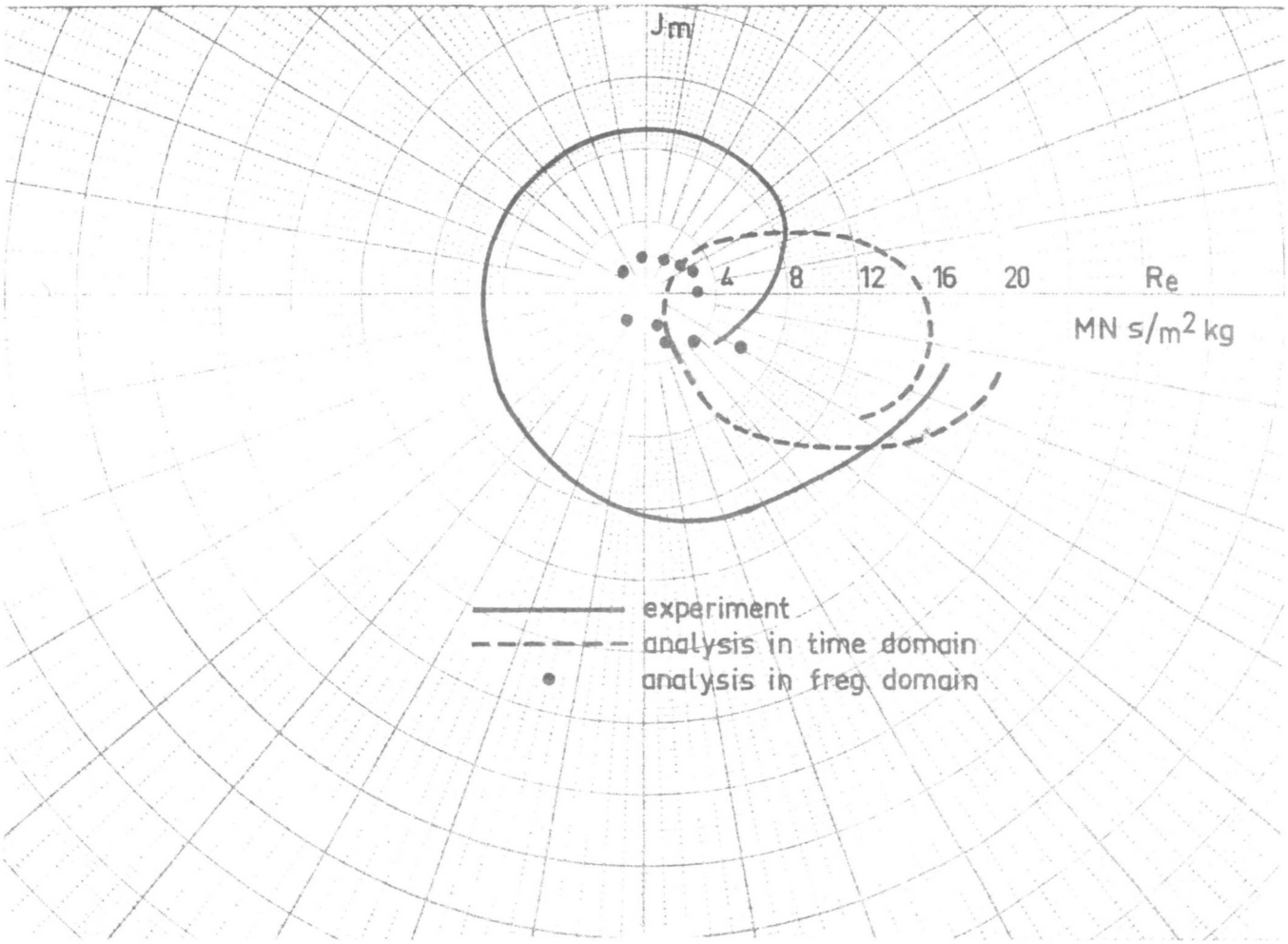

FIGURE 4.6-38f.

Polar plot of the inlet impedance of the DMSP bayonet tube steam generator test module (30% load).

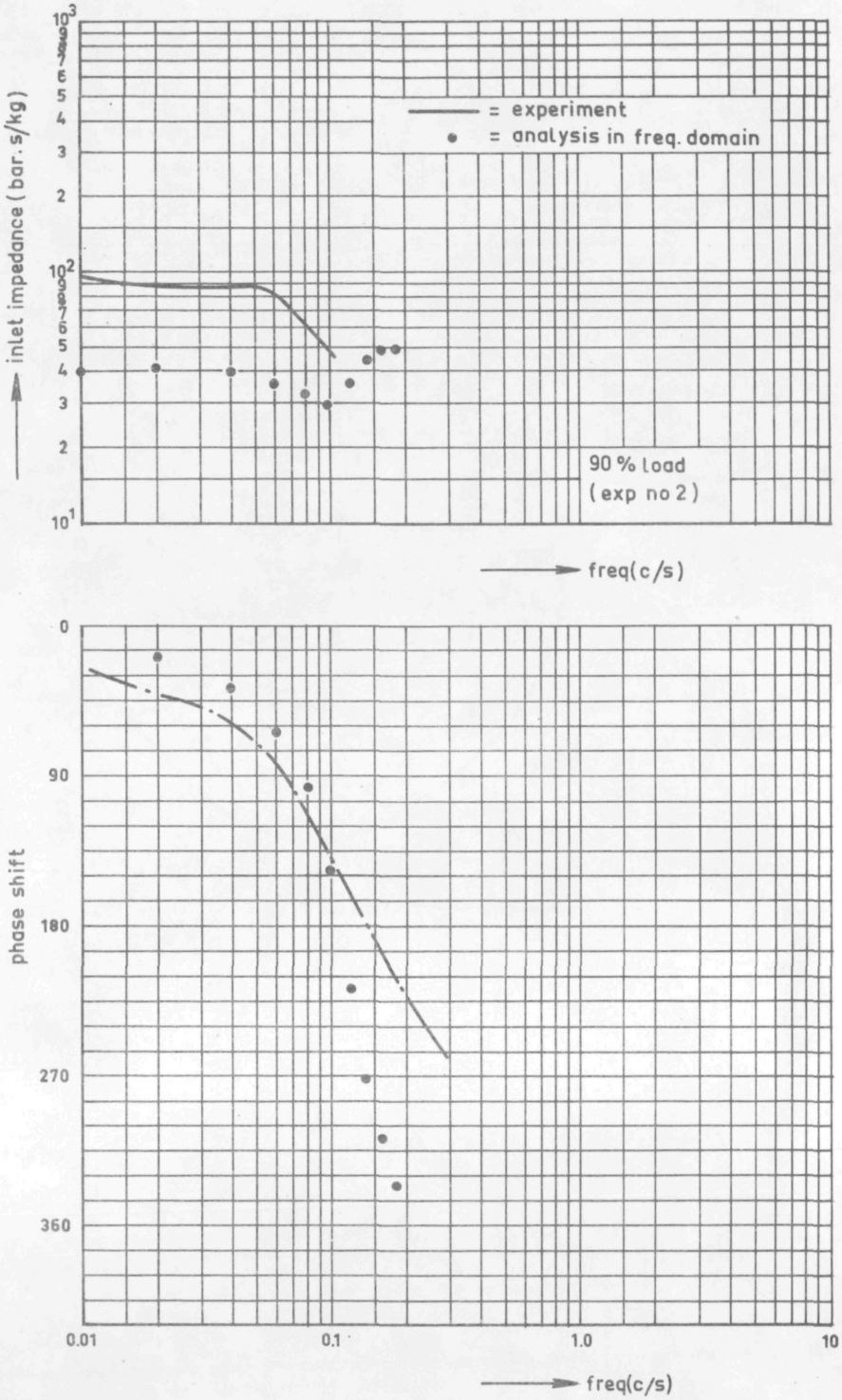

FIGURE 4.6-38 g + h.

Amplitude ratio and phase shift of the inlet impedance of the DMSP bayonet tube steam generator test module (90% load).

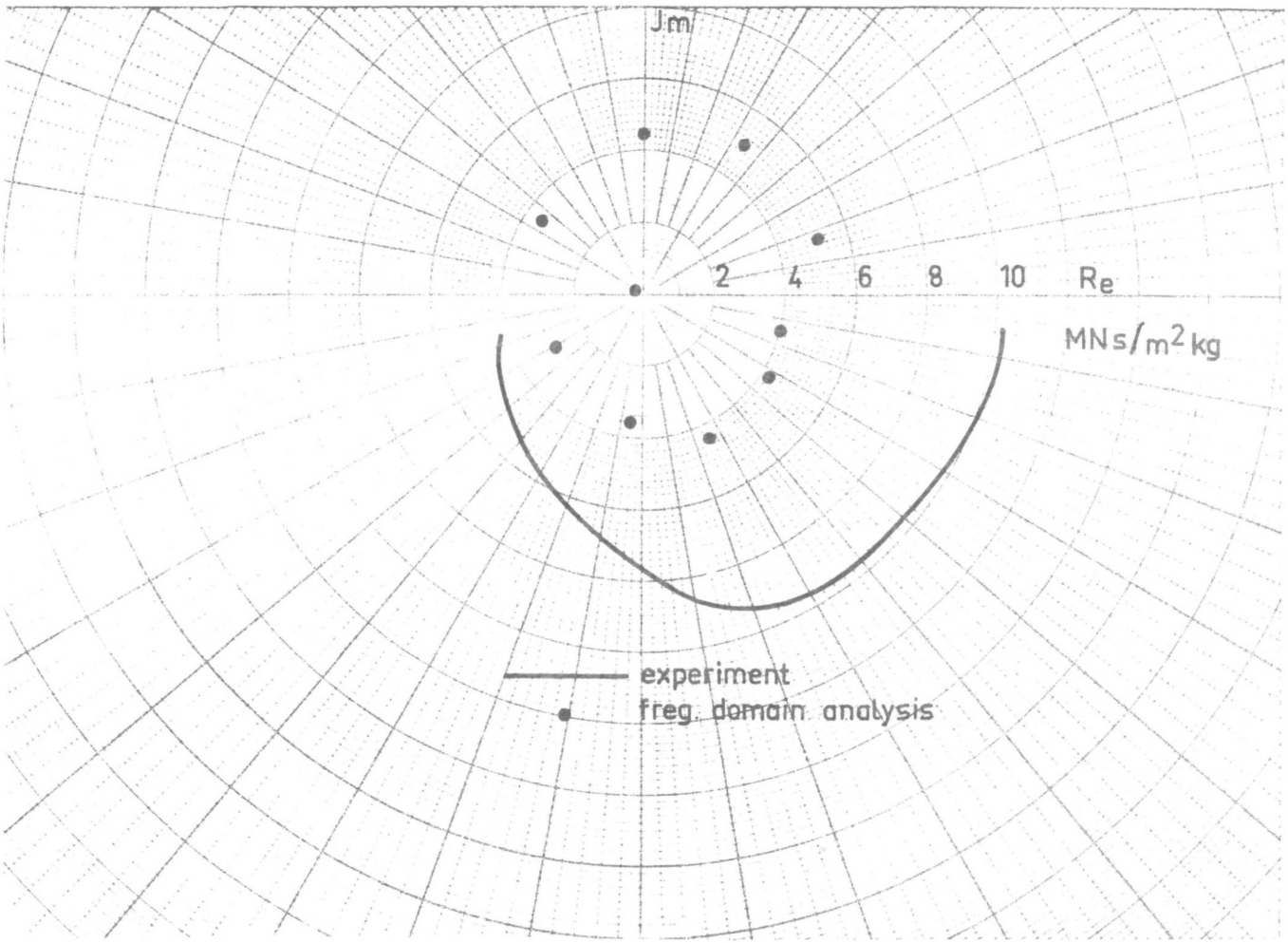

FIGURE 4.6-38i.

Polar plot of the inlet impedance of the DMSP bayonet tube steam generator test module (30% load).

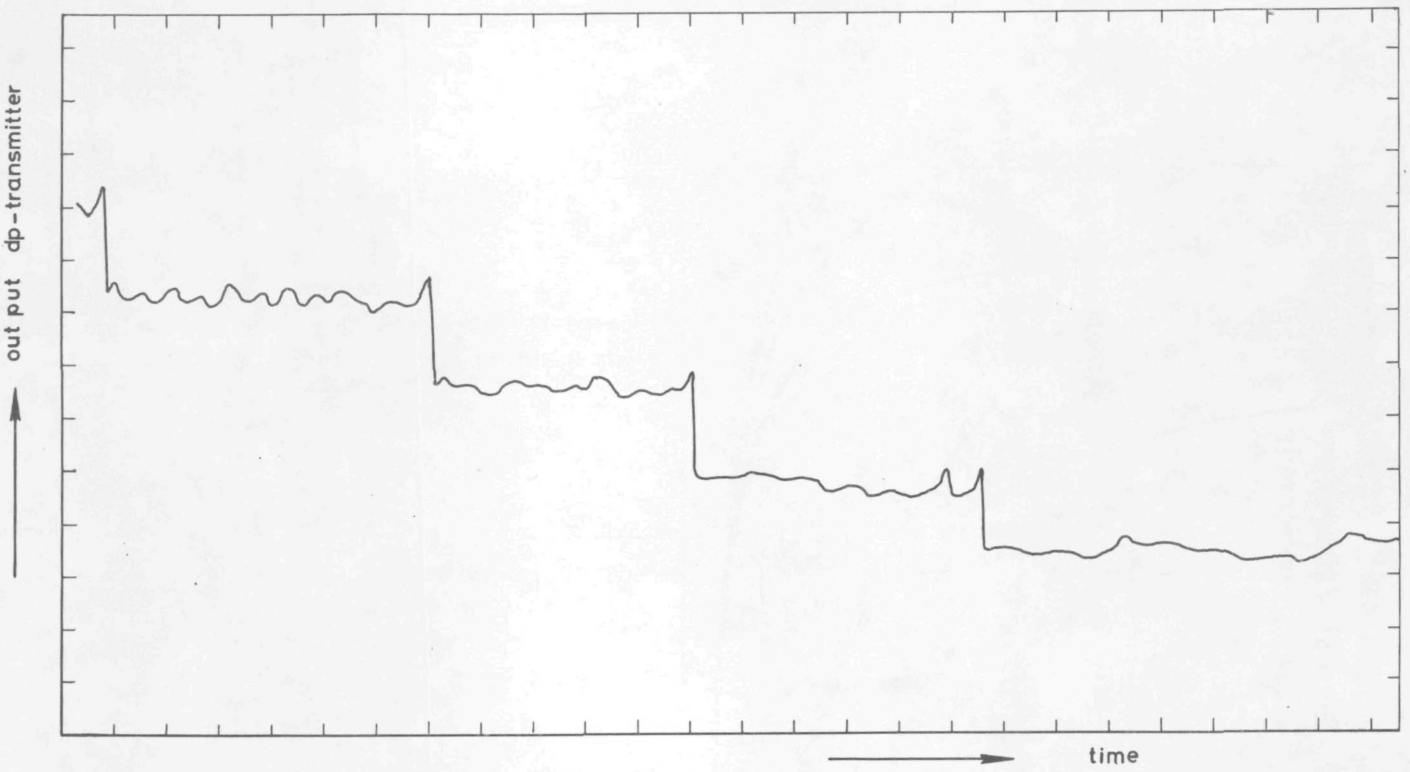

FIGURE 3A-1.

Output signal of the dP-meter.

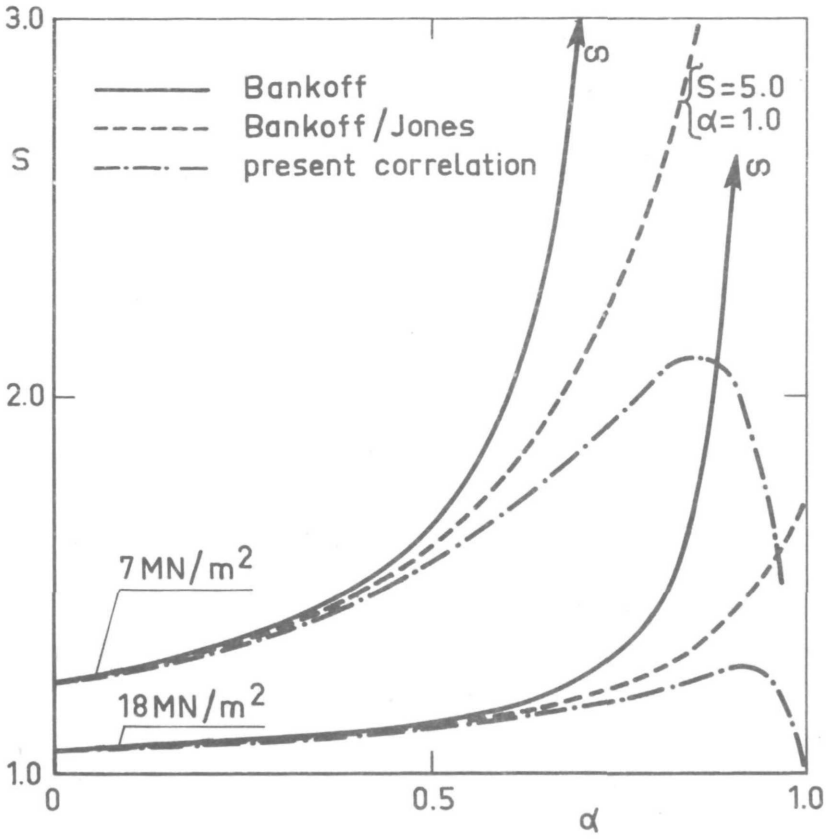

FIGURE 4B-1.

Slip values as given by Bankoff, Bankoff-Jones and present correlation.

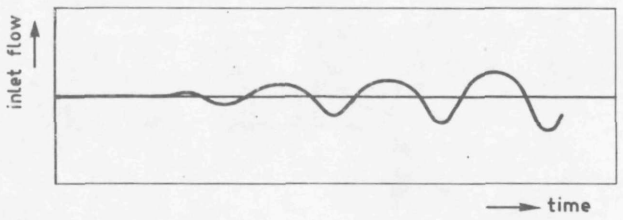

FIGURE 4F-1.

Typical shape of a developing oscillation.

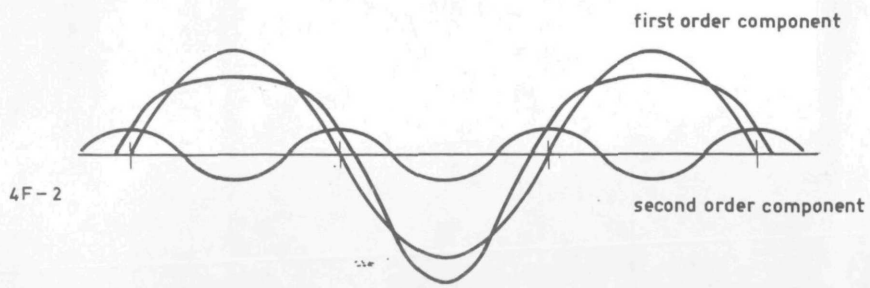

4F-2

FIGURE 4F-2.

Super position of a first order and a second order component

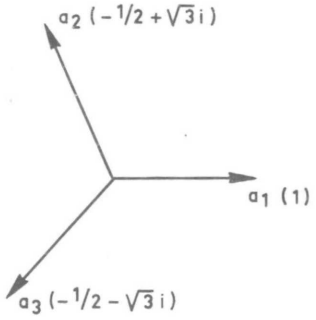

FIGURE 4F-3.

Graphical representation of the solution of equations (4F-4).

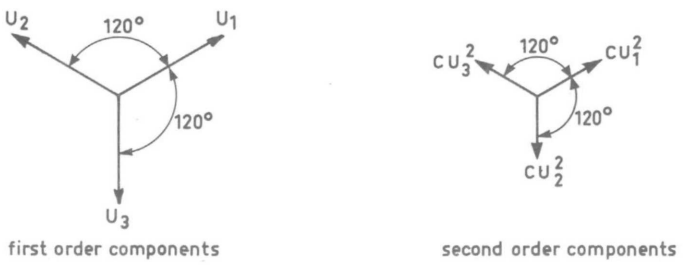

FIGURE 4F-4.

First and second order components of the predominant mode of oscillation.

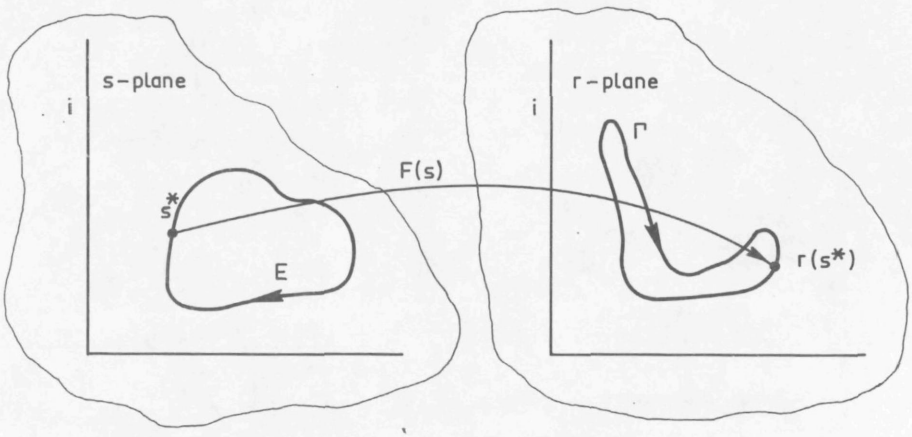

FIGURE 4G-1.

Mapping of a contour by a complex function.

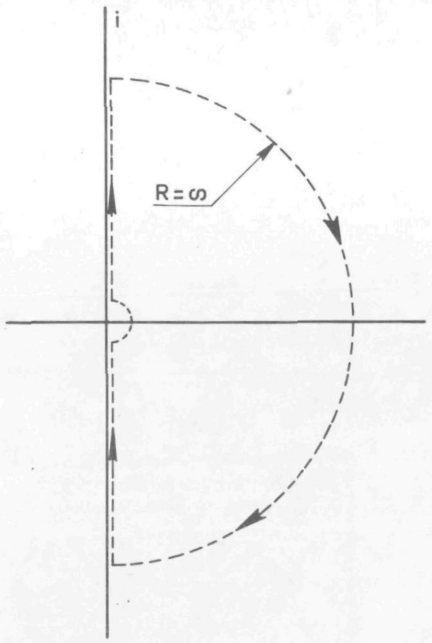

FIGURE 4G-2.

The Nyguist path.

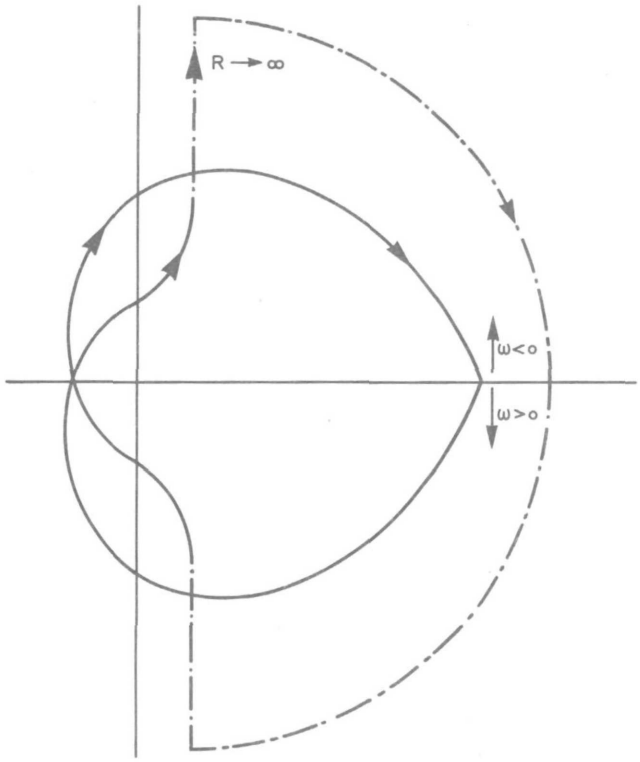

FIGURE 4G-3.
Schematized inlet impedance curve.

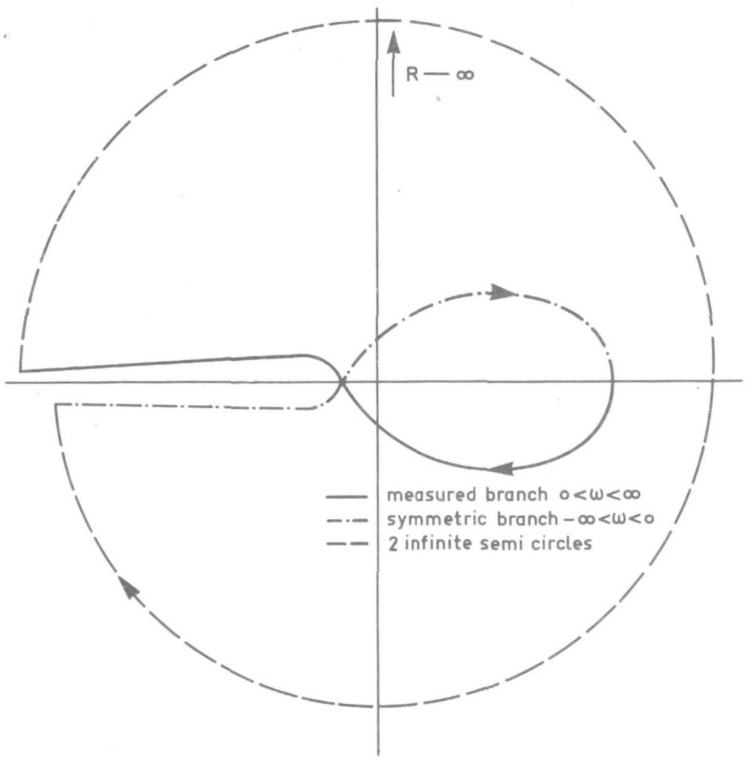

FIGURE 4G-4.
Mapping of the Nyguist path by M_{res}.

```
     ENERG  =EVP2*VP2+EVP1*VP1+EVH2*VH2+EVH1*VH1+EVG1*VG1+EVG2*VG2+EDTVP2*DTVP2+EDTVP1*DTVP1+EDTVH2*DTVH2+EDTVH1*DTVH1+E
VQ*VQ

UIT DE VOLGENDE 88 VERGELIJKINGEN :

   1. ENERG  =NRG1+NRG2+NRG3+NRG4
   2. NRG1   =E201+E202+E203+E204+E205
   3. NRG2   =E206+E207+E208+E209+E210
   4. NRG3   =E211+E212+E213+E214+E215
   5. NRG4   =E216+E217+E218+E219
   6. E213   =E2131*DZVUL+E2132*VVL+E2133*VAL+E2134*VRL
   7. E216   =E2161*DZVAL+E2162*VVG+E2163*VP
   8. E215   =E2151*DZVVG+E2152*VAL+E2153*VP
   9. E207   =E2071*DZVVG+E2072*VAL+E2073*VUG+E2074*VRG
  10. E214   =E2141*DZVRL+E2142*VVL+E2143*VAL+E2144*VUL
  11. E217   =E2171*DZVVL+E2172*VAL+E2173*VP
  12. E211   =E2111*DZVVL+E2112*VAL+E2113*VUL+E2114*VRL
  13. E212   =E2121*DZVAL+E2122*VVL+E2123*VUL+E2124*VRL
  14. E208   =E2081*DZVAL+E2082*VVG+E2083*VUG+E2084*VRG
  15. E218   =E2181*DZVAL+E2182*VVL+E2183*VP
  16. DTVRL1 =DRLDP1*DTVP1
  17. DTVX1  =DXDH1*DTVH1+DXDP1*DTVP1
  18. DTVHG1 =DHGDP1*DTVP1
  19. DTVRG1 =DRGDP1*DTVP1
  20. DTVHL1 =CHLP1*DTVP1+CHLH1*DTVH1+CHLX1*DTVX1
  21. DTVRL2 =DRLDP2*DTVP2
  22. VRL1   =DRLDP1*VP1
  23. VX1    =DXDH1*VH1+DXDP1*VP1
  24. VHG1   =DHGDP1*VP1
  25. VRG1   =DRGDP1*VP1
  26. VRL2   =DRLDP2*VP2
  27. VHL1   =DHLDP1*VP1+DHLDH1*VH1+DHLDX1*VX1
  28. DZVRL  =CDZ1*VRL1+CDZ2*VRL2
  29. VRM1   =CRMRL1*VRL1+CRMAL1*VAL1+CRMRG1*VRG1
  30. VX2    =DXDH2*VH2+DXDP2*VP2
  31. VVM1   =CVMG1*VG1+CVMRM1*VRM1
  32. VRG2   =DRGDP2*VP2
  33. E219   =CVQ*VQ
  34. DTVX2  =DXDH2*DTVH2+DXDP2*DTVP2
  35. DTVRG2 =DRGDP2*DTVP2
  36. DTVRG  =0.5*DTVRG1+0.5*DTVRG2
  37. E203   =CE203*DTVRG
  38. DTVAL  =0.5*DTVAL1+0.5*DTVAL2
  39. DTVRL  =0.5*DTVRL1+0.5*DTVRL2
  40. E206   =CE206*DTVRL
  41. E204   =CE204*DTVAL
  42. DTVUG1 =1.0*DTVHG1+CVUG21*DTVRG1+CVUG21*DTVP1
  43. DTVHG2 =DHGDP2*DTVP2
  44. DTVUL1 =1.0*DTVHL1+CVUL11*DTVRL1+CVUL21*DTVP1
  45. DTVHL2 =CHLP2*DTVP2+CHLH2*DTVH2+CHLX2*DTVX2
  46. DTVUG2 =1.0*DTVHG2+CVUG22*DTVRG2+CVUG21*DTVP2
  47. DTVUG  =0.5*DTVUG1+0.5*DTVUG2
  48. E202   =CE202*DTVUG
  49. DTVUL2 =1.0*DTVHL2+CVUL12*DTVRL2+CVUL22*DTVP2
  50. DTVUL  =0.5*DTVUL1+0.5*DTVUL2
  51. E205   =CE205*DTVUL
  52. E201   =CE201*DTVAL
```

FIGURE 4J-1a.

List of equations to be combined.
(two-phase energy balance)

```
53. DZVRG  =CDZ1*VRG1+CDZ2*VRG2
54. VUG1   =1.0*VHG1+CVUG11*VRG1+CVUG21*VP1
55. VUL1   =1.0*VHL1+CVUL11*VRL1+CVUL21*VP1
56. VRM2   =CRMRL2*VRL2+CRMAL2*VAL2+CRMRG2*VRG2
57. VVM2   =CVMG2*VG2+CVMRM2*VRM2
58. VAL    =0.5*VAL1+0.5*VAL2
59. DZVAL  =CDZ1*VAL1+CDZ2*VAL2
60. VHG2   =DHGDP2*VP2
61. VUG2   =1.0*VHG2+CVUG12*VRG2+CVUG22*VP2
62. VHL2   =DHLDP2*VP2+DHLDH2*VH2+DHLDX2*VX2
63. VUL2   =1.0*VHL2+CVUL12*VRL2+CVUL22*VP2
64. VRG    =0.5*VRG1+0.5*VRG2
65. VVG    =0.5*VVG1+0.5*VVG2
66. VRL    =0.5*VRL1+0.5*VRL2
67. DZVVL  =CDZ1*VVL1+CDZ2*VVL2
68. VVL    =0.5*VVL1+0.5*VVL2
69. DZVVG  =CDZ1*VVG1+CDZ2*VVG2
70. VUG    =0.5*VUG1+0.5*VUG2
71. VP     =0.5*VP1+0.5*VP2
72. E210   =E2101*DZVRG+E2102*VVG+E2103*VAL+E2104*VUG
73. DZVUG  =CDZ1*VUG1+CDZ2*VUG2
74. E209   =E2091*DZVUG+E2092*VVG+E2093*VAL+E2094*VRG
75. VUL    =0.5*VUL1+0.5*VUL2
76. DZVUL  =CDZ1*VUL1+CDZ2*VUL2
77. VVG2   =CVGRM2*VRM2+CVGVM2*VVM2+CVGAL2*VAL2+CVGRG2*VRG2+CVGRL2*VRL2+CVGS2*VS2
78. VVG1   =CVGRM1*VRM1+CVGVM1*VVM1+CVGAL1*VAL1+CVGRG1*VRG1+CVGRL1*VRL1+CVGS1*VS1
79. VS1    =CSH1*VH1+CSP1*VP1+CSG1*VG1
80. VS2    =CSH2*VH2+CSP2*VP2+CSG2*VG2
81. DTVS1  =CSH1*DTVH1+CSP1*DTVP1+CSG1*DTVG1
82. DTVS2  =CSH2*DTVH2+CSP2*DTVP2+CSG2*DTVG2
83. VAL1   =CALRL1*VRL1+CALX1*VX1+CALRG1*VRG1+CALS1*VS1
84. VAL2   =CALRL2*VRL2+CALX2*VX2+CALRG2*VRG2+CALS2*VS2
85. VVL2   =CVLRM2*VRM2+CVLVM2*VVM2+CVLAL2*VAL2+CVLRG2*VRG2+CVLRL2*VRL2+CVLS2*VS2
86. VVL1   =CVLRM1*VRM1+CVLVM1*VVM1+CVLAL1*VAL1+CVLRG1*VRG1+CVLRL1*VRL1+CVLS1*VS1
87. DTVAL2 =CALRL2*DTVRL2+CALX2*DTVX2+CALRG2*DTVRG2+CALS2*DTVS2
88. DTVAL1 =CALRL1*DTVRL1+CALX1*DTVX1+CALRG1*DTVRG1+CALS1*DTVS1
```

FIGURE 4J-1b.

List of equations to be combined.
(two-phase energy balance)

```
ENR001=E2082+E2092+E2102                                                ENERG  0
ENR002=E2071*CDZ2+ENR001*0.5                                            ENERG  5
ENR003=ENR002*CVGRM2+ENR002*CVGVM2*CVMRM2                               ENERG 10
ENR004=E2072+E2093+E2103                                                ENERG 15
ENR005=ENR003*CRMAL2+ENR002*CVGAL2+ENR004*0.5+E2081*CDZ2                ENERG 20
ENR006=E2073+E2083+E2104                                                ENERG 25
ENR007=ENR006*0.5+E2091*CDZ2                                            ENERG 30
ENR008=E2074+E2084+E2094                                                ENERG 35
ENR009=ENR005*CALS2+ENR002*CVGS2                                        ENERG 40
ENR010=E2071*CDZ1+ENR001*0.5                                            ENERG 45
ENR011=ENR010*CVGVM1+E2111*CDZ1*CVLVM1                                  ENERG 50
ENR012=ENR010*CVGRM1+ENR011*CVMRM1+E2111*CDZ1*CVLRM1                    ENERG 55
ENR013=ENR012*CRMAL1+ENR010*CVGAL1+ENR004*0.5+E2081*CDZ1                ENERG 60
ENR014=ENR010*CVGRM1+ENR010*CVGVM1*CVMRM1+E2111*CDZ1*CVLRM1             ENERG 65
ENR015=ENR014*CRMAL1+ENR010*CVGAL1+ENR004*0.5+E2081*CDZ1                ENERG 70
ENR016=ENR006*0.5+E2091*CDZ1                                            ENERG 75
ENR017=ENR015*CALS1+ENR010*CVGS1                                        ENERG 80
ENR018=CE201+CE204                                                      ENERG 85
ENR019=ENR018*0.5*CALX2+CE205*0.5*CHLX2                                 ENERG 90
ENR020=ENR018*0.5*CALX1+CE205*0.5*CHLX1                                 ENERG 95
ENR021=E2122+E2132+E2142                                                ENERG100
ENR022=E2111*CDZ2+ENR021*0.5                                            ENERG105
ENR023=ENR003+ENR022*CVLRM2+ENR022*CVLVM2*CVMRM2                        ENERG110
ENR024=ENR022*CVLRM2+ENR022*CVLVM2*CVMRM2                               ENERG115
ENR025=E2112+E2133+E2143                                                ENERG120
ENR026=ENR005+ENR024*CRMAL2+ENR022*CVLAL2+ENR025*0.5+E2121*CDZ2         ENERG125
ENR027=E2113+E2123+E2144                                                ENERG130
ENR028=ENR027*0.5+E2131*CDZ2                                            ENERG135
ENR029=E2114+E2124+E2134                                                ENERG140
ENR030=ENR026*CALX2+ENR028*DHLDX2                                       ENERG145
ENR031=ENR024*CRMAL2+ENR022*CVLAL2+ENR025*0.5+E2121*CDZ2                ENERG150
ENR032=ENR009+ENR031*CALS2+ENR022*CVLS2                                 ENERG155
ENR033=E2111*CDZ1+ENR021*0.5                                            ENERG160
ENR034=ENR021*0.5*CVLRM1+ENR021*0.5*CVLVM1*CVMRM1+E2151*CDZ1*           ENERG165
& CVGRM1                                                                ENERG170
ENR035=ENR013+ENR033*CVLAL1+ENR025*0.5+E2121*CDZ1+ENR034*CRMAL1         ENERG175
ENR036=ENR027*0.5+E2131*CDZ1                                            ENERG180
ENR037=ENR035*CALX1+ENR036*DHLDX1                                       ENERG185
ENR038=ENR033*CVLVM1*CVMRM1+ENR021*0.5*CVLRM1+E2151*CDZ1*CVGRM1         ENERG190
ENR039=ENR038*CRMAL1+ENR033*CVLAL1+ENR025*0.5+E2121*CDZ1                ENERG195
ENR040=ENR017+ENR039*CALS1+ENR033*CVLS1                                 ENERG200
ENR041=E2151*CDZ2+E2162*0.5                                             ENERG205
ENR042=ENR041*CVGVM2+E2171*CDZ2*CVLVM2                                  ENERG210
ENR043=ENR023+ENR041*CVGRM2+ENR042*CVMRM2+E2171*CDZ2*CVLRM2             ENERG215
ENR044=ENR041*CVGRM2+ENR042*CVMRM2+E2171*CDZ2*CVLRM2                    ENERG220
ENR045=E2152+E2172                                                      ENERG225
ENR046=ENR026+ENR044*CRMAL2+ENR041*CVGAL2+ENR045*0.5+E2161*CDZ2+        ENERG230
& E2171*CDZ2*CVLAL2                                                     ENERG235
ENR047=ENR002+E2151*CDZ2+E2162*0.5                                      ENERG240
ENR048=ENR022+E2171*CDZ2                                                ENERG245
ENR049=ENR044*CRMAL2+ENR041*CVGAL2+ENR045*0.5+E2161*CDZ2+E2171*         ENERG250
& CDZ2*CVLAL2                                                           ENERG255
ENR050=ENR030+ENR049*CALX2                                              ENERG260
ENR051=ENR032+ENR049*CALS2+ENR041*CVGS2+E2171*CDZ2*CVLS2                ENERG265
ENR052=E2153+E2163+E2173                                                ENERG270
ENR053=ENR021*0.5+E2171*CDZ1                                            ENERG275
ENR054=E2151*CDZ1+E2162*0.5                                             ENERG280
ENR055=ENR054*CVGVM1+E2171*CDZ1*CVLVM1                                  ENERG285
ENR056=ENR055*CVMRM1+E2162*0.5*CVGRM1+E2171*CDZ1*CVLRM1                 ENERG290
ENR057=E2161+E2181                                                      ENERG295
ENR058=ENR010+E2151*CDZ1+E2162*0.5                                      ENERG300
ENR059=ENR033+E2171*CDZ1                                                ENERG305
ENR060=ENR056*CRMAL1+ENR054*CVGAL1+ENR045*0.5+ENR057*CDZ1+E2171*        ENERG310
& CDZ1*CVLAL1                                                           ENERG315
ENR061=ENR037+ENR060*CALX1                                              ENERG320
ENR062=ENR056*CRMAL1+ENR054*CVGAL1+ENR045*0.5+E2161*CDZ1+E2171*         ENERG325
& CDZ1*CVLAL1                                                           ENERG330
ENR063=ENR040+ENR062*CALS1+ENR054*CVGS1+E2171*CDZ1*CVLS1                ENERG335
ENR064=ENR043+E2182*0.5*CVLRM2+E2182*0.5*CVLVM2*CVMRM2                  ENERG340
ENR065=E2182*0.5*CVLRM2+E2182*0.5*CVLVM2*CVMRM2                         ENERG345
ENR066=ENR046+E2181*CDZ2+ENR065*CRMAL2+E2182*0.5*CVLAL2                 ENERG350
ENR067=ENR048+E2182*0.5                                                 ENERG355
ENR068=E2181*CDZ2+ENR065*CRMAL2+E2182*0.5*CVLAL2                        ENERG360
ENR069=ENR050+ENR068*CALX2                                              ENERG365
ENR070=ENR051+ENR068*CALS2+E2182*0.5*CVLS2                              ENERG370
ENR071=ENR052+E2183                                                     ENERG375
ENR072=ENR053+E2182*0.5                                                 ENERG380
ENR073=E2171*CDZ1+E2182*0.5                                             ENERG385
ENR074=ENR059+E2182*0.5                                                 ENERG390
ENR075=E2182*0.5*CVLRM1+E2182*0.5*CVLVM1*CVMRM1                         ENERG395
ENR076=ENR075*CRMAL1+E2182*0.5*CVLAL1                                   ENERG400
ENR077=ENR061+ENR076*CALX1                                              ENERG405
ENR078=E2181*CDZ1+ENR075*CRMAL1+E2182*0.5*CVLAL1                        ENERG410
ENR079=ENR063+ENR078*CALS1+E2182*0.5*CVLS1                              ENERG415
```

FIGURE 4J-2.

List of common factors (punched automatically).

```
 EVP2=(ENR064*CRMRL2+ENR066*CALRL2+ENR047*CVGRL2+ENR067*CVLRL2+      ENERG420
&ENR028*CVUL12+ENR029*0.5+E2141*CDZ2)*DRLDP2+ENR069*DXDP2+          ENERG425
&(ENR066*CALRG2+ENR064*CRMRG2+ENR047*CVGRG2+ENR007*CVUG12+ENR008*   ENERG430
&0.5+E2101*CDZ2+ENR067*CVLRG2)*DRGDP2+ENR070*CSP2+ENR007*DHGDP2+    ENERG435
&ENR007*CVUG22+ENR028*DHLDP2+ENR028*CVUL22+ENR071*0.5               ENERG440
 EVP1=((ENR012+ENR072*CVLRM1+(ENR072*CVLVM1+ENR054*CVGVM1)*CVMRM1+  ENERG445
&ENR054*CVGRM1)*CRMRL1+(ENR035+(ENR056+E2182*0.5*CVLRM1+E2182*      ENERG450
&0.5*CVLVM1*CVMRM1)*CRMAL1+ENR054*CVGAL1+ENR045*0.5+ENR057*CDZ1+    ENERG455
&ENR073*CVLAL1)*CALRL1+ENR058*CVGRL1+ENR074*CVLRL1+ENR036*CVUL11+   ENERG460
&ENR029*0.5+E2141*CDZ1)*DRLDP1+ENR077*DXDP1+((ENR015+(ENR038+       ENERG465
&(ENR055+E2182*0.5*CVLVM1)*CVMRM1+E2162*0.5*CVGRM1+ENR073*          ENERG470
&CVLRM1)*CRMAL1+ENR074*CVLAL1+(ENR025+ENR045)*0.5+(E2121+ENR057)*   ENERG475
&CDZ1+ENR054*CVGAL1)*CALRG1+(ENR014+(ENR074*CVLVM1+ENR054*          ENERG480
&CVGVM1)*CVMRM1+ENR072*CVLRM1+ENR054*CVGRM1)*CRMRG1+ENR058*         ENERG485
&CVGRG1+ENR016*CVUG11+ENR008*0.5+E2101*CDZ1+ENR074*CVLRG1)*         ENERG490
&DRGDP1+ENR079*CSP1+ENR016*DHGDP1+ENR016*CVUG21+ENR036*DHLDP1+      ENERG495
&ENR036*CVUL21+ENR071*0.5                                           ENERG500
 EVH2=ENR069*DXDH2+ENR070*CSH2+ENR028*DHLDH2                        ENERG505
 EVH1=ENR077*DXDH1+(ENR040+(ENR060+ENR075*CRMAL1+E2182*0.5*         ENERG510
&CVLAL1)*CALS1+ENR054*CVGS1+ENR073*CVLS1)*CSH1+ENR036*DHLDH1        ENERG515
 EVG1=ENR079*CSG1+(ENR011+ENR072*CVLVM1+ENR054*CVGVM1)*CVMG1        ENERG520
 EVG2=ENR070*CSG2+(ENR047*CVGVM2+ENR067*CVLVM2)*CVMG2               ENERG525
 EDTVP2=(ENR018*0.5*CALRL2+CE205*0.5*CVUL12+CE206*0.5)*DRLDP2+      ENERG530
&ENR019*DXDP2+(ENR018*0.5*CALRG2+CE202*0.5*CVUG22+CE203*0.5)*       ENERG535
&DRGDP2+ENR018*0.5*CALS2*CSP2+CE202*0.5*DHGDP2+CE202*0.5*CVUG21+    ENERG540
&CE205*0.5*CHLP2+CE205*0.5*CVUL22                                   ENERG545
 EDTVP1=(ENR018*0.5*CALRL1+CE205*0.5*CVUL11+CE206*0.5)*DRLDP1+      ENERG550
&ENR020*DXDP1+(ENR018*0.5*CALRG1+CE202*0.5*CVUG21+CE203*0.5)*       ENERG555
&DRGDP1+ENR018*0.5*CALS1*CSP1+CE202*0.5*DHGDP1+CE202*0.5*CVUG21+    ENERG560
&CE205*0.5*CHLP1+CE205*0.5*CVUL21                                   ENERG565
 EDTVH2=ENR019*DXDH2+ENR018*0.5*CALS2*CSH2+CE205*0.5*CHLH2          ENERG570
 EDTVH1=ENR020*DXDH1+ENR018*0.5*CALS1*CSH1+CE205*0.5*CHLH1          ENERG575
 EVQ=CVQ                                                            ENERG580
 EDTVG1=ENR018*0.5*CALS1*CSG1                                       ENERG585
 EDTVG2=ENR018*0.5*CALS2*CSG2                                       ENERG590
 ENERG=EVP2*VP2+EVP1*VP1+EVH2*VH2+EVH1*VH1+EVG1*VG1+EVG2*VG2+       ENERG595
&EDTVP2*DTVP2+EDTVP1*DTVP1+EDTVH2*DTVH2+EDTVH1*DTVH1+EVQ*VQ+        ENERG600
&EDTVG1*DTVG1+EDTVG2*DTVG2                                          ENERG605
```

FIGURE 4J-3.

Expressions in the coefficients of the 88 combined equations.

```
0.54876033273007990D 15
0.10833243125568500D 14
0.33203737508817200D 15
0.56185135931479990D 13
0.50568733984969990D 13
0.18727571739981650D 15
0.32766090000000000D 07
0.57746100000000000D 06
0.18100440000000000D 07
0.20344800000000000D 06
0.10500000000000000D 03
0.15984000000000000D 06
0.79409400000000000D 06

ENERG=  4.12047665440432000D 16
```

FIGURE 4J-4.

Output of the check: the two-numerical values to be compared have been underlined. Following these a message is printed indicating that the substitution has been successfull.